Implantable Intracranial Pressure Sensor to Control Hydrocephalus

By

Xuan Zhang

A dissertation submitted in partial fulfillment of

the requirements for the degree of

Doctor of Philosophy

(Electrical Engineering)

at the

UNIVERSITY OF WISCONSIN-MADISON

2018

Date of final oral examination: 4/24/2018

The dissertation is approved by the following members of the Final Oral Committee:

Yuhen Hu, Professor, Electrical and computer engineering

John G. Webster, Professor, Biomedical Engineering

Joshua E. Medow, Associate Professor, Neurological Surgery

Bermans J. Iskandar, Professor, Neurological Surgery

Hongrui Jiang, Professor, Electrical and computer engineering

ABSTRACT

Hydrocephalus is a medical condition where excessive accumulation of CerebroSpinal Fluid (CSF) leads to an abnormal increase of Intracranial Pressure (ICP). Early and timely detection of elevated ICP is very important to mitigate symptoms during the entire life of the patient to avoid headaches, mental disability and death caused by abnormal increased ICP.

We present a smart shunt system instead of a traditional passive shunt. The system includes an ICP sensor, Radio-frequency identification (RFID)-based sensor tag, active piezoelectric-valve, valve driver, rechargeable battery, and external wireless communication as well as a wireless charging system. We describe own fabricated active capacitance pressure, and also a passive resonance pressure sensor design for continuous ICP measurement. The active sensor consist of two metal plates transduces the pressure change to capacitance change, and the passive sensor consisting of two spiral coils transduces the pressure change to a resonant frequency shift. Prototypes were developed, and measurement results demonstrate that the active capacitive sensor achieves good performance: 0 – 1000 mmHg measurement range, 0.033% accuracy, 0.022 mmHg (0.001 pF) resolution, and from ±0.136 mmHg to ±0.5 mmHg 2 months long term drift value for 10 different capacitive pressure sensors. Here 0.5 mmHg corresponds to 0.05% Full Scale Output (FSO) with a full range of 0 to 1000 mmHg.

ACKNOWLEDGMENTS

I would like to express my special thanks to my senior advisor Professor John Webster and my advisor Professor Yu Hen Hu, who have been tremendous mentors for me and contributed immensely to my professional and personal time at the University of Wisconsin-Madison. I appreciate all your contributions of time, ideas, and encouragement to make my Ph.D. experience productive. It has been an honor to be one of Prof. Webster's last Ph.D. students. I would also like to thank my committee members and project PIs, Professor Joshua E. Medow and Professor Bermans J. Iskandar, thank you so much for supporting me and guiding me in the past years. I appreciate all your contributions of time, ideas, and wonderful suggestions. The joy and enthusiasm you have for my research was contagious and motivational. I would like to extend my best words of thanks to committee member Professor Hongrui Jiang, for your brilliant comments and nice suggestions.

Many thanks for Hartwell Family Foundation and Batterman Family Foundation who generously financed and supported me for my Ph. D. research.

I would like to acknowledge Mr. Quinn Leonard, Mr. Hal Gilles, Mr. Dan Christensen, Mr. Kurt Kupcho and Mr. Felex Lu, the professional and nice staff of the Wisconsin Center for Applied Microelectronics who have contributed immensely to my technical question and helped me during my Ph.D. research life. I appreciated your time and willingness to help me.

I would like to acknowledge Dr. Fa Wang, Dr. Mehdi Shokoueinejad, Mrs Elena bezrukova, Mr. Chenxiao Guan, Mr. Zhe Yang and other team members. We worked together and I appreciated your enthusiasm, intensity, willingness to help me. I really enjoy the time working with you in the past years.

Special thanks send to my mother and father for all their love, accompany and encouragement. Words cannot express how grateful I am. Thank you for all sacrifices that you've made on my

behalf since I was a little girl. Very special appreciation to my beloved supportive husband and my loving encouraging friends. Thank you for the faithful support during my entire Ph.D. life.

Contents

ABSTRACT i
ACKNOWLEDGMENTS ii
GLOSSARY viii
CHAPTER 1: INTRODUCTION 1
1.1 Background and motivation 1
1.2 Physiology and pathophysiology of intracranial pressure 3
1.3 Role of ICP monitoring in current clinical practice 4
1.4 Complications of intracranial pressure monitoring 4
CHAPTER 2: METHODS OF MEASURING ICP 6
2.1 Invasive methods of measuring ICP 7
2.1.1 Lumbar puncture (LP) or lumbar drain (LD) 7
2.1.2 External ventricular drainage (EVD) by catheter 9
2.1.3 Microsensor devices 10
2.1.4 Telemetric ICP measurement 10
2.2 Non- Invasive methods of measuring ICP 11
2.2.1 Fluid dynamics 13
2.2.2 Ophthalmic 17
2.2.3 Otic 20
2.2.4 Electrophysiologic 22
2.2.5 Others 24
CHAPTER 3: COMPARISON AND LIMITATION OF METHODS OF MEASURING ICP 27
3.1 Comparison and limitation of invasive methods of measuring ICP 27
3.2 Comparison and properties of non-invasive methods of measuring ICP 28
CHAPTER 4: IMPLANTABLE MICROSENSOR DEVICES 31
4.1 Epidural and subdural sensor devices 31
4.2 Intraparenchymal sensor devices 32
4.3 Comparison of different commercial microsensor ICP monitoring devices 34
4.3.1 Fiberoptic devices 34
4.3.2 Strain gauge devices 35
4.3.3 Pneumatic sensors 36
4.3.4 Properties of microsensor ICP monitoring devices 36
CHAPTER 5: ACTIVE SENSOR DESIGN AND FABRICATION FOR ICP 38

5.1 Active sensor system overview 38
5.1.1 Active sensor location 39
5.1.2 Active sensor parameters 39
5.2 Capacitive sensor 40
5.2.1 Capacitive sensor design 40
5.2.2 Capacitive sensor layout 42
5.2.3 Capacitive sensor WCAM fabrication 45
5.2.4 Challenges 48
5.2.5 Capacitive sensors comparison 50
5.3 Piezo-resistive sensor 51
5.3.1 Piezo-resistive sensor die based layout 51
5.3.2 Piezo-resistive sensor product based layout 53
CHAPTER 6: PASSIVE SENSOR DESIGN AND FABRICATION FOR ICP 54
6.1 Passive sensor system overview 54
6.2 Passive capacitive sensor 55
6.2.1 Passive sensor design 55
6.2.2 Passive sensor circuit model 57
6.2.3 Passive sensor parameters and layout 64
6.2.4 PCB fabrication of Passive Sensor 65
6.2.5 WCAM fabrication of Passive Sensor 67
6.2.6 Sensor measurement: Reader's antenna and sensor coupling system 69
6.2.7 Sensor Parameter Optimization 71
6.2.8 Challenge 78
6.3 Conclusion 80
CHAPTER 7: SENSOR PERFORMANCE ANALYSIS 82
7.1 Active sensor 82
7.1.1 Active sensor simulation 82
7.1.2 Resolution/sensitivity calculation 84
7.1.3 Active sensor measurement set up 85
7.1.4 Active sensor measurement result analysis 92
7.2 Passive sensor 94
7.2.1 Passive sensor simulation 94
7.2.2 Passive sensor measurement 95

7.2.3 Resolution and measurement accuracy 98
7.3 Commercial sensor measurement 100
7.3.1 Commercial piezo-resistive sensor die long term measurement 100
7.3.2 Commercial piezoresistive sensor product long term measurement 103
CHAPTER 8: RFID BASED ICP MANAGEMENT SYSTEM: SMART SHUNT 107
8.1 System overview 107
8.2 Telemetric ICP measurement 108
8.2.1 Current telemetric ICP measurement 108
8.2.2 Problem of current telemetry 113
8.2.3 Our telemetric ICP measurement 114
8.3 Valve and Valve Driver 116
8.3.1 Valve 116
8.3.2 Driver circuit and actuator 117
8.4 Communication 118
8.5 Battery management and remote charging module 119
8.6 Specific absorption rate (SAR) 120
CHAPTER 9: SENSOR FABRICATION PROCESS 121
9.1 Mask Design 121
9.1.1 Passive sensor mask 121
9.1.2 Active sensor mask 1st version 123
9.1.3 Active sensor mask 2nd version 126
9.1.4 Mask Alignment Mark 127
9.2 Passive sensor fabrication procedure – structural sequence summary 128
9.2.1 Deposit nitride layer onto silicon wafer 128
9.2.2 Etch wells in the silicon wafer 129
9.2.3 Insulation layer on silicon well 130
9.2.4 Create 300 nm seed metal tracks in silicon and glass wafers 131
9.2.5 Realized final metal thickness 132
9.2.6 Etching metal layer to trim to final shape on both Silicon and glass wafer 134
9.2.7 Yield calculation on Silicon and glass wafer 135
9.2.8 Anodic bonding 135
9.2.9 Dicing 138
9.2.10 Silicon layer desired membrane thickness realization 139

9.3 Active sensor fabrication procedure – structural sequence summary 139
9.3.1 Deposit nitride layer onto silicon wafer 139
9.3.2 Etch wells in the silicon wafer 140
9.3.3 Insulation layer on silicon well 140
9.3.4 Deposit metal plate on silicon and glass wafers 141
9.3.5 Yield calculation on Silicon and glass wafer 142
9.3.6 Anodic bonding 142
9.3.7 Dicing 143
9.3.8 Silicon layer desired membrane thickness yield 144
9.3.9 Side connection metal pads deposition 144
9.4 Detailed fabrication information inside the WCAM 144
9.4.1 Passive sensor: silicon layer fabrication 144
9.4.2 Passive sensor: glass layer fabrication 151
9.4.3 Bonding and dicing process for passive sensor 154
9.4.4 Active sensor: silicon layer fabrication 155
9.4.5 Active sensor: glass layer fabrication 159
9.4.5 Bonding, dicing and grinding process for active sensor 161
CONCLUSION 164
REFERENCES 166

GLOSSARY

ABP	Arterial Blood Pressure
AP	Arterial Pressure
BOE	Buffered Oxide Etch
CA	Cerebrovascular Autoregulation
CBFV	Cerebral Blood Flow Velocity
CBV	Cerebral Blood Volume
cICC	continuous Intracranial Compliance
CNS	Central Nervous System
CPP	Cerebral Perfusion Pressure
CSF	Cerebrospinal Fluid
CSFP	CSF Pressure
CVR	Cerebrovascular Resistance
EEG	Electroencephalography
EVD	External Ventricular Drainage
FSO	Full Scale Output
FV	Flow Velocity
FVEP	Flash Visual-evoked Potential
IBV	Intracranial Blood Volume
ICH	Intracerebral Hemorrhage
ICP	Intracranial Pressure
IH	Intracranial Hypertension
IIH	Idiopathic Intracranial Hypertension
IOP	Intraocular Pressure
IPA	Isopropyl Alcohol
KOH	Potassium Hydroxide

LD	Lumbar Drain
LP	Lumbar Puncture
MAP	Mean Arterial Blood Pressure
MCA	Middle Cerebral Artery
MEMs	Microelectromechanical Systems
MRI	Magnetic Resonance Imaging
nCPP	noninvasive determination of CPP
NFC	Near-field Communication
nICP	noninvasive ICP
NIH	National Institutes of Health
NIRS	Near-infrared Spectroscopy
OAE	Otoacoustic Emissions
OAEs	Otoacoustic Acoustic Emissions
OCT	Optical Coherence Tomography
ODM	Ophthalmodynamometry
ONSD	Optic Nerve Sheath Diameter
PDMS	Poly (Dimethyl Siloxane)
PHCH	Post-hemorrhagic Communicating Hydrocephalus
PI	Pulsatility Index
PR	Photoresist
RIE	Reactive-Ion Etching
RNFL	Retinal Nerve Fiber Layer
SAH	Subarachnoid Hemorrhage
SBS	Styrene-butadiene-styrene
SD	Standard Deviation
SiO_2	Silicon Dioxide

Si_3N_4	Silicon Nitride
SVPs	Spontaneous Venous Pulsations
TCBF	Total Cerebral Blood Flow
TCD	Transcranial Doppler
TMD	Tympanic Membrane Displacement
TRA	Tissue Resonance Analysis
TST	Trans Systolic Time
VEP	Visual Evoked Potentials
VOP	Venous Outflow Pressure
VP	Ventriculoperitoneal
WCAM	Wisconsin Center for Applied Microelectronics

CHAPTER 1: INTRODUCTION

1.1 Background and motivation

Hydrocephalus is a medical condition in which there is an excessive accumulation of cerebrospinal fluid (CSF) thus an abnormal increase of Intracranial Pressure (ICP). Hydrocephalus occurs in children and adults, but it is most common with infants. It affects one to two of every 1000 live births, making it by far the leading cause of brain surgery in U.S. children. National Institutes of Health (NIH) estimates 700,000 children and adults living with hydrocephalus, with less than 20% being properly diagnosed. The medical cost of hydrocephalus is over $1 billion per year. Since CSF shunting was introduced in the early 1900s and one-way valve systems in the 1950s, countless lives were saved. However, CSF shunt systems have not been significantly improved in the past 60 years. We need better treatments, more positive long-term monitoring, and diagnostic tests that are accurate, low cost, and noninvasive (Hydrocephalus Association 2016).

This kind of abnormal CSF accumulation can cause headaches, mental disability and death. Once the disease is identified, treatment may consist of endoscopic techniques to restore adequate CSF flow, or the placing of a ventriculoperitoneal (VP) shunt to relieve the elevated ICP by shunting the fluid to other bodily cavities such as the pleural space, cardiac atrium or, most commonly, peritoneum. However, this disease currently cannot be cured and the CSF fluid will accumulate again. Early and timely detection of abnormal elevated ICP is essential to mitigate symptoms during the entire life of the patients in reducing the risk of mental disability, permanent brain damage and death. Monitoring ICP is very important to mitigate hydrocephalus symptoms during the entire life of the patient.

There are several methods either invasive or noninvasive to detect the ICP and hence CSF fluid accumulation. A comprehensive literature review on how to measure ICP invasively and noninvasively is performed by my review paper (Zhang et al 2017). It discusses the advantages and disadvantages of current invasive and noninvasive approaches.

Invasive methods remain the most accurate at measuring ICP, but they are prone to a variety of complications including infection, hemorrhage and neurological deficits. Ventricular catheters and external sensor remain the gold standard but also carry the highest risk of complications, such as catheter bacterial colonization as well as subsequent retrograde infection (North 1997). In addition, most patients being monitored for ICP are likely to be suffering from head injury and they will usually have narrow ventricles, making ventricular surgery more difficult and easier leading to incorrect placement. One of the market leaders Codman Micro ICP Sensor uses a strain gauge to measure ICP pressure directly inside the brain. Changes in ICP pressure are measured as changes in the sensor resistance. However, Codman ICP sensor can only be kept in the place/brain for a maximum of two weeks in order to avoid infection and other complications due to external wiring through the skin (Medow et al 2011). Direct telemetric intraparenchymal ICP monitoring devices are a good alternative. Noninvasive methods for measuring and evaluating ICP have been developed and classified in five broad categories, but have not been reliable enough to use on a routine basis. These methods include Fluid dynamic, Ophthalmic, Otic, Electrophysiologic, Magnetic resonance imaging (MRI), Transcranial Doppler Ultrasonography (TCD), Cerebral blood flow velocity (CBFV), Near-infrared spectroscopy (NIRS), Transcranial time-of-flight, Spontaneous venous pulsations (SVPs), Venous ophthalmodynamometry, Optical coherence tomography (OCT) of retina, Optic nerve sheath diameter (ONSD) assessment, Pupillometry constriction, Sensing tympanic membrane displacement (TMD), Analyzing otoacoustic emissions (OAE)/acoustic measure, Transcranial acoustic (TCA) signals, Visual-evoked potentials, Electroencephalography (EEG), Skull vibrations, Brain tissue resonance and Jugular vein. At present, none of the non-invasive methods demonstrates sufficient accuracy and ease of use while allowing continuous monitoring in routine clinical use. Also, some non-invasive methods such as MRI, are expensive and not portable. The patients must go to MRI facilities for examination. However, they provide a realizable ICP measurement in specific patients especially when invasive monitoring is contraindicated or unavailable. Among all non-invasive ICP measurement methods, ONSD and TCD are attractive and may be useful in selected settings though they cannot be used as invasive ICP measurement substitutes. For a sufficiently accurate and universal

continuous ICP monitoring method/device, future research and developments are needed to integrate further refinements of the existing methods, combine telemetric sensors and/or technologies, and validate large numbers of clinical studies on relevant patient populations. More research and effort will be concentrated on developing new or improved ICP monitoring methods, development, and optimization of signal processing techniques, identification and optimization of effective algorithms. The future of the field should take into consideration the cost, accuracy, ease of use and continuous monitoring ability. Commercial research is also needed to design a bio-sensor, which could be permanently implanted.

1.2 Physiology and pathophysiology of intracranial pressure

Intracranial pressure is the pressure inside the brain. Its value is conventionally referenced to atmospheric pressure and expressed in millimeters of mercury. Normal ICP varies with age and body posture but is maintained in the range 5–15 mmHg in healthy supine adults, 3–7 mmHg in children, and 1.5–6 mmHg in term infants (Smith et al. 2008, Raboel et al. 2012).

The ICP value is significantly influenced by volume equilibrium within the brain (1100−1300 cm3), CSF (130−150 cm3), and blood contained in intracranial vessels (60−80 cm3). Considering that brain volume is fixed, CSF and blood are the two most important determining factors of ICP. Cerebral blood flow is nearly constant and is based on mean blood pressure. For ICP to remain constant, an increase in one of the constituents (blood or CSF) should be accompanied by a decrease in the other, this is known as "the Monroe-Kelly doctrine". (Mokri 2001, Popovic et al. 2009).

Cerebral perfusion pressure (CPP), the pressure of blood in the brain, is normally fairly constant in healthy people due to auto-regulation (Steiner and Andrews 2006). CPP is defined as the difference between mean arterial blood pressure (MAP) and ICP (CPP = MAP – ICP). In cases of elevated ICP, the CPP decreases. When treating increased ICP, CPP is therefore an important parameter to monitor and maintain (Steiner and Andrews 2006, Duschek and Schandry 2007).

Elevated ICP occurs in a variety of medical conditions. Frequent causes include intracranial mass lesions, disorders of CSF circulation such as hydrocephalus, more diffuse pathological processes, and head injury

leading to intracranial hematoma or cerebral edema. Elevated ICP can compress and damage brain structures, cause brain herniation, and restrict blood supply to the brain (Graham et al. 2000, Steiner and Andrews 2006).

1.3 Role of ICP monitoring in current clinical practice

ICP monitoring plays an important role in various medical conditions. ICP monitoring is an important tool in clinical practice to determine brain pressure and compliance (Di Ieva et al. 2013). Currently, this area lacks universally accepted guidelines, and hospitals use different standards of ICP monitoring (Raboel et al. 2012).

Continuous ICP monitoring is utilized in the management of severe closed head injury in adults and children (Dunn 2002), such as subarachnoid and other brain hemorrhages, meningitis, acute liver failure causing cerebral edema, stroke, benign intracranial hypertension (IH), and head shape deformities (craniosynostosis), as well as hydrocephalus and CSF shunt function (Czosnyka and Pickard 2004).

There is now a great need to study and integrate ICP monitoring into a multimodality and individualized approach to clinical care (Hawthorne and Piper 2014) with patient-specific parameters for ICP and CPP. Even more importantly, however, is to develop noninvasive ICP monitors, an essential future direction that is yet poorly supported by technology (Di Leva et al. 2013, Hawthorne and Piper 2014). The current ICP monitoring systems are invasive, and require opening of the skull and implanting sensors with wires or catheters that exit the skin to connect to various monitors.

1.4 Complications of intracranial pressure monitoring

ICP monitoring complications include disconnection, device failure, infection, and hemorrhage. Ventricular-catheter related infection rates are around 10% and are associated with the duration of catheter placement (Fried 2016, Lozier 2002). The use of antibiotic impregnated catheters can potentially reduce the risk of infection by prolonging the mean duration to onset of infection (Fried 2016). Clinically symptomatic hemorrhages due to the catheter range from 0.7%–2.4% (Fried 2016). Table 1-1 summarizes

the different complication rates (Schade et al. 2005, Wiegand and Richards 2007, Rangel-Castillo et al. 2008, Bekar et al. 2009, Binz et al. 2009, Gardner et al. 2009, Raboel et al. 2012).

Table 1-1 Complications associated with ICP monitoring (%)

	Parenchymal	Ventricular
Infections	1–2	1–12
Neurological deficits (surgical intervention)	0.2–1.4	0.5–2.5; average 0.61
Bleeding		
Epidural hematoma, intracerebral hematoma, contusion	0.15–0.47	1–2
Technical complications		
Disconnection of the transducer	2.37	
Breakage of the fiberoptic cable	0.31	
Dislocation of the fixation screw	0.15	
Probe defective for unknown reason	0.31	
Malfunction, obstruction, defective devices, malposition	1.4–3.1	6.3

CHAPTER 2: METHODS OF MEASURING ICP

Chapter 2 discusses the advantages and disadvantages of current invasive and noninvasive approaches. Invasive methods remain the most accurate at measuring ICP, but they are prone to a variety of complications including infection, hemorrhage and neurological deficits. Ventricular catheters remain the gold standard but also carry the highest risk of complications, including difficult or incorrect placement. Direct telemetric intraparenchymal ICP monitoring devices are a good alternative. Noninvasive methods for measuring and evaluating ICP have been developed and classified in five broad categories, but have not been reliable enough to use on a routine basis. These methods include Fluid dynamic, Ophthalmic, Otic, Electrophysiologic, Magnetic resonance imaging (MRI), Transcranial Doppler Ultrasonography (TCD), Cerebral blood flow velocity (CBFV), Near-infrared spectroscopy (NIRS), Transcranial time-of-flight, Spontaneous venous pulsations (SVPs), Venous ophthalmodynamometry, Optical coherence tomography (OCT) of retina, Optic nerve sheath diameter (ONSD) assessment, Pupillometry constriction, Sensing tympanic membrane displacement (TMD), Analyzing otoacoustic emissions (OAE)/acoustic measure, Transcranial acoustic (TCA) signals, Visual-evoked potentials, Electroencephalography (EEG), Skull vibrations, Brain tissue resonance and Jugular vein. At present, none of the non-invasive methods demonstrates sufficient accuracy and ease of use while allowing continuous monitoring in routine clinical use. However, they provide a realizable ICP measurement in specific patients especially when invasive monitoring is contraindicated or unavailable. Among all non-invasive ICP measurement methods, ONSD and TCD are attractive and may be useful in selected settings though they cannot be used as invasive ICP measurement substitutes. For a sufficiently accurate and universal continuous ICP monitoring method/device, future research and developments are needed to integrate further refinements of the existing methods, combine telemetric sensors and/or technologies, and validate large numbers of clinical studies on relevant patient populations.

2.1 Invasive methods of measuring ICP

Invasive measurements of pressure are the standard method for direct ICP monitoring. Several different invasive ICP measuring methods exist. ICP measurement can be undertaken at various intracranial anatomical locations determined by different techniques: intraventricular, epidural, subdural, subarachnoidal, and intraparenchymal. Furthermore, under certain circumstances ICP may be assessed by lumbar puncture for patients with communicating CSF pathways (Eide and Brean 2006, Lenfeldt et al. 2007, Speck et al. 2011).

ICP can be measured at different sites of the brain. Intraventricular and intraparenchymal measurements are more common, whereas extradural and subdural measurements are only rarely used. The standard technique is an invasive procedure that involves catheter insertion into the intracranial compartment, usually through a small hole drilled in the skull. A pressure probe/sensor is then advanced through the brain tissue into the ventricular space, or the brain parenchyma, epidural space (between skull and dura), or subdural space (between brain and dura) (Zhong et al. 2003, Ross and Eynon 2005, Rai and Varadan 2010, Kashif et al. 2012).

2.1.1 Lumbar puncture (LP) or lumbar drain (LD)

Quincke (1891) introduced the lumbar puncture (LP) technique as an option to investigate the intrathecal environment. It involves the percutaneous introduction of a needle into the lumbar spinal CSF space and the measurement of a column of water, which reflects intraspinal pressure. Langfitt et al. (1964) believed that LP could accurately estimate ICP when CSF circulates freely and when the fluid column is appropriately positioned with respect to the brain. As mentioned above, under certain circumstances ICP may be assessed by lumbar puncture for patients with communicating CSF pathways. Lumbar puncture is not strictly an ICP measurement, but a neuraxis CSF pressure measurement. Mertz et al. (2004) found that there is a good correlation between the brain sensor's CSF pressure and lumbar pressure. Wiegand and Richards (2007) noted that performing an LP and observing the opening and closing pressure is the most simple and longest-standing ICP measurement method. CSF pressure measured by LP is usually recorded

in cmH2O, whereas ICP is ordinarily measured in mmHg. A conversion factor of 13.6 to convert mmHg to cmH2O is therefore required.

Kapadia and Jha (1996) showed that, following aneurysm surgery, drainage of lumbar CSF results in an equivalent fall of both lumbar and ventricular pressures in most patients. Simultaneous measurement of lumbar and ventricular pressures allows the identification of patients at risk of transtentorial or transforamenal herniation following CSF drainage by lumbar puncture, as a pressure gradient between the two cavities starts to build up.

Lumbar drainage (LD) is similar to LP, except that a catheter is placed into the lumbar spinal intrathecal space through a spinal needle before the needle is removed. This allows pressure measurement as well as the ability to drain CSF as needed. Speck et al. (2011) performed a total of 1806 lumbar drain measurements in 43 patients with subarachnoid hemorrhage (SAH, n = 21) or intracerebral hemorrhage (ICH, n = 22), to assess feasibility and reliability of a lumbar drain when compared to EVD. They showed that LD-ICP recordings correlate well with EVD-ICP recordings, implying that LD an accurate albeit less-invasive option for ICP monitoring in patients suffering from post-hemorrhagic communicating hydrocephalus (PHCH) after SAH and ICH.

Eide and Brean (2006) assessed simultaneous CSF pressure (CSFP)/ICP recordings during lumbar infusion and long-term, overnight ICP monitoring in 27 consecutive idiopathic normal-pressure hydrocephalus patients, recording a total of 35,532 CSFP/ICP wave pairs. The results showed that, during lumbar infusion, the amplitudes of lumbar cerebrospinal fluid pulse pressure could be used to predict the amplitudes of intracranial pulse pressure during long-term, overnight ICP monitoring.

ICP monitoring via LD may have several advantages compared to direct EVD measurement or a parenchymal probe. The major advantage of the LD technique is that lumbar CSF pressure monitoring is less invasive and can be performed at the bedside within minutes (Speck, 2011). Intracranial device placement is always associated with brain injury and hemorrhage risk (Gardner et al. 2009). Additionally,

lumbar drainage allows therapeutic CSF release for lowering ICP; this is not feasible with intracranial probes, with the exception of EVD (Münch et al. 2001, Tuettenberg et al. 2009).

LP and LD are not recommended when ICP is suspected to be high from a mass lesion or obstruction because of brain herniation risk (Kashif et al. 2012). Although LP provides a spot estimate of ICP, it cannot capture dynamic ICP trends which are often more accurate indicators of pathology. In addition, LP may give a falsely high reading for children requiring anesthesia or heavy sedation, depending on the different anesthetic agents used and their length of application (Wiegand and Richards 2007). Instant CSF pressure measurement using the height of a fluid column via lumbar puncture may therefore be misleading (Czosnyka and Pickard 2004).

In addition, CSF data may not reflect ICP, especially in the setting of an obstruction between the intracranial and intraspinal cavities (Eide and Brean 2006). An LP in a patient with such an obstruction can result in brain herniation because of the difference in pressure between the intracranial and intraspinal compartments. Positioning should also be considered while performing a lumbar puncture. A seated LP can impair the measurement and lead to a falsely high pressure because of the column of water created in the sitting position. Further research is required to investigate whether lumbar catheter ICP monitoring—with or without CSF release—is safe and accurate in patients with other underlying cerebral diseases. LD is absolutely contraindicated when an intracranial mass lesion is suspected. However, a lumbar puncture may be therapeutic as well as diagnostic in communicating hydrocephalus or benign intracranial hypertension, in which case there is full communication between the ventricular and subarachnoid spaces.

2.1.2 External ventricular drainage (EVD) by catheter

This technique is the original method described for monitoring ICP, and intraventricular catheters are still considered as the gold standard (The Brain Trauma Foundation 2000). A ventricular catheter is placed through a twist drill or burr hole into the ventricle, and CSF pressure is measured via an external pressure sensor.

A significant advantage of this system is that CSF drainage can be used as a therapeutic measure when the ICP is elevated. Currently, systems exist in which catheters and ICP probes are used together as one device, so that ICP can continue to be monitored even if the catheter were to obstruct.

The disadvantages of an EVD are as follows. (1) CSF leakage may lead to falsely low readings. (2) There is a higher risk of CSF infection (up to 10% in some series) and mechanical complications than when using ICP probes (Czosnyka et al. 1996). EVD catheter infections can be mild and easily treatable or can be severe such as meningitis and ventriculitis, causing neurological symptoms and possible death. (3) Incorrect placement can lead to injuries to important cerebral structures such as the internal capsule, thalamus, basal ganglia, and others (Raboel et al. 2012). Saladino et al. (2009) found that, among 138 patients who underwent placement of intra-ventricular catheters for EVD, the rate of mal-placed catheters was 12.3%. (4) Insertion of the catheter into very small ventricles, often related to brain swelling, may be difficult and more hazardous.

2.1.3 Microsensor devices

In the early 1990s, microsensor devices that read ICP when placed within the brain parenchyma were developed based on either fiberoptics (Camino) or electrical impedance (Codman 'Microsensor', Spiegelberg pressure sensor). These devices provide readings comparable to intraventricular catheters, are minimally invasive, and have minimal baseline drift if placed for a few days. They have become the standard method for measuring ICP accurately by neurosurgical teams worldwide (Luerssen 1997) when ventricular drainage is either not needed or not safely performed. Advances in monitoring technology and new microsensor tips have improved the ease, safety, and ICP measurement accuracy, allowing more widespread use in emergency and elective situations (Wiegand and Richards 2007).

2.1.4 Telemetric ICP measurement

To realize longer-term usability, implanted microsensors such as the Codman ICP sensor must not have wires exiting the body, must have very limited drift potential, and must have wireless communication to the outside so that pressure values can be evalutated by a reader. A few non-commercialized attempts have

so far been made to create such a system, most of them using inductive coupling to an external antenna and various active elements in the design that would influence incoming power and outgoing signal. Such miniaturized devices would also be useful in monitoring various other pressures in the body, and commercial efforts have used microelectromechanical systems (MEMs) type devices particularly for cardiac and ocular applications. Implantable catheter-tip sensor ICP devices have also been connected to a telemetry unit. The telemetric technique is an invasive way to monitor ICP with risk limited to the implantation of the pressure probe only. It allows for ICP monitoring under normal daily living conditions in an outpatient setting. The telemetric catheter can be implanted up to 3 months in some studies. However, telemetric pressure sensors are not presently in wide use because the technology is not yet reliable and readily available. And even if an implantable sensor were to become technically feasible, the sensor would require multiple procedures for recalibration or surgical replacement to achieve zero drift stability. Miyake et al. (1997) described telemetric monitors used for long-term ICP monitoring in hydrocephalus patients with ventriculoperitoneal shunts. The telesensor was implanted up to 44 months in some patients. Their telesensor also exhibited zero drift. However, the device suffered from drift inconsistency and need to recalibrate.

2.2 Non- Invasive methods of measuring ICP

Several different invasive ICP measurement methods exist, but the development of a noninvasive ICP (nICP) monitoring system with clinically acceptable accuracy is needed. The idea of measuring ICP noninvasively is attractive for the following reasons: (1) a non-invasive estimate of ICP helps in deciding which patient warrants invasive ICP monitoring, (2) there is no risk of complications seen in invasive monitoring such as hemorrhage and infection (3) and it provides ongoing long-term measurements of ICP without having to insert a new device every time. The major disadvantage is that it requires placement by a neurosurgeon in a specialized facility. The correlation coefficient between nICP and ICP describes how well ICP can be predicted using nICP. A variety of methods have been suggested for nICP monitoring (Popovic et al. 2009, Kashif et al. 2012), which in general measure physiological variables that indirectly correlate with ICP. To

assess accuracy of a non-invasive method, the Association of Advancement of Medical Instrumentation stated that when the ICP that ranges between 0–20 mmHg, a difference of 2 mmHg is acceptable when compared to an invasive method; however, when ICP is between 20–100 mmHg, the difference should not exceed 10% (Popovic et al. 2009).

Different numerous non-invasive methods have been proposed and developed for nICP monitoring and are classified in the following five broad categories: Fluid dynamic, Ophthalmic, Otic, Electrophysiologic and Others. Magnetic resonance imaging (MRI), Transcranial Doppler Ultrasonography (TCD), Cerebral blood flow velocity (CBFV), Near-infrared spectroscopy (NIRS), and Transcranial time-of-flight are discussed in the Fluid dynamic section. They have been applied to dynamic fluid changes study in ICP, cerebral blood flow and cerebral compliance. Spontaneous venous pulsations (SVPs), Venous ophthalmodynamometry, Optical coherence tomography (OCT) of retina, Optic nerve sheath diameter (ONSD) assessment, and Pupillometry are discussed in the Ophthalmic section. Use of the eye is one possible way for ICP estimation because of the dural extension of the optic nerve sheath and communication between the perioptic nerve CSF and cerebral CSF (Bruce 2014). Sensing tympanic membrane displacement (TMD), Analyzing otoacoustic emissions (OAE)/acoustic measure and Transcranial acoustic (TCA) signals methods are discussed in the Otic section. The ear has a direct communication with CSF, ear leverage and the cochlear aqueduct help realize connection between the perilymph of the cochlea and posterior cranial fossa CSF for ICP evaluation. Visual evoked potentials (VEP) and Electroencephalogram (EEG) are discussed in the Electrophysiologic section. ICP has been predicted using nICP from recordings of VEP and EEG methods to record the electrical brain activity and derived ICP levels. Skull vibrations, Brain tissue resonance, and Jugular vein are discussed in the Others section for ICP prediction and evaluation.

2.2.1 Fluid dynamics

2.2.1.1 Magnetic resonance imaging (MRI)

MRI can be used to measure transcranial blood and CSF volumetric flow rates, which allow the ICP to be determined via an elastance index (Alperin et al. 2000). This method calculates the change of intracranial volume, which is obtained by analyzing the arterial inflow and venous outflow in the brain. The flow is calculated by multiplying the blood velocity and cross-sectional areas of arterial and blood vessels. Velocity is proportional to the difference between the incident and resonant RF signals, and cross-sectional areas are obtained from static MRI scans (Popovic et al. 2009). Normal values have been shown to be a strong predictor of elevated ICP resolution in patients with hydrocephalus without a surgical intervention (Glick et al. 2006), as well as to correlate with the shunt valve opening pressure in children with hydrocephalus (Muehlmann et al. 2013).

Overall, MRI could potentially detect chronic disorders associated with increased ICP values. However, the method is expensive (a basic MRI scan costs over US$1000), cumbersome, and impractical for continuous monitoring of ICP. The equipment is not flexible and portable (Smith 2008); instead, it is heavy and consumes high quantities of energy.

2.2.1.2 Transcranial Doppler Ultrasonography

Transcranial Doppler (TCD) ultrasonography may be useful for nICP. TCD can measure red cell flow velocity in real time, which can provide an estimate of ICP. It is non-invasive and inexpensive. Some of its clinical applications include assessing cerebral autoregulation, vasoreactivity, and cerebral perfusion pressure (CPP) (Bhatia and Gupta 2007). The TCD technique is developed from basic ultrasound, but minimum probe pressure is required to prevent a decrease in blood flow velocity (Tranquart et al. 2003) when applying ultrasound to measure the blood flow velocity (FV) in the middle cerebral artery (MCA). The ophthalmic artery is affected by the ICP intracranially, and the extracranial segment can be affected by applying pressure externally to the orbit. The pressure cuff is used to gradually compress the orbital tissues, while TCD is used to determine the point at which blood flow in the intra- and extracranial segments of the

ophthalmic artery equalize. The externally applied pressure is equal to the ICP at this time (Bruce 2014). ICP can be estimated from the TCD measurements because it impedes the blood flow and consequently decreases the velocity of blood (Popovic et al. 2009).

The difference between systolic and diastolic flow velocity, divided by the mean flow velocity, is referred to as the pulsatility index (PI) (Raboel et al. 2012). PI correlates with invasively measured ICP with coefficients ranging over 0.439–0.938 (Moreno et al. 2000, Bellner et al. 2004, Voulgaris et al. 2005). As well as allowing calculation of PI, TCD can also be used for noninvasive determination of CPP (nCPP). This method involves CPP estimation from parameters derived from the middle cerebral artery (MCA), blood flow velocity (FV), and the arterial blood pressure (ABP) (Eide and Sæhle 2010). Furthermore, mean velocity and PI, cycles in systole, and slopes of TCD waveforms have been correlated with ICP.

Taylor and Madsen (1996) found that hemodynamic response to fontanelle compression during TCD can assess ICP indirectly and can help to determine the need for further treatment of elevated ICP. The hemodynamic response to fontanelle compression can be used as a noninvasive predictor for elevated ICP in neonates with hydrocephalus (Wiegand and Richards 2007). Previously, the main disadvantage of TCD was the need for a trained and skilled physician (Shen et al 1999) to find the correct vessel, with the ability to interpret the results. Currently, in many hospital centers with good quality recording ability, TCD was routinely obtained in the hands of trained technicians. There are also intra- and interobserver variations as noted earlier (Raboel et al 2012). Furthermore, the technique is not practical for older patients because ultrasound cannot penetrate their skull; in medical terms, older patients demonstrate a lack of TCD windows (Tsivgoulis et al 2009).

In spite of the insufficient accuracy of ICP estimates, TCD is still attractive in the area of detecting ischemia when compared to standard methods, since it measures flow velocity and not volume. TCD is also affordable and mobile, it provides real-time information with high temporal resolution, and is readily available in most hospitals and healthcare facilities. Before it can be recommended for routine use, the TCD technique needs to be evaluated and developed, focusing on its accuracy, cost-effectiveness, and validity.

2.2.1.3 Cerebral blood flow velocity (CBFV)

Cerebral arterial blood flow velocity is related to both cerebral perfusion pressure (CPP) and cerebrovascular resistance (CVR). CPP is decreased in cases of elevated ICP. CVR is significantly increased as a result of cerebrovascular system compression due to increased ICP. Hanlo et al (1995) defined a new Doppler index, trans systolic time (TST), which reflects specific changes in TCD waveforms induced by changes in the mean ICP. Alperin et al (2005) discussed the postural-related changes in total cerebral blood flow (TCBF) and ICP. Schmidt et al (2003) Popovic et al (2009) and Xu et al (2010) proposed noninvasive assessment of ICP approaches based on ABP and cerebral blood flow velocity (CBFV). Kashif et al (2012) used routinely acquired signals with a physiological model to generate patient-specific estimates of ICP from CBFV and arterial pressure (AP). The advantages of the described model are: there is no requirement for calibration or training before application; and ICP can be estimated noninvasively.

However, Liebeskind et al (2013) noted that the model consists of a small number of physiological parameters, which leads to computation time reduction and limits its real-time predictions. The short time delay is because BFV and AP need to be detected first and then serve as inputs to the model, which significantly influences the real-time predictions for critical/serious patients. The Division of Neurosurgery in the Department of Clinical Neurosciences of the University of Cambridge developed a commercial form of a noninvasive ICP measurement product based on CBFV and AP.

2.2.1.4 Near-infrared spectroscopy (NIRS)

Near-infrared spectroscopy (NIRS) is commonly used to measure the tissue oxygenation index. It can provide an estimation of cerebral blood volume by recording the concentration of deoxygenated (Hb) and oxygenated (HbO2) hemoglobin in the blood. It is suitable for continuous detection of cerebral blood volume changes (Zweifel et al. 2010). Weerakkody et al. (2010) discussed the relationship of slow fluctuation in cerebral oximetry detected by NIRS. NIRS allows detection of changes in brain tissue, cerebral blood volume (CBV), and CBF by recording relative Hb and HbO2 changes associated with slow

ventilation. It could be used as a noninvasive marker of increased ICP slow waves. Weerakkody et al. (2012) and Asiedu et al. (2014) described the study of a group of hydrocephalus patients after traumatic brain injury. They explored the synchronization between ICP and NIRS variables induced by vasogenic waves of ICP. However, data regarding the sensitivity of NIRS to detect or predict changes in ICP are sparse.

The method is currently limited by NIRS equipment availability. Further, the required parameters for the individual patient take several hours of monitoring to obtain, and can only be reliably measured in about 50% of recordings (Zweifel et al. 2010). Prospective clinical trials are needed to validate this method. However, NIRS technology is developing and improving rapidly, and mixing with other imaging applications. In addition, it may have benefits for patients for whom invasive ICP monitoring would be particularly risky.

2.2.1.5 Transcranial time-of-flight

Ragauskas and Daubaris (1995) first developed ultrasonic transcranial time-of-flight as a brain physiological monitoring technology. Piper (1997) and Ragauskas et al (2003) then discussed the possibility of adding an acoustic path through the head. This technology is based on the measurement of acoustic properties of ultrasound speed and attenuation across an acoustic path. In addition, the majority of patented methods for this technology are based on the assumption that ICP changes affect acoustic properties (Michaeli and Rappaport 2002, Fountas et al 2005, Popovic et al 2009). The time-of-flight related methods are influenced by many acoustic properties of tissue and fluids in the brain, and not just by pressure alone. Changes in the volume of any of these components change the time-of-flight (Ragauskas et al 2003).

The transcranial time-of-flight method can only measure ICP changes relative to a baseline measurement with a known reference of absolute ICP. Ultrasound readout therefore requires invasive measurement calibration. Yost and Cantrell (2004) developed a method of extracting pulsatile changes in the ultrasound signal caused by systolic and diastolic blood pressure oscillations. However, stability with a wide range of ICP values requires more research and validation. Ragauskas et al (2005) used an ultrasonic time-of-flight

monitor for continuous monitoring of intracranial blood volume (IBV) pulse and other characteristics such as respiratory slow waves and cerebrovascular autoregulation (CA).

In conclusion, for the majority of transcranial non-invasive methods, accuracy remains unclear and the methods have had little validation for clinical use. The specific angles and locations of transducer placement influence ICP estimations and therefore aren't reliable. More research is needed regarding how the measurements are affected by the presence of brain shift or intracranial pathologic masses in the ultrasound wave path, such as blood collections or tumors.

2.2.2 Ophthalmic

2.2.2.1 Spontaneous venous pulsations (SVPs)

Another method of optic nerve examinations used to approximate ICP is observation of spontaneous venous pulsations (SVPs). SVPs consist of subtle variations in retinal vein caliber seen on the optic disc. Jacks and Miller (2003) described a useful technique in the use of digital pressure on the globe through the eyelid to induce venous pulsations in patients for whom SVPs do not appear to be present. Once venous pulsations are observed at a particular location, the pressure is removed and observation of the area is continued to determine whether venous pulsations, not detected initially, remain.

SVPs occur due to the pressure gradient variation caused by differences between the intraocular and CSF pulse pressures as the retinal vein traverses the lamina cribosa. Firsching et al (2000) and Jonas et al (2012) demonstrated that SVPs are in phase with the ICP pulsations, and when the central retinal vein collapses the pressure of the eye is higher than the venous outflow pressure (VOP), that is, the pressure within the optic nerve.

SVPs are absent from 10% of normal people and are not interpretable, showing that pulsations do not always indicate increased ICP; Levin (1978) and Jacks and Miller (2003) have however suggested that SVPs are only present when ICP is normal. Further, an optic disc edema is not always related to elevated ICP.

SVPs are absent from 10% of normal people and are not interpretable, showing that pulsations do not always indicate increased ICP; Levin (1978) and Jacks and Miller (2003) have however suggested that SVPs are only present when ICP is normal. Further, an optic disc edema is not always related to elevated ICP. Wong and White (2013) reported that the sensitivity of the presence of SVPs for normal ICP is 94% instead of 100%. Interpretation becomes complicated because of both the absence of SVPs and sensitivity rate. In summary, SVPs have high sensitivity to normal ICP, but their absence should be interpreted in the context of the overall clinical scenario, since it is absent in 10% of population.

2.2.2.2 Venous ophthalmodynamometry

Baurmann (1925) first suggested that the pressure within the central retinal vein depends on ICP. For decades, ophthalmologists have been familiar with ophthalmodynamometry (ODM), a technique that allows the physician to determine pressure within the central retinal vein. Jonas et al (2008) set up an experiment for a 28-year-old female patient with blurred vision and nuchal pain, in which they used prominent optic discs and modified ophthalmodynamometry to determine ICP. ODM showed increased central retinal vein pressure in both eyes which corresponded to elevated cerebrospinal fluid pressure measurements on lumbar puncture; this led to the diagnosis of idiopathic intracranial hypertension, proving that ODM can be helpful in the diagnosis of an elevated ICP.

ODM is useful when continuous ICP monitoring is not necessary. It is a simple noninvasive technique for neurologists, ophthalmologists, and general practitioners. In addition, ophthalmodynamometry attempts to quantify ICP. Further studies are needed to determine the sensitivity and specificity of this modality (Rosenberg et al 2011). Ophthalmodynamometry is unsuitable for continuous ICP monitoring, and is cumbersome for frequent repeated measurements since this method requires dilated pupils, a physician skilled in eye examinations, and patient collaboration.

2.2.2.3 Optical coherence tomography (OCT) of retina

IH causes cellular or axonal level changes such as the swelling of the retinal nerve fiber layer (RNFL) that forms the innermost layer of the retina (Popovic et al 2009). Optical coherence tomography (OCT)

measures total retinal thickness, RNFL thickness, and optic nerve head morphology based on infrared light (Hee et al 1995).

Borchert and Lambert (1998) patented a method that utilizes OCT to measure the RNFL thickness and infer ICP. OCT is effective in distinguishing papilledema nerves from normal nerves and can be used for monitoring and quantitative measurement of RNFL in papilledema (Savini et al 2006, El-Dairi et al 2007 and Rebolleda et al 2009). However, there exist significant limitations in the use of this method in clinical practice. The rate of development of disc edema is generally very slow unless ICP is extremely high. OCT may therefore serve as a valuable supplement for subjective papilledema assessment in patients with IIH. However, for long-term idiopathic intracranial hypertension (IIH) patients who have previously been treated, OCT appears to be of limited value (Skau et al 2013).

2.2.2.4 Optic nerve sheath diameter (ONSD) assessment

The optic nerve sheath complex consists of the optic nerve, which is a white matter tract of the central nervous system (CNS), and the perioptic nerve sheath, which is formed from the leptomeninges and is continuous with the dura mater of the brain. The sheath around the optic nerve is in fact a continuation of the dura, and the subarachnoid space extends along the optic nerve within the sheath.

Optic nerve sheath diameter assessment has been discussed and developed by multiple researchers (e.g., Rajajee et al 2011, Borchert and Lambert 2000). Optic nerve sheath distension occurs within seconds of ICP elevation, making ONSD potentially useful for acute ICP elevation detection. Enlargement of the optic nerve sheath has been described in patients with increased ICP (Soldatos et al 2008). Raised ICP is transmitted around the optic nerve through the cerebrospinal fluid, causing distention of the optic nerve sheath diameter (ONSD). Previous work has shown that patients with increased ICP have increased ONSDs. Optic nerve sonography offers rapid bedside optic nerve sheath diameter assessment and has been introduced for measuring ICP noninvasively, especially in severe brain injury patients (Tsung et al. 2005). High-resolution MRI has also been used to estimate the optic nerve and its sheath for evidence of elevated

ICP (Rosenberg et al 2011). Transorbital sonography is a safe method to measure the ONSD for rapid diagnosis of increased ICP in children (Wiegand and Richards 2007).

Except for the quantitative drawbacks of the ONSD method, another disadvantage described by Rajajee et al (2011) is that measurement of ONSD is a point-in-time/snapshot assessment instead of continuous ICP measurement. Rajajee et al (2011) concluded that ONSD measurement based on ocular sonography is an accurate, noninvasive technique for the detection of ICP performed by an experienced operator. However, internal institutional validation of optimal ONSD for ICP detection may be required.

2.2.2.5 Pupillometry

Preliminary studies have been performed on another noninvasive ICP measurement. Quantitative pupillometers can measure subtle changes/constriction in the pupillary light response. Meeker et al (2005) and Du et al (2005) described how pupillometers are more accurate than manual scoring, and have the ability to measure subtle pupillary constrictions that are too small to be seen using manual examination (Larson and Muhiudeen 1995, Rosenberg et al 2011).

Fountas et al (2006) showed that certain medical, ocular, and non-ICP related neurological conditions, as well as various medications, individual emotional states, and the time of day, may also affect pupillometry measurements. Furthermore, it is unclear whether the initial findings in head trauma translate to other causes of increased ICP. The pupillometry preliminary study shows why further study is needed to determine the clinical applicability of pupillometry.

2.2.3 Otic

2.2.3.1 Sensing tympanic membrane displacement (TMD)

Marchbanks (1989) developed the tympanic membrane displacement (TMD) technique, which was the first proposed audiological method for assessing ICP noninvasively. The technique is based on measurements of TMD in response to elicitation of the acoustic reflex. It indirectly measures cochlear fluid pressure, which is a direct measure of ICP (Stettin et al 2011, Pranevicius et al 2012). TMD takes advantage of the communication between the CSF and the perilymph via the perilymphatic duct. Stimulation of the stapedial

reflex causes a movement of the tympanic membrane, which is correlated to ICP (Raboel et al 2012). These pressure waves displace the tympanic membrane. Specific tympanic membrane displacement changes are indicative of high or low ICP (Gaihede et al 1995). Since the membrane is flexible, CSF and perilymph communicate through the cochlear aqueduct and elevated ICP is directly transmitted to the stapes footplate, changing its initial position and thereby affecting the direction and magnitude of displacement of the eardrum in response to the sound (Popovic et al 2009).

Phillips and Marchbanks (1989) and Reid et al (1989) concluded that TMD could be a useful tool for classifying ICP as normal or high, although it was not possible to obtain an absolute ICP value. Kristiansson et al (2013) found that the predictive limits of the linear regression were too wide, approximately ±25 mmHg, to make a clinically useful ICP measurement. A correlation between the TMD and invasively obtained ICP values was found. However, the variability was so great that it precluded the method for clinical use (Shimbles et al 2005, Raboel et al 2012). Rosenberg et al (2011) suggested that serial TMD recordings could be used to find a change in ICP if an individual baseline value has previously been obtained; elaborate hardware and an audiologist are required to interpret results, however, and testing takes up to 60 min. Even though TMD has some limitations, it may serve as a useful noninvasive adjunct for ICP monitoring.

2.2.3.2 Analyzing otoacoustic emissions (OAE)/acoustic measure

Otoacoustic acoustic emissions (OAEs) were first recorded by Kemp (1978). They are sounds generated by the inner ear in response to a loud sound, and can be evoked by several techniques (Popovic et al 2009, Bruce 2014). The sounds are transmitted to the stapes, then further to the tympanic membrane through the ossicles. Avan et al (1996), Voss et al (2006), Olzowy et al (2008), and Bruce (2014) reported that distortion-product OAEs change with ICP. The characteristics of the OAE response vary with ICP, and can therefore be used as a relative indicator of ICP. Similarly to TMD, changes in OAE require a patent cochlear aqueduct and demonstrate significant patient variability; OAEs are not related to additional middle-ear reflex arc components such as the brainstem however, required for TMD measurements.

OAE equipment is portable and relatively easy to use. Similar to TMD, OAE could be a reliable clinical technique if it includes prebaseline measurement. However, the quality of OAE measurements can easily be influenced by factors such as sedative and intersubject variability (Kristiansson et al 2013). OAE measurements may also be valuable for monitoring patients when the ICP has already been established by another method.

2.2.3.3 Transcranial acoustic (TCA) signals

Levinsky et al (2016) proposed a novel method for non-invasive ICP estimation based on transcranial acoustic (TCA) signals mixed with head-generated sounds that estimate the static and pulsatile invasive ICP (iICP) through an ear probe placed in the right outer ear channel. They observed total 39 patients and realized 5789 predictions for static iICP and 6791 for pulsatile iICP respectively. Their validation showed a good agreement between iICP/nICP observations, with mean difference of 0.39 mmHg for static ICP and 0.53 mmHg for pulsatile ICP.

Unlike the TMD and OAE methods which rely on extra-cranial organs/structures being connected to the intracranial compartment measurements, TCA signals for nICP estimation relies on intracranial structure properties (Popovic et al 2009, Bershad et al 2014, Schmutzhard et al 2013, Levinsky et al 2016). TCA method depends on ear-bud probes placement in the outer ear channel, which is rather convenient and user-friendly. Moreover, this method has the functionality for continuous nICP monitoring. Though the validation demonstrated clear ability TCA method to estimate static and pulsatile iICP non-invasively with rather high accuracy. The number of patients is limited as well as rather narrow range of ICP values within mean ICP < 15 mmHg. More research is required to evaluate usefulness and functionality of mixed TCA signals for static and pulsatile nICP measurement.

2.2.4 Electrophysiologic

2.2.4.1 Visual-evoked potentials

Visual-evoked potentials (VEP) accurately reflect visual pathway disturbances. York et al (1981, 1984) demonstrated a strong linear relationship between VEP N2 wave increased latency and ICP elevations, with

correlation coefficients of 0.8–0.9 and best predictive value of VEP for ICP measurements of 300 mmH2O. Zhao et al (2005) found a similar correlation between N2 wave latencies and ICP in response to mannitol administration, obtaining a 0.97 correlation coefficient based on a larger study of 152 patients with mixed intracranial pathologies. These study results may not be representative however, since they do not consider patients with hypophyseal tumors, oxygen saturation less than 95%, liver dysfunction, uremia, severe acidosis, and diseases affecting visual acuity. In addition, VEP is not suitable for many specific patients, such as with frontal hematomas, retinal injuries, or optic nerve pathologies.

Zhong et al (2012) described how several methods, such as flash visual-evoked potential (FVEP) and transcranial Doppler (TCD), have been studied with regard to noninvasively assessing ICP. Based on the advantages of FVEP and TCD for ICP assessment, the two methods were integrated to develop a specific instrument to noninvasively measure ICP more reliably and applicably, overcoming the disadvantages of a single method of ICP measurement.

VEP is not yet fully developed and limitations of this technique include: the requirement of neurophysiological expertise; and the difficulty in achieving prolonged continuous monitoring (Wiegand and Richards 2007) and visual function of the patient.

2.2.4.2 Electroencephalography (EEG)

A method patented by Rosenfeld (1986) is based on electroencephalographic visual-evoked potentials (VEP) and uses a few occipital EEG electrodes to record electrical brain activity. Wu et al (2007) improved and investigated the relationship between ICP and the third positive-going wave of VEP recorded with high-density electrode arrays. The accuracy of EEG-derived ICP levels is difficult to estimate rigorously because the above assessment is only semiquantitative; further, there are large interindividual variabilities of latencies of VEP components, making it difficult to discern between physiological long latencies and pathological delays caused by moderate increases in ICP (Popovic et al 2009).

Continuous ICP monitoring from the EEG is theoretically possible, but difficult to achieve practically. EEG can be recorded continuously at most for 8−12 h before the conductive gel on the electrodes dries up and the electrodes need to be replaced. In addition, continuous visual stimulation would certainly be fatiguing for conscious subjects (Popovic et al 2009).

The EEG to measure ICP is both sensitive and cumbersome for dynamic settings or use in an emergency room, intensive care unit, or neurosurgery department. The accuracy of ICP levels from EEG signals is difficult to estimate; further validation and refining of EEG power spectrum analysis is therefore needed to determine its clinical utility. However, portable wireless field-deployable EEG systems by advanced brain monitoring (http://www.b-alert.com/) have recently become available and can be easily applied by various medical personnel after minimal training (Popovic et al 2009).

2.2.5 Others

2.2.5.1 Skull vibrations

The cranium can move in relation to the dura mater, which is deformed as the ICP fluctuates. Mick (1992) disclosed a method for noninvasively measuring changes in ICP by measuring changes in the natural frequency of the skull bone and its response spectrum. Changes in the natural frequency and its skull response spectrum are measured using a mechanically forced oscillation stimulus. A mechanical wave is created to transmit through the bone, and then to sense the frequency response spectrum. ICP trends and changes are shown by comparing spectral response data over time (Yue and Wang 2009). Variation in ICP alters the stress level experienced by the skull bone (Mick 1991, Sinha et al 2000). An ICP produces an initial stress field in the skull, leading to a stress-related term describing skull stiffness. Head vibrational responses are related to the stiffness of the skull (Li and Luo 2010).

As a result of the above relationship, it is possible to develop a noninvasive method for evaluating ICP based on the correlation between ICP and external vibration, although it is very difficult to establish a model for the complex anatomical structure as well as the complicated material composition of the human head.

2.2.5.2 Brain tissue resonance

The heart beat radiates through the organs and tissues and imparts a characteristic vibration and resonant response to the soft tissue and fluid of the brain. Tissue resonance analysis allows for characterization of physiological characteristics of various organs. Michaeli et al (2002) developed a new portable and computerized device based on tissue resonance analysis (TRA) technology for noninvasive ICP monitoring and measurement. It creates a series of encephalograms using ultrasonography with minimal bone attenuation. These build up over time, and as the intracranial contents pulsate with the inflow and outflow of blood from the heart, the amplitude of the ultrasound energy reflected from the various anatomical structures change in response to the pulsation. ICP is then thought to be dependent on the brain tissue mechanical resonance level value measured (Maloney-Wilensky et al 2009). Results using the method by Michaeli et al (2002) and the traditional method for blinded tests in 40 patients with different diseases, with various ICP values over the range 1–66 mmHg, were highly correlated ($r = 0.99$), proving that TRA allows for accurate noninvasive ICP recordings. The method and device for noninvasive ICP measurement based on tissue resonance analysis have both qualitative and quantitative options. The qualitative method determines a specific ICP range: (either 10–20 mmHg, 20–40 mmHg, or >40 mmHg) based on long-term recording of ICP wave patterns. The quantitative method yields an ICP result in mmHg. Combining the transit times with measured acoustic impedance, resonant frequency, or ultrasound wave through the brain parenchyma tissue have been proposed.

2.2.5.3 Jugular vein

Jugular vein occlusion is known to increase ICP. Allocca (1980) described occluding the jugular vein for a short period of time (c. 5 s) and noninvasively measuring blood flow in the occluded jugular vein upstream with a Hall sensor or an ultrasound transducer. There exists a linear relationship between jugular blood flow change rate and ICP (Verwei et al 2001). The jugular vein method is simple and can easily be made portable and field-deployable.

Elevated ICP is complex and can occur from venous restriction. If it occurs from syndromic craniosynostosis, it is possible that it is caused by venous hypertension if there are no other identifiable problems such as calvarial volume. Ultrasound allows internal jugular vein dimension assessment, measured via rigid collar application due to an interruption of venous outflow, which may yield information regarding elevated ICP.

CHAPTER 3: COMPARISON AND LIMITATION OF METHODS OF MEASURING ICP

3.1 Comparison and limitation of invasive methods of measuring ICP

Each invasive method of measuring ICP is discussed in detail in chapter 2, and Table 2 summarizes the pros and cons of these devices. EVD/ventricular catheter is the traditional gold standard in providing accurate ICP and continuous measurement. However, there is a tangible risk of complications such as bleeding, infection, and technical problems upon insertion. The LP method reflects only instantaneous ICP values rather than average continuous ICP, is susceptible to positioning effects (sitting, standing, abdominal pressure) and may be hazardous in the setting of a CSF flow obstruction. Epidural devices do not provide the necessary accuracy for routine/clinical use, and are arguably less reliable in detecting elevated ICP. Intraparenchymal and subdural devices are inaccurate if intraparenchymal gradients exist between fossas of the skull. Telemetric ICP measurement technology is not yet reliable or readily available. Thus far, none of invasive ICP monitoring techniques available can be regarded as a gold standard because of their own significant limitations and disadvantages.

In addition, Table 3-1 shows that invasive methods for monitoring ICP have several common drawbacks (Popovic et al. 2009; Asiedu et al. 2014): (1) pressure sensor drift stability requiring recalibration/continuous calibration or replacement over 2 or more weeks; (2) nervous system injury caused by inserting the sensor or from frequent operations due to failure that both increase bleeding/traumatic complications and infection risk; and (3) insertion that can only be performed by highly trained individuals (neurosurgeons), and finally invasive ICP monitoring is limited to neuro-intensive care units and special hospitals, and cannot be routinely used in general hospitals, emergency rooms, and ambulatory settings because of the required equipment and vigilance of trained staff to help ensure that the device is not inadvertently broken or dislodged (Popovic et al 2009, Raboel et al 2012).

Table 3-1 Methods for invasive monitoring of ICP

Methods	Advantages	Disadvantages

External ventricular drainage (EVD) ventricular cannulation/ ventricular catheter-tip	Gold standard for accurate ICP measurement; CSF drainage, CSF sampling and administration of drugs; in vivo calibration/control ability; inexpensive	Most invasive and challenging insertion; high infection rate; Occlusion of catheter by blood or tissue; needs sensor level repositioning with change in head position. False reading if leakage of CSF is present
Lumbar puncture (LP)	Extracranial procedure; outpatient procedure; easiest technique to release CSF for therapy	May only reflect instantaneous rather than average ICP; may be hazardous if CSF flow obstruction is present and ICP is high; positioning (sitting or lying) should be considered
Epidural and subdural device	Easy to insert; Doesn't penetrate the brain, lower risk of infection compared to EVD	Low accuracy; drift of the sensor output over time; accuracy and reliability are questionable; in vivo calibration not possible; cannot drain or sample CSF
Intraparenchymal device (fiberoptic or strain gauge)	Insertion and handling simpler than EVD; lower complication rate than EVD; good alternative to EVD; easy patient transport; minimal artifact and drift; high waveform resolution, lower risk of infection; no need to account for patient position	Inaccurate if intraparenchymal gradients exist; cannot be recalibrated after placement, unless an EVD is used simultaneously for reference; cannot drain or sample CSF; potential fiberoptic cable breakage; high cost
Telemetric ICP measurement	Does not require external wiring, so can be used longer term	Technology not yet reliable and readily available. complications related to insertion; high cost

3.2 Comparison and properties of non-invasive methods of measuring ICP

Table 3-2 provides a summary of the accuracy, skill level requirement, cost of technology, continuous monitoring ability, time consumption, bedside and emergency setting ability, and other advantages or drawbacks for each non-invasive ICP measurement method. The accuracy comparison below is performed as either training or testing. Training represents comparisons which can potentially predict the correlation between the invasive and non-invasive method of ICP monitoring. Testing represents the utility of noninvasive method being used to the reference method – ie. Invasive method.

The noninvasive methods for ICP monitoring are still in the exploratory phase because none of the methods described here are sufficiently accurate and easy to use. In addition, most methods cannot yet be readily used for the continuous monitoring of ICP. There exists more room for further research and development in non-invasive ICP measurement.

Table 3-2 Characteristics of noninvasive ICP measurements methods

		Accuracy	Skill level	Cost of technology	Continuous monitoring	Time consumption	Bedside setting	Emergency setting	Other properties
Magnetic resonance imaging (MRI)	Training	Not validated	Expert	High	No	Yes	No	No	Not a bedside assessment
Transcranial Doppler ultrasonography (TCD)	Testing	±10–15 mmHg	Expert	Moderate	No	No	Yes	Yes	Finding correct vessels difficult even for experts; high percentage of unsuccessful measurements
Cerebral blood flow velocity (CBFV)	Testing	±1.5 mmHg	Low	Moderate	No	Yes	Yes	No	No calibration or training required before application
Near-infrared spectroscopy (NIRS)	Training	Not validated	Low	Moderate	Yes (for cerebral blood volume)	Yes	Yes	No	For individual patient takes several hours to obtain parameters; only reliably measured in about 50% of patients
Ultrasound time-of-flight	Training	±9 mmHg	Low	Moderate	Possible	No	Yes	No	Easily portable and field deployable. Not validated for clinical use since difficult to replicate
Spontaneous venous pulsations (SVPs)	Training	Not validated	Moderate	Moderate	No	No	No	No	SVPs are absent in 10% of normal people
Venous ophthalmo-dynamometry	Testing	± 3–5 mmHg	Expert	Low	No	Yes	Yes	No	Cumbersome; portable
Optical coherence tomography of retina	Training	Not validated	Expert	Moderate	No	Yes	No	No	Quantitative measurement and monitoring retinal nerve fiber layer
Optic nerve sheath diameter assessment (ONSD)	Testing	± 5–10 mmHg	Moderate/High	Moderate	No	No with sonography;	Yes	Yes with sonography	Can potentially be used as a screening method of detecting raised ICP

						yes with magnetic resonance			
Pupillometry	Training	Not validated	Low	Low	No	No	Yes	Yes	Some medical conditions and medications interfer in pupil size and reactivity
Sensing tympanic membrane displacement (TMD)	Training	± 15–20 mmHg	Moderate	Low	No	Yes	Yes	No	Useful in classifying ICP as high or normal. Best results in young population. Inapplicable to older patients; time-consuming
Analyzing otoacoustic emissions (OAE)/ acoustic measure	Training	± 15–20 mmHg	Moderate	Low	No	Yes	Yes	No	Intersubject variability, Can't be performed in case of consuctive or sensorineural hearing loss
Transcranial acoustic (TCA) signals	Training	± 5 mmHg	Moderate	Moderate	Possible	No	Yes	No	Estimate both static and pulsatile iICP non-invasively
Visual-evoked potentials (VEP)	Training	Not validated	Expert	Low	No	Yes	Yes	No	Not suitable for many patients such as for bifrontal hematomas, retinal injuries or optic nerve pathologies
Electro-encephalography (EEG)	Training	Not validated	Moderate	Moderate	Possible	Yes	Yes	No	Repeated visual stimulation needed; cumbersome
Skull vibrations	Testing	Not validated	Expert	Low/ moderate	No	Yes	No	No	Cranial cavity strains are coincident with ICP variation
Brain tissue resonance	Training	Not validated	Expert	Moderate	No	No	Yes	No	Both qualitative and quantitative
Jugular vein	Training	Not validated	Expert	Low/ moderate	No	Yes	No	No	Cumbersome; unpleasant; portable and field-deployable

HAPTER 4: IMPLANTABLE MICROSENSOR DEVICES

4.1 Epidural and subdural sensor devices

Epidural pressure sensors are small tongue-shaped sensors that fit into the space between the dura and the skull and in which the pressure-sensor diaphragm faces the dura and the brain. Subdural pressure sensors fit under the dura and the pressure sensor faces the brain.

Even though epidural and subdural pressure sensors have the disadvantage of not allowing therapeutic CSF drainage, they carry a lower rate of infection, hemorrhage, and seizures compared to the EVD (Gaab et al 1989, Raabe et al 1998). A specific advantage of epidural probes is the avoidance of dural penetration and the hazard of CSF leak and infection. However, the relationship between ICP and extradural space pressure is unclear.

Epidural devices however, do not provide the necessary accuracy for routine/clinical use. Bruder et al (1995) showed that an epidural Camino sensor considerably overestimated ICP with a mean of about 9 mmHg, extending to almost 30 mmHg. Eide et al (2008) described a significantly different mean ICP of 10.8 ±2.3 mmHg however, with comparable parameters such as mean wave amplitude of 3.4 ±1.0 mmHg and wave rise time of 0.27 ±0.02 s as related to ICP.

Epidural devices have been virtually abandoned because they are bulky and their insertion requires a large skull opening. One reusable device named Gaeltec ICP/B solid-state miniature ICP sensor was designed for use in the epidural space with zero reference-checking ability in vivo. However, measurement artifacts and measurement quality decay caused by repeated use were the limiting factors for this technology (Morgalla et al 1997).

Subdural catheters are inserted almost exclusively following craniotomy because they require a much bigger dural opening than a burr hole allows. They are arguably less reliable in measuring elevated ICP (Bhatia and Gupta 2007, Wiegand and Richards 2007).

4.2 Intraparenchymal sensor devices

Intraparenchymal systems are inserted through a support bolt or are tunneled subcutaneously from a burr hole. Intraparenchymal devices are easy to place, have very few infectious complications, and are simple to handle, meaning they are the most reliable devices in daily practice. Mechanical complications can be due to placement problems or later problems during the monitoring period. Intraparenchymal probes are the most widely used devices to measure ICP. They are usually placed in the right frontal region at depths of approximately 2 cm. However, the placement can be modified depending on clinical needs or anatomical variations (Popovic et al 2009). This type of device is the current choice in the emergency room and for elective surgical cases.

Camino and the Codman MicroSensor are the current two market leaders using the intraparenchymal technique. Both companies place a thin disposable wire through a twist drill hole into the cranial cavity. Considering the accuracy, most clinicians end the tip in the brain parenchyma, ideally 1–2 cm into the brain tissue.

The Camino Innerspace device is based on fiberoptic technology, so the wire needs to be kept in a straight line without kinking. Pressure change results in an alteration of the reflection of the light beam. A bolt for passing the wire is an essential part of the package (Gelabert-Gonzalez et al 2006).

The Codman MicroSensor device has a micro-miniature strain gauge pressure sensor—pressure change results in a change of resistance—and can be inserted without a bolt. Wiegand and Richards (2007) state that ICP trace shifting used to be a problem for first-generation devices; however, it is not a significant problem in current models (Pople et al 1995, Rossi et al 1998, Anderson et al 2004).

Intraparenchymal probes are a good alternative to ventricular catheters and usually have a low infection rate (Mack et al 2003). The main disadvantage of this technique is a small drift of the zero line and the inability to drain CSF. This device is zeroed with respect to the atmosphere before insertion and is not able to be recalibrated after insertion without removing it from the human (Luerssen 1997, Gelabert-Gonzalez et al 2006). The output is significantly dependent on the sensor zero drift, but both systems are only zeroed

relative to atmospheric pressure before insertion instead of using in vivo calibration. Technical complications such as kinking of the cable for the Camino device and dislocation of the sensor for first-generation Codman devices have also been reported (Stende et al 2003). Furthermore, the local pressure value detected by the device may be misleading since the ICP is not uniform within the skull. In other words, supratentorial measurements may not reflect ICP as well as other methods such as intraventricular catheters. Wiegand and Richards (2007) described how direct intraparenchymal ICP monitoring based on various devices in the market is technically straightforward, accurate, and carries a low risk. It has become routine in pediatric neurosurgery.

Hummingbird Neuromonitoring products manage patients with conditions causing elevated ICP. Berlin et al (2015) compared the ventricular and parenchymal ICP readings from a multi-parametric neurological Hummingbird® Synergy Ventricular System. This system indicated that congruence from a total of 2259 observations is within ±0–3 mmHg of 93% of readings between ventricular ICP and parenchymal ICP. Following prescribed interventions, 98% of readings became congruent (within ±0–3 mmHg). The mean difference between the two methods was −0.95 mmHg and all mean ICP readings were between −2 and +2 mmHg. The results recommend use of the parenchymal ICP component for routine ICP monitoring, also permitting the ventricular catheter to drain cerebrospinal fluid (CSF) without having to be clamped off to obtain measurements.

An external ventricular drain (EVD) instead of an intraparenchymal fiberoptic monitor (IPM) may be better at controlling refractory intracranial hypertension. Liu et al (2015) monitored and treated 122 patients with traumatic brain injury (TBI) of age ≥13 years in neurosurgical intensive care units between January 2009 and December 2012. For randomly monitoring either EVD or intraparenchymal fiberoptic enrolled patients, there was no significant difference between the groups in device-related complications ($p = 0.448$). Refractory intracranial hypertension was diagnosed in 44 of 122 patients, and the IPM group had a higher percentage of refractory intracranial hypertension compared to the EVD group (51.7% v. 21.0%, $p < 0.001$). The 1-month survival rate was 76.7% in the IPM group and 90.3% in the EVD group. In addition, the EVD

group had a significantly higher 6-month post-injury survival rate compared to the IPM group (88.7% v. 68.3%). Based on these findings, Liu et al (2015) recommend routine placement of an EVD in patients with TBI, unless only parenchymal-type monitoring is available. Further, well-designed, multicenter studies, instead of a single-institution study, are needed to confirm these results as well as consider individual variability.

4.3 Comparison of different commercial microsensor ICP monitoring devices

Microsensors have been used for several years to record ICP. Depending on the technique mentioned above, the monitoring device can be inserted in the intraventricular, epidural, subdural, intraparenchymal or subarachnoidal compartment. Invasive ICP monitoring devices can be categorized into fiberoptic devices, strain gauge devices, and pneumatic sensors.

4.3.1 Fiberoptic devices

For fiberoptic devices, such as the Camino ICP Monitor, light is transmitted via a fiberoptic cable towards a mirror, which is displaced by a flexible diaphragm at the tip of a narrow fiberoptic catheter. ICP changes move the mirror, and the changes in reflected light intensity to a return fiberoptic are translated to an ICP value. The outside diameter of the Camino device is only 1.3 mm and this catheter-tip sensor is not dependent on an external sensor.

Gelabert-Gonzalez et al (2006) tested 1071 Camino ICP devices on 1000 patients. A total of 92.2% of patients were scanned by CT. It was found that 2.5% had evidence of hemorrhage related to sensor insertion and 0.66% (6 cases) had significant hemorrhage, including four intraparenchymal and two epidural. Subsequent bacterial growth cultivation was 8.5% among 574 examined probe tips, although this may be related to contamination during the removal process. A number (4.5%) of devices demonstrated technical errors, which were mostly related to the fiberoptic cable itself. Piper et al (2001) tested the Camino device on 328 patients and found 3.14% of sensors had technical errors, 1.1% sensors resulted in hemorrhage, and 4.75% sensors resulted in infection.

4.3.2 Strain gauge devices

Strain gauge devices include Codman MicroSensor, the Raumedic Neurovent-P ICP sensor, and the Pressio sensor. ICP changes bend the sensor diaphragm and the piezoresistive strain gauge changes resistance, yielding the ICP value.

The Codman MicroSensor consists of a miniature solid-state pressure sensor mounted in a very small titanium case of 1.2 mm diameter at the tip of a 100 cm long flexible nylon tube with 0.7 mm diameter. The sensor tip contains a silicon microchip, in which diffused piezoresistive strain gauges are connected to complete a Wheatstone-bridge-type circuit by wires in the nylon tube. The silicon diaphragm deflects a small amount (less than 1 μm for 100 mmHg applied pressure), causing strain in the embedded piezoresistors. The top layer is exposed to the applied CSF directly or pressure on brain tissue, while the bottom diaphragm layer is vented to the sealed nylon tube.

The Codman MicroSensor has been thoroughly examined in several studies. Hong et al (2006) tested the Codman MicroSensor on 120 patients, and 85% of them had CT scans after insertion. The results showed no incidence of hemorrhage and only one infection post-operatively. Koskinen et al (2005) tested 1000 Codman MicroSensors, and found no infections linked to MicroSensor placement and only three surgically related hemorrhages that did not require surgical intervention. Citerio et al (2008) tested 99 Raumedic Neurovent-P Sensors sensors on 99 patients. Two patients suffered small hemorrhages without surgical intervention. No CNS infections were recorded. The Codman ICP sensor is traditionally only kept in the brain for a maximum of two weeks in order to avoid infection and other complications due to the external wiring through the skin (Medow et al 2011).

Lescot et al (2012) tested the accuracy of 15 Pressio sensors and 15 Codman MicroSensors, then compared the ICP results by an EVD. The two types of sensor demonstrated similar results, with a mean difference of 7 mmHg from EVD ICP results.

4.3.3 Pneumatic sensors

For the pneumatic devices, such as the fluid-filled catheter-sensor system product from Spiegelberg, ICP changes influence the air-pouch balloon in the catheter distal end, allowing ICP compliance to be measured quantitatively. This kind of device automatically zeroes in vivo and has lower zero drift compared to standard catheter-tip ICP devices. However, this system is not widely used and requires further evaluation (Bhatia and Gupta 2007).

Lang et al (2003) tested the Spiegelberg sensor on 87 patients, all of whom were CT-scanned after insertion. The results showed no hemorrhage incidence as well as no meningitis clinical signs. Three patients had a sensor leak, leading to incorrect measurements. Kiening et al (2003) tested the Spiegelberg sensor for continuous intracranial compliance monitoring in 10 TBI patients. The results showed poor overall continuous intracranial compliance (cICC) data quality, and poor predictive capabilities in identifying increased ICP and for cerebral hypoxia correlation. Kiening et al (2005) found the correlation between increasing age and decreasing compliance, then conjectured that the outcome of elderly patients with TBI was poorer as a result of this correlation however this speculation is not uniformly accepted.

4.3.4 Properties of microsensor ICP monitoring devices

One important property for monitoring devices is MRI compatibility. The Neurovent-P sensor, Spiegelberg sensor, and Codman MicroSensor are all compatible with MRI with no danger to the patient. The Camino monitor and Pressio sensor contain ferromagnetic components however, which are not MRI compatible (Raboel et al 2012).

Lang et al (2003), Bratton et al (2006), and Raboel et al (2012) concluded that microsensors have ICP measurement results as accurate as EVDs. EVDs have recalibration ability by resetting the sensor to atmospheric pressure at the zero-point level at any time since the sensor resides outside the brain. However, no recalibration after insertion exists, except for the Spiegelberg catheter with its per hour recalibration ability. Pressure gradients from the ventricle and the height of the column of fluid outside of the head determine CSF drainage and tubing caliber along with the pressure gradient determine the rate of CSF flow.

A difference exists for all strain gauge devices between first-time device calibration before insertion (0 mmHg) and device removal (zero drift). With EVDs, the ability to recalibrate the sensor makes this method of monitoring ICP advantageous. However, the inability of the EVD to measure ICP and drain simultaneously is a disadvantage that must be understood. The entire force of the ICP pulsation must effectively deform the sensor otherwise the actual pressure may be underestimated as is seen when the EVD is opened to both the burr hole and sensor at the same time. A solution to this problem is to have the sensor not be connected to the column of fluid being drained.

CHAPTER 5: ACTIVE SENSOR DESIGN AND FABRICATION FOR ICP

5.1 Active sensor system overview

Real-time intracranial pressure (ICP) data could also be applied to the implantable ICP management system, as the part of the closed loop control system. The whole system consists of: a catheter implanted within the brain of the patient with a proximal portion within the brain opposite a distal portion diverting cerebrospinal fluid (CSF) out of the brain to another region of the patient; an active sensor implanted within the brain of the patient and producing a signal representing an ICP; a valve that permits excess CSF to drain out of the brain through the catheter in an open position and prevents the excess CSF from passing out of the brain through the catheter in a closed position; and a valve driver receiving the signal representing the ICP controlling the valve to switch the valve between the open position and closed position in a cycle for successive

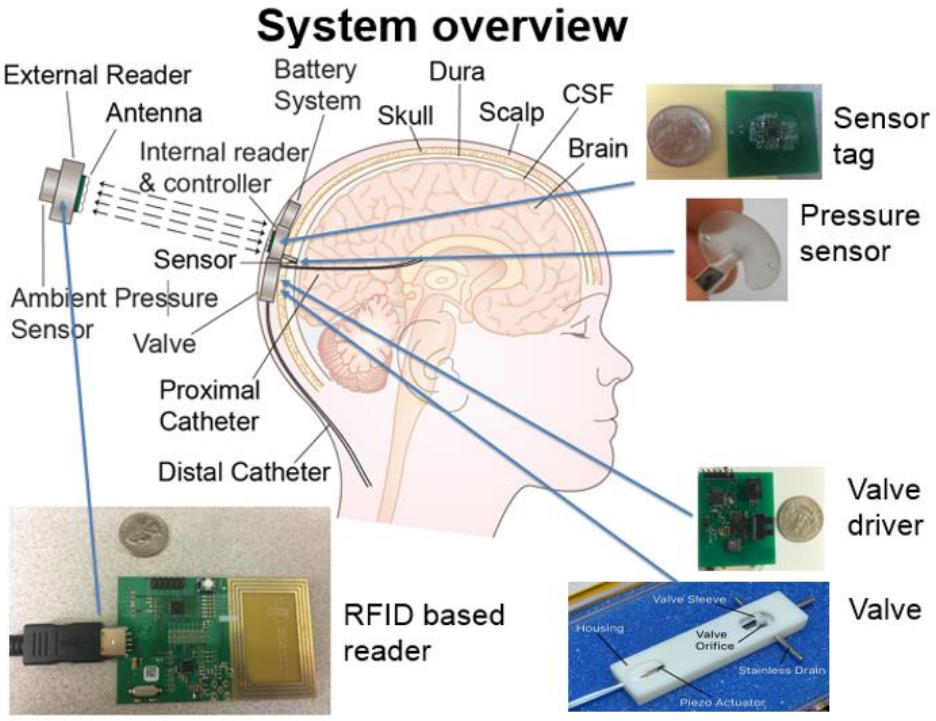

Fig. 5-1. ICP management system overview: RFID based reader, sensor tag, pressure sensor, valve driver and valve

cycles so that the relative time that the valve is in the open position versus the closed position is a function of ICP as shown in Fig. 5-1.

The RFID based reader may be located outside the human head. The sensor tag, pressure sensor, valve driver and ICP valve are implanted between the skull and scalp, and the sensor is implanted through dura layer so that the diaphragm contacts CSF.

5.1.1 Active sensor location

The pressure sensor could be either capacitive or piezo-resistive. Three semi passive/active style ICP design approaches are discussed in this chapter. Fig. 5-2 shows more details for location of the sensor based on hand-held reader based on Radio-Frequency Identification (RFID). The catheter keeps the sensor in place and exposes the diaphragm to the ICP. 75 μm diameter wires connect the ICP sensor to the coil and RFID electronics.

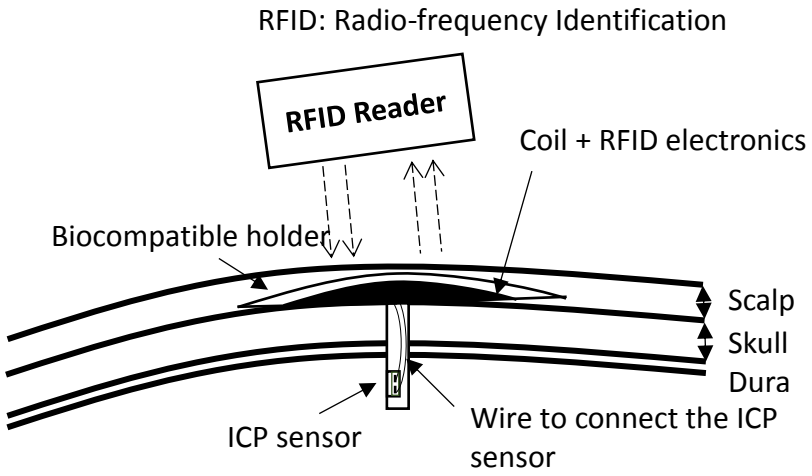

Fig. 5-2 Active ICP Sensor location

5.1.2 Active sensor parameters

An active sensor has higher signal-to-noise ratio (SNR) and longer measurement distance compared to a passive sensor. In real practice, acquiring a high SNR at a reasonable distance (larger than the scalp plus the skull plus the dura thickness) is a challenge for a passive sensor, because SNR decreases rapidly as measurement distance increases. Male adult scalp thickness ranges from 2 to 3.5 mm (Hori et al 1972), and skull thickness average ranges from 6.08 mm to 8.09 mm, and

differs at locations (Law 1993). SNR is constrained first by electromagnetic (EM) wave absorption in the scalp and skull, second by limited transmitting power for biosafety, and third by limited sensor size for biocompatibility.

In addition, the communication method for the active sensor is digital communication, which has better anti-noise ability compared to the analog communication method of passive sensors. It is barely possible for passive sensors to realize timely ICP monitoring because seconds of waiting time are required for a reader to complete one measurement. Usually, to realize real time ICP tracking, the minimal sample frequency should be higher than 10 Hz.

5.2 Capacitive sensor

5.2.1 Capacitive sensor design

Capacitive sensors have the advantages of high sensitivity and resolution, low temperature sensitivity, and low noise performance (Baxter 1997, Lemkin and Boser 1999). Capacitive pressure bio-sensor technology has been proposed by (Collins et al 1967). A low-cost but effective capacitive sensing measurement system was developed to determine properties of ocular structures (Mukherjee et al 2014).

A preliminary evaluation of capacitive sensors for ICP monitoring yielded difference values 1.8 ± 1.42 mmHg between mean capacitive ICP and fluid-transduced ICP and proved that the capacitance-pressure relationship was constant over 4 weeks (Aquilina et al 2011). Use of capacitive sensors and the encapsulation scheme guarantees a drift-free performance over time (Frischholz et al 2007). The aluminum-based diaphragm capacitive pressure sensor as well as valve control devices have been discussed for intracranial fluid pressure measuring, which exhibits little or no drift even over extended periods of time (Miesel et al 2001). Capacitive pressure sensing technology itself has been shown to be suitable for nanometer position resolution (Lee et al 2009, Faller et al 2017, Hicks et al 1997).

The basic idea behind our capacitive sensor design is two parallel metal plates with variable capacitance corresponding to variable distance of metal plates under different applied pressure. Fig. 5-3 shows the structure of the active sensor. Fig. 5-3 (a) shows a silicon membrane acting as a diaphragm on a glass substrate. The silicon is etched to allow placement of two thin Cr adhesion layer and Gold layer combination plates, creating a capacitor as shown in equation (1). *C* is the formed variable capacitance between two thin metal plates, *A* is the area of overlap of the two parallel plates, ϵ_r is the dielectric constant of the material between the plates, ϵ_0 is the electric constant ($\epsilon_0 \approx 8.854 \times 10^{-12}$ F·m^{-1}), and *d* is the separation distance between the two plates. When implanted in the brain, ICP increases and deforms the silicon membrane, the two plates move closer, as shown in Fig. 5-3 (b), the separation distance *d* between two coils decreases, which causes increase of the capacitance *C* of the system. Increased ICP pushes two thin gold plates closer together and changes their capacitance value, which can be read out using an implanted or external hand-held reader.

$$C = \epsilon_r \epsilon_0 \frac{A}{d} \quad (1)$$

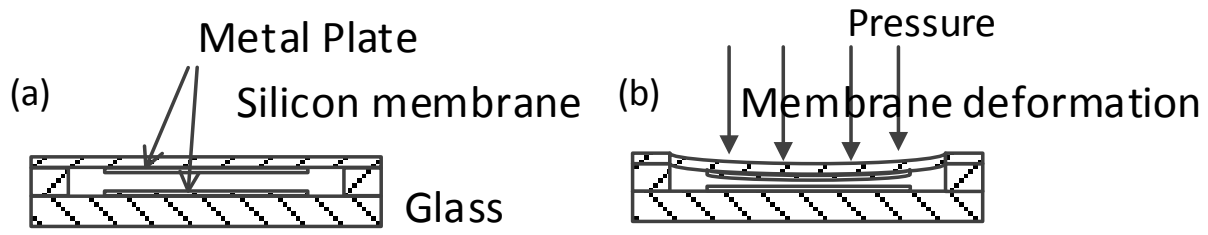

Fig. 5-3. The sensor model. (a) Two Cr adhesion layer and Gold layer combination planar plate face each other, creating a variable capacitor. (b) When pressure is applied on the top membrane, the two plates move closer to each other.

The materials chosen for fabricating this sensor are silicon, glass and gold. Silicon is a crystal with dimensional stability, glass has dimensional stability and gold has low resistivity and high conductivity. In order to reduce resistive loss, parasitic capacitance and parasitic resistance

between the tracks, the pressure membrane layer silicon must have a low level of dopant to raise its intrinsic conductivity. Also as Fig. 5-3 (a) shows, the pressure sensing cavity is carved out of the silicon part of the assembly, since silicon etching methods produce a perfect surface suited for Cr adhesion layer and Gold layer combination deposition. Glass is chosen as the second component for two reasons: 1) It takes fewer steps and is more accurate to align the two halves when one of them is transparent, and 2) The most reliable way to bond the two together and create a vacuum cavity is anodic bonding, which is a bond between silicon and glass.

5.2.2 Capacitive sensor layout

Capacitive sensors are developed and fabricated in the Wisconsin Center for Applied Microelectronics (WCAM) cleanroom.

Previous version sensor design dimensions are 5 × 5 × 0.61 mm. Fig. 5-4(a) and Fig. 5-4(b) show the silicon membrane and glass have gold plating with two thin extended channels on the same side. Fig. 5-5 shows the three-dimensional geometric structure of 1st version capacitive sensor.

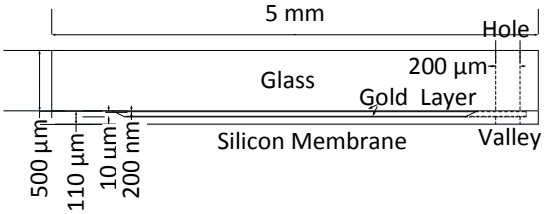

Fig. 5-4 (a) 1st version capacitive sensor front view

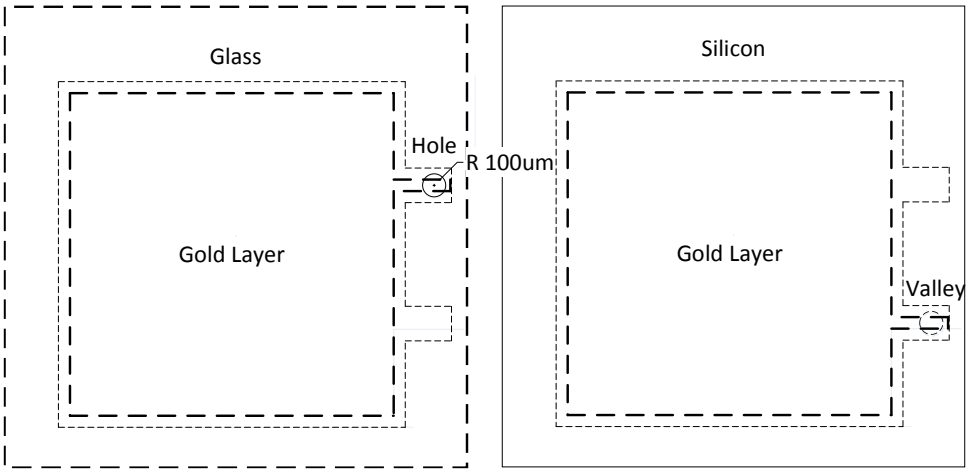

Fig. 5-4 (b) 1st version capacitive sensor top view

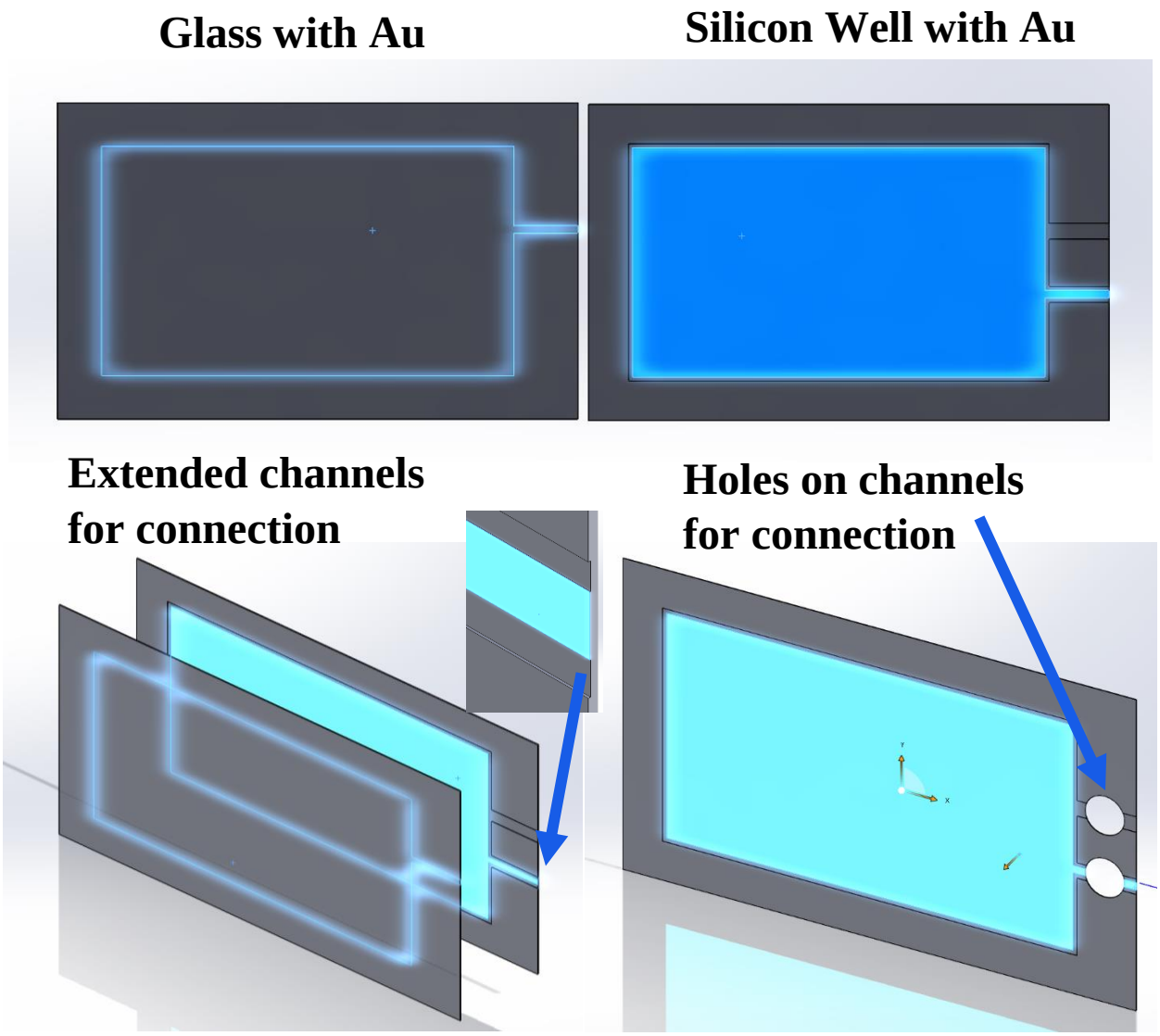

Fig 5-5. Three-dimensional geometric structure of 1st version capacitive sensor

Current sensor design dimensions are 4 × 6 × 0.61 mm. Fig. 5-6(a) and Fig. 5-6(b) show the silicon membrane and glass have gold plating with wide channels on two separate sides. Fig. 5-7 shows the three-dimensional geometric structure of 2nd version capacitive sensor. The 4 × 6 × 0.61 mm chip will fit vertically through a skull hole less than 5 mm diameter.

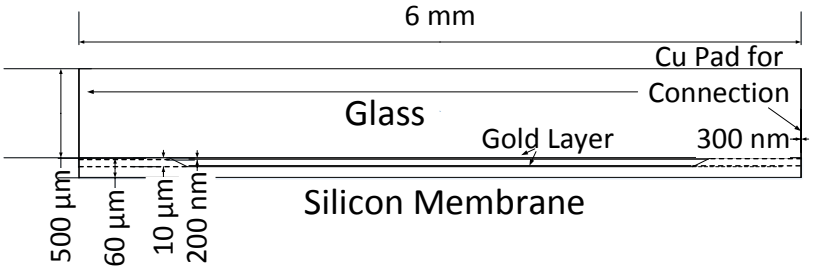

Fig. 5-6 (a) 2nd version capacitive sensor front view

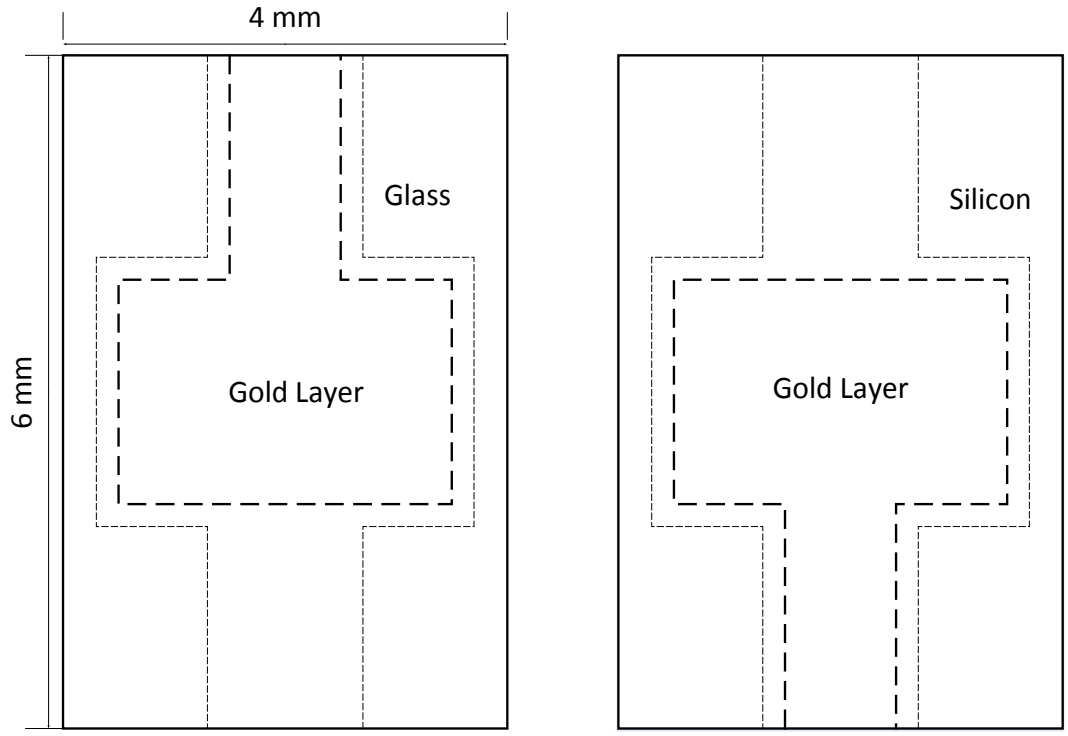

Fig. 5-6 (b) 2nd version capacitive sensor top view

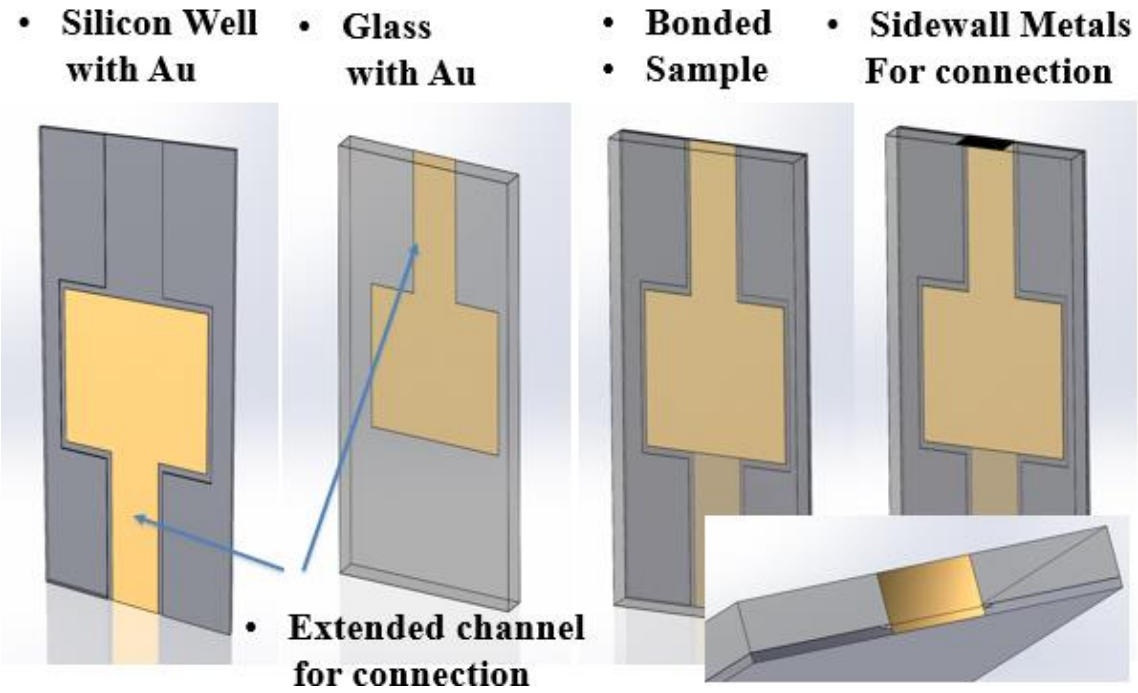

Fig 5-7. Three-dimensional geometric structure of 2nd version capacitive sensor.

5.2.3 Capacitive sensor WCAM fabrication

The real prototype for the capacitive sensor was developed and fabricated in the Wisconsin Center for Applied Microelectronics (WCAM) cleanroom. Fig. 5-8 shows the fabrication process for the 1st version capacitive sensor and Fig. 5-9 shows the fabrication process for the 2nd version. A 10 cm diameter 600 μm thick silicon wafer was cleaned in the Prefurnace Clean, then a thin layer of silicon nitride was deposited in the thermal processing Nitride furnace as a protective layer for multiple 10 μm deep silicon wells as well as two channels (for later hole and valley placement) were etched in the potassium hydroxide (KOH) bench. A 10 cm diameter 500 μm thick glass wafer was cleaned in the Piranha Bench to make sure the surface was clean by removing organic material. E-beam evaporation provided a 200 nm deposition of Au plate as well as a thin Cr adhesion layer with real-time film thickness monitoring onto both silicon and glass substrate in a vacuum. Lithography and liftoff processes yielded the Cr adhesion layer and Gold layer combination pattern

needed after metal evaporation. A wafer aligner and bonding tool was used to yield anodic bonding between the silicon and glass wafers. A dicing saw with a programmable high-speed blade cut the bonded substrates into 5 × 5 × 1.1 mm dies with a 4 × 4 mm deformation diaphragm and 0.5 mm on the boundary for anodic bonding for the 1st version or 4 × 6 × 1.1 mm dies with 3.2 × 2.2 mm deformation diaphragm with extended 2 × 1.2 mm channels for connection for the 2nd version. A grinding tool polished the thick silicon layer to a 50/100 µm thin silicon membrane to decrease the sample thickness from 1.1 mm to 0.55/0.61 mm. Fig. 5-10 shows a laser drill made 2 holes for 75 µm wires through both silicon and glass layers for the 1st version capacitive sensor design. Then a thin glass tool with 50 µm diameter tip immersed in liquid gold is used to fill through glass vias/holes by laser drill for connection between inner Cr adhesion layer and Gold layer combination layers and external sensor electronics. Fig. 5-11 shows a CVC sputter machine with a special holder deposits a Cu layer on the side wall for connection to the external sensor electronics for the 2nd version capacitive sensor design.

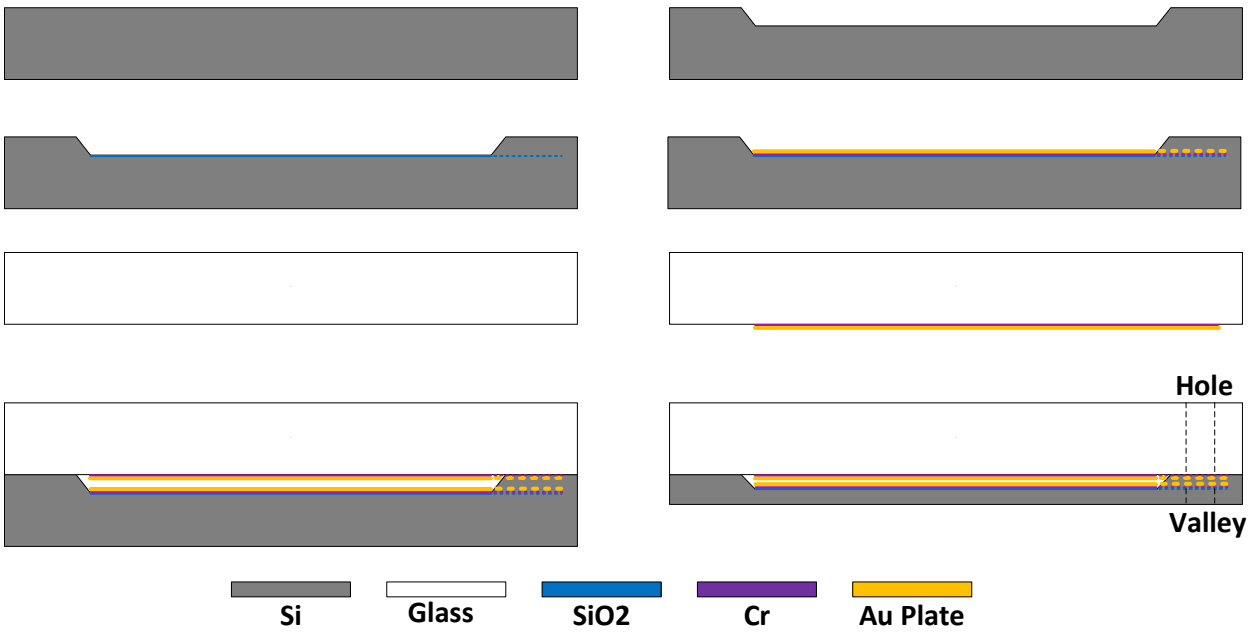

Fig. 5-8 Fabrication process of 1st version capacitive sensor

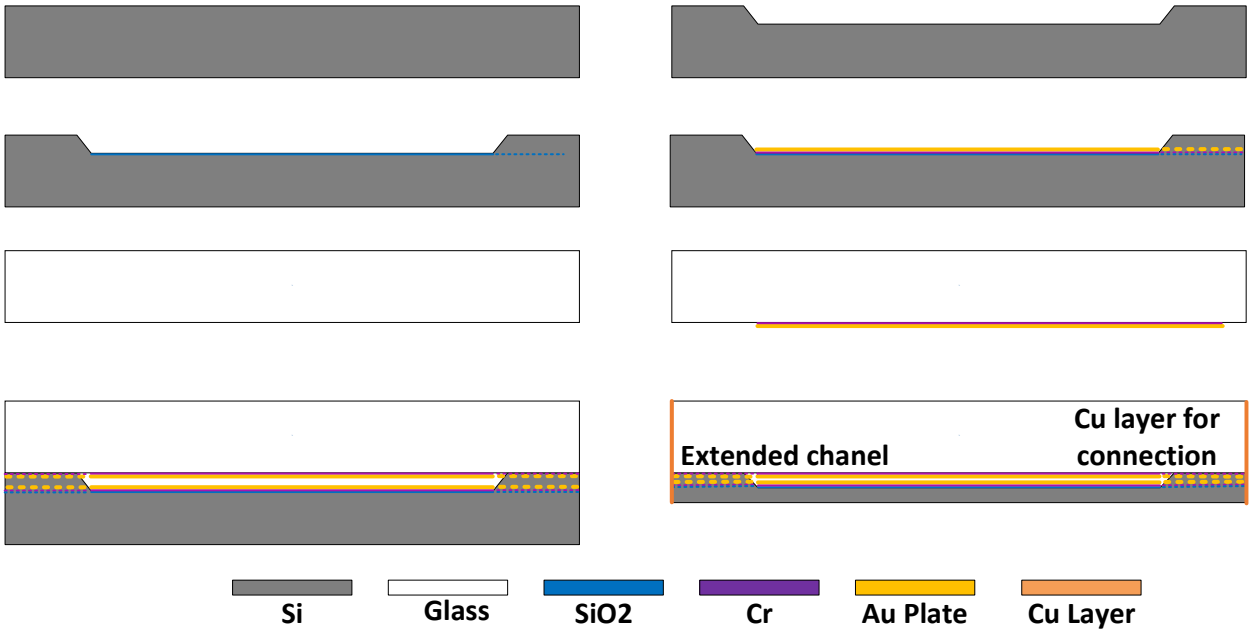

Fig. 5-9 Fabrication process of 2nd version capacitive sensor

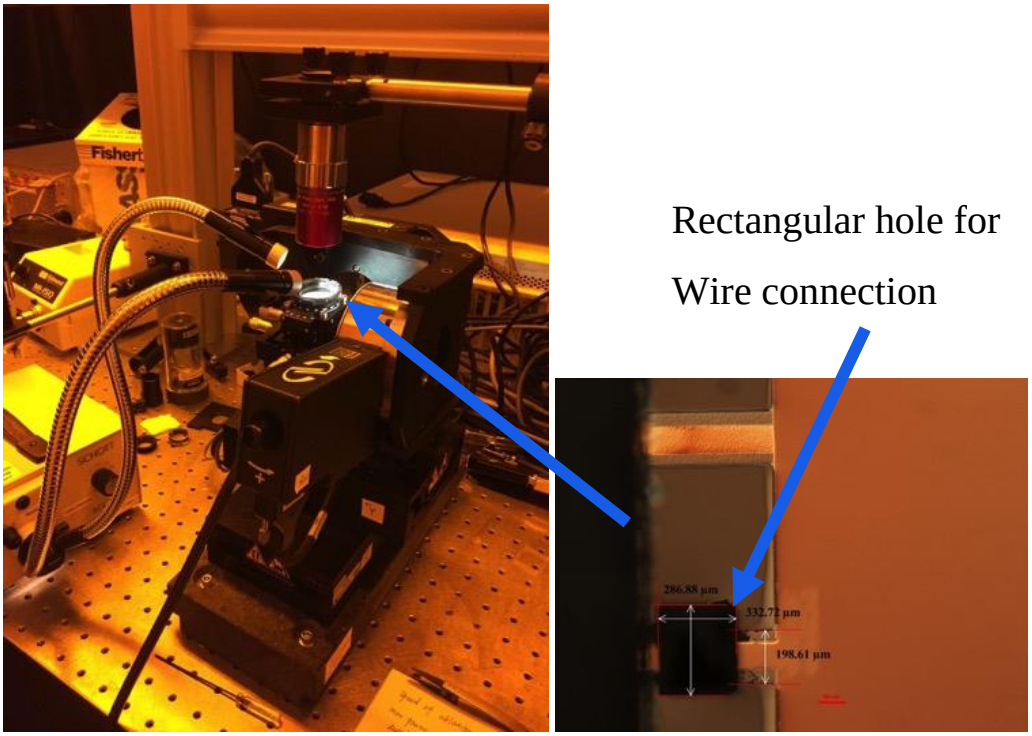

Fig. 5-10 (a) Glass Laser Ablation Machine (b) Sample with hole on one channel (Microscope top view)

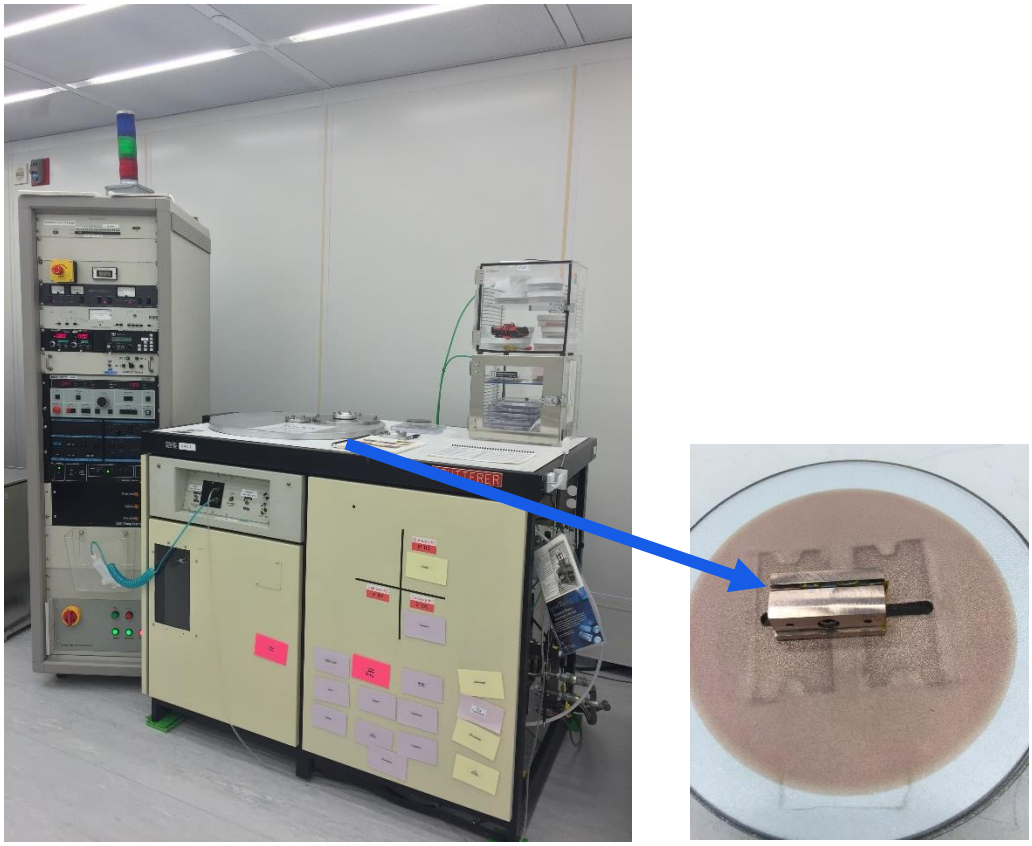

Fig. 5-11 (a) CVC sputter machine (b) Special holder put in chamber to fix the samples and expose sidewall

5.2.4 Challenges

The active capacitive sensor needs a connection between the two Cr adhesion layer and Gold layer combination plates and the sensor tag/electronics. Realizing a solid connection for communication is a challenge.

Considering that anodic bonding must be completed between the silicon and glass wafers, the 1st version sensor has two thin channels on the same side with a hole and a valley. One hole around one channel goes through the glass layer as shown in Fig. 5-4(b) left, one valley around the other channel goes through the silicon layer as shown in Fig. 5-4(b) right.

The laser ablation tool has been tried to make 2 holes for 75 μm wires connections as shown in Fig. 5-10(a). This very expensive laser is designed to make tiny micrometer level holes in a

precise manner. The disadvantages of this method are (1) high time cost and (2) hole shape considering. (1) One rectangular hole around 200 μm × 300 μm size with 500 μm depth needs up to 4 – 5 h for the process itself in addition to the machine setup and sample position corrections. (2) The side view of the rectangular hole is trapezoidal with a narrow top or pyramid because of the silicon/glass particle residue and obstruction during the process of removing material from a solid surface by irradiating it with a laser beam.

The hole shape created by laser ablation makes it hard to make the wire bonding through the wire bonder machine named WestBond as shown in Fig. 5-12, which makes electrical connections by ultrasonically bonding 75 μm Al wire.

Fig. 5-12 Westbond 747677 Aluminum wedge bonder

We tried another idea after the failure of wire bonder machine. The plan was using a special tiny thin glass tool with 50 μm diameter tip as shown in Fig. 5-13 to dip liquid gold at the front tip, then touch the inner sidewall of the trapezoid or pyramid. We put the sample in a high temperature oven for 30 min to evaporate the liquid and yield a solid gold connection. Unfortunately, we could not avoid capillarity because of the tiny 10 μm distance between the two

metal plates. Once there exists liquid gold between the two metal plates, a short circuit connection occurs, then this experimental method fails.

Fig. 5-13 Glass tool with thin tip for liquid gold dip and hole connection

5.2.5 Capacitive sensors comparison

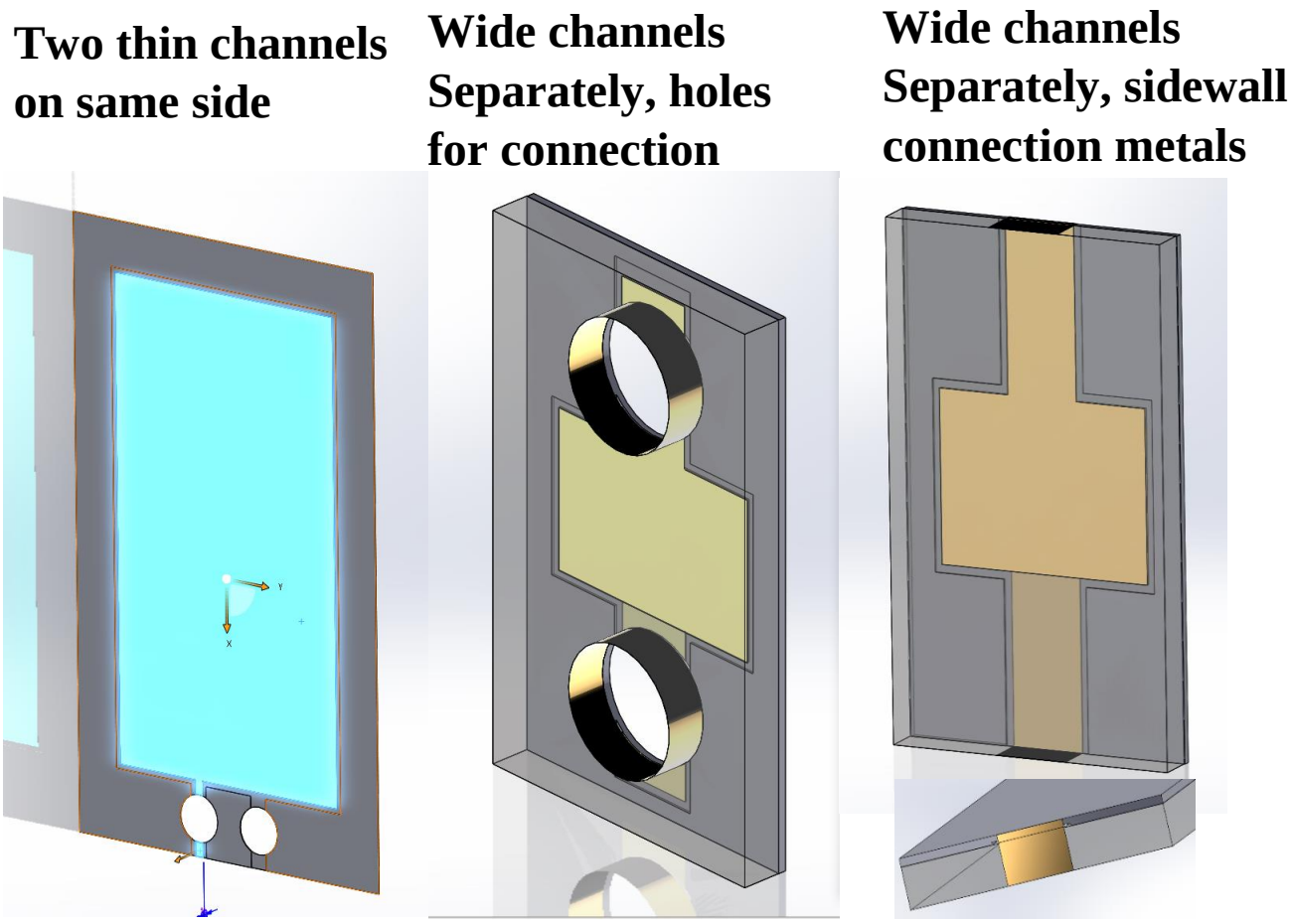

Fig. 5-14 Comparison of different capacitive sensors designs: channel position and connection method

To overcome these challenges, we tried different capacitive sensor designs. The main differences are extended channel positions of the two metal plates and reliable connection methods. The same side two thin channels were changed to different side wide channels. The connection method for 1st version was two holes on the same side of channels, then next version two holes separately on different sides of wide channel and finally 2nd version adding sidewall Copper metal deposition. Fig. 5-14 shows the improvement and comparison of different capacitive sensors design. The advantages of the improved 2nd version are solid connection between two capacitive metal plates and prevention of possible short circuit connection.

5.3 Piezo-resistive sensor

A piezo-resistive sensor option is based on using a commercial piezo-resistive sensor die with metal wire bond pads where the silicon ICP diaphragm is exposed to the ICP and gold wires are electrically insulated. A Gold Ball Bonder Machine makes electrical connections by ultrasonically bonding Au wire, then soldering to the electronic circuit for a 3rd version. Pressure applied to the sensor membrane changes the Wheatstone bridge resistances of the piezo-resistive sensor. The sensor electronics detects this resistance change and calculates the corresponding pressure. A similar approach is based on a sealed ICP sensor product and implants it between the skull and the scalp with a tube through the dura to measure ICP. This piezo-resistive sensor die and product both need protective layers to be used in a corrosive environment such as CSF. Thus, a biocompatible protective material must be deposited to avoid liquid CSF access to the membrane. The protections could be silastic, n cyanoacrylate, or parylene.

5.3.1 Piezo-resistive sensor die based layout

Fig. 5-15(a) shows one possible commercial piezo-resistive sensor die for the 3rd version is Amphenol P330 series, which is 900 × 330 × 180 μm. The pressure range is 450 to 1050 mmHg absolute and it offers good stability and 10 μV/V/mmHg sensitivity. It has low power consumption

2.81 mW because of its 3 V excitation voltage and 3 kΩ high impedance. This extremely small size sensor is ideal for medical device applications. Fig. 15 (b) shows another possible commercial piezo-resistive sensor die for the 3rd version is All Sensors DS-0287 series, which is 2 × 2 × 0.85 mm. The pressure range is 9 to 56 mmHg gage style (relative to the atmosphere). It has power consumption 2.61 mW because of its 2.8 V excitation voltage and 3.2 kΩ high impedance. This sensor realizes low pressure sensing using silicon based longitudinal and transverse strain technology. Both sensor dies need the diaphragm protective material coating when exposed in CSF/ICP.

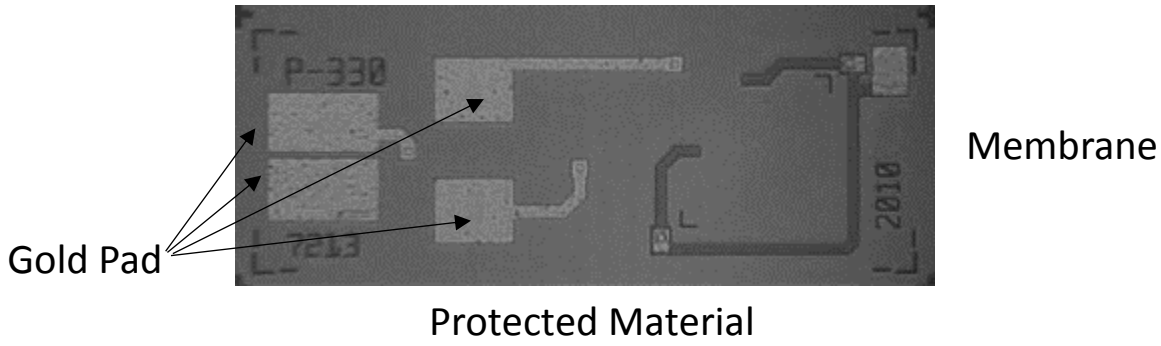

Fig. 5-15 (a) Commercial Amphenol P330 Series Pressure Sensor Die piezo-resistive sensor.

Square deformable membrane filling most of the right side is connected to gold wire bond pads on the left to permit wire connection to the electronic circuit.

http://www.amphenol-sensors.com/en/products/pressure-mems/3235-p330-series?gclid=Cj0KEQjwiKS3BRCU-7XQ75Te3NoBEiQAA2t_xIqHbsm7IbQZSGb1vO-h79mu4hOlbri1HD1B_1EGlyQaAn5S8P8HAQ#specifications

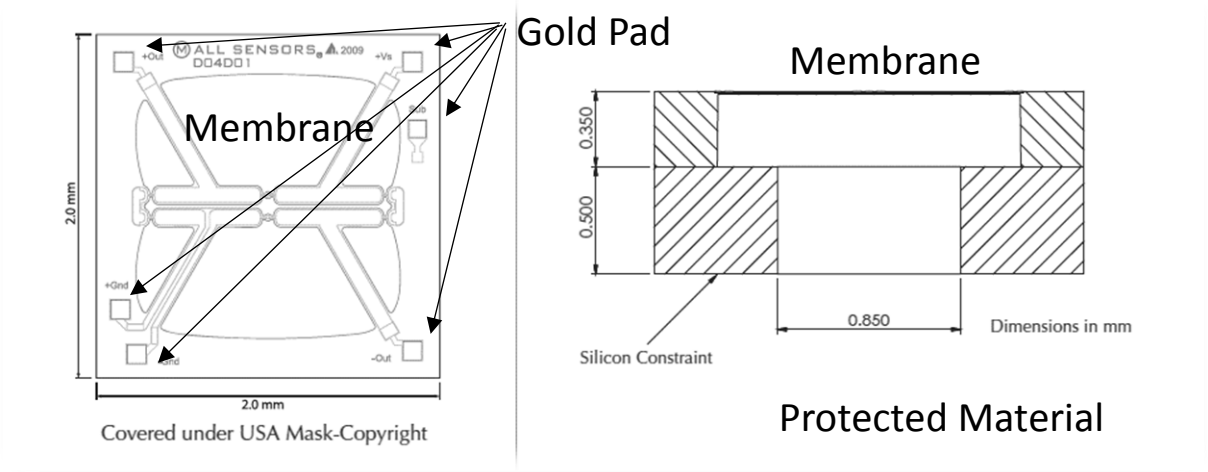

Fig. 5-15 (b) Commercial All Sensors DS-0287 series Pressure Sensor Die piezo-resistive sensor

The square deformable membrane filling most of the center is connected to gold wire bond pads on the boundary to permit wire connection to the electronic circuit. https://www.allsensors.com/datasheets/DS-0287-Rev-A1-1.pdf

5.3.2 Piezo-resistive sensor product based layout

Fig. 16(a) shows another approach example. It is a commercial piezo-resistive sealed ICP sensor Keller America, Inc 9LD which is 19 mm in diameter and 5 mm thick. It is large but would fit between the skull and scalp. A sealed metal tube could transmit the ICP to the O ring without a leak. Similar to piezo-resistive sensor die based, the piezo-resistive sensor product based needs protective layers when exposed in CSF/ICP as well. Thus, biocompatible protected material will be deposited to avoid liquid access to the membrane.

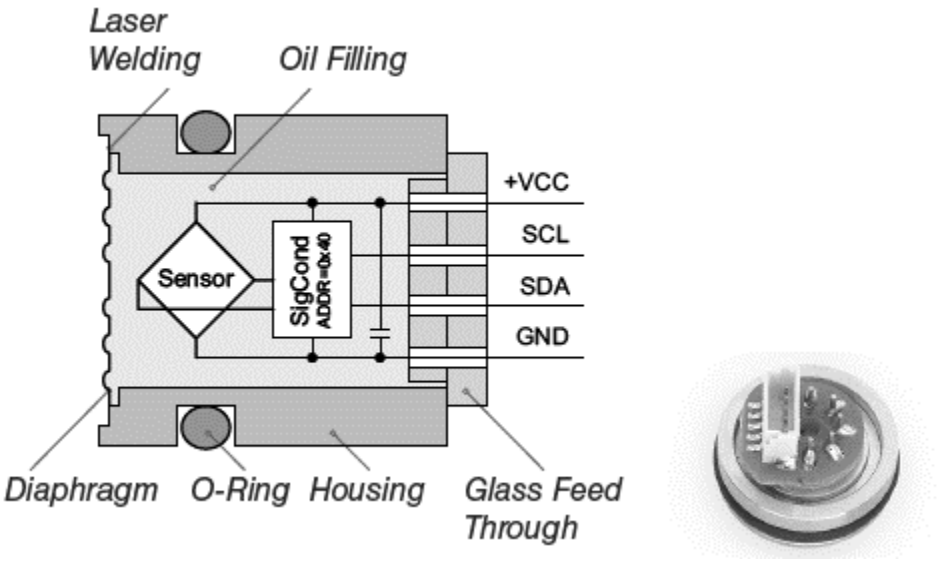

Fig. 5-16 (a) Commercial Keller America, Inc 9LD piezo-resistive sealed ICP sensor stretch. (b) sealed ICP sensor product view. http://www.keller-druck.com/picts/pdf/engl/4ld_9ld_e.pdf

CHAPTER 6: PASSIVE SENSOR DESIGN AND FABRICATION FOR ICP

Portions of this chapter are taken from Wang F, Zhang X, Shokoueinejad M, Iskandar B J, Medow J E, Webster J G 2017 A Novel Intracranial Pressure Readout Circuit for Passive Wireless LC Sensor *IEEE Trans Biomed Circuits Syst.* 11(5):1123-32

6.1 Passive sensor system overview

Our goal is to design a permanently implantable pressure sensor to provide continuous intracranial pressure (ICP) monitoring so the ICP pressure can be read out wirelessly using a hand-held external reader/telemeter with an antenna employed as shown in Fig. 6-1. A fully implantable passive sensor is attractive for ICP measurement, for its low cost, tiny size, simple circuit, and fabrication. In addition, its battery-free and wireless features make it easier to achieve long term stability. Tiny size is attractive for biosafety and biocompatibility. In addition, the system's total power radiation will be lower compared to an active sensor.

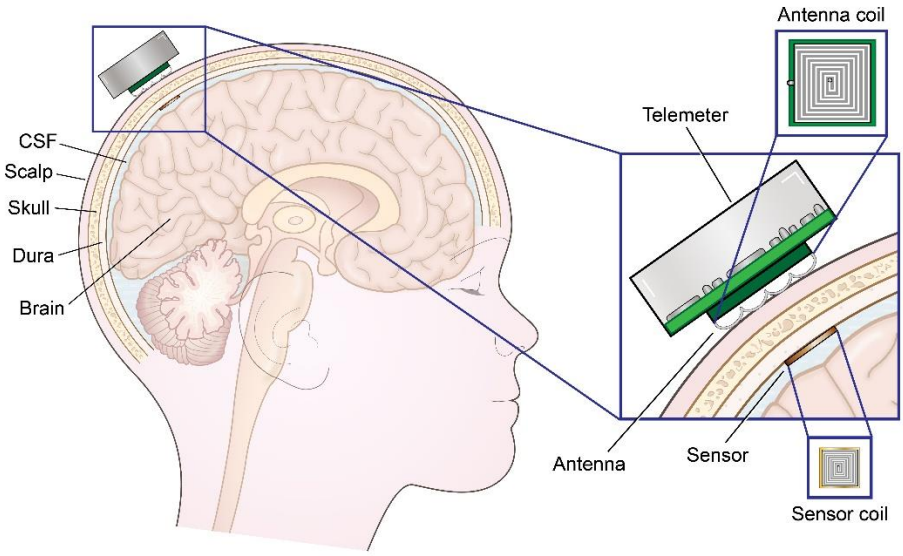

Fig. 6-1 ICP pressure diaphragm will face the cerebrospinal fluid (CSF) and the brain.

This sensor will be placed on the protective thick membrane layer covering the brain, known as Dura mater. It will require a much simpler surgical procedure compared to that required for

inserting a ventricular catheter (North 1997) and can be read out at the bedside. Wireless telemetry reduces the risk of infection and inconvenience caused by invasive wires. The external reader will display to the clinician the internally measured ICP and waveform. The physician will be able to receive the pressure readings to facilitate real time assessment of the patient's condition.

Our permanently implantable pressure sensor will provide constant ICP pressure monitoring ability. Compared to active sensors in chapter 5, in this chapter another approach uses a wireless passive ICP design. Increased ICP pushes two spiral copper coils closer together and changes their resonant frequency, which can be read out wirelessly using an external hand-held reader/telemetry.

6.2 Passive capacitive sensor

6.2.1 Passive sensor design

The passive sensor based on a resonant tank circuit dates to the 1960s and was developed by (Collins et al 1967). Then, more sensors were made using a similar principle using thick film technology such as ceramics (Fonseca et al 2002, Fonseca et al 2006, Tan et al 2013) or micro-electromechanical systems technology such as silicone rubber membrane (Baldi et al 2003), liquid crystal polymers (Fonseca et al 2006) and polyimide (Chen et al 2014). However, none of the above design materials could achieve long term stability with small drift. *LC* sensors applied to health care for biomedical applications such as blood pressure and intraocular pressure (IOP) have been presented (Fonseca et al 2006, Cong et al 2008, Cong et al 2009, Chen et al 2011, Xue et al 2012, Kiefer et al 2012, Cheong et al 2012 and Chitnis et al 2013). However, none of the above designs are used for measuring ICP. Our research is to design a permanent/long term implantable pressure sensor to provide ICP monitoring.

The basic idea behind our passive sensor design is a resonant tank circuit with variable resonance frequency and a new structure of a passive sensor. Fig. 6-2(a) shows a glass substrate and silicon membrane acting as a diaphragm. The silicon is etched to allow placement of two spiral

metal coils separated by a gap filled with vacuum, creating a capacitor as shown in equation (1). *C* is the formed variable capacitance between two spiral coils, *A* is the area of overlap of the two parallel plates, ϵ_r is the dielectric constant of the material between the plates, ϵ_0 is the electric constant ($\epsilon_0 \approx 8.854 \times 10^{-12}$ F·m^{-1}), and *d* is the separation distance between two plates. When implanted in the brain, ICP increases and deforms the silicon membrane, the two coils move closer, as shown in Fig. 6-2(b), the separation distance between two metal coils *d* decreases, which causes increase of the capacitance *C* of the system, and hence decreases the natural resonant frequency *f* of the tank circuit as shown in equation (2), *L* is the coil inductance and *Q* is the quality factor. Here *Q* is a dimensionless parameter that describes/characterizes a resonator's bandwidth relative

$$C = \epsilon_r \epsilon_0 \frac{A}{d} \tag{1}$$

$$f = \frac{1}{2\pi\sqrt{LC}} \tag{2}$$

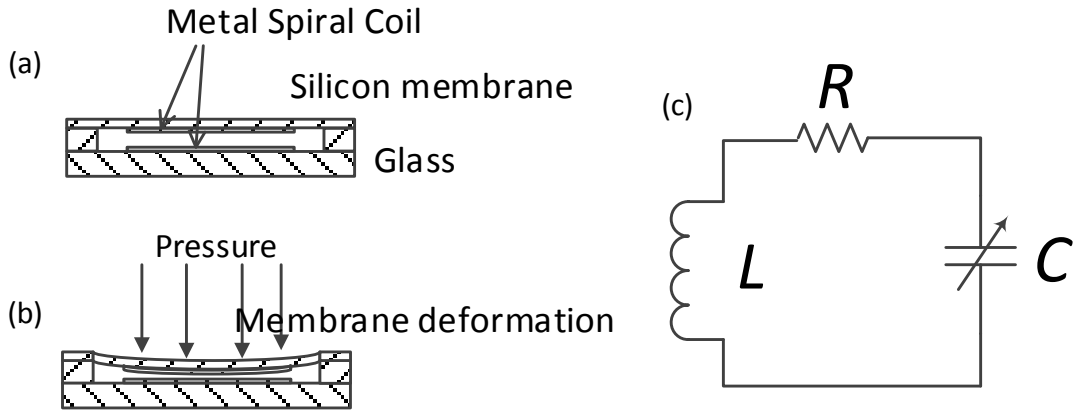

Fig. 6-2. The sensor model. (a) Two metal planar coils face each other (double layer spiral planar coil), creating a resonant tank. (b) When pressure is applied on the top membrane, the two coils move closer to each other. (c) Equivalent circuit model of system, where *R* is parasitic resistance of planar coils, *L* is the coil inductance, and *C* is the variable capacitance between the coils, which is dependent on the pressure.

to its center frequency. Therefore, pressure applied on the sensor can be detected by measuring the resonant frequency of the tank. Tiny dimensions as well as micro spiral planar coil patterns are

desirable for brain implantation. Micro Electro Mechanical Systems (MEMS) enables small sensors fabrication. The implanted ICP sensor is a (MEMS) sensor that transforms increase of pressure to decrease of the resonant frequency of a variable *LC* tuner as shown in Fig. 6-2 (c).

The overall structure is also restricted in terms of geometry and orientation. Geometric limitations on the sensor are the range and overall transmitting/receiving power of the inductor. If the coils are too small, the range to the external reader may not be large enough to carry the signal and power a long enough distance. At the same time, the capacitance needs to be reasonably matched to the inductance to create a balanced tank circuit.

6.2.2 Passive sensor circuit model

6.2.2.1 Single layer spiral planar coil circuit model

Fig. 6-3 shows a typical spiral planar coil structure, which consists of the substrate and copper trace. The trace forms a coil L, and a series resistor R_s, which exists because the copper is not an ideal conductor. The adjacent trace forms a series capacitor, C_s, which is not desirable. Current flowing inside the copper may leak to the ground (space), R_{sub}, due to the substrate which is not an ideal insulator. The copper layer also forms a parallel capacitor C_{sub} to the ground for which C_{sub}'s dielectric layer is the substrate. Thus, Fig. 6-4 shows an equivalent circuit model, in which $C_p = 2C_{sub}$ and $R_p = \frac{1}{2}R_{sub}$. The value of these components is determined by the sensor's pattern and material properties. D is the diameter of sensor, W is the trace width, s is the spacing width, and β is the spacing to trace ratio s/W. n is the turns of the coil, l is the total trace length, b is the outer diameter/length of the coil, and b_{in} is the inner diameter. α is the inner diameter to outer diameter ratio b_{in}/b. t_{co} is the copper thickness and t_{sub} is the substrate thickness shown in Fig. 6-4.

The geometry of Fig. 6-4 yields the following formulas (Jow et al 2007):

$$2(1+\beta)Wn = (1-\alpha)D \tag{3}$$

$$\mathrm{l} = 4nD - 4nW - (2n+1)^2(1+\beta)W \tag{4}$$

If trace width and spacing are small enough when compared to the sensor side length (diameter), (4) could be simplified as:

$$\mathrm{l} = 2n(1+\alpha)D \tag{5}$$

Subtracting (4) from (5) yields the error of (5), which is $-4nW - (4n+1)s$

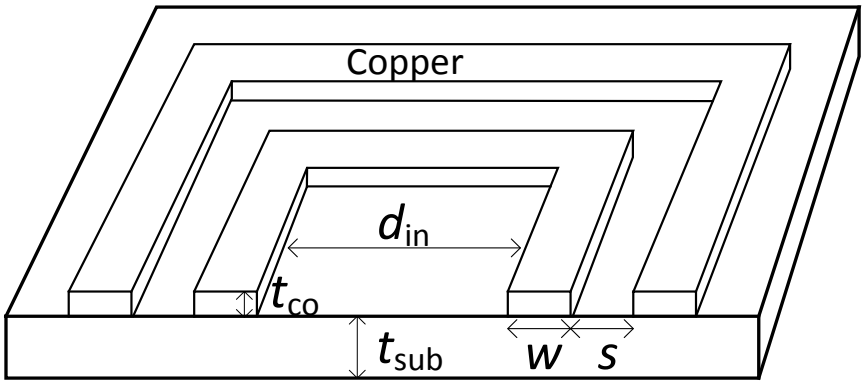

Fig. 6-3 Printed single layer of spiral planar coil and substrate

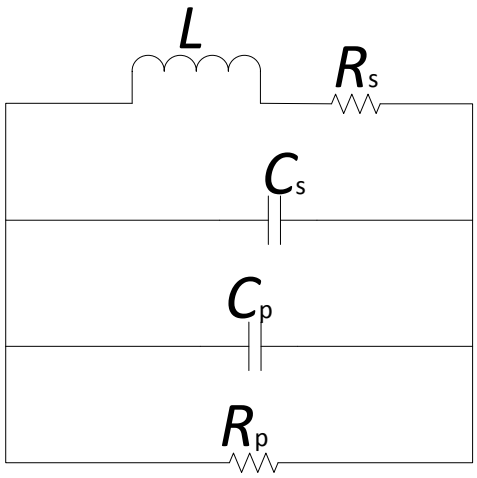

Fig.6-4 Equivalent circuit model for single layer spiral planar coil

6.2.2.2 Approximated value of components in the single layer spiral planar coil circuit model

Self-inductance *L*

The planar spiral coil's inductance has been well studied. Mohan et al (1999) suggested that, for the square shape spiral planar coil, the self-inductance is

$$L = \frac{2\mu}{\pi} n^2 d_{\text{avg}} \left(\ln\left(\frac{2.07}{\varphi}\right) + 0.18\varphi + 0.13\varphi^2 \right) \tag{6}$$

Where μ is the magnetic permeability of the metal (copper) traces, which is approximately equal to $\mu_0 = 4\pi \times 10^{-7}$ (H/m). d_{avg} is the average diameter of the square, which is $\frac{D+D_{in}}{2} = \frac{1+\alpha}{2} D$, and $\varphi = \frac{1-\alpha}{1+\alpha}$. The accuracy degrades when $\varphi < 0.1$ or $n < 2$ (Jow et al 2007).

(6) is rewritten for future discussion which includes the symbols from section 6.2.2.1:

$$L = \frac{\mu}{\pi} n^2 D(1+\alpha) \left(\ln\left(\frac{1+\alpha}{1-\alpha}\right) + 0.18\left(\frac{1-\alpha}{1+\alpha}\right) + 0.13\left(\frac{1-\alpha}{1+\alpha}\right)^2 + 0.726 \right) \tag{7}$$

Series resistance R_s

Considering the skin effect, the expression of series resistance along the copper trace is:

$$R_{\text{s}} = \frac{\rho_{\text{co}} l}{W\delta(1 - e^{-\frac{t}{\delta}})} \tag{8}$$

Where ρ_{co} is the resistivity of copper, which is $1.7 \times 10^{-8}\,\Omega/\text{m}$, δ is the skin depth of the copper, which depends on the material property and frequency:

$$\delta = \sqrt{\frac{\rho_{co}}{\pi \mu f}} \tag{9}$$

Parallel resistance R_p

R_p could be expressed as:

$$R_\mathrm{p} = \frac{\rho_\mathrm{sub} t_\mathrm{sub}}{Wl} \tag{10}$$

R_p depends on the substrate material. When the sensor is fabricated on a printed circuit board (PCB), the substrate material is FR4 and ρ_sub (10.8 MΩ/mm) is large enough so R_p can be neglected. However, for silicon substrate sensors, R_p is in the kΩ range which should be taken into consideration.

Series capacitance C_s

C_s is the capacitance of the adjunct coplanar strip. Neagu et al (1997) roughly modeled C_s as two long parallel wires with diameter W:

$$C_\mathrm{s} = \frac{\pi \epsilon_o \epsilon_r (l - 4D)}{n ln\left(1 + \beta + \sqrt{\beta^2 + 2\beta}\right)} \tag{11}$$

(11) is sufficient when series capacitance does not dominate the capacitance of the whole system. Gevorgian et al (2003) and Troedsson et al (2004) give a more accurate model, which consists of two parts of series capacitance, shown in Fig.6-5.

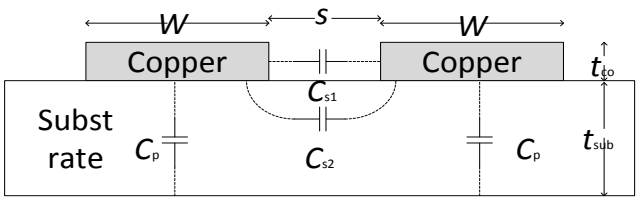

Fig. 6-5 Series capacitance consists of two parts: capacitance between two copper trace capacitance C_{s1}, and adjunct coplanar strip C_{s2}. Parallel capacitance from trace to substrate is also shown.

C_{s1} is the capacitance between the two sidewalls of the trace per unit length, which is similar to the parallel plate capacitor and could be expressed as:

$$C_{s1} = \epsilon_0 \frac{t_{co}}{s} \tag{12}$$

C_{s2} is the capacitance of adjunct coplanar strip:

$$C_{s2} = \epsilon_o \epsilon_{eff} \frac{K(k_0')}{K(k_0)} \tag{13}$$

Where ϵ_{eff}:

$$\epsilon_{eff} = 1 + (\epsilon_r - 1) \frac{K(k')K(k_0)}{2K(k)K(k_0')} \tag{14}$$

Where $\epsilon_r$is the permittivity of the substrate. $K(k)$ is the complete elliptic integral of the first kind:

$$K(k) = \frac{\pi}{2} \sum_{n=0}^{\infty} \left[\frac{(2n-1)!!}{(2n)!!} \right]^2 k^{2n} \tag{15}$$

And $k_0, k, k',\ k_0'$ in (14) are defined as:

$$k = \frac{\tan h\left(\frac{\pi s}{4t_{sub}}\right)}{\tan h\left(\frac{\pi(s+W)}{4t_{sub}}\right)} \tag{16}$$

$$k_0 = \frac{s}{s+2W} = \frac{\beta}{\beta+2} \tag{17}$$

$$k' = \sqrt{1-k^2} \tag{18}$$

$$k_0' = \sqrt{1-k_0^2} \tag{19}$$

(12) and (13) give the unit length capacitance, which is multiplied by the total length of the trace. Troedsson et al (2004) suggested that total capacitance should be divided by a series factor K_s due to the voltage drops along the trace, which are determined by the geometry and pattern of the plate.

For commonly used geometries and patterns $K_s \approx n^2$. So if n is sufficiently large, C_s can be neglected.

The final expression of C_s is:

$$C_s = \left(\epsilon_0 \frac{t_{co}}{s} + \epsilon_0 \epsilon_{\text{eff}} \frac{K(k_0')}{K(k_0)}\right) * \frac{l}{K_s} \tag{20}$$

Parallel capacitance

The substrate capacitance to the ground could be expressed as:

$$C_p = \epsilon_0 \epsilon_r \frac{Wl}{t_{sub}} \tag{21}$$

(21) demonstrates $C_p$is determined by the copper cover area and substrate thickness. Troedsson et al (2004) suggested that C_p should be divided by a parallel factor K_p due to the fringe capacitance. K_p is determined by β, and for a typical pattern, $K_p \approx 1.5$, and slightly decreases when β decreases:

$$C_p = \epsilon_0 \epsilon_r \frac{Wl}{t_{sub} K_p} \tag{22}$$

6.2.2.3 Double layer spiral planar coils circuit model

Previous sections focused on the single planar layer circuit model of the sensor. We introduce the circuit model of the whole sensor which includes two planar spiral planar coil circuit models. The top plate and bottom plate face each other in the sensor. The sensor lumped circuit model is based on the single plate model:

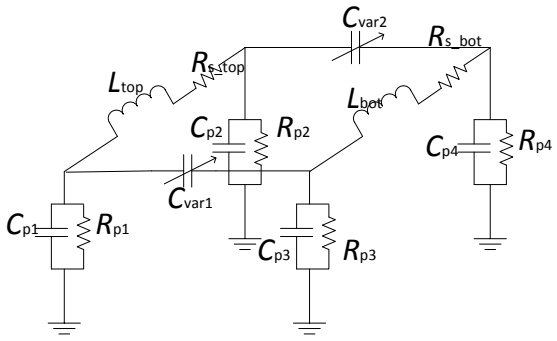

Fig. 6-6 Lumped circuit model for double layer spiral planar coils

C_{var} is the capacitance between two plates, which increases with pressure. If two plates have the same pattern, it is:

$$C_{\text{var}} = \epsilon_0 \frac{Wl}{\text{distance}} \tag{23}$$

L_{top} and L_{bot} have the same voltage in the electromagnetic field, which makes them parallel to each other. Fig. 6-6 is simplified as Fig. 6-7(a), and each component value is:

$$C_{\text{p}} = C_{\text{ptop}} + C_{\text{pbot}} \tag{24}$$

$$C_{\text{s}} = C_{\text{stop}} + C_{\text{sbot}} \tag{25}$$

$$R_{\text{s}} = {1}\Big/{\frac{1}{R_{\text{stop}}} + \frac{1}{R_{\text{sbot}}}} \tag{26}$$

$$L_2 = \frac{L_{\text{top}}L_{\text{bot}} - M_{\text{tb}}^2}{L_{\text{top}} + L_{\text{bot}} - 2M_{\text{tb}}} \tag{27}$$

M_{tb} is the mutual inductance between top and bottom plates. If these two plates have the same pattern, and they are close enough to each other, then we can assume $L_{top} \approx L_{bot} \approx M_{tb}$ which results in $L_2 \approx L_{top}$.

If we use $C_{tot} = C_p + C_s + C_{var}$, a simpler equivalent circuit model results modeled in Fig. 6-7(b).

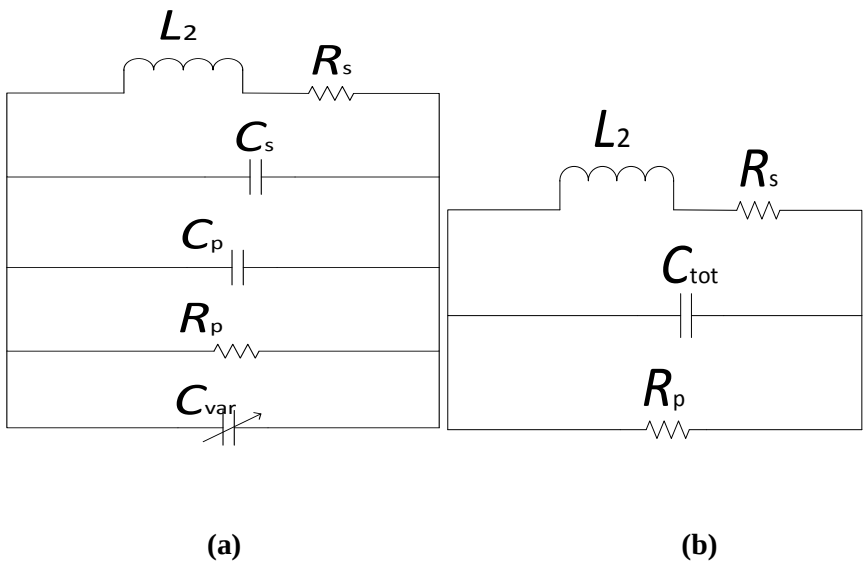

Fig. 6-7 (a) Equivalent circuit model for double layer spiral planar ICP sensor (b) simplified circuit of model Fig. 6-7(a) in which $C_{tot} = C_p + C_s + C_{var}$

6.2.3 Passive sensor parameters and layout

Building a prototype of the MEMS-based sensor is a major challenge of this project. To realize the tiny size and to ensure accuracy, the sensor is manufactured and fabricated inside the Wisconsin Center for Applied Microelectronics (WCAM) cleanroom using a suite of semiconductor and microfabrication processing tools.

Minimal drift would ensure long term implantation. Our application necessitated minimal drift properties over time that only crystalline structures offer. The most commonly used, cheapest single crystal material with very well-defined processing techniques is silicon. We chose silicon as our membrane because it is possible to pattern metal structures on it and it works as a thin pressure diaphragm.

Similar to an active capacitive MEMS-based sensor, the materials chosen for fabricating this sensor are silicon and glass. Copper is chosen here instead of gold because of the thickness (10

μm range) restriction. Both copper and gold have low resistivity and high conductivity and copper has a much lower price.

The sensors are 5 × 5 × 0.63 mm. The assembly consists of a thick glass base that is hard and protected by a plastic housing, a thin silicon membrane that deforms with changes in ICP, and a chamber. The silicon membrane is 4 × 4 mm with 0.5 mm on the boundary for anodic bonding. Fig. 6-8(a) and Fig. 6-8(b) show that the silicon and glass have spiral copper coils. In addition, an insulation layer is added between the silicon substrate and copper coil layer to avoid power attenuation and current leakage.

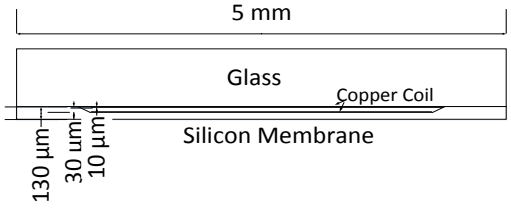

Fig. 6-8 (a) Passive wireless capacitive sensor front view

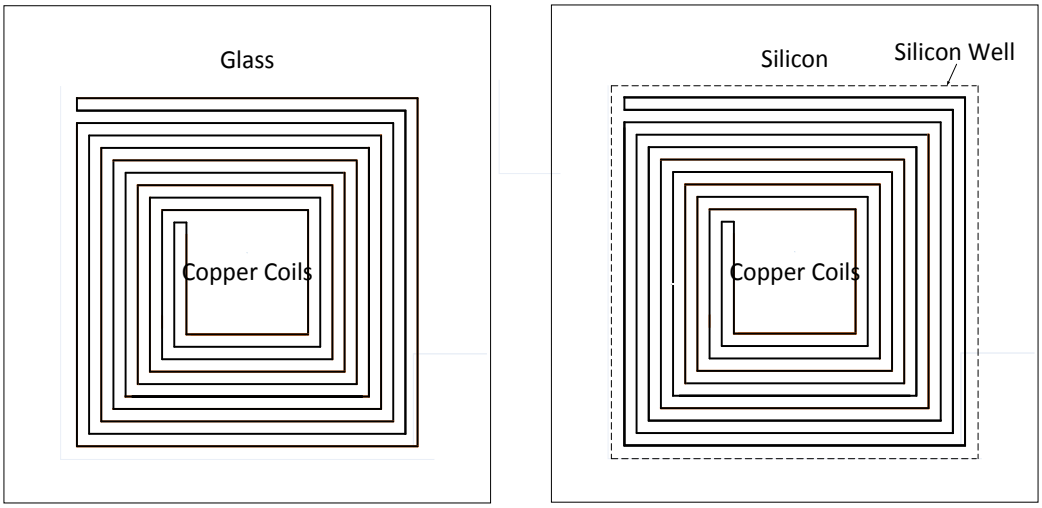

Fig. 6-8 (b) Passive wireless capacitive sensor top view

6.2.4 PCB fabrication of Passive Sensor

We designed an optimized sensor pattern parameter model to increase the signal strength between the sensor and the reader to achieve a better passive sensor system. Previous publications listed parameter numbers directly without detailed discussion (Coosemans et al 2004, Marioli et al 2005,

Kaiser 2006, Nopper et al 2010). Based on the discussion in section III, we fabricated a PCB sensor, which is: D = 5 mm, n = 2, W = s = 0.254 mm (which leads to α = 0.7859, β = 1), t_{cu} = 35 µm, plated separation distance = 75 µm. Our model considers all the parameters that impact the signal strength, such as: parasitic capacitance, skin effect on the parasitic resistance, and substrate resistance. We designed 19 different types of square sensors on a 5 mm diameter with different turns, spacing widths and trace widths on a PCB to verify our sensor optimization model as shown in Fig. 6-9(a). Double sided tape was used to bond the two plates together. Trace thicknesses were 0.889 mm and plate distance was around 70 µm. A Vector Networking Analyzer (VNA) measured the sensor's phase shift signal strength. The distance between the VNA probe and the sensors was constant (1 cm). Considering both transmitting power for the reader and implanted geometry, the current dimensions for both passive sensor and second approach active sensor were 4 × 4 mm. VNA signal strength measurement results for 19 styles were compared to our model results. Calculation results were transferred to a dB scale and normalized to 1 to compare to the VNA measured results. Fig. 6-9(b) demonstrates that the model successfully predicted which coil sensor had the maximum signal strength and which one had the minimum signal strength among the 19 sensors, with average error of 7.68%. The sensor pattern parameter's measurement results shown in Fig. 6-9(c) determined the resonant frequency for the reader to detect and the resulting narrow frequency range.

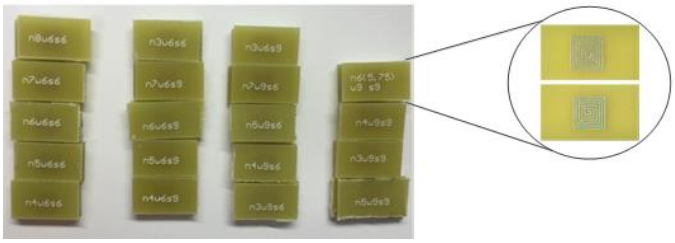

(a) PCB sensors fabricated

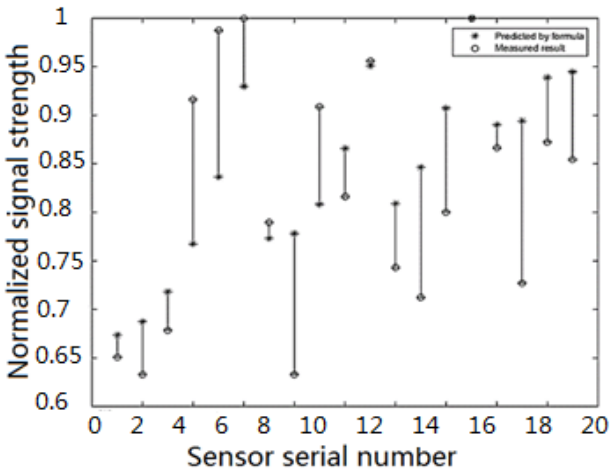

(b) Measured signal strength compared to the predicted signal strength

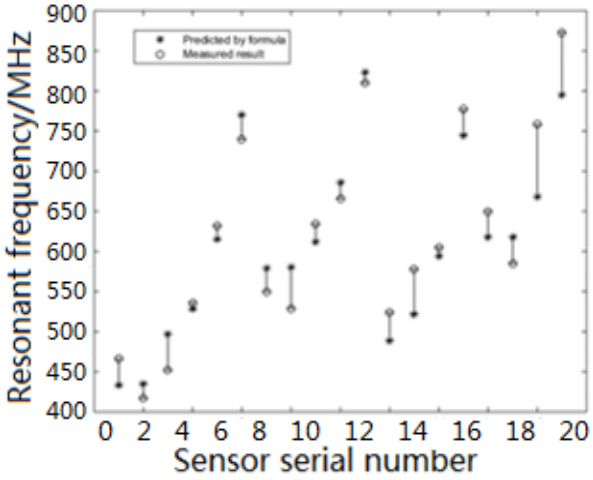

(c) Measured resonant frequency compared to the predicted resonant frequency

Fig. 6-9 (a) PCB sensors fabricated for 19 different types with different turns, spacing width and trace width (b) measured signal strength compared to predicted signal strength for 19 styles on 5 mm sensors, (c) measured resonant frequency compared to predicted resonant frequency for 19 styles on 5 mm sensors.

6.2.5 WCAM fabrication of Passive Sensor

After PCB design and fabrication to verify the first approach passive sensor design, the real prototype was developed and fabricated in the Wisconsin Center for Applied Microelectronics (WCAM) cleanroom.

Fig. 6-10 shows a flowchart of the process. A 10 cm diameter 600 µm thick silicon wafer is cleaned in Prefurnace Clean, which is a flow hood and chemical bench for preparing substrates before thermal processing in the Nitride furnace. Then a thin layer of Silicon nitride is deposited as a protection layer for multiple 30 µm deep silicon wells etched in the KOH bench. A 10 cm diameter 500 µm thick glass wafer is cleaned in the Piranha Bench to make sure the surface is clean by removing organic material. Combining the lithography process and plasma etching yields the structures (patterning) needed for the sensor. The Wafer spinner and vacuum hotplate are used for coating and baking substrate photoresists. The Mask aligner and exposure tool are used for photoresist exposure. The photoresist exposed to light becomes soluble/insoluble in the photoresist developer depending on the photoresist properties. The Plasma tool can selectively remove

material by reactive ion etching (RIE) with a designed mask. RIE uses a RF plasma system to selectively remove (etch) various thin films. CVC-sputtering deposition provides a 10 µm deposition of copper as well as a thin 20 nm Cr adhesion layer onto both silicon and glass substrates in vacuum. Copper Etchant APS-100 is used to etch Cu, then form desired Cu coils structures (patterning) and Cr etchant recipe on PlasmaTherm 770 ICP used to etch Cr with a designed photoresist mask. A wafer aligner and bonding tool is used to yield anodic bonding between the silicon and glass wafers. A sufficiently powerful electrostatic field yields atomic contact between the clean bonding substrates. A dicing saw with programmable high-speed blade cuts bonded substrates into 5 × 5 × 1.3 mm dies with a 4 × 4 mm deformation diaphragm and 0.5 mm boundary for anodic bonding. A grinding tool polishes the thick silicon layer to a 100 µm thin silicon membrane.

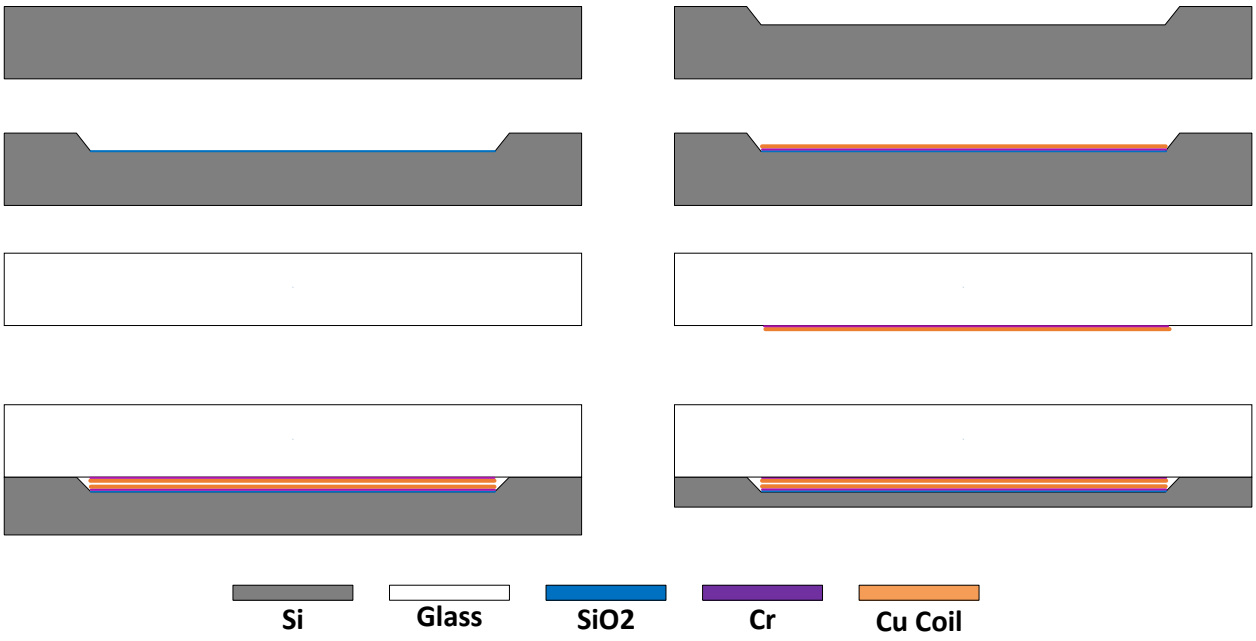

Fig. 6-10 Fabrication process of passive wireless capacitive sensor

6.2.6 Sensor measurement: Reader's antenna and sensor coupling system

The passive *LC* pressure sensor for intraocular pressure (IOP) monitoring has matured since Collins et al (1967) presented the idea. However, when applying this similar approach to the field of ICP measurement, the distance between the implanted sensor and the external reader is much longer as required by physiological factors, when compared to IOP measurement. In ICP monitoring practice, achieving enough measurement distance (larger than skull thickness) was a challenge, because of the poor coupling factor at that long distance. Nopper et al. (2010) proposed an ICP sensor that could achieve a measurement distance of 8.5 mm. Coosemans et al (2004) proposed a similar approach for IOP measurement with a maximum distance of 7.5 mm, however, male adult scalp thickness ranges from 2 to 3.5 mm (Hori et al 1972), and skull thickness average ranges from 6.08 mm to 8.09 mm, at different locations (Law 1993). The optimized design proposed, could achieve measurement distance at 21 mm, which could meet medical practice requirement.

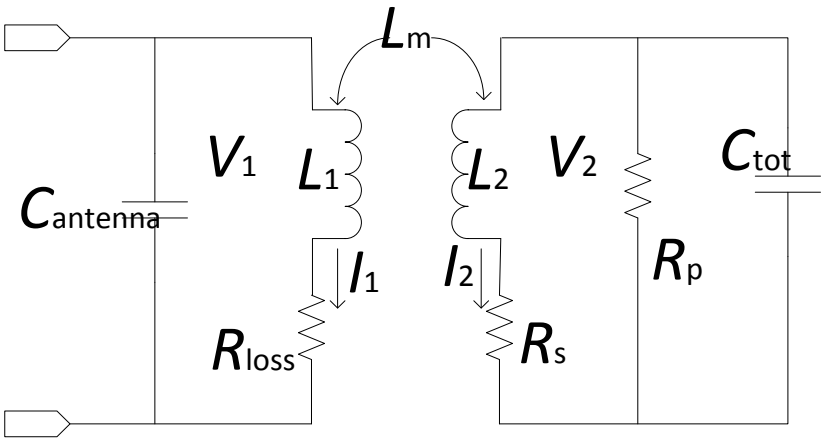

Fig.6-11 Reader and sensor coupling system equivalent circuit model

Assuming the antenna's parasitic capacitance is C_{ant} and series resistance is R_{loss}, Fig. 6-11 shows the reader's antenna employed to measure the wireless sensor. It shows reader's antenna and sensor coupling system's equivalent circuit model.

L_m is the mutual inductance between the telemeter's antenna and spiral planar mircocoil on the sensor. L_m is expressed as shown in the following equations (Raju et al 2014):

$$L_m = \left(\frac{4}{\pi}\right)^2 \sum_{i=1}^{i=n_a} \sum_{j=1}^{j=n_b} M_{ij} \tag{28}$$

$$M_{ij} = \frac{\mu_0 \pi a_i^2 b_j^2}{2\left(a_i^2 + b_j^2 + z^2\right)^{\frac{3}{2}}} \left(1 + \frac{15}{32}\gamma_{ij}^2 + \frac{315}{1024}\gamma_{ij}^4\right) \tag{29}$$

$$\gamma_{ij} = \frac{2a_i b_j}{a_i^2 + b_j^2 + z^2} \tag{30}$$

Where a_i is the i^{th} turn's antenna radius, and b_j is the j^{th} turn radius of spiral planar coil ICP sensor. z is the distance between antenna and ICP sensor. If spacing and trace width of the ICP sensor is relatively small compared to the whole sensor diameter, b_j could be expressed as:

$$b_j = \frac{D}{2} - (n_j - 1)(1 + \beta)W \tag{31}$$

Based on Kirchhoff's law the following equations (32) (33) (34) are derived from Fig. 6-11:

$$V_1 = j\omega L_1 I_1 + j\omega L_m I_2 \tag{32}$$

$$V_2 = j\omega L_2 I_2 + j\omega L_m I_1 \tag{33}$$

$$V_2 = -R_s I_2 - \frac{R_P}{j\omega C_{tot} R_p + 1} * I_2 \tag{34}$$

The impedance seen from V_1 could be derived from (32) (33) (34)

$$Z_1 = \frac{V_1}{I_1} = j\omega L_1 - \frac{\omega^2 L_m{}^2}{j\omega L_2 + R_s + \frac{R_P}{j\omega C_{tot} R_p + 1}} \tag{35}$$

At the resonant angular frequency ω_0 which is shown in (36), the reader could detect the maximum phase drop amplitude (PD), which is given in (37). The amplitude of phase drop is a signal that can be measured by the reader.

$$\omega_0 = \sqrt{\frac{1}{L_2 C_{tot}} - \frac{1}{R_p^2 C_{tot}^2}} \tag{36}$$

$$\text{Amplitude} = \frac{\omega L_m{}^2}{R_s L_1 + \frac{R_p L_1}{1 + R_p^2 \omega^2 C_{tot}^2}} \tag{37}$$

6.2.7 Sensor Parameter Optimization

6.2.7.1 Sensor size

After summing terms of (28), we eliminated the influence of γ^2 and γ^4, and assuming b_j is much smaller than $a_i + z$, which simplifies $\frac{\mu_0 \pi a_i^2 b_j^2}{2\left(a_i^2 + b_j^2 + z^2\right)^{\frac{3}{2}}}\left(1 + \frac{15}{32}\gamma_{ij}^2 + \frac{315}{1024}\gamma_{ij}^4\right)$ to $\frac{\mu_0 \pi a_i^2 b_j^2}{2\left(a_i^2 + z^2\right)^{\frac{3}{2}}}$:

$$L_m = \left(\frac{4}{\pi}\right)^2 \sum_{i=1}^{i=n_a} \frac{\mu_0 \pi a_i^2}{2(a_i^2 + z^2)^{\frac{3}{2}}} \left(\left(\frac{(2n-1)(n-1)}{6}(1+\beta)^2 W^2 + \frac{\alpha D (n-1)(1+\beta) W}{2} + \frac{1}{4}\alpha^2 D^2\right) n\right) \tag{38}$$

(38) is derived based on the sum of an arithmetic progression's square, since $\sum_{j=1}^{j=n_b} b_{\mathrm{j}}$ is an arithmetic series where the first item is αb and the common difference is $(1+\beta)W$, and $b = \frac{1}{2}D$, respectively.

Treat the size of antenna a and distance z as constants, then (38) is:

$$L_{\mathrm{m}} = K_{\mathrm{Lm}} \left(\left(\frac{(2n-1)(n-1)}{6}(1+\beta)^2 W^2 + \frac{\alpha D(n-1)(1+\beta)W}{2} + \frac{1}{4}\alpha^2 D^2 \right) n \right) \tag{39}$$

Where

$$K_{\mathrm{Lm}} = \left(\frac{4}{\pi}\right)^2 \sum_{i=1}^{i=n_{\mathrm{a}}} \frac{\mu_0 \pi a_{\mathrm{i}}^2}{2(a_{\mathrm{i}}^2 + z^2)^{\frac{3}{2}}} \tag{40}$$

Substitute (3), (4), (5), (8), (10), (20), (22) into (37) which yields:

$$\text{Amplitude} = \frac{\omega_0 {K_{\mathrm{Lm}}}^2 \left(\left(\frac{(2n-1)(n-1)}{24n^2}(1-\alpha)^2 D^2 + \frac{\alpha(1-\alpha)D^2(n-1)}{4n} + \frac{1}{4}\alpha^2 D^2 \right) n \right)^2}{L_1 \left(\frac{\rho_{co} n^2 (1+\alpha)(1+\beta)}{(1-\alpha)\delta(1-e^{-\frac{t}{\delta}})} + \frac{\frac{\rho_{\mathrm{sub}} t_{\mathrm{sub}}(1+\beta)}{(1+\alpha)(1-\alpha)D^2}}{1 + \left(\frac{\rho_{\mathrm{sub}} t_{\mathrm{sub}}(1+\beta)}{(1+\alpha)(1-\alpha)D^2} \right)^2 \omega_0^2 C_{\mathrm{tot}}^2} \right)} \tag{41}$$

Where

$$C_{\mathrm{tot}} = \epsilon_0 \epsilon_{\mathrm{r}} \frac{2(1+\alpha)(1-\alpha)D}{t_{\mathrm{sub}}(1+\beta)} + \frac{\pi \epsilon_{\mathrm{o}} \epsilon_{\mathrm{r}} (2n(1+\alpha)D - 4D)}{n ln\left(1+\beta+\sqrt{\beta^2+2\beta}\right)} + \epsilon_0 \frac{2(1+\alpha)(1-\alpha)D}{\mathrm{distance}(1+\beta)} \tag{42}$$

(41) has been simplified based on the assumption that the top plate and bottom plate's patterns are the same. From (41), we conclude signal strength amplitude increases with D^4, since the effect of D is negligible in the denominator of (41). Therefore we could fabricate the sensor as large as possible. Our measurement result also supports this idea, the signal strength of 5 mm diameter

sensors is 0.1491 dB average and 0.0408 dB standard deviation (SD), compared to 0.0566 dB average and 0.0141 deviation for 4 mm diameter sensor, and 0.0135 dB average and 0.0032 deviation for 3 mm diameter sensor. However, the implanted sensor's diameter is limited by the largest holes that could be drilled through the skull.

6.2.7.2 Sensor coil turns n

In (41) and (42), R_p and C_{tot} are determined by the copper covered area, and are not sensitive to the number of turns. R_s increases with n^2, and L_m increases with n. $\frac{\omega_0^2 {L_m}^2}{R_s+\frac{R_p}{1+R_p^2\omega_0^2C_{tot}^2}}$ plateaus when n is sufficiently large and the influence of R_p can be ignored. So the lower bound for n is given by

$$\frac{\rho_{co}(1+\alpha)(1+\beta)}{2(1-\alpha)\delta(1-e^{-\frac{t}{\delta}})}n^2 \gg \frac{R_p}{1+R_p^2\omega_0^2C_{tot}^2} \tag{43}$$

Or

$$n > \sqrt{10\frac{R_p 2(1-\alpha)\delta(1-e^{-\frac{t}{\delta}})}{(1+R_p^2\omega_0^2C_{tot}^2)\rho_{co}(1+\alpha)(1+\beta)}} \tag{44}$$

If R_p is large enough, n could be chosen to be 1 or 2 without damaging the signal strength.

If n is too large, the inductance of the sensor coil, which is specified by (6) increases dramatically, thus self-resonant frequency f_{SR}, which is specified by (45) may decrease too quickly. f_{SR} should always be greater than f_0, which may prevent us from obtaining a desirable f_0, thus we found the upper bound for n as shown in (46):

$$f_{SR} = \frac{1}{2\pi}\sqrt{\frac{1}{L_2(C_p+C_s)} - \frac{1}{R_p^2(C_p+C_s)^2}} \tag{45}$$

$$n < \sqrt{\frac{R_p^2(C_p + C_s)}{\frac{\mu}{\pi} D(1+\alpha)\left(\ln\left(\frac{1+\alpha}{1-\alpha}\right) + 0.18\left(\frac{1-\alpha}{1+\alpha}\right) + 0.13\left(\frac{1-\alpha}{1+\alpha}\right)^2 + 0.726\right)\left(4\pi^2 f_0^2 R_p^2\left(C_s + C_p\right)^2 + 1\right)}} \quad (46)$$

6.2.7.3 Inner diameter to outer diameter ratio α

α approaches 0 when copper trace covers all the plate's surface, and approaches 1 when there is only one turn. The first conjecture would suggest that α should be as small as possible, to make full use of limited plate surface area. But the numerical calculation result in Fig. 6-12 by (44) shows us that when the turns number is small, optimized α is around 0.8, which results in a large uncovered area on the plate. When n increases, the optimized α converges to 0.38, which leaves some area uncovered. When the inner turns radiuses are too small, the turn's contribution to the mutual inductance is relatively small compared to the contribution to the series resistance, thus reducing the signal strength amplitude. The measurement results of PCB sensors have also been taken to verify the correctness of (42), as shown in Fig. 6-13, which could match the simulated curve. Because in the progress of α optimization, we assumed that the other parameters (f_0, D, n, β) were kept same. But it was hard to control the same f_0 for every PCB sensor, thus the y-axis in Fig. 6-13 is amplitude/resonant frequency.

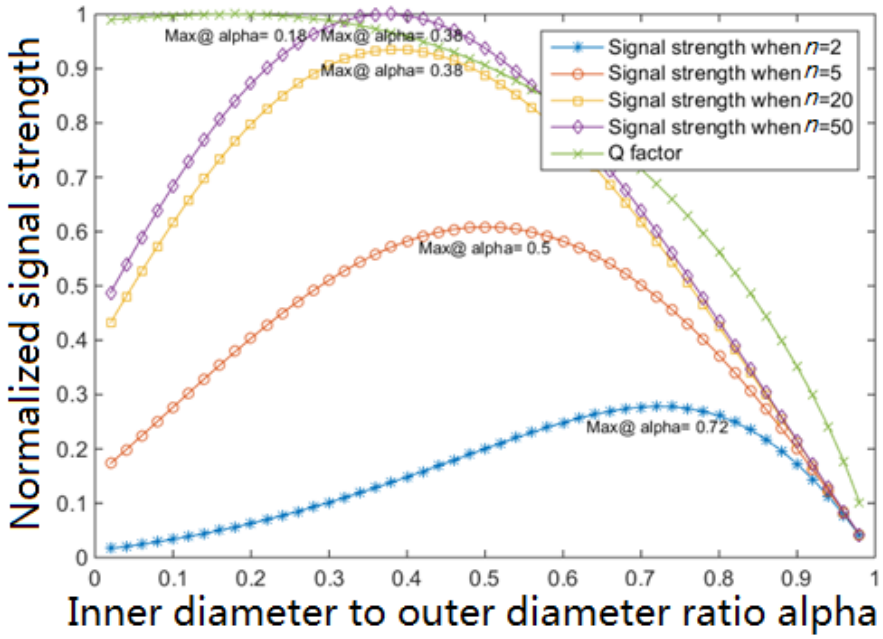

Fig. 6-12 Normalized signal strength vs. turns increase for a typical ICP sensor, for D = 5 mm, β = 0.8.

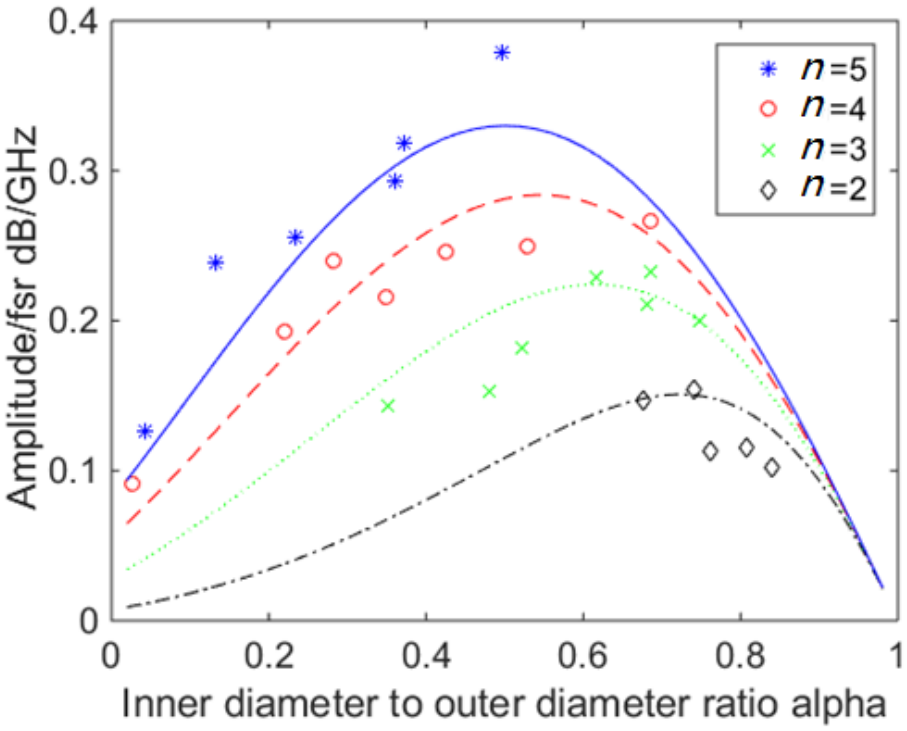

Fig. 6-13 Measurement result matches the numerical calculation result of (42)

6.2.7.4 Spacing width to trace width ratio β

If D, n, α have been determined, the summation of trace width and spacing width, which is $s + W = (1 + \beta)W$. Given this fixed summation width, the β ratio could determine the trace width and spacing width respectively. Mutual inductance is not influenced by the β change. On the other hand decreasing β could increase the trace width, thus decreasing the series resistance R_s, which may improve the signal performance. However, the only way this approach works is when C_s is relatively small when compared to C_{tot}. Equations (11) – (19) show that C_s increases if β decreases. If C_s dominates C_{tot}, and the influence of R_p is ignored, ω_0 is roughly estimated as：

$$\omega_0 = \sqrt{\frac{1}{L_2 C_s}} \tag{47}$$

And (41) is approximately

$$\text{Amplitude} = \frac{{L_m}^2}{\frac{L_2 \rho_{co} n^2 (1+\alpha)(1+\beta)}{2(1-\alpha)\delta\left(1-e^{-\frac{t}{\delta}}\right)} \frac{\pi \epsilon_o \epsilon_r (l-4D)}{n ln\left(1+\beta+\sqrt{\beta^2+2\beta}\right)}} \tag{48}$$

$$= K_\beta \frac{ln\left(1+\beta+\sqrt{\beta^2+2\beta}\right)}{(1+\beta)}$$

K_β represents the parameters which are not related to β. By solving $\frac{\partial R_{sensor}}{\partial \beta} = 0$, $\beta = 0.8$. Using numerical analysis, we find that $\text{Amplitude}(0.4 < \beta < 1.8) > 0.9\text{Amplitude}(\beta = 0.8)$

Therefore, β in the range of [0.4, 1.8] is acceptable.

6.2.7.5 Substrate thickness

Substrate thickness could influence the R_p and C_p, but for the typical ICP sensor, the influence of these is relatively small. A more important factor to determine substrate thickness is the bend factor (Timoshenko et al 1959)**:**

$$y = \frac{\eta \cdot p \cdot D^4 12 \cdot (1 - v^2)}{E \cdot {t_{\text{sub}}}^3} \tag{49}$$

Where, *E* is the substrate material elastic modulus, *v* is the Poisson ratio, *b* is a factor determined by the shape of the sensor plate, and *p* is the pressure applied on the sensor. The bend factor determines the maximum pressure the sensor can withstand and the resolution of pressure measurement.

6.2.7.6 Other sensor shapes

Previous discussions focused on the square shaped coil. For the circular shaped coil, (5) becomes

$$l = \frac{\pi}{2} n(1 + \alpha)D \tag{50}$$

(6) becomes (Stojanović et al 2005)

$$L = \frac{2\mu}{\pi} n^2 d_{\text{avg}} \left(\ln\left(\frac{2.46}{\varphi}\right) + 0.2\varphi^2 \right) \tag{51}$$

The $\left(\frac{4}{\pi}\right)^2$ factor in (28) is eliminated.

For the rectangular coil, use (52), (53) where *D*1 and *D*2 are the side lengths of the rectangular coil, and *g* is the diagonal length.

$$l = n(1 + \alpha)(D1 + D2) \tag{52}$$

$$L = \frac{\mu}{\pi} * n\text{^}2\left(-2(D1 + D2) + 2g - D1\ln\left(\frac{D1 + g}{D2}\right)\right. \\ \left. - D2\ln\left(\frac{D2 + g}{D1}\right) + D1\ln\left(\frac{2D1}{W}\right) + D2\ln\left(\frac{2D2}{W}\right)\right) \quad (53)$$

6.2.8 Challenge

The first prototype of passive sensor WCAM fabrication could not be measured by both spectrum analyzer and Vector Network Analyzer (VNA) machines. After experiment and theoretical analysis, the main problems are from (1) Low quality factor, which is due to the high series resistance, (2) Current leakage due to the low substrate resistance. The solutions to solve these two problems are (1) increase Cu trace thickness and (2) add an insulation layer between Si substrate and metal trace.

6.2.8.1 Copper trace thickness

Copper trace thickness for both silicon and glass substrates of the first prototype was 2 μm through E-beam evaporation Cu deposition with real-time film thickness monitoring in vacuum. A lift-off process created copper structures (patterning) on the silicon and glass substrate using a sacrificial photoresist.

δ is the skin depth of the copper as shown in equation (3), which depends on the material property and frequency. ρ_{co} is the resistivity of copper, which is $1.7 \times 10^{-8}\ \Omega \cdot \mathrm{m}$.

$$\delta = \sqrt{\frac{\rho_{co}}{\pi\mu f}} \quad (54)$$

The effective copper trace thickness is $\delta(1 - e^{-\frac{t}{\delta}})$, which is dependent on the skin depth. When $t = \delta$, the effective thickness is 0.632 δ. When $t = 3\delta$, the effective thickness increases to 0.95 δ.

So $t = 3\delta$ is a desirable choice of copper thickness. Excessive thickness may increase the complexity of the progress to fabricate sensors in the clean room.

For example, for a 500 MHz resonant frequency, $\delta = 3.29$ μm and $t = 3\delta = 9.87$ μm. 2 μm is not enough to achieve high effective thickness. Cu electroplating equipment outside the cleanroom was tried first to increase Cu trace thickness. The quality of electroplating is affected by many factors, such as stress of materials, uniformity of plating layer, temperature, current control and timing, which need to be carefully adjusted. Then CVC-sputtering deposition inside the cleanroom was used to increase Cu trace thickness up to 20 μm with better uniformity surface and higher quality of deposited Cu layer.

Equation (55) shows the expression of series resistance along the copper trace:

$$R_s = \frac{\rho_{co} l}{W\delta(1 - e^{-\frac{t}{\delta}})} \tag{55}$$

Cu resistance is inverse to the Cu trace thickness. Quality factor Q is inverse to the Cu resistance. Larger Cu trace thickness leads to higher Q, improving detection of the resonator's bandwidth relative to its center frequency.

6.2.8.2 Insulator layer between trace and substrate

The parallel resistance R_p depends on the substrate material. When the sensor is fabricated on the printed circuit board (PCB), the substrate material is FR4, which is a good insulator and whose ρ_{sub} (10.8 MΩ/mm) is large enough so R_p can be neglected in the whole resistance of the equivalent model. But for the silicon substrate, resistivity is relatively small, so R_p is normally in the kΩ range, which cannot be neglected. Adding an insulator layer between the copper and silicon can improve the sensor performance. The Silicon dioxide (SiO_2) layer's capacitance is:

$$C_{\mathrm{p}} = \epsilon_0 \epsilon_{\mathrm{ox}} \frac{Wl}{t_{\mathrm{ox}}} \tag{56}$$

An equivalent circuit model, shown in Fig. 6-14(a), is transferred to Fig. 6-14(b), which is similar to Fig. 6-4. But R_{p} and C_{p} are modified as:

$$C_{\mathrm{p}} = C_{\mathrm{ox}} \left(\frac{1+\omega^2 (C_{\mathrm{si}}+C_{\mathrm{ox}}) C_{\mathrm{si}} R_{\mathrm{si}}^2}{1+\omega^2 (C_{\mathrm{si}}+C_{\mathrm{ox}})^2 R_{\mathrm{si}}^2} \right) \tag{57}$$

$$R_p = \frac{1}{\omega^2 C_{\mathrm{ox}}^2 R_{\mathrm{si}}} + \left(R_{\mathrm{si}} \left(\frac{(C_{\mathrm{si}} + C_{\mathrm{ox}})^2}{C_{\mathrm{ox}}^2} \right) \right) \tag{58}$$

From the equations, the insulator layer increases C_p slightly, but increases R_p dramatically. Normally 500 μm thickness of insulator SiO_2 ($\rho = 123 \sim 127\ \Omega \cdot \mathrm{m}$) could increase the R_p large enough to be negligible Therefore, it is recommended to add an insulator layer on the silicon substrate.

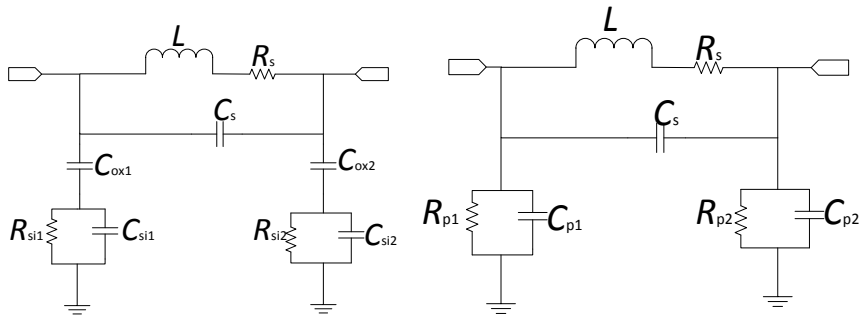

(a) (b)

Fig. 6-14 lumped (a) and equivalent (b) circuit model after adding SiO_2 insulator layer

6.3 Conclusion

Both PCB and MEMS optimized capacitive sensors were fabricated and tested through the VNA.

5 mm diameter MEMS sensor could not be measured by VNA because of the two challenges discussed in section 6.2.8. High series resistance influenced by the Cu trace thickness leads to low quality factor and current leakage due to the low substrate resistance. Although the increased Cu trace thickness leads to higher *Q*, detection of the resonator's bandwidth relative to its center frequency is still difficult because of the weak signal easily influenced by the environmental interference. Although the insulation SiO_2 layer was added between Si layer and Cr & Cu combination metal layer, the whole passive sensor signal strength is still very lossy in the electromagnetic field. Another method that could be tried to increase the signal strength is increasing the passive sensor diameter. As discussed in 6.2.7.1, the signal strength amplitude increases with D^4. The larger the sensor diameter, the stronger the signal. However, the implanted sensor's diameter is limited by the largest holes that could be drilled through the human skull. Currently our design with 5 mm diameter already approaches the physician's normal surgery limit. If we could make the hole bigger, the MEMS passive capacitive sensor might be a possible solution to wirelessly measure the ICP.

CHAPTER 7: SENSOR PERFORMANCE ANALYSIS

Portions of this chapter are taken from Wang F, Zhang X, Shokoueinejad M, Iskandar B J, Medow J E, Webster J G 2017 A Novel Intracranial Pressure Readout Circuit for Passive Wireless *LC* Sensor *IEEE Trans Biomed Circuits Syst.* 11(5):1123-32

7.1 Active sensor

7.1.1 Active sensor simulation

Based on the dimensions of the sensor, the thickness of the diaphragm can be determined to maximize sensitivity. The etch mask has the 3.2 mm × 2.2 mm wells for the metal plates to fit in. Each well has 2 channels on the separate sides with size of 1.2 mm × 2 mm. The wells are spaced 0.5 mm apart on all sides

The substrate is 3 × 6 mm with 0.5 mm on each side for bonding and silicon diaphragm area. The silicon layer has 3.2 mm × 2.2 mm etched wells for the metal plates to fit in. Each well has 2 channels on separate sides with size of 1.2 mm × 2 mm. The active capacitive sensor is modeled in SolidWorks with 500 μm thickness of glass, 20 μm thickness of silicon membrane, 10 μm depth well for gold plate deposition, 1 μm gold and copper (connection pads) materials to better understand the shape of the deflection across the entire diaphragm. The boundary of the model is fixed and the pressure is set at 10 mmHg to simulate the ICP of the human brain. The yield strength and tensile strength of silicon are satisfactory, and both values are 7.0 TPa. The yield strength and tensile strength of gold are satisfactory, and values are 205 MPa and 103 MPa respectively. The compressive strength of glass is satisfactory, and value is 100 MPa.

Fig. 7- 1(a) shows the results of the deflection simulation when the pressure was 10 mmHg with a 20 μm thickness membrane. The maximum deflection is greatest with value 0.64 μm in the middle of the membrane and average deformation is 0.23 μm for the membrane. The max stress with value of 3.249 MPa and average stress with value around 9.78×10^{-5} Pa, which is smaller

than the stress strength value stated before. Fig. 7-1(b) shows the stress simulation results when pressure is 10 mmHg. Table 7-1 shows the silicon, glass, gold and copper properties used in SolidWorks software.

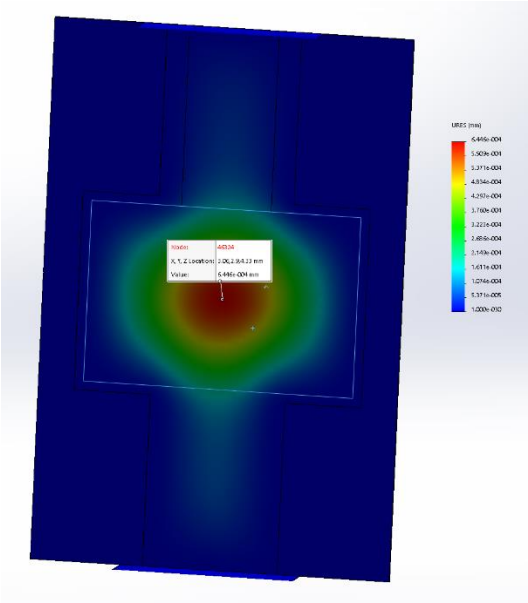

Fig. 7-1(a) Deflection simulation result when pressure is 10 mmHg

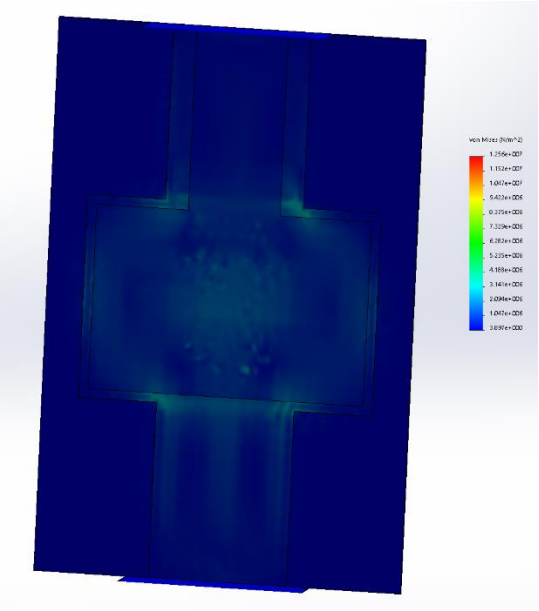

Fig. 7-1(b) Stress simulation result when pressure is 10 mmHg

Table 7-1(a). Silicon material properties in SolidWorks software

Property	Value	Units
Elastic Modulus	11.24	MPa
Poissons Ratio	0.28	N/A
Shear Modulus	490	MPa
Density	2330	kg/m^3
Tensile Strength in X	7	TPa
Compressive Strength in X		Pa
Yield Strength	7	TPa
Thermal Expansion Coefficient		/K
Thermal Conductivity	124	W/(m·K)
Specific Heat		J/(kg·K)
Material Damping Ratio		N/A

Table 7-1(b). Gold material properties in SolidWorks software

Property	Value	Units
Elastic Modulus	780	MPa

Poissons Ratio	0.42	N/A
Shear Modulus	260e+010	MPa
Density	19000	kg/m^3
Tensile Strength in X	103	MPa
Compressive Strength in X		Pa
Yield Strength	205	MPa
Thermal Expansion Coefficient	1.4e-005	/K
Thermal Conductivity	300	W/(m·K)
Specific Heat		J/(kg·K)
Material Damping Ratio		N/A

Table 7-1(c). Glass material properties in SolidWorks software

Property	Value	Units
Elastic Modulus	689.35	MPa
Poissons Ratio	0.23	N/A
Shear Modulus	280.22	MPa
Density	2457.6	kg/m^3
Tensile Strength in X	40	Pa
Compressive Strength in X	100	MPa
Yield Strength		Pa
Thermal Expansion Coefficient	9e-006	/K
Thermal Conductivity	0.74976	W/(m·K)
Specific Heat		J/(kg·K)
Material Damping Ratio		N/A

Table 7-1(d). Copper material properties in SolidWorks software

Property	Value	Units
Elastic Modulus	11	MPa
Poissons Ratio	0.37	N/A
Shear Modulus	400	MPa
Density	8900	kg/m^3
Tensile Strength	394.38	MPa
Compressive Strength in X		Pa
Yield Strength	258.646	MPa
Thermal Expansion Coefficient	2.4e-005	/K
Thermal Conductivity	390	W/(m·K)
Specific Heat	390	J/(kg·K)
Material Damping Ratio		N/A

7.1.2 Resolution/sensitivity calculation

The calculated capacitance value of the parallel gold plate capacitor is 5.3153 pF with 6 mm^2 gold plates area and 8 μm distance between two metal plates. From the previous simulation result, when

10 mmHg pressure is applied, the corresponding average capacitance value is changed by 0.0026 pF with sensitivity of 0.00026 pF/mmHg for 100 μm thickness of silicon membrane and 0.0166 pF with sensitivity of 0.00166 pF/mmHg for 50 μm thickness of silicon membrane; the corresponding maximum capacitance value is changed by 0.0066 pF for 100 μm thickness of silicon membrane and 0.0436 pF for 50 μm thickness of silicon membrane. For small values of changed pressure such as 1 mmHg, a thinner membrane yields larger membrane deformation and larger capacitance changed value of the capacitor. However, considering both my handing ability based on WCAM fabrication technique reality and silicon membrane sensitivity, I chose 50 μm thickness of silicon membrane for the active sensor.

7.1.3 Active sensor measurement set up

7.1.3.1 Capacitance value measurement

Fig. 7-2 shows the capacitive sensor measurement set up which yields a capacitance value around 17 pF. This is similar to our calculation result 13.3 pF with 6 mm^2 gold plates area and 4 μm distance between two gold plates. The unexpected parasitic capacitance comes from the copper connection pad of sidewalls and the values vary with different samples. The capacitance between connection wires should be less than 0.1 pF considering the wire diameter and distances between the two wires. A calibration is needed after wire connections are added between the ICP sensor and RFID electronics. Fig. 7-3 shows the parylene material as insulator is deposited on the silicon membrane side to expose the membrane area and protect wires from salt water.

For the initial measurement test, the capacitive sensor is mounted on the PCB board (two Cu plates on the left side) using the silver paste as shown in Fig. 7-4. Then using the 3000 Parylene coater machine, 10 μm thickness of parylene C is deposited on the PCB board next to the two connection holes on the right side. Parylene C has a high resistance value and low gas permeability as shown in Table 7-2. It also shows other properties of deposited parylene C.

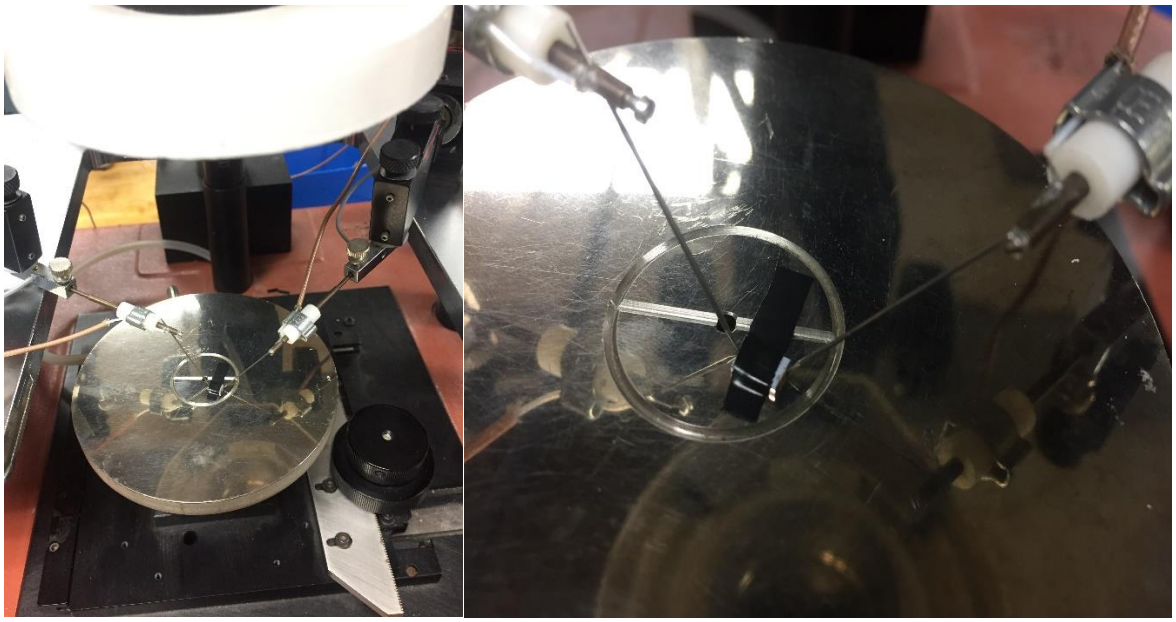

Fig. 7-2 Capacitive sensor capacitance value measurement

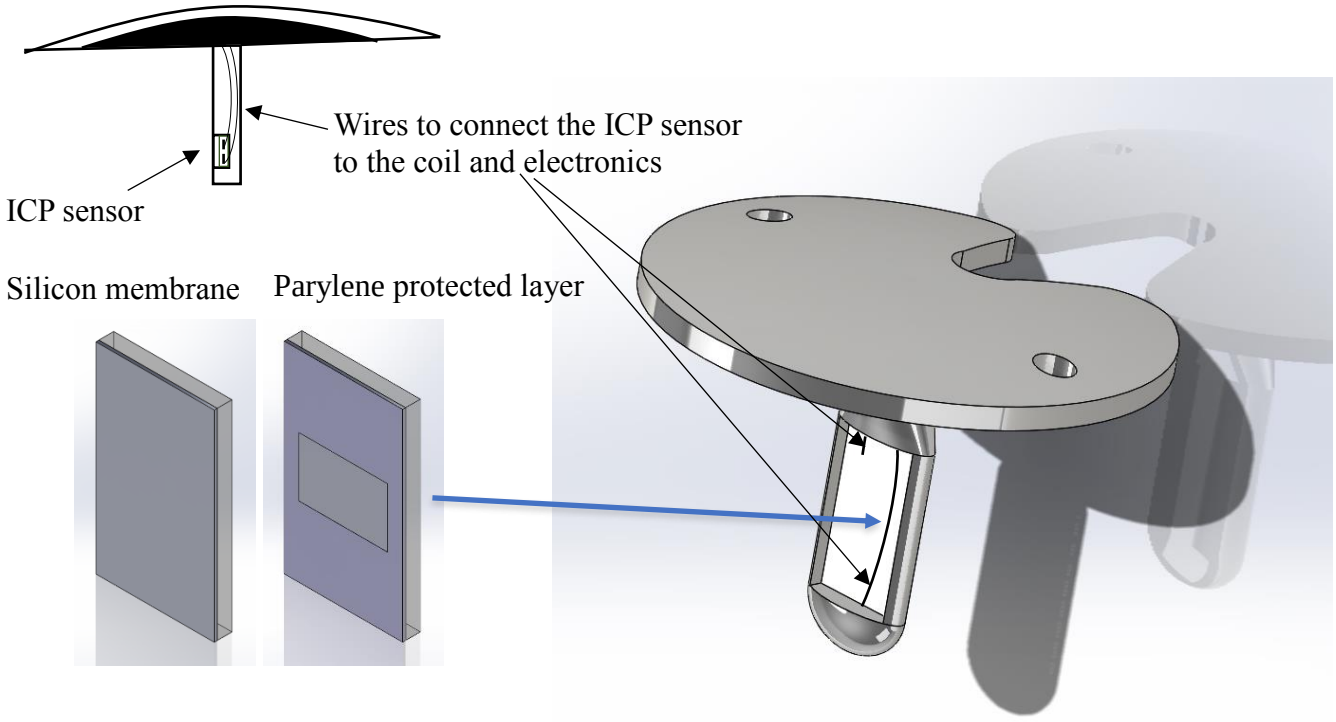

Fig. 7-3 10 μm parylene layer as protection

Fig. 7-4 PCB connection board for initial measurement

Table 7-2. Parylene C material properties

Property	Value	Units
Density	1289	g/cm^3
Tensile Strength	69	MPa
Yield Strength	3200	MPa
Dielectric Strength	6800	V/mil at 1 mil
Volume Resistivity (23 ºC)	6e+016	50% RH (Ohm-cm)
Surface Resistivity (23 ºC)	1e+015	50% RH (Ohm-cm)
Dielectric constant: 60 Hz	3.15	
1 kHz	3.10	
1 Hz	2.95	
Dissipation Factor: 60 Hz	0.020	
1 kHz	0.019	
1 MHz	0.013	
Melting Temperature	410	ºC
Gas Permeability: Nitrogen	0.95	cm^3-mil/100 in^2-24h-atm (23 ºC)
Oxygen	7.1	
Carbon Dioxide	7.7	
Hydrogen Sulfide	13	
Sulphur Dioxide	11	
Chlorine	0.35	
Moisture Vapor Transmission	0.14	g-mil/100 in^2-24h 37 ºC 90% RH

7.1.3.2 Long term stability measurement

Sensor size is 4 × 6 × 0.61/0.55 mm to permit implantation through a 5 mm diameter skull burr hole, then into the ventricle. The sensor is protected from body fluids by 10 μm thickness of

Parylene C. As shown in Fig. 7-5, the sensor with 10 µm thickness of Parylene C protection is placed at the bottom of 2000 ml cylinder in saline. Different height of the saline yields different pressures from 760 to 790 mmHg

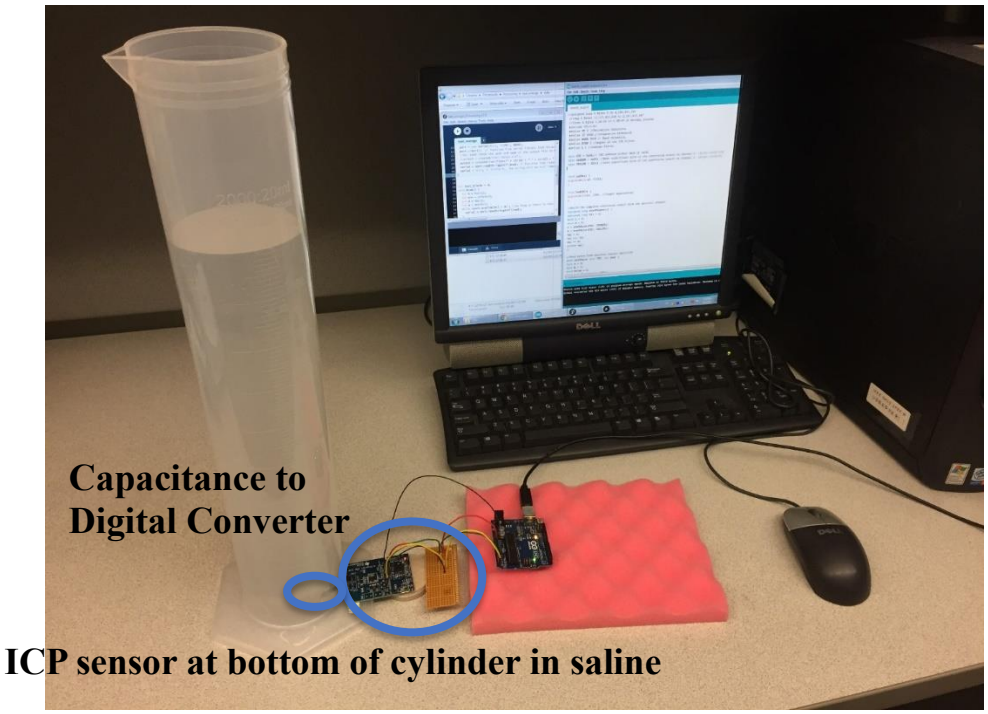

Fig. 7-5. Sensor pressure value measurement set up.
We are currently testing pressure sensor range from 760 to 790 mmHg

In addition, the sensor should measure absolute pressures from 550 to 760 mmHg range to accommodate ICPs from sea level to pressures in airplanes at 8000 feet altitude as well as high pressure range from 760 to 900 mmHg. Instead of just the 760 to 790 mmHg range, the entire pressure range from 550 mmHg to 900 mmHg for pressure sensor measurement is measured with the help of a vacuum pump and nitrogen cylinder from Prof. John Pfotenhauer's lab as shown in Fig. 7-6(a). A special feedthrough flange tool to make the sensor connection and measure the desired pressure value is shown in Fig. 7-6(b). An accurate digital pressure gauge with measurement range from vacuum to 1000 mmHg helps to record the theoretical pressure value.

Fig. 7-7 shows the measurement result using the vacuum pump and nitrogen cylinder set up of Fig. 7-6.

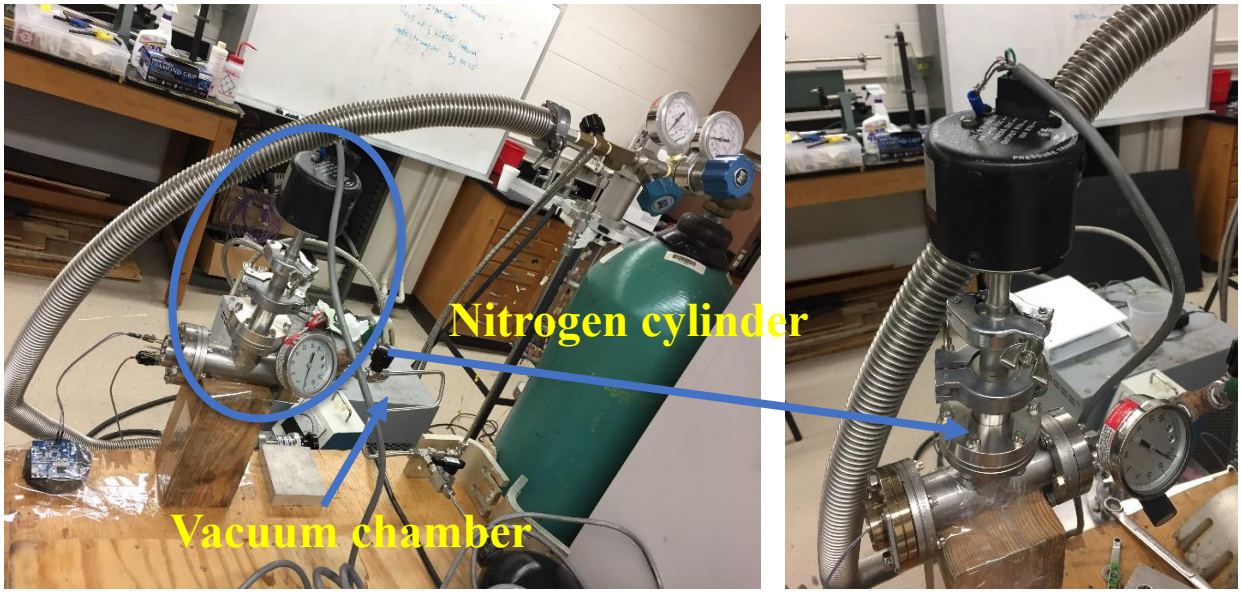

Fig 7-6(a) Fig 7-6(b)

Fig 7-6(a). Sensor pressure measurement set up from 500 mmHg to 900 mmHg with the help of nitrogen cylinder and vacuum chamber. **Fig 7-6(b)**. Special feedthrough tool for sensor connection.

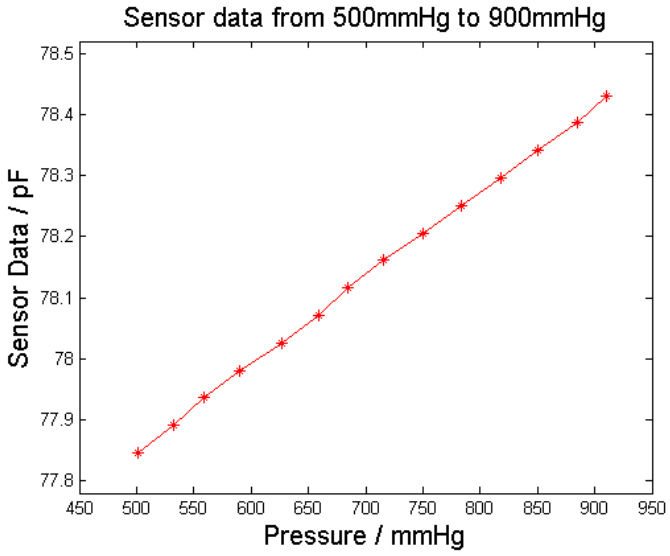

Fig. 7-7 Sensor output from 500 to 900 mmHg of chamber pressure

Our capacitive sensor long term stability needs repetitive measurement every day for at least one month. Unfortunately, the nitrogen cylinder and vacuum chamber was not available to us for long term stability measurement. Another simple set up to simulate pressure from 500 mmHg to 900 mmHg is shown in Fig. 7-8. A 60 ml syringe is used to simulate the chamber. When the head is covered with a sealed cap, the movable piston will simulate different pressures from 500 mmHg to 900 mmHg. A rectangular hole is drilled near the head side, the PCB mounted with capacitive sensor is placed at the left side of the syringe. Epoxy is used to glue the PCB board to syringe to avoid leakage during the increasing and decreasing wide pressure range. Dupont wires are used to connect between sensor electronics FDC2214EVM. An accurate digital pressure meter HHC 281 with measurement range from 225 mmHg to 900 mmHg records the theoretical pressure value. Fig. 7-9 shows the measurement result from set up of syringe with piston with capacitive pressure sensor. 10 capacitive sensors are measured with 0.022 mmHg resolution and drift value from ±0.136 mmHg to ±0.5 mmHg (0.05% Full Scale Output (FSO)) for 2 months.

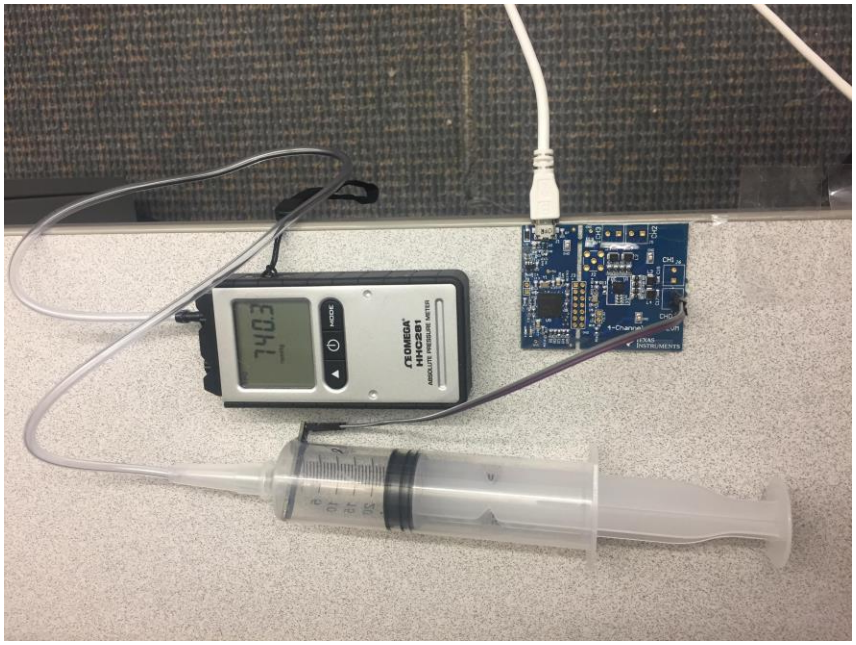

Fig. 7-8 Springe with piston, pressure sensor, digital pressure meter HHC 281 and sensor electronics FDC2214EVM

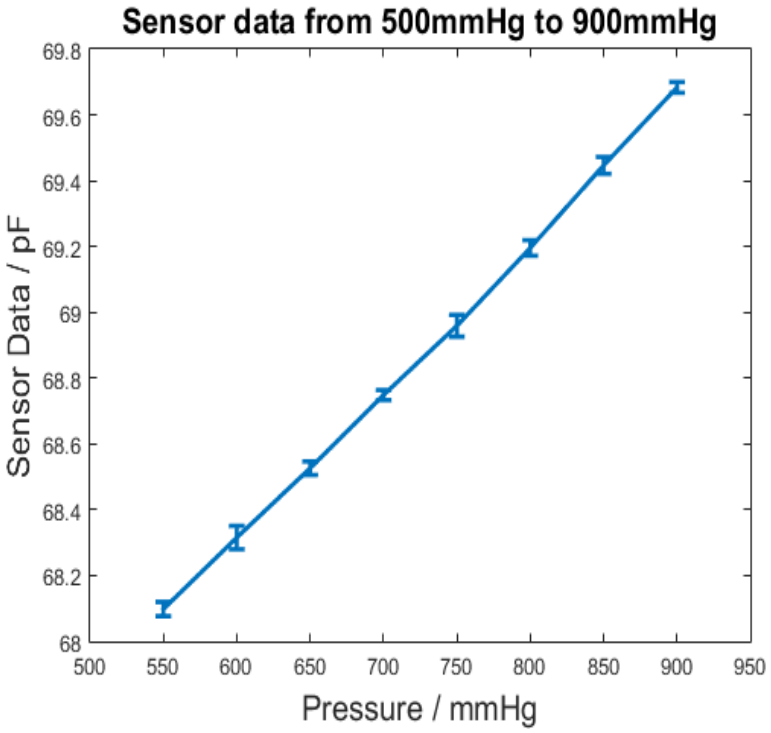

Fig. 7-9 Sensor output from 500 to 900 mmHg of chamber

7.1.3.3 Sensor test platform

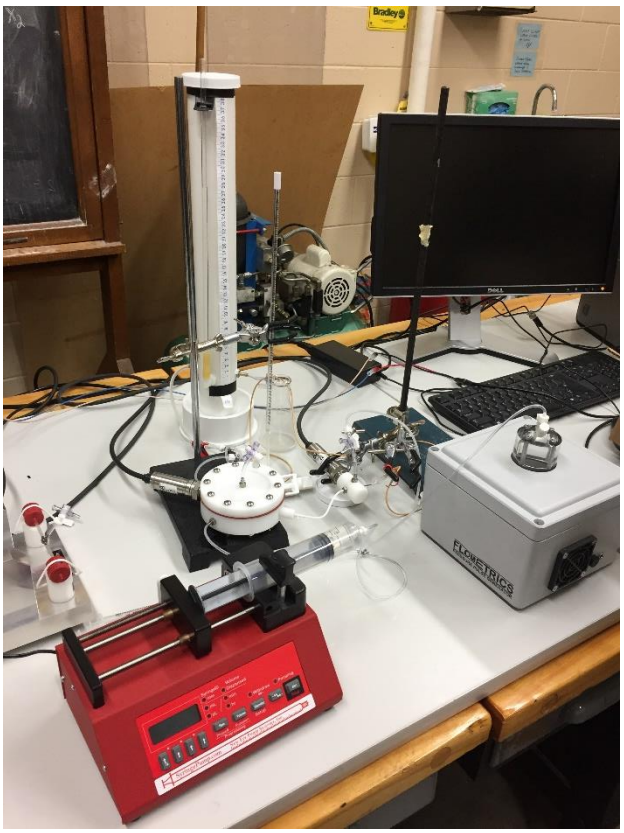

Fig. 7-10 Automatic sensor test platform

In the future, an automatic sensor test platform will be set up as shown in Fig. 7-10. With the help of a power supply, measuring cylinder, temperature meter and pulsation/pressure generator, the sensor test platform will yield pressure measurement of the capacitive sensor from 500 mmHg to 900 mmHg automatically and repeatedly without manual control. This sensor test platform will save much time as well as avoid important fluctuations from manual control and environment.

7.1.4 Active sensor measurement result analysis

Quantitative criterias for the performance of our own fabricated capacitive sensor are needed.

7.1.3.1 Accuracy and Linearity

The accuracy of a single measured quantity is the difference between the true value and the measured value divided by the true value. This ratio is usually expressed as a percent. Accuracy is a measure of the total error without regard to the type or source of the error (Olson, 2010). The accuracy can be expressed as percent of full scale as well. The full scale of our capacitive sensor is 0 mmHg to 1000 mmHg and accuracy is 0.033% for two months. About the linearity, for up-scale readings, the percent-of-reading is desirable because most errors are proportional to the reading. For small numbers near zero, however, percentage of full scale is more realistic because it is not feasible to test for small percent-of-reading deviations near zero (Olson, 2010). As shown in Fig 7-9, our capacitive sensor measurement result demonstrates the sensor's good linearity: r = 0.96.

7.1.3.2 Precision and resolution

The precision is the parameter to express the number of distinguishable alternatives from which a selected given result. The precision of our sensor is 0.01 mmHg, which shows high precision. The smallest quantity/step that can be measured is the resolution. The resolution of our sensor is 0.022 mmHg (0.001 pF).

7.1.3.3 Reproducibility and drift

The ability of an instrument to give the same output for equal inputs applied over some period is called reproducibility or repeatability. Zero drift is desired for pressure sensor and any other medical instrument. Interfering and/or modifying inputs may affect the corresponding outputs. Zero drift is defined as all output values increase or decrease by changing the same absolute amount of input (Olson, 2010). Many factors will keep the real pressure sensor and medical instrument away from zero drift such as material properties, manufacturing process, variations of temperature, vibration, hysteresis, and so on. The drift value of our 10 capacitive pressure sensors are from ±0.136 mmHg to ±0.5 mmHg for 2 months. 0.5 mmHg is corresponding to 0.05% FSO with full range of 0 to 1000 mmHg.

7.1.3.4 Other parameters

Statistical control is a good method to improve accuracy. All factors such as the environment noise and manual handling control ability will add random variations in measured quantities. The systematic errors or bias can be removed by calibration and correction factors. But random variations present as a more difficult issue, which may lead to unreproducible results. Considering the small pressure changing range we need (0.0045 pF/mmHg), the statistical analysis method is used to decrease error variation by making 15 multiple measurements and averaging the results per pressure point measurement.

Temperature drift is another parameter should be considered for the pressure sensor and medical device. The capacitive pressure sensor demonstrates much better temperature sensitivity (0.05 mm Hg/^{o}C) compared to the piezoresistive pressure sensor (> 1 mm Hg/^{o}C) (Lee Y S 1982, Kowalski 1987, Akbar and Shanblatt 1992).

In addition, the non-pressure-sensitive parasitic capacitance of the capacitive pressure sensor will degrade the relative pressure sensitivity. Parasitic capacitance is inevitable during fabrication but can be reduced during design.

7.2 Passive sensor

7.2.1 Passive sensor simulation

Based on the dimensions of the sensor, the thickness of the diaphragm can be determined to maximize sensitivity. The substrate is 5 × 5 mm with 0.5 mm on each side for bonding and silicon diaphragm area is 4 × 4 mm with possible deflection space. To better understand the shape of the deflection across the entire diaphragm, the sensor is modeled in SolidWorks with silicon and copper materials. The boundary of the model is fixed and the pressure is set at 20 mmHg to simulate the ICP of the human brain. The yield strength and tensile strength of Copper and tensile strength of silicon are satisfactory, and values were 394.38 MPa, 258.646 MPa, and 120. MPa separately. Fig. 7-11(a) shows the results of the deflection simulation when the pressure was 20 mmHg with 50 μm thickness membrane. The maximum deflection is greatest with value 0.27 μm in the middle of the membrane with value 2.651 MPa and average stress is around 0.9 MPa, which is smaller than the stress strength value stated before. Fig. 7-11(b) shows the stress simulation results when pressure is 20 mmHg. Table 7-3 summarizes the different deformation and stress values for different thicknesses of silicon membrane corresponding to selected values of the applied pressure. A thinner membrane yields larger membrane deformation. However, considering both my handing ability based on WCAM fabrication technique reality and silicon membrane sensitivity, I choose 50 μm thickness of silicon membrane for passive sensor.

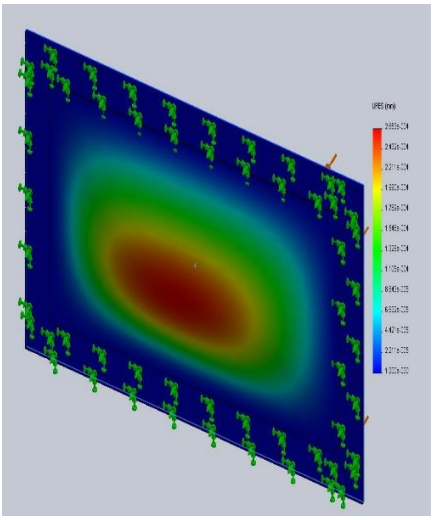

Fig. 7-11(a) Deflection simulation result when pressure is 20 mmHg

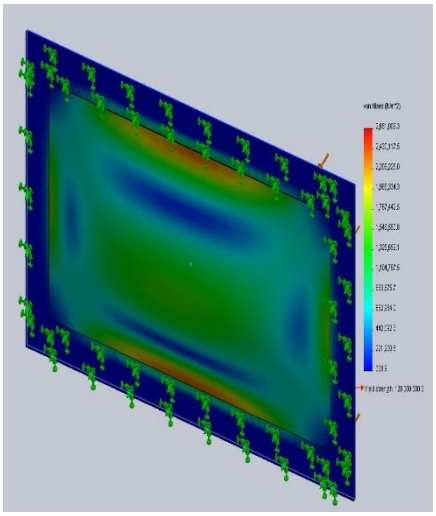

Fig. 7-11(b) Stress simulation result when pressure is 20 mmHg

Table 7-3 Different deformation and stress value for different thicknesses of silicon membrane corresponding to selected values of the applied pressure

	Stress 10^6 N/m^2			**Deformation** μm		
Membrane thickness (μm)	5	10	20	5	10	20
20 μm	1.8	3.6	7.1	0.4	0.8	1.6
50 μm	0.7	1.3	2.7	0.07	0.13	0.27
100 μm	0.2	0.4	0.8	0.01	0.02	0.05
200 μm	0.1	0.2	0.4	0.002	0.004	0.008

7.2.2 Passive sensor measurement

7.2.2.1 Resonant frequency measurement theory

The Spectrum analyzer machine and my colleague Fa Wang's self-designed reader are used to measure the sensor resonant frequency based on impedance load and impedance matching. Impedance seen from the spectrum analyzer has two peak points based on the equation calculation. Fig. 7-12(a) shows the maximum impedance is located somewhere at a just lower than the resonant

frequency, and the minimum impedance is located at a just higher frequency. The resonant frequency could be tracked by finding these two impedance points. The impedance seen from my colleague Fa Wang's self-designed reader has one minimum point. Any load impedance which is not matched to 50 Ω (no matter whether higher or lower) leads to lower signal amplitude. Thus, the resonant frequency could be detected by measuring the impedance of antenna and sensor system from the machine and the reader side. Fig. 7-12(b) shows with the same coupling factor *k* between sensor and antenna system, a higher *Q* value could enhance the signal and make the resonant frequency easier to detect.

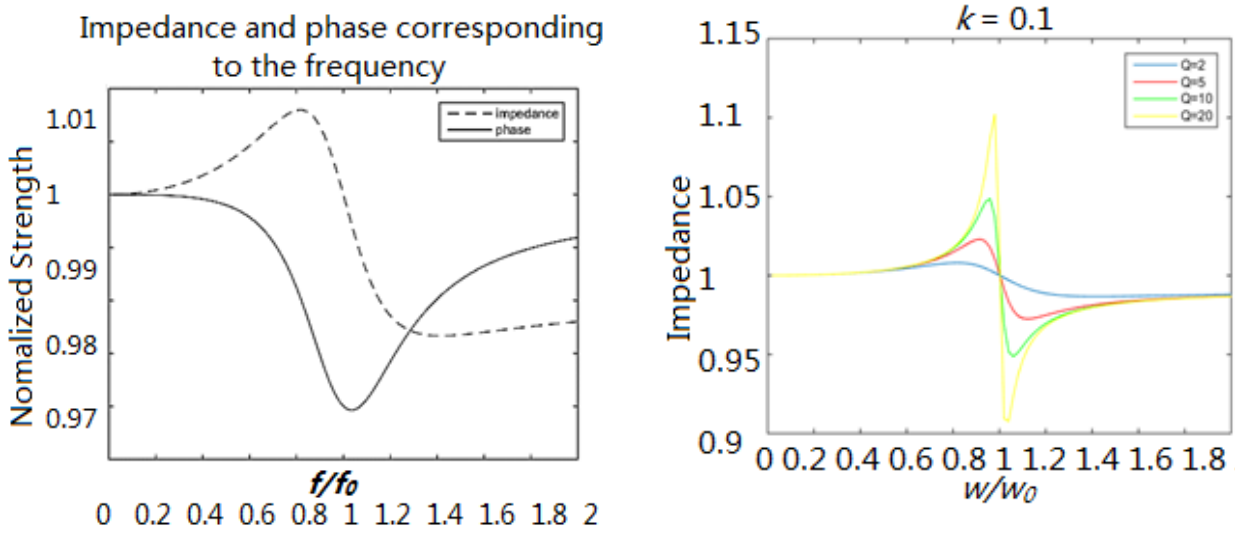

(a) Typical sensor's impedance and phase change as a function of frequency

(b) *Q* factor impact on the signal

Fig. 7-12(a) A typical sensor's impedance and phase change as a function of frequency. **(b)** *Q* factor impact on the signal with same coupling factor

7.2.2.2 Resonant frequency measurement setup

A Spectrum analyzer is used to measure the sensor resonant frequency based on the notable phase changing around the resonant frequency. As we discussed in the previous resonant frequency measurement theory section, the impedance and phase of the system have obvious changes at the resonant frequency, which help us to determine the current sensor's resonant frequency.

Fig. 7-13(a) shows the spectrum analyzer machine setup for one PCB fabricated style sensor resonant frequency measurement and Fig. 7-13(b) shows the amplitude and obvious impedance change around the resonant frequency as a function of frequency.

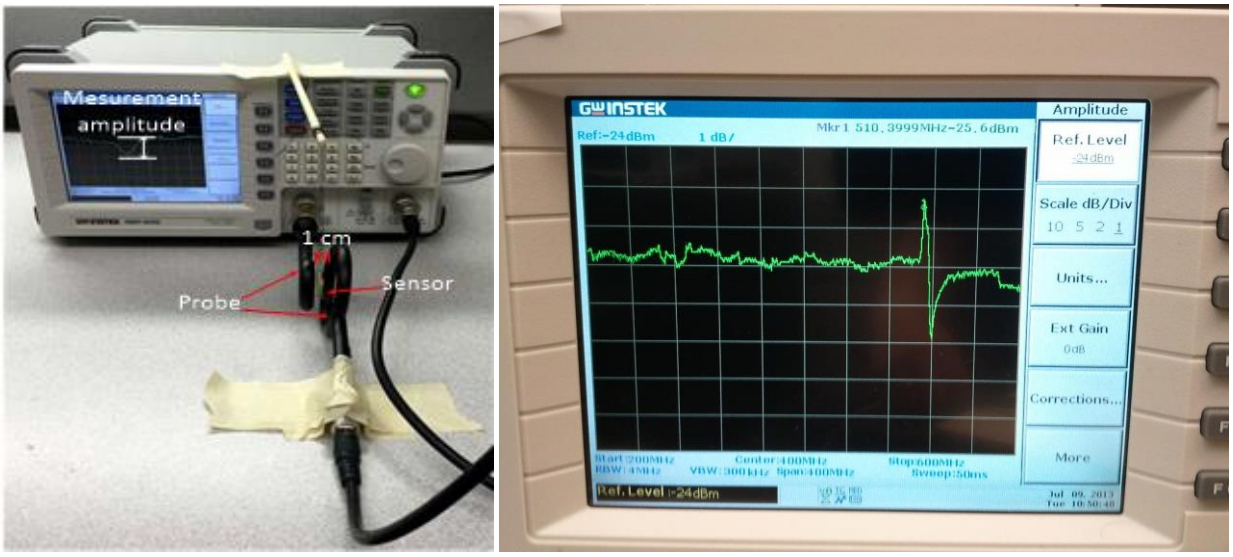

Fig. 7-13(a) Spectrum analyzer machine setup for the sensor resonant frequency measurement **(b)** Sensor's impedance change as a function of frequency

For PCB styled fabricated sensors, double sided tape is used to bond two plates together. It is easier to simulate different ICPs by controlling the thickness of polymer style tape then putting pressure on the bonded sensor. Fig. 7-14 shows that increasing pressure causes increasing deformation which leads to decreasing resonant frequency shifts.

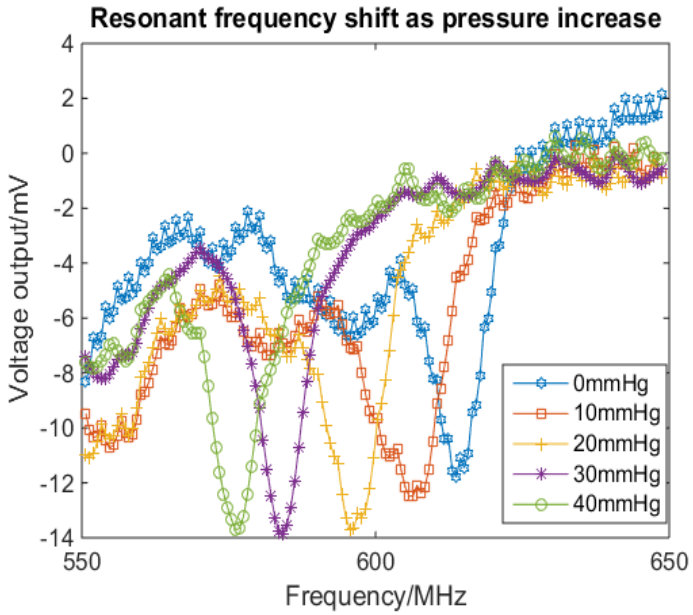

Fig. 7-14 Resonant frequency decreases as pressure increases

7.2.3 Resolution and measurement accuracy

The frequency-to-pressure responsivity of this sample PCB sensor is 0.92 MHz/mmHg. The MEMS sensor usually has lower responsivity because of the high Young's modulus of silicon, for example: 120 kHz/mmHg (Akar et al 2001); 160 kHz/mmHg (Chen et al 2010). The minimal resolution of my colleague Fa Wang's telemetry device is 0.5 kHz, which corresponds to 0.84×10^{-3} mmHg, with the phase noise at 600 MHz specified in Fig. 7-15.

A Solidworks simulation in Fig.7-16 showed that the capacitance change corresponded to the pressure. It demonstrates the sensor's good linearity: $r = 0.99$, and frequency/pressure resolution is 40.9 kHz/mmHg, as shown in Fig. 7-17.

The trick of MEMS sensor design is the coil is connected to a circular pad at the center. It is because the silicon elastic modulus is much smaller than FR4, and the most obvious diaphragm deflection occurs at the center. To increase the frequency/pressure resolution, a 2.4 mm diameter circular pad is necessary.

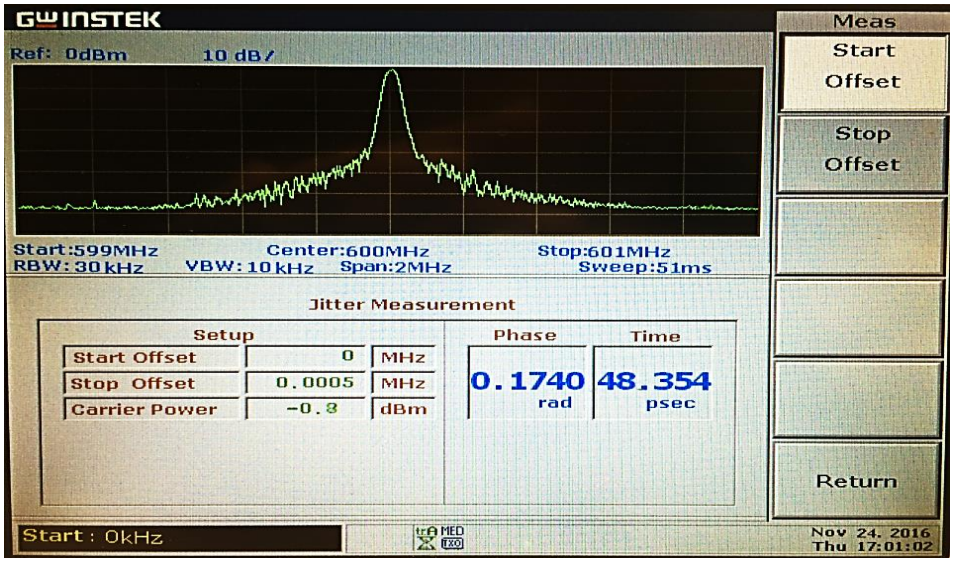

Fig. 7-15. Phase noise at 600 MHz

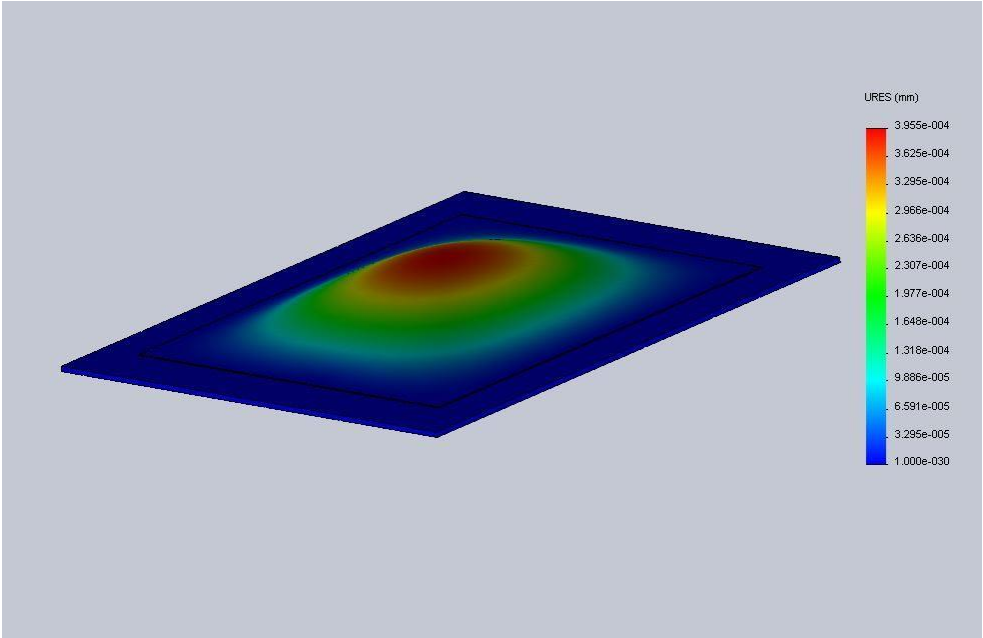

Fig. 7-16 Solidworks simulation result of diaphragm deformation at pressure when pressure = 20 mmHg. Maximal deformation is 3.96e-04 mm at this pressure

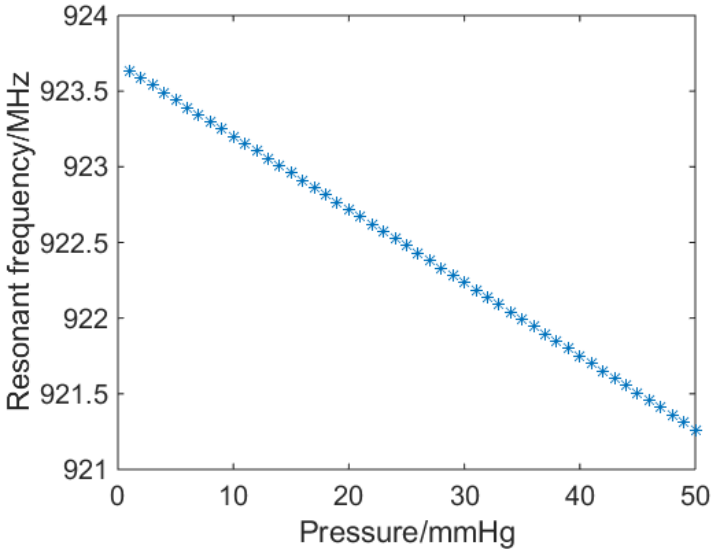

Fig 7-17. Simulated resonant frequency under pressure for MEMS sensor

7.3 Commercial sensor measurement

As discussed in section 5.3, both commercial piezo-resistive sensor die and commercial piezo-resistive sensor product are used for long term stability measurement to compare with our own fabricated capacitive sensor performance.

7.3.1 Commercial piezo-resistive sensor die long term measurement

We set up a long-duration stability test for commercial piezo-resistive sensor die experiments. The sensor we got from Allsensors corporation company. The sensor is 1 psi (50 mmHg) mounted die but not calibrated as shown in Fig. 7-18. The sensor is a silicon micromachined (MEMS) pressure sensor in a ceramic surface mount configuration. The piezo-resistive sensor cover is removed and the diaphragm of the sensor die is exposed as shown in Fig.7-19. The best temperature compensation should be achieved when the sensor has constant current excitation.

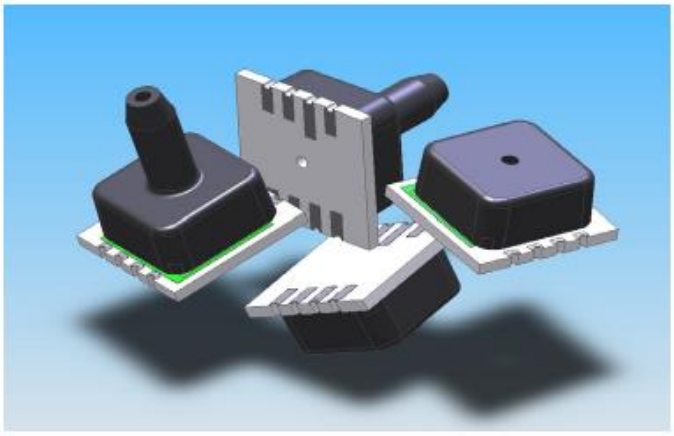

Fig 7-18 Surface Mount Basic Pressure Sensors
https://www.allsensors.com/datasheets/DS-0165_Rev_C1.pdf

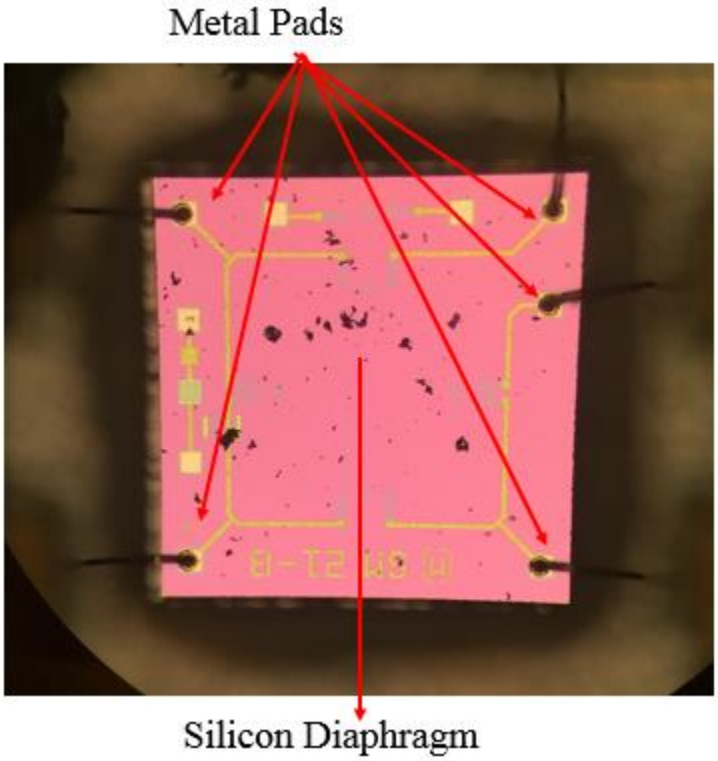

Fig 7-19. Remove the sensor cover and expose the diaphragm of the sensor die

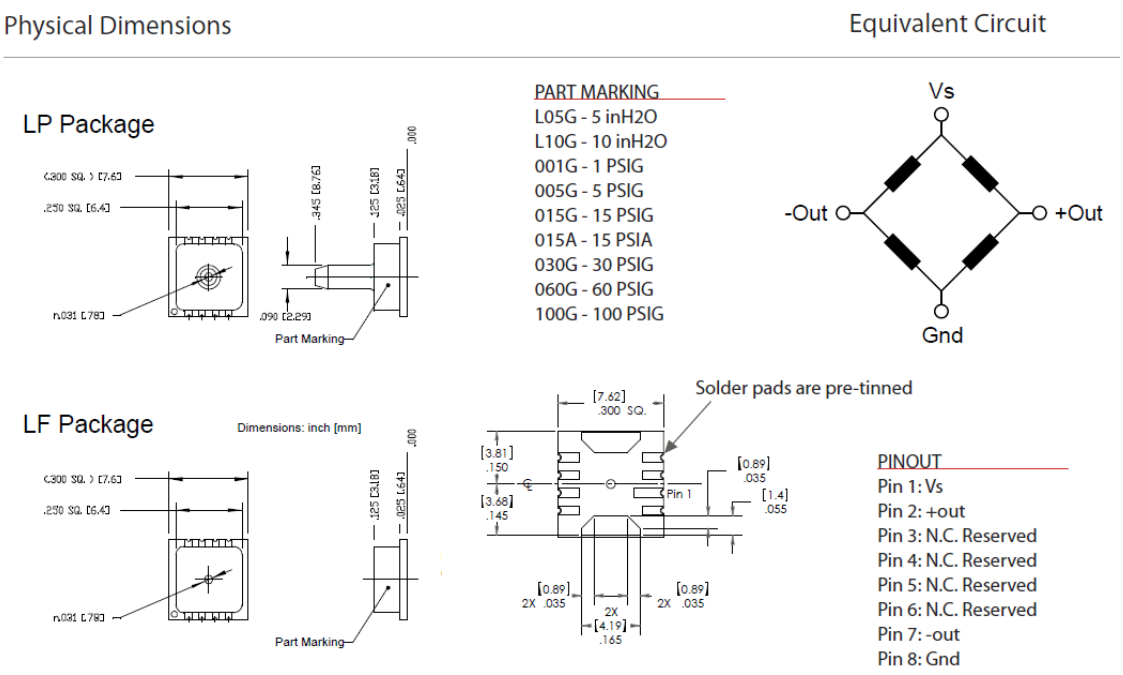

Fig 7-20 Pressure Sensor physical dimension (left) and equivalent circuit (right) https://www.allsensors.com/datasheets/DS-0165_Rev_C1.pdf

The sensor dimension is 7.62 mm × 7.49 mm as shown in Fig. 7-20 left. The pressure range is 0 to 50 mmHg and it offers 22.8 ± 2.60 mV/PSI sensitivity when 258.6 mmHg pressure is applied. It has low power consumption because of its high impedance. Pressure applied to the sensor membrane changes the bridge resistance of the piezo resistive pressure sensor. The equivalent circuit is shown in Fig. 7-20 right. The microchip detects this resistance change and calculates the corresponding pressure.

This kind of sensor originally is intended for use with non-corrosive, non-ionic working fluids such as air, dry gases and the like. We inserted this sensor membrane side in a plastic tube then put the tube into a plastic 2000 ml capacity cylinder (up to 25.745 mmHg). The long plastic tube was fixed vertically along the inner wall of the plastic cylinder using glass glue as shown in Fig. 7-21. The air in the tube between the sensor side and the bottom side into the water is constant, transmitting the applied water pressure to the sensor membrane side. Specifications are written for

constant voltage of 3.0 V. The output of the device is ratiometric to the supply voltage. By applying pressure on the same height of water, we measured the sensor voltage/output through microchip every day for two months to check the stability parameter. The average output was 8.658 with minimum 8.24 and maximum 9, the drift value was 5% FSO for two months, which is much larger than our drift value estimation such as 2% or 1% FSO per year.

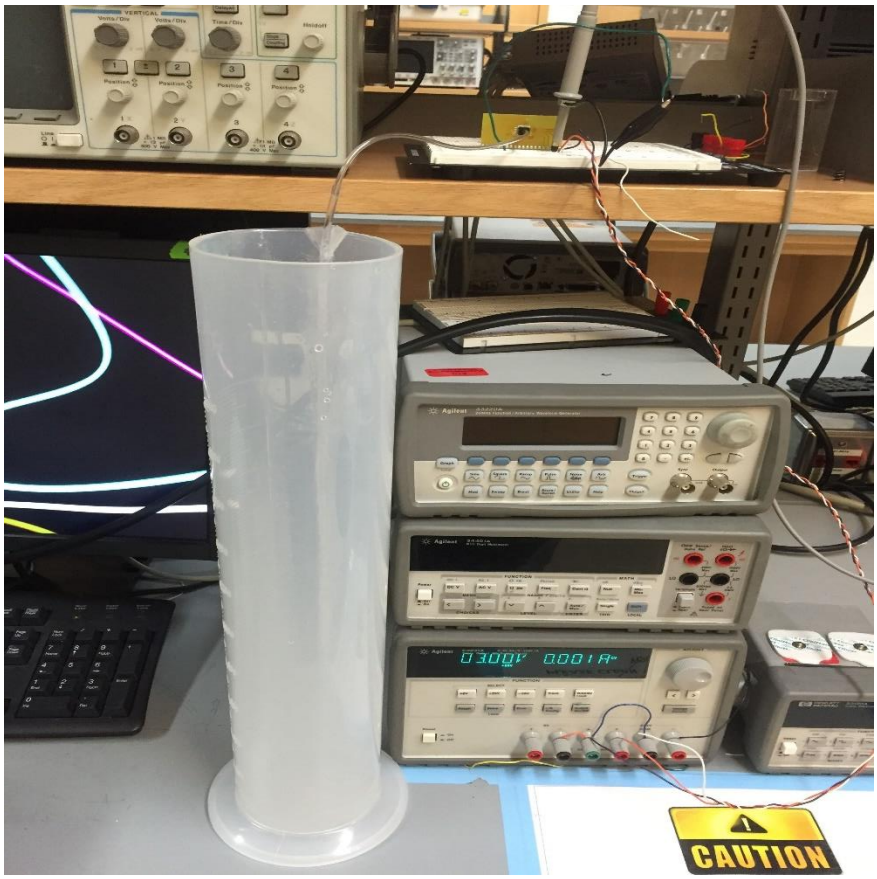

Fig. 7-21 Pressure Sensor Die long term stability experiment set up

7.3.2 Commercial piezoresistive sensor product long term measurement

This approach is based on using a commercial piezoresistive sensor product to measure the pressure change. We soldered the sensor footprints to the electronic circuit. Pressure applied to the sensor membrane changes the Wheatstone bridge resistance of the piezoresistive sensor. The sensor electronics detects this resistance change and calculates the corresponding pressure. The piezoresistive sensor needs protective layers to be used in a corrosive environment such as CSF.

Thus this biocompatible protected material will be deposited to avoid liquid access to the membrane. The protection could be parylene.

We ordered the one-piece 9LD stainless steel version for this approach. We finished the preliminary experiment for this sensor. The pressure range is 375 to 1125 mmHg absolute and the temperature range is –50 °C to 150 °C. One of the advantages for this constant temperature measurement feature is to help calibrate the accuracy of the sensor. In addition, this kind of the sensor has a titanium version housing for the whole sensor to realize good MRI capability.

A long-duration sensor stability experiment for this approach was set up as shown in Fig. 7-22. The sensor was placed at the bottom of the 2000 ml capacity cylinder. Every day, pressure value under empty cylinder, 400 ml, 800 ml, 1200 ml, 1600 ml and 2000 ml volume water condition were measured separately then displayed on the computer using the Arduino board as shown in Fig. 7-23. By applying pressure on the same height of water, we measured the sensor pressure/output through the Arduino and microchip every day for a month to check stability parameter.

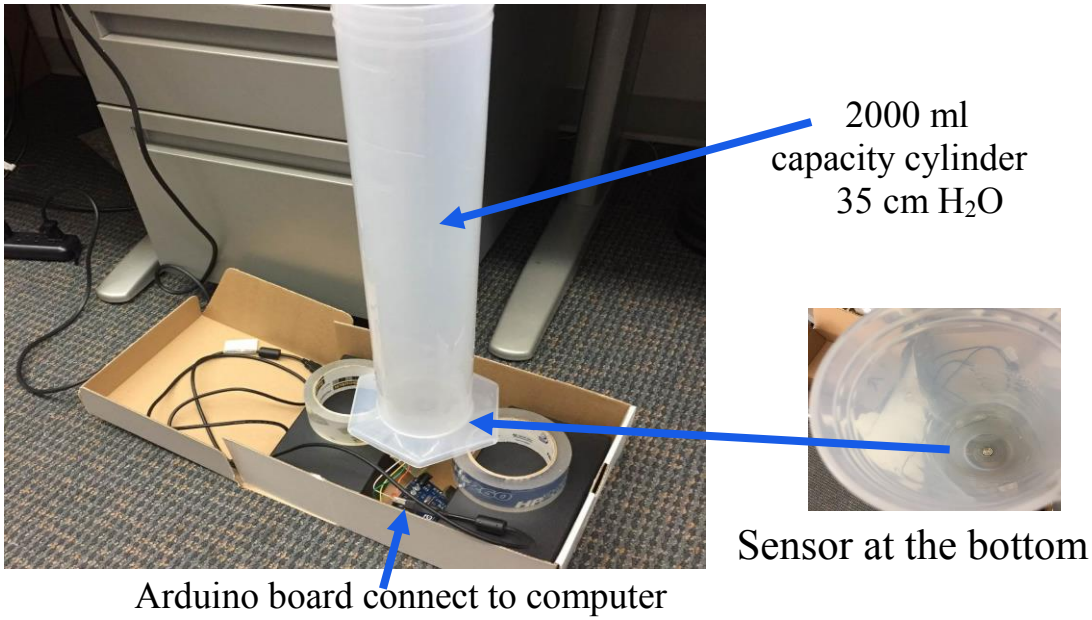

Fig. 7-22 Pressure Sensor product long-duration stability experiment set up

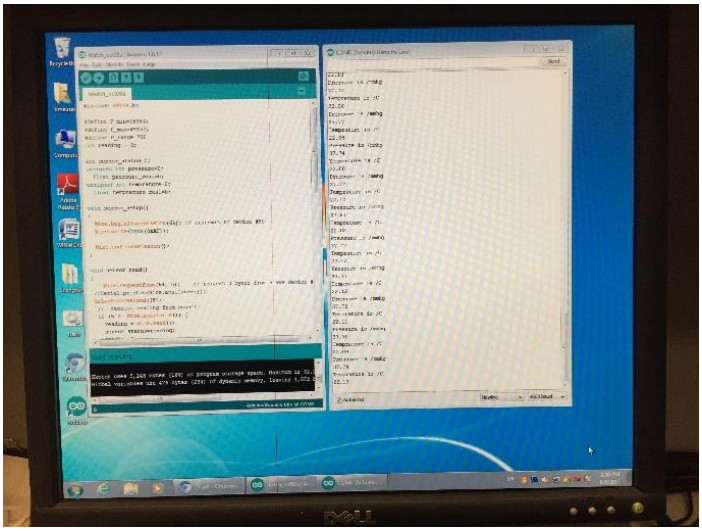

Fig. 7-23 Arduino board screen to show the sensor pressure value

During measurement, temperature was controlled to reduce the drift. As shown in Table 7-4, the measured pressure range for empty cylinder (just atmosphere pressure) was from 8.56 mmHg to 29.11 mmHg with an average value of 20.19 mmHg. The measured pressure range for 2000 ml volume water (35 cmH_2O) plus atmosphere is from 34.86 mmHg to 55.37 mmHg with average value of 46.20 mmHg and yielded quite a big error -24.5% ~ 19.8%. Table 7-4 also shows the minimum value, max value and average ones of pressure for corresponding 400 ml, 800 ml, 1200 ml, 1600 ml volume water. The measurement baseline with wide range deviation was extremely unstable and showed that long duration stability of this kind of commercial sensor is really bad.

Table 7-4. Pressure sensor value under different pressure conditions yielded by different water volumes

Pressure Value for	Minimum Value /mmHg	Maximum Value/mmHg	Average Value/mmHg
Empty Cylinder	8.56	29.11	20.1875
400 ml water	13.57	34.12	25.026
800 ml water	18.97	39.6	30.373
1200 ml water	24.26	44.68	35.5805
1600 ml water	29.39	49.64	40.6795
2000 ml water	34.86	55.37	46.195

The fixed 3.3 V power supply for sensor communication through the Arduino board is digital, in theory it does not influence the unstable results. To exclude that the unstable baseline is caused by power input value deviation, another experiment was set up by changing the power supply from 3.0 V to 3.6 V with 0.1 V step differences as shown in Fig. 7-24. For the same condition, the averaged pressure value of 25 times measurement was 27.0896 mmHg, 27.0496 mmHg and 27.0608 mmHg corresponding to 3.3 V, 3.0 V and 3.6 V condition as shown in Table 7-5. The small pressure value deviation showed that power supply value deviation made no influence on the sensor value reading.

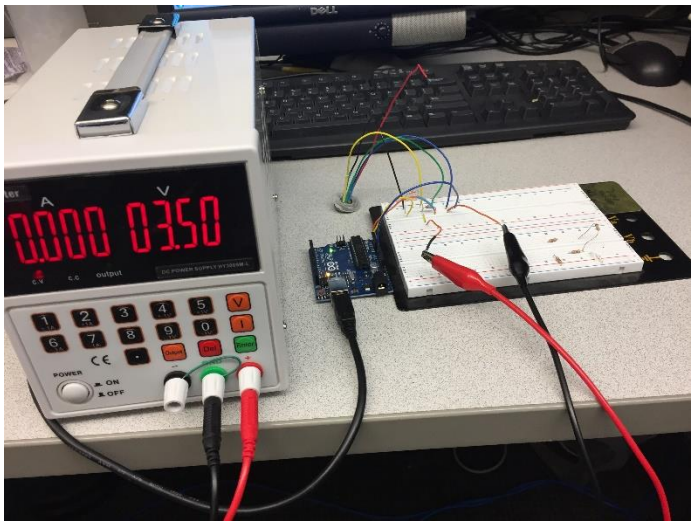

Fig. 7-24 Power Supply Value changing set up for sensor pressure value experiment

Table 7-5. Pressure sensor value under different power supply value

Power Supply Value	Minimum Value/mmHg	Maximum Value/mmHg	Average Value/mmHg
3.3 V	27.01	27.21	27.0896
3.0 V	26.99	27.1	27.0496
3.6 V	26.94	27.15	27.0608

CHAPTER 8: RFID BASED ICP MANAGEMENT SYSTEM: SMART SHUNT

8.1 System overview

The standard treatment for hydrocephalus involves the insertion of a flexible plastic tube into the ventricular system of the brain to drain the excess fluid. This is controlled by a passive valve system. Passive valve systems open undesirably by gravity, systolic pulsations, and Valsalva maneuvers. This may lead to excessive drainage of CSF which leads to ventricular maldevelopment and premature shunt failure.

Real-time ICP data could also be applied to the implantable ICP management system, as the part of the closed loop control system. In this chapter, I present the work our group has accomplished to replace the passive system with an active smart shunt system as shown in Fig. 8-1 and Fig. 8-2 that consists of: (1) An intracranial pressure sensor, which is implanted within the brain of the patient and produces a signal representing an intracranial pressure (ICP) wave form with 0.6 mmHg sensitivity and less than ± 1 mmHg dift, (2) Circuitry to reject noise, Valsalva, and pulsation related pressure spikes, (3) An active piezo-valve with driver circuit that does not siphon regardless of gravity and opens and closes based on the ICP sensor data; (4) An RFID based sensor tag, which permits valve programming and ICP waveform transmission between caretakers, provider, and patients. It also provides wireless power to charge the shunt system eliminating the need for battery replacement. Currently this system is tested to be functional ex-vivo. Next steps involve lengthening the distance from the antenna to the patient by a distance of 3 meters through ultra-high frequency module so that patients with developmental problems such as autism will not be disturbed by the system when the shunt is being interrogated or charged.

Telemeter is located outside the human head. Sensor tag, pressure sensor, valve driver and ICP valve are implantable parts, among them, sensor tag, pressure sensor and valve driver are

implanted between skull and scalp, and sensor is implanted through dura layer which membrane may contact CSF.

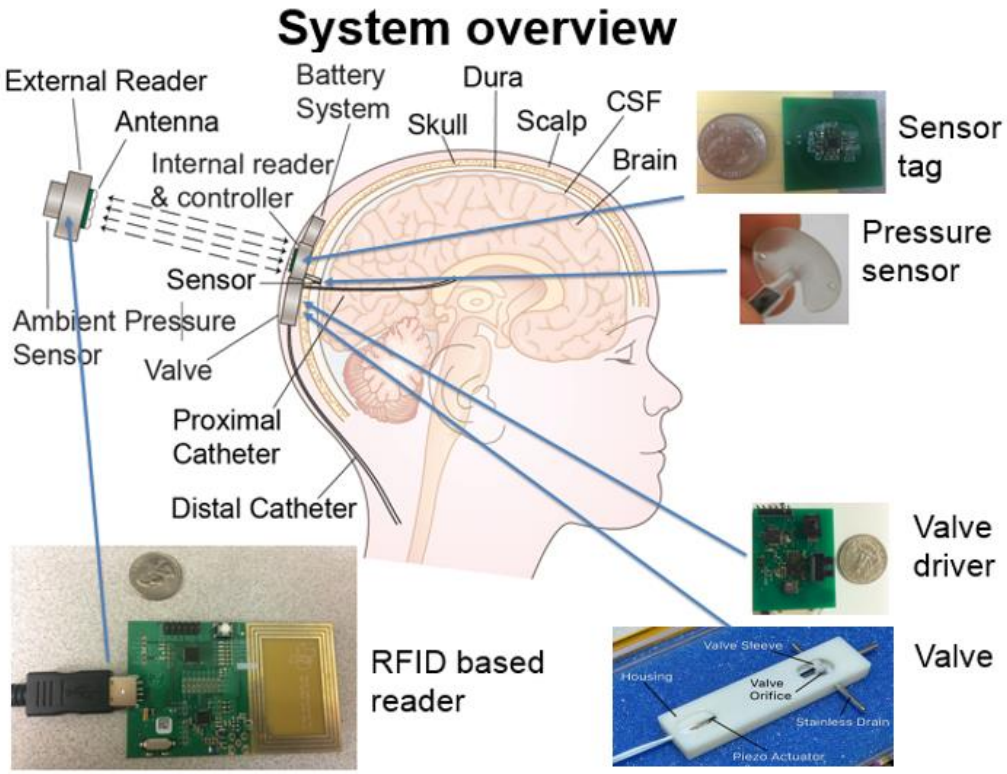

Fig. 8-1. ICP management system overview: RFID based reader, sensor tag, pressure sensor, valve driver and valve

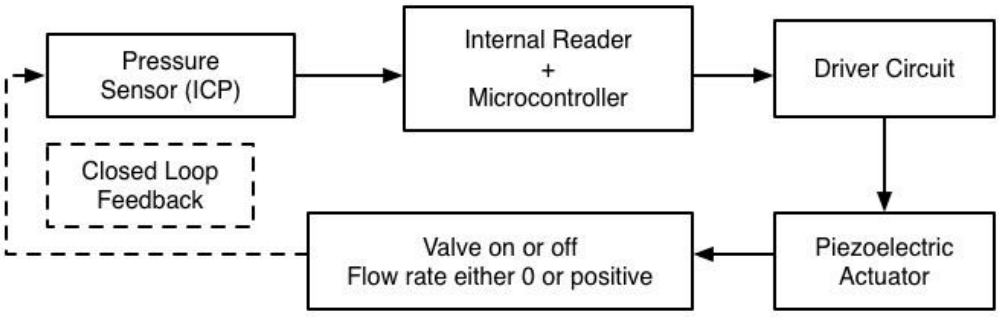

Fig. 8-2. Simplified version of ICP management system

8.2 Telemetric ICP measurement

8.2.1 Current telemetric ICP measurement

To realize longer-term usability, implanted microsensors must not have wires exiting the body, must have very limited drift potential, and must have wireless communication to the outside so

that pressure values can be evalutated by an external reader. A few non-commercialized attempts have so far been made to create such a system, most of them using inductive coupling to an external antenna and various active elements in the design that would influence incoming power and outgoing signal. Such miniaturized devices would also be useful in monitoring various other pressures in the body, and commercial efforts have used microelectromechanical systems (MEMs) type devices particularly for cardiac and ocular applications. Implantable catheter-tip sensor ICP devices have also been connected to a telemetry unit. The telemetric technique is an invasive way to monitor ICP with risk limited to the implantation of the pressure probe only. It allows for ICP monitoring under normal daily living conditions in an outpatient setting. The telemetric catheter can be implanted up to 3 months in some studies. However, telemetric pressure sensors are not presently in wide use because the technology is not yet reliable and readily available. And even if an implantable sensor were to become technically feasible, the sensor would require multiple procedures for recalibration or surgical replacement to achieve zero drift stability. Miyake et al (1997) described telemetric monitors used for long-term ICP monitoring in hydrocephalus patients with ventriculoperitoneal shunts. The telesensor was implanted up to 44 months in some patients. Their telesensor also exhibited zero drift. However, the device suffered from drift inconsistency and need to recalibrate.

Welschehold et al (2012) presented a system consisting of an implantable Neurovent-P-tel telemetric ICP probe, a reading device, a portable recording device, and PC software for storing and analyzing data manufactured by Raumedic AG, Helmbrechts, Germany. The telemetric transducer was placed between the calvarium and galea in 10 patients. Recording was achieved only when the reading device was in proximity to the telemetic sensor. The measurements were

reasonably reliable and no calibration was needed. However, ICP monitoring was not continuous, leading to frequent disconnection between the reader and monitoring unit.

Yoon et al (2004) reported a micro telemetry pressure sensor for CSF shunt systems. This sensor was based on an LC tank circuit (where L represents an inductor and C, a capacitor). When pressure was applied to the senor, the phase would shift. This phase shift change decreased from –33 to –42° when pressure increased from 0 to 110 mmHg in a linearly proportional manner as measured by a network analyzer (HP 8510C). The total size of the sensor was 8.05×7.8 mm. There were no description of in vivo experimentations.

Kawoos et al (2005) proposed a fully implantable MEMs-based ICP sensor, and a portable monitor to read out the sensor's data. This sensor was cylindrical, 10 mm in diameter and 8.85 mm in height, and was packaged within an MRI-compatible titanium cylinder. The wireless communication method was based on bluetooth at 2.4 GHz frequency. Later in 2014, the authors developed an implantable device for long-term telemetric ICP measurements in a small animal model of blast-induced brain injury. They presented an analog implant for long-term ICP dynamics study after brain injuries of different origin. When measuring over the range 0–50 mmHg in steps of 5 mmHg, the pressure values shifted by 2.1 ±0.33 mmHg. The devices were calibrated prior to placement. The maximum estimated error was 4.86% while making ICP measurements. Exposure to blast showed biphasic significant increase in ICP, the first occurring within an hour of the blast, the second delayed and more prolonged on day 2 after the blast. ICP measurement was done for a maximum of 3 hours per day over a seven-day period. In addition, after implantation in the animals, the device required a longer stabilization period than the analog version.

Chen et al (2014) reported a wireless, real-time ICP monitoring system with passive, flexible, millimeter-scale sensors as small as 1×1×0.1 mm. This miniature novel sensor overcomes the

traditional operating frequency limits and exhibits insensitivity to lossy tissue environments. They tested real-time continuous wireless monitoring of rat ICP in vivo. The tiny sensor structure is a distributed resonant tank, formed by stacking a deformable dielectric layer (microstructured styrene-butadiene-styrene (SBS) elastomer) between the two inductive spirals on flexible polyimide substrates in a sandwich structure. Pressure reduces the separation distance between the spiral layers, increases the effective coupling capacitance, and shifts the resonant frequency to lower frequencies with an increase in the measured pressure. SBS has low loss in the high-frequency range compared to poly (dimethyl siloxane) (PDMS) or polyurethane. However, drift in capacitance values is a drawback of SBS during cycling measurements.

Lilja et al (2014) tested 21 patients in a Danish neurosurgical center clinic with an implanted Raumedic® telemetric ICP probe (NEUROVENT®-P-tel). They recorded diagnosis, implantation indication, surgical complications, ICP reading duration, number of ICP recording sessions related to symptoms of elevated ICP, and corresponding clinical consequences. The median duration of implantation was 248 (49–666) days and median duration from implantation to last recording session was 154 (8–433) days. Only 86 recording sessions were performed and contributed to the clinical treatment intervention of patients. The drift reported was +/- 2mmHg per month. The ICP wasn't continuously monitored, as the telemetric probe had no integral memory or power source, and ICP was monitored only when the reader or recording unit was placed over the probe.

Data on the accuracy of the Neurovent-P-tel telemetric monitoring device within a broad ICP range are missing. Freimann et al (2013) applied a porcine model for studying the accuracy of Neurovent-P-tel telemetric device on high non-physiologic range ICP. Simultaneous measurement of ICP was recorded using the Neurovent-P-tel telemetric device and a water column within a riser tube. 34 valid telemetric ICP measurements were then compared. The mean difference between

the telemetric ICP sensor and direct measurement from a water column within a riser tube was 0.4 mmHg, showing higher values with Neurovent-P with 95% CI [–2.4 to 3.1 mmHg] and a p value of 0.58. This experiment showed that the telemetric Neurovent-P-tel sensor system afforded acceptable accuracy over a limited pressure range exceeding normal ICP values in animal model for a short period of time.

Guild et al (2015) examined intracranial pressure in conscious rats via telemetry for 1 month only, to verify the long-term stability and viability of this technology in freely moving rats. They found that the signals were stable throughout the 1 month period with an average ICP value of 6 ±0.8 mmHg.

Stehlin et al (2015) proposed a prototype of an implantable ICP monitoring device, and investigated the potential patient risk related to interactions between the device and an MR scanner. The prototype consisted of a 2.4 GHz wireless data antenna link, an inductive coil for transcutaneous energy transfer, a rechargeable lithium ion battery, and a related circuit for signal conditioning and amplification. This was encapsulated in a silicone jacket that was not suitable for long-term implantation as it doesn't provide an impermeable barrier, with the quality of MRI images and image artifacts being dependent on the encapsulation material. Multiple exposures to 3T MRI showed no interference with the prototype device's function, and posed no safety concerns though RF-induced heating. However, the silicon-based piezoresistive sensor catheter had a drift of nearing 2 mmHg over a 100-day period, which was not acceptable for long-term monitoring over the course of many years.

Kang et al (2016) tested the precision of a bioresorbable silicon-based electronic sensor for the brain. These devices dissolve completely into biocompatible end products in aqueous solutions

such as cerebrospinal fluid. Continous operation is possible for up to three days before the accuracy and sensitivity decrease. In vivo and in vitro experiments demonstrated precise measurements.

Yang et al (2015) studied histopathologic changes in rat brains 60 days after implantation of silicone beads and Arbomatrix™ (based on polyisobutylene) coated telemetric ICP sensor. No observable histopathologic reactions of the implanted material, such as glial reactions, was noted. They concluded that Arbomatrix™ is well tolerated and may be an excellent protective coating for a new telemetric ICP monitoring chip.

Kiefer et al (2012) reported that long-term telemetric ICP measuring devices Neurovent P-Tel and S-Tel, could provide reliable dynamic measurements over an 18-month period.

Thus far, wireless telemetry with a biocompatible sensor has not yielded a device capable of long-term measurement of ICP without having problems with recalibration and drift. Materials have however been proven to permit compatability without significant biofouling that would lead to inaccurate measurements. There remains a need for long-term, continous ICP monitoring in an outpatient setting, while patients are doing activitites of daily living. With a functional device the patient, cartaker/providers, and physicians would have access to representative pressure readings that might aid in the early detection of CSF shunt malfunction. (Zhang 2014).

8.2.2 Problem of current telemetry

Some studies (Nopper et al 2010, Coosemans et al 2010, Butler et al 2002) developed similar telemetry devices based on traditional grid dip oscillator technology. But grid dip oscillator technology has some constraints which prevent it from being applied to ultrasmall sensors, which always resonate at GHz frequencies: First, its sweeping frequency range is limited by the tuner capacitor, thus the frequency range is usually around 20 MHz (10 MHz to 30 MHz in (Nopper et al 2010); 22–41 MH (Coosemans et al 2010); 12.76 and 13.01 MHz in (Butler et al 2002)), which is narrow. Second, the center and highest frequency of the oscillator is limited by the oscillator's

parasitic capacitance, which won't reach up to the GHz range. Third, the oscillator's resonant frequency is determined by the imaginary portion of the system, including the antenna and the sensor. Especially when the sweeping frequency approaches the sensor resonant frequency, the capacitance components of the sensor influence the oscillator's resonant frequency to form a "frequency drift". This phenomenon inhibits us from getting accurate measurement results when trying to detect the tiny pressure change on the sensor. Also, this is an analog circuit with limited frequency resolution. Our reader overcomes these constraints. Its output frequency ranges from 35 MHz to 2.7 GHz, with a minimal 0.5 kHz resolution. In addition, the output frequency is only determined by the microcontroller's commands, and is isolated from the antenna and sensor.

Measurement distance is also a challenge and a significant consideration for ICP monitor design. Nopper et al (2010) proposed a reader that could achieve a measurement distance of 8.5 mm. Coosemans et al (2010) proposed a similar reader for intraocular pressure measurement with maximum distance of 7.5 mm. In real practice, the male adult scalp thickness ranges from 2 to 3.5 mm (Hori et al 1972), and skull thickness average ranges from 6.08 mm to 8.09 mm, differs with location, and SD range from 1.15 to 1.88 mm (Law 1993). The dura is a thick membrane surrounding the brain, which has an average thickness of 0.27 mm (Reina et al 1996). So the minimal measurement distance should be at least 10 mm and desirably larger than 15 mm.

8.2.3 Our telemetric ICP measurement

The telemeter is an ISO15693 RFID based reader, which based on the TRF7970 (Texas Instruments Inc). The telemeter could provide up to 200 mW radiation power to wirelessly charge the whole implantable part. The CLRC663 based (NXP Semiconductors N.V.) RFID reader, which could provide up to 2W radiation power is also developed. With the help with our own designed sensor tag as well as the signal processing technology, our RFID based telemeter could

detect small ICP changes. The whole design could be packaged into a helmet, with small weight (<50 g), which provides automatic and continuous daily ICP monitoring. With the help of UHF RFID frequency technology discussed in section 8.4, measurement distance has been adopted for communication range of over 3 meters, which will solve the limited measurement distance problem discussed in section 8.2.2.

8.2.3.1 Sensor tag

The sensor tag developed by my previous colleague Fa Wang is based on the RF430FRL15xH Near-field Communication (NFC) ISO 15693 Sensor Transponder (Texas Instruments Inc), as shown in Fig 8-3.

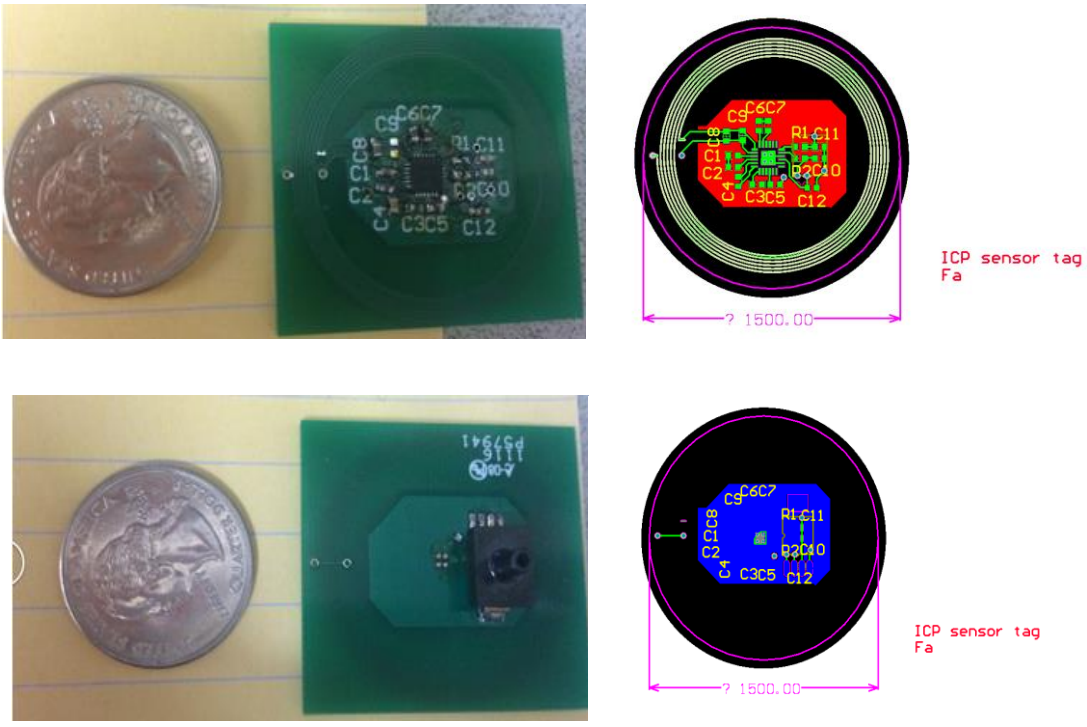

Fig. 8-3. Sensor tag: PCB design and prototype

8.2.3.2 ICP Data Signal Processing

Fig. 8-4 shows ICP data collected from patients, and the effect of applying a low pass filter on these data. It shows great enhancement between original and filtered data. These improvements

include removing the effects of high spikes (as a result of coughing, sneezing, and other artifacts), smoothing all data, and decreasing overall peak-to-peak values. To effectively control the smart shunt system, the ON/OFF valve works only according to average values and is not affected by spikes and variations. These spikes cause a siphoning effect that leads to over drainage complications in current passive valves. Also, lower peak-to-peak values decrease overall valve toggles and therefore minimizes power consumption. The microcontroller monitors the battery power to prevent power outages.

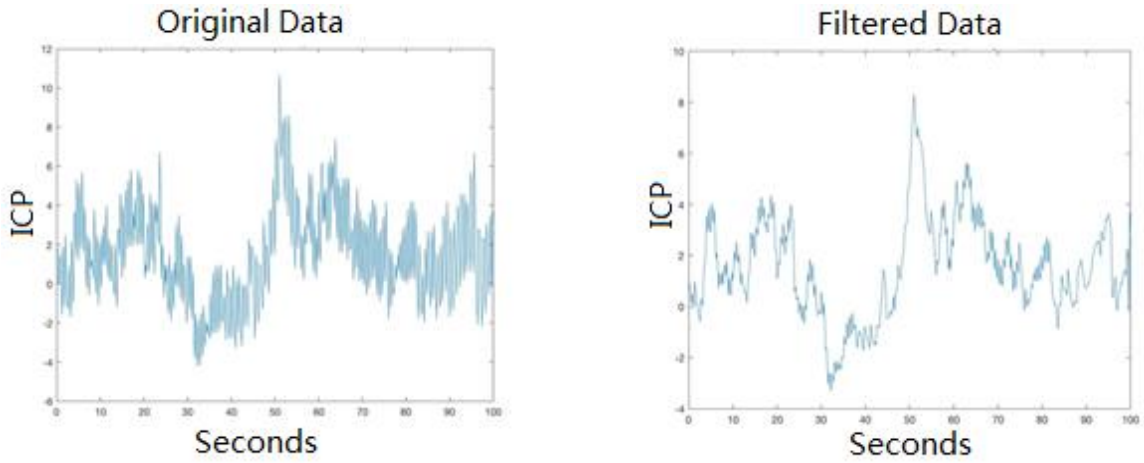

(b) Original measured ICP data with 5MHz sampling frequency (c) Filtered ICP data with 5MHz sampling frequency

Fig. 8-4. Original and filtered ICP data comparison

8.3 Valve and Valve Driver

8.3.1 Valve

Our group developed and fabricated the piezo electric valve component of the smart-valve VP-shunt system as sown in Fig 8-5. It works effectively in closed-loop control, regulating shunt pressures with insignificant leakage. The piezo arm moves a circular sleeve surrounding 1.59mm diameter stainless-steel hypodermic needle drain tubing with a 0.021" diameter hole drilled as valve orifice. The valve housing is 50.8mm x 12.7mm x 6.35mm. The fabrication technique,

design, and size make it easily reproducible and fine-tunable for animal and in-vitro experimentation; the drain tubing can be slid right or left to locate precisely the valve orifice with respect to the valve sleeve. The housing can be further reduced in size if necessary.

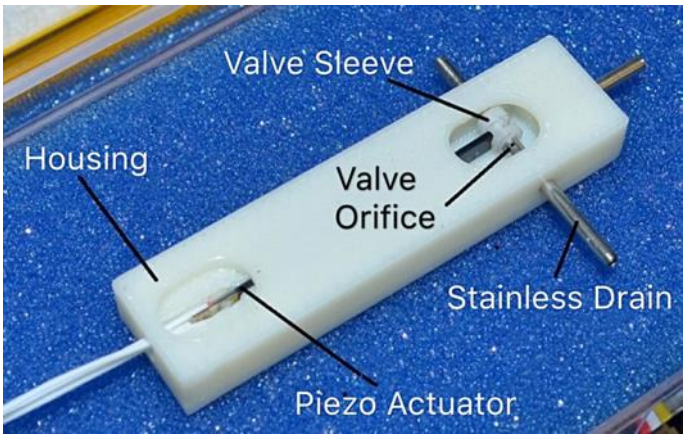

Fig 8-5. The black piezoelectric bender moves the white sleeve to expose the valve opening.

8.3.2 Driver circuit and actuator

My previous colleague Fa Wang and current colleague Chenxiao Guan designed and improved our current driver circuit and actuator system. A simple moving average program uses a Microchip microcontroller (dsPIC33F). This program collects the ICP sensor capacitance readings for 1 min then calculates the average of these readings. Using the average value, the microcontroller sends the output signal to the driver circuit which in turn opens/closes the valve, if needed. The average value is updated each 1 s by removing the oldest 1 s from the 1 min value and adding new 1 s data, using a moving average algorithm. Fig. 8-6 shows the flow chart of this control algorithm.

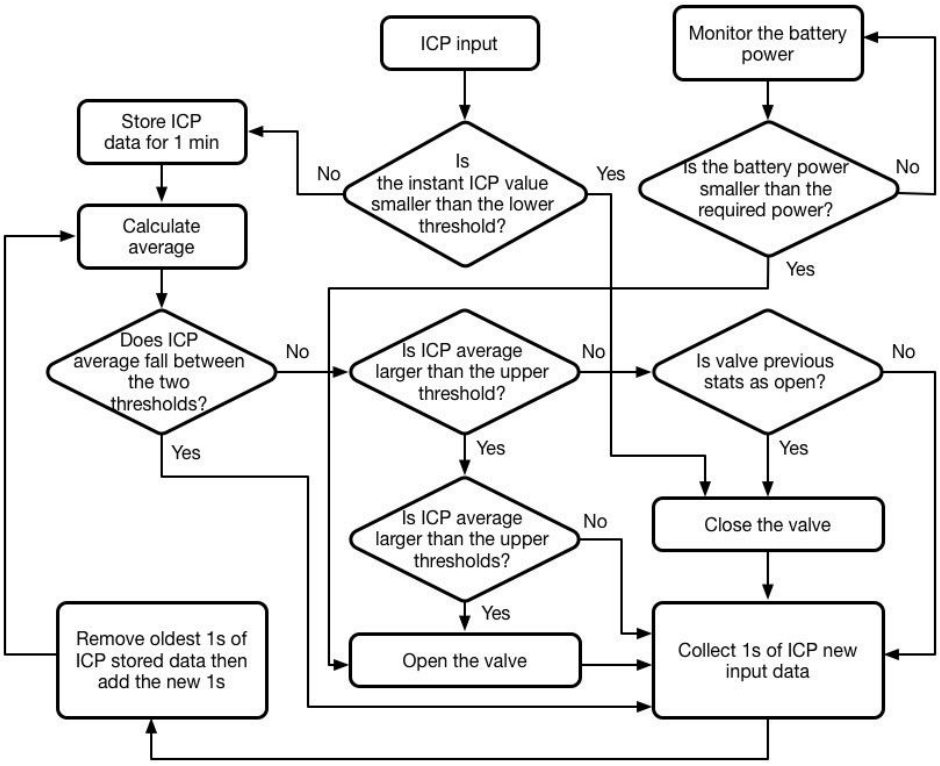

Fig. 8-6. Smart shunt controlling algorithm flowchart

8.4 Communication

My previous colleague Fa Wang developed communication and current colleague Zhe Yang is working to improve communication. The sensor, microcontroller, and shunt valve will operate together so a child can go out and play with no need of an external controller. But an external controller would be useful (1) to measure and report ICP via display or smart phone to parent or physician, (2) to daily measure ambient pressure and correct for any changes in internal ICP.

As shown in Fig. 8-7, a new frequency of 915MHz for communication has been adopted for communication range of over 3 meters. This new UHF RFID frequency is capable of both data communication and wireless energy harvesting. In this RFID communication module, the sensed pressure data will be sent through the active RFID tag and received by the external reader.

The main goal of communication is to transfer the signal to external receiver (can be integrated with the power radiator) while range and stability is the main concern. The RFID technique could

use the same antenna for wireless charging and could penetrate human tissue better than Bluetooth. The concerns are additional module to design and integrate to the transmitting and receiving antenna of the wireless charging module. And the RFID communication frequency could interfere with the charging frequency (they are on one single frequency).

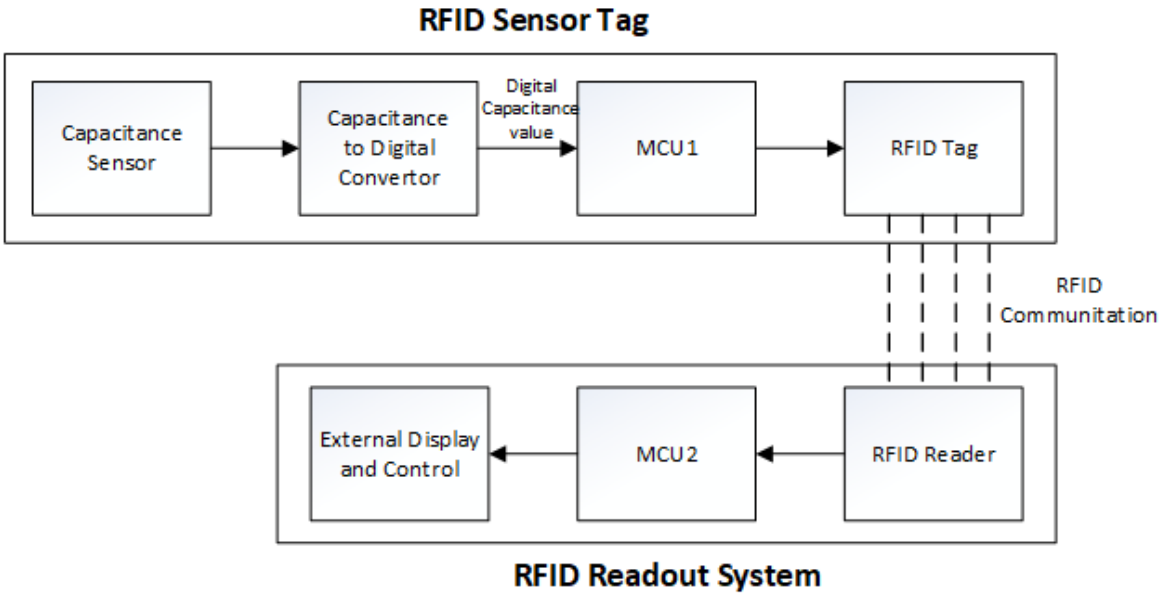

Fig. 8-7. RFID communication system integrated with ICP sensor

8.5 Battery management and remote charging module

My colleague Zhe Yang proposed remote charging module as shown in Fig. 8-8. An external antenna will deliver UHF radiation to the direction of the receiving coil. The receiver end will consist of a rectifier and a battery management circuit that are further monitored by the implanted MCU. The major power consumption is from the wireless transceiver module of RFID tag that is about 25 mA. We will limit the connectivity such that transceiver module is on only when wireless charging is present. The current state of the art miniaturized rechargeable battery has a capability of 38 mAh, which would yield around a week of operating time (only activated when pressure change calls for valve activation). The charging module could charge when the patient is asleep.

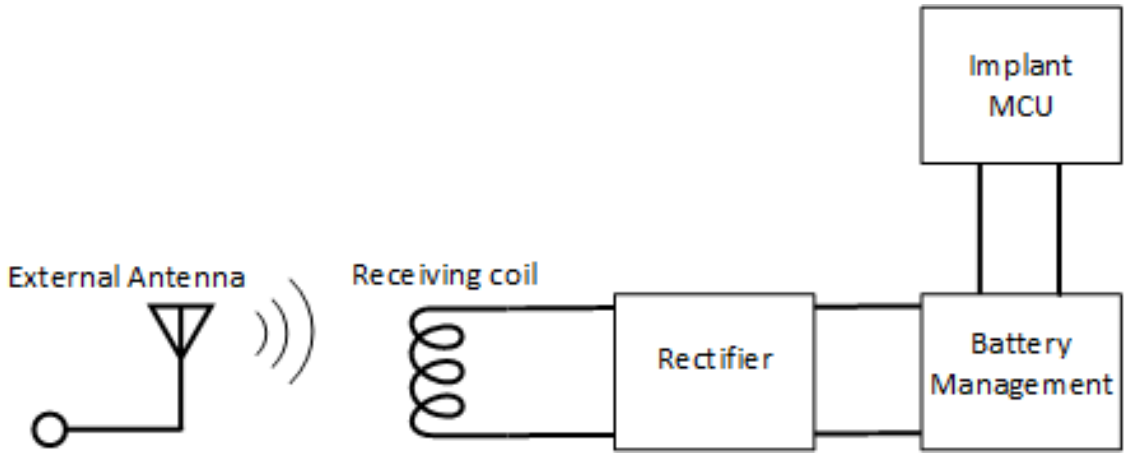

Fig. 8-8. Illustration of charging module and battery management system

8.6 Specific absorption rate (SAR)

We developed a COMSOL stimulation to test our prototype's SAR simulation. The antenna was placed 1 mm away from the left side of the head. Fig. 8-9 demonstrates that spatial peak SAR is less than 5 W/kg as averaged over 1 g of tissue, which is below the IEEE regulations maximal 8 W/kg as averaged over 1 g of tissue and 0.4 W/kg as averaged over the whole body.

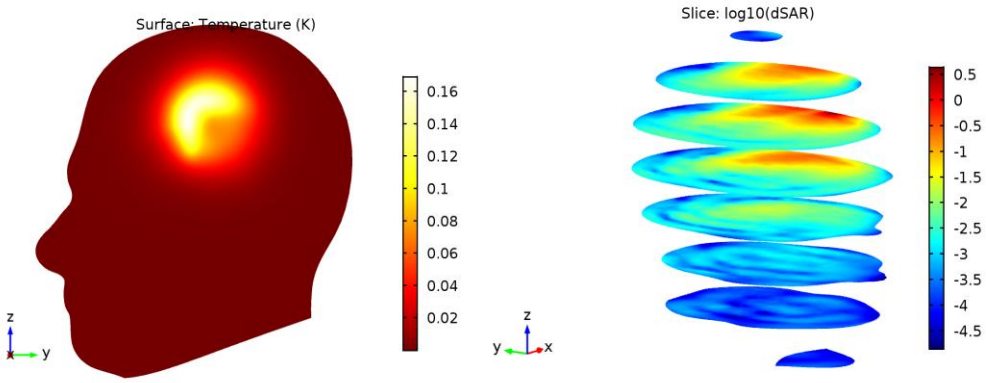

Fig. 8-9. Biosafety simulation result. Left is the simulation model in COMSOL. PCB antenna is placed close to the left side of the human head. Right is the SAR distribution in the head tissue. The result is in log scale.

CHAPTER 9: SENSOR FABRICATION PROCESS

9.1 Mask Design

9.1.1 Passive sensor mask

This passive sensor mask corresponds to the passive sensor design in chapter 6. The mask design layout was drawn using AutoCad software. Two masks had to be made, one to etch the silicon well for the sensor outline, and the other one to place the metal tracks.

The etch mask has the 4 mm × 4 mm wells for the metal coils to fit in. The wells are spaced 0.5 mm apart on all sides. There are cut marks placed between the wells to ensure a straight slicing. When the coils are sliced, the final sensor is 5 mm × 5 mm since there is an extra 0.5 mm on all sides. Also, this space is for the anodic bonding process, which will be introduced later. The etch mask is shown in Fig. 9-1.

When two of the coils are put together to make a sensor, the direction of the turns must be opposite, i.e. one coil must be wrapped clockwise, while the other is counterclockwise. This is so current can flow continuously though the two coils and the mutual inductance will add to the overall inductance. Otherwise, the inductance would subtract, lowering the inductance. Some coils are 3.9 mm × 3.9 mm, leaving a 50 µm gap at all sides from the edge of the etched wells. The other coils with small number of turns are 3.6 mm × 3.6 mm, leaving a 200 µm gap at all sides from the edge of the etched wells. This is to ensure the coils fit entirely inside the wells. Fig. 9-2 shows the coil mask. The process is designed so that only the coil mask needs to be changed to try other inductor designs, allowing for multiple iterations. Each row of the coil mask presents one coil design with a different number of turns, trace width and the spacing width before the adjacent trace. 16 rows show 16 combinations: 150 µm trace width, 150 µm spacing width with 2 turns and 5 turns; 125 µm trace width, 125 µm spacing width with 2 turns and 5 turns; 100 µm trace width, 100 µm spacing width with 2 turns, 5 turns, and 8 turns; 75 µm trace width, 75 µm spacing width

with 2 turns, 5 turns, and 10 turns; 50 µm trace width, 50 µm spacing width with 2 turns, 5 turns, and 10 turns; 25 µm trace width, 25 µm spacing width with 5 turns, 10 turns, and 20 turns.

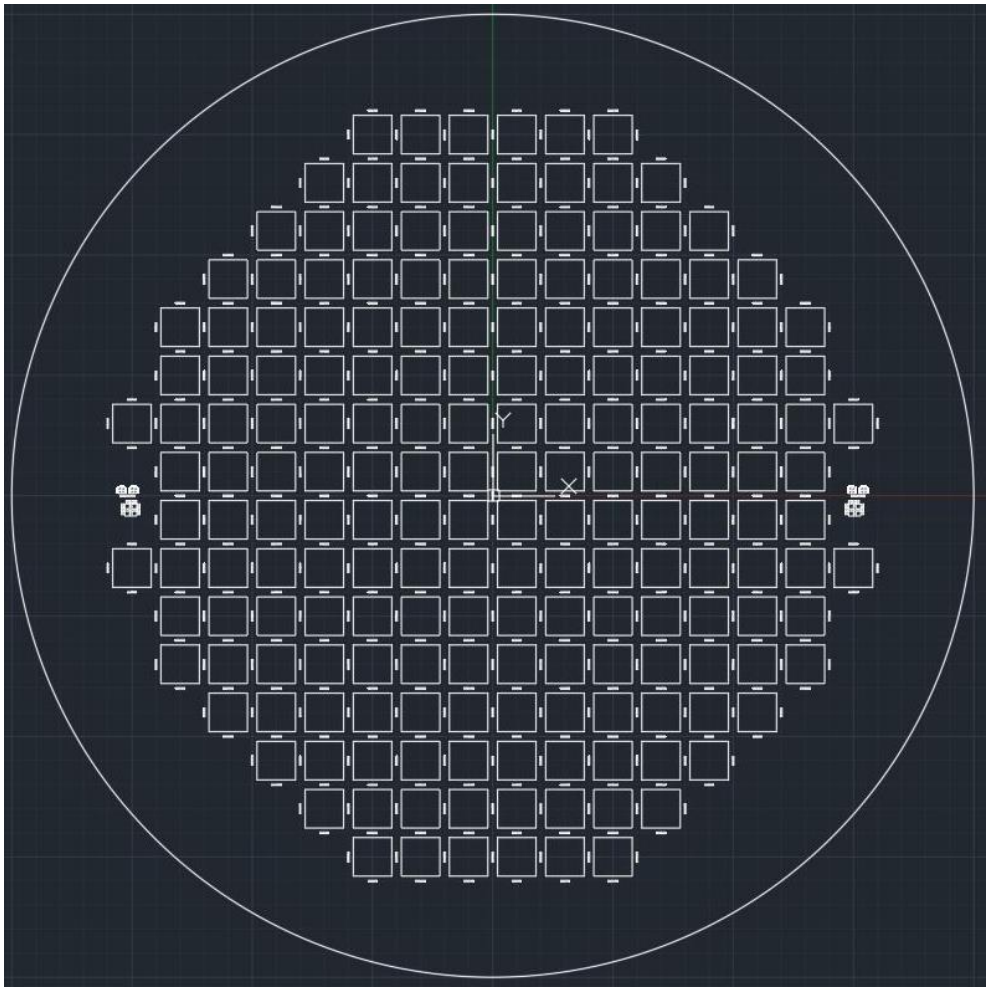

Fig. 9-1. Passive sensor etch mask for creating the sensor wells.

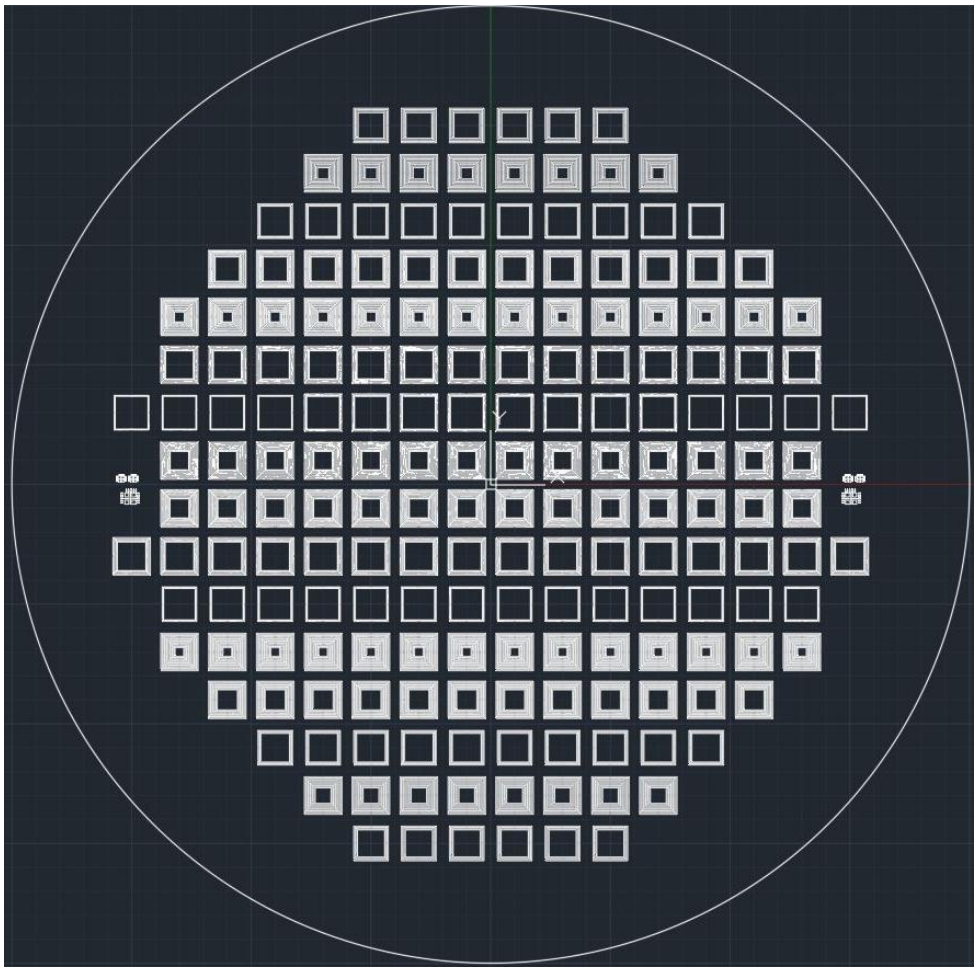

Fig. 9-2. Passive sensor coil mask for creating different combinations of trace width, spacing width, and number of turns

9.1.2 Active sensor mask 1st version

This active sensor mask 1st version corresponds to the active sensor design in chapter 5. The etch mask has the 3 mm × 5 mm/5.5 mm wells for the metal plates to fit in. Each well has 2 channels the on the same side with size of 0.2 mm/0.4 mm × 1 mm/0.5 mm. The wells are spaced 0.5 mm apart on all sides next to the channels sides. There are cut marks placed between the wells to ensure a straight slicing. The etch well mask is shown in Fig. 9-3.

The metal plate mask is shown in Fig. 9-4. The 2.8 mm × 4.8 mm/5.3 mm metal plate is designed to leave 0.1 mm spacing so the wells fit entirely inside the wells. Only one channel has the extended metal plate. This mask is used for both silicon and glass wafers. One side of the metal plate has

only one extended channel to avoid a potential short circuit connection between two metal layers on silicon wafer and glass wafer. Of importance for the metal plate mask, is the symmetry of the metal plates. A vertical line of symmetry is created in the middle of the mask. If the mask is flipped horizontally, the metal plates will line up perfectly, allowing two wafers to be bonded easily as well when one channel has an extended connection metal for the silicon wafer metal plate and the other channel has an extended connection metal for the glass wafer metal plate.

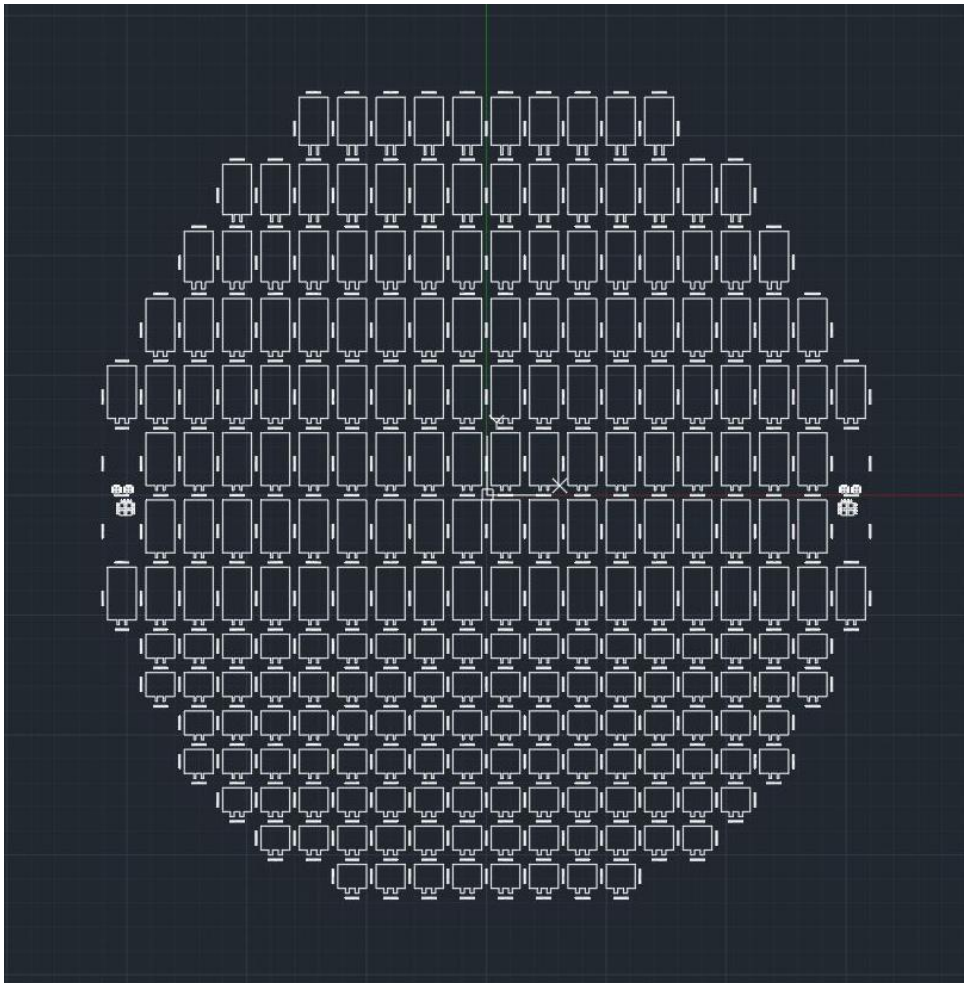

Fig. 9-3. Active sensor 1st version: etch mask for creating the sensor wells.

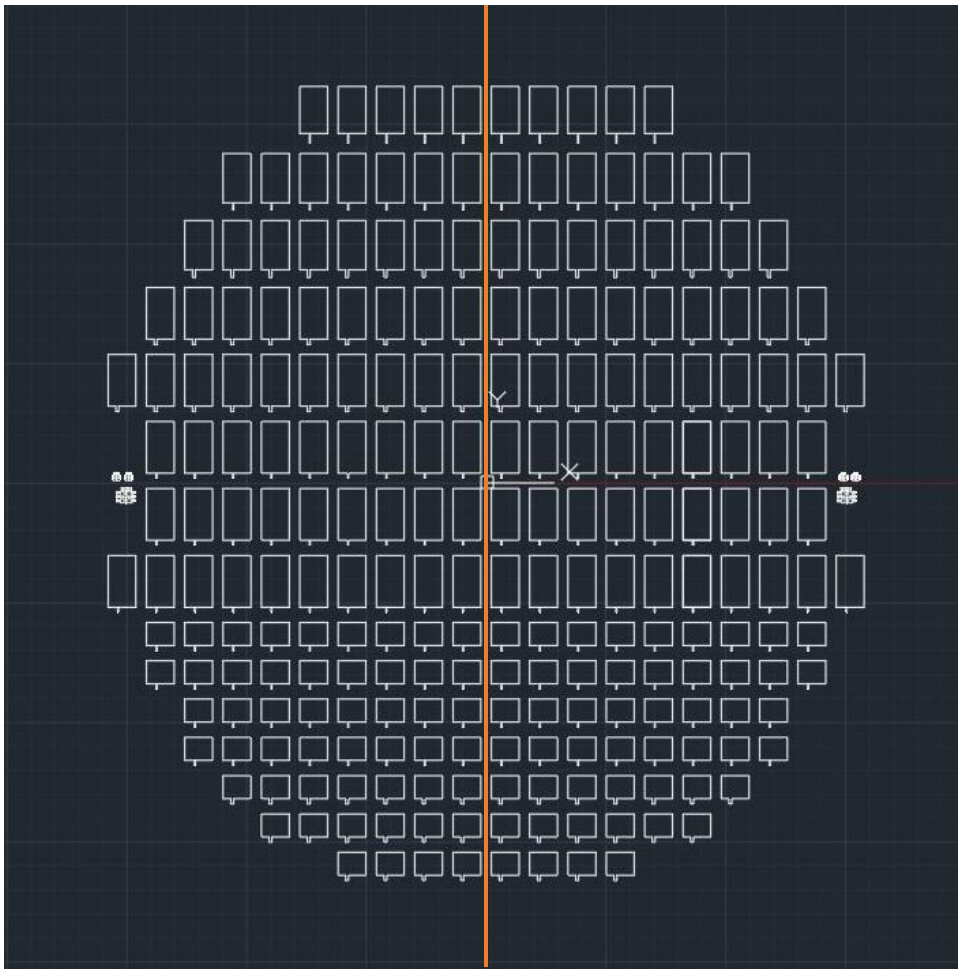

Fig. 9-4. Active sensor 1st version mask for creating metal plates

9.1.3 Active sensor mask 2nd version

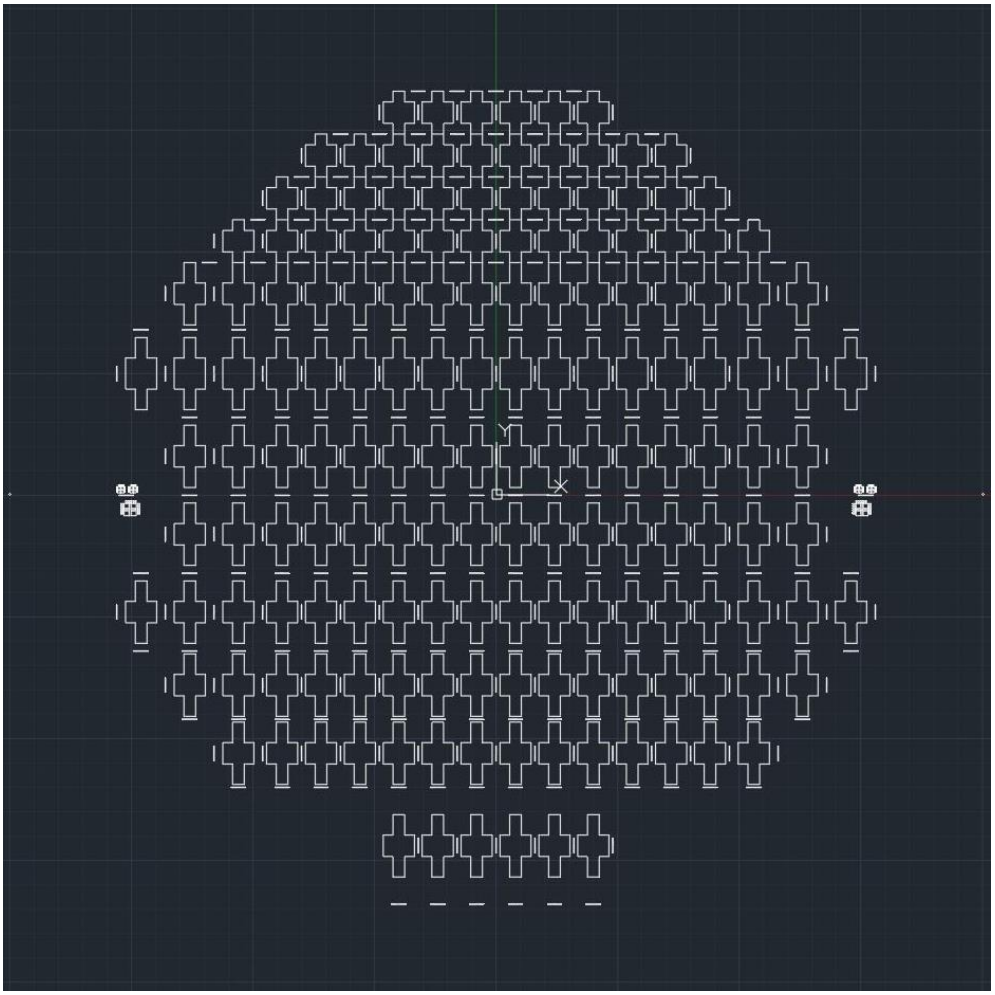

Fig. 9-5. Active sensor 2nd version: etch mask for creating the sensor wells.

This active sensor mask 2nd version corresponds to the active sensor design in chapter 5. To achieve easy and reliable connection, the same side two thin extended connection channels are changed to different side wide channels as shown in Fig. 9-5. The etch mask has the 3.2 mm × 2.2 mm wells for the metal plates to fit in. Each well has 2 channels on the separate side with a size of 1.2 mm × 2 mm. The wells are spaced 0.5 mm apart on all sides. There are cut marks placed between the wells to ensure a straight slicing.

As with the 1st version active sensor, only one channel has the extended metal plate. Considering the metal plates layout and symmetry, one mask is designed for the silicon wafer with the metal

plate 3 mm × 2 mm inside the well and an extended channel of 2.1 mm × 1 mm on the up side, another mask is designed for the glass wafer with the metal plate 3 mm × 2 mm inside the well and an extended channel of 2.1 mm × 1 mm on the down side as shown in Fig. 9-6(a) and Fig. 9-6(b). (the reverse is also fine)

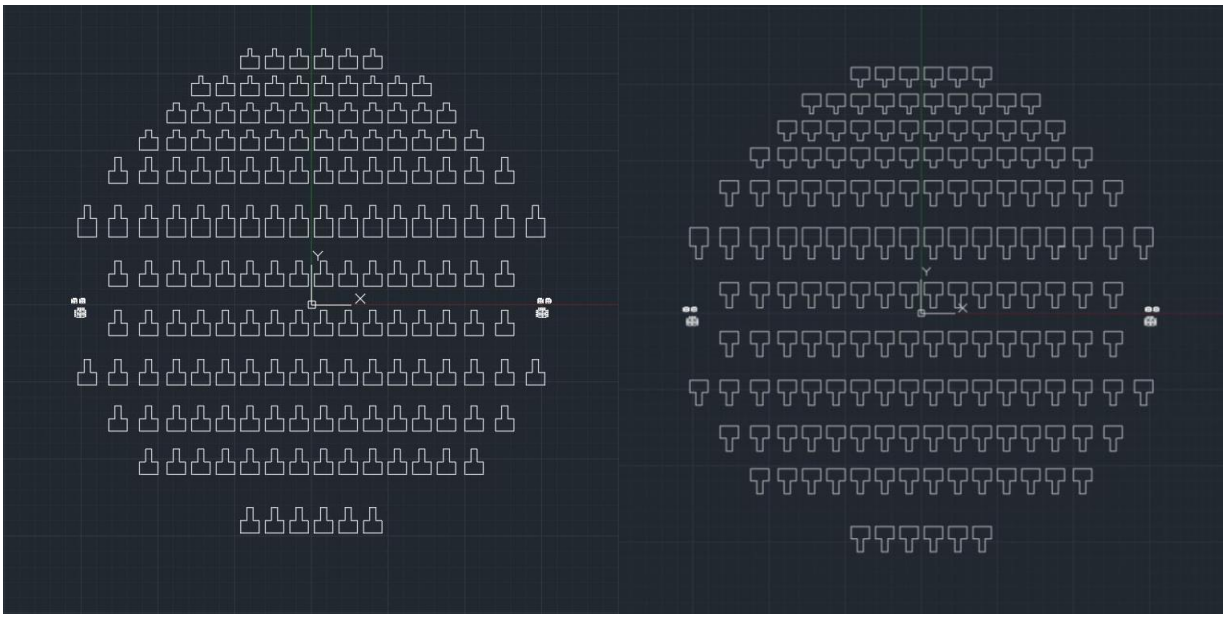

Fig. 9-6. (a) Active sensor 2nd version mask for creating metal plates on silicon wafer

Fig. 9-6. (b) Active sensor 2nd version mask for creating metal plates on glass wafer

9.1.4 Mask Alignment Mark

The alignment mark is important to make sure the different layer patterns are in the same desired positions. There must be two alignment marks, one on each side of the wafer, and these must permit accurate alignment in the *x*, *y*, and theta orientations. In addition, the alignment mark must fit within the field of view of the microscope objectives. A cross alignment mark is used for our wafers as shown in Fig. 9-7(a) and Fig. 9-7(b). Both the cross and the verniers are used to check accurate alignments. It is important to check that the alignment mark location and the die size are compatible.

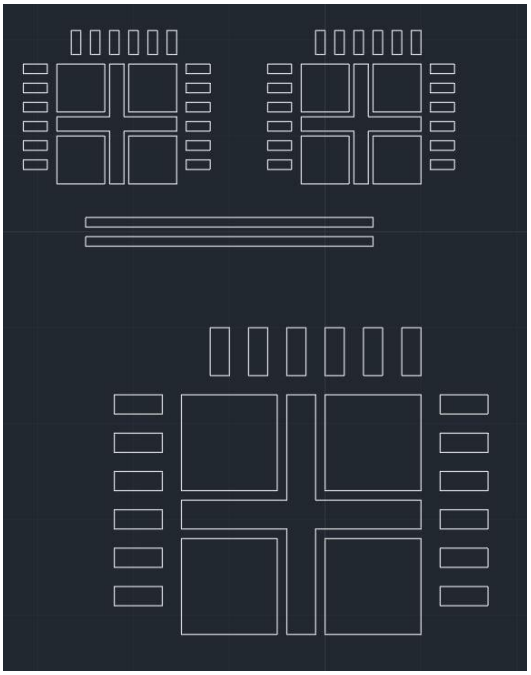

Fig. 9-7. (a) Alignment Mark for creating wells on the silicon wafer

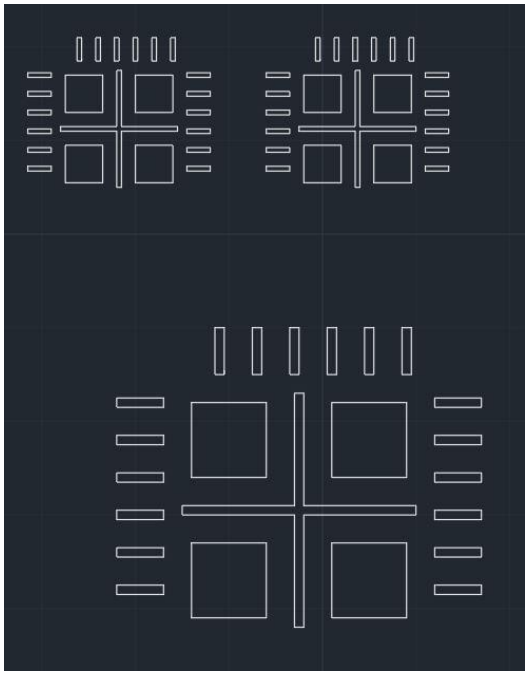

Fig. 9-7. (b) Alignment Mark for creating metal plates on silicon/glass wafers

9.2 Passive sensor fabrication procedure – structural sequence summary

The entire fabrication process contains 10 main steps. Each step needs to be handled carefully and cautiously. Fine tuning parameter values of every step has become the most challenging task to develop a working sensor prototype.

9.2.1 Deposit nitride layer onto silicon wafer

Silicon nitride, Si_3N_4, is used to create a "hard" mask as shown in Fig. 9-8. Often in harsh processing conditions, for example wet chemical etches, photoresist is unable to withstand the environment and thus adequately transfer the pattern into a physical structure on the wafer. In this case we use a nitride hard mask to create the wells that form sensor cavities, as the processing occurs at a high temperature and pH.

Using photoresist to create the pattern and subsequently etching the not covered Si_3N_4 areas to transfer the pattern into the nitride layer, we create the hard mask for the next step. Photoresist is removed before proceeding to the next step, leaving just the patterned nitride layer in place.

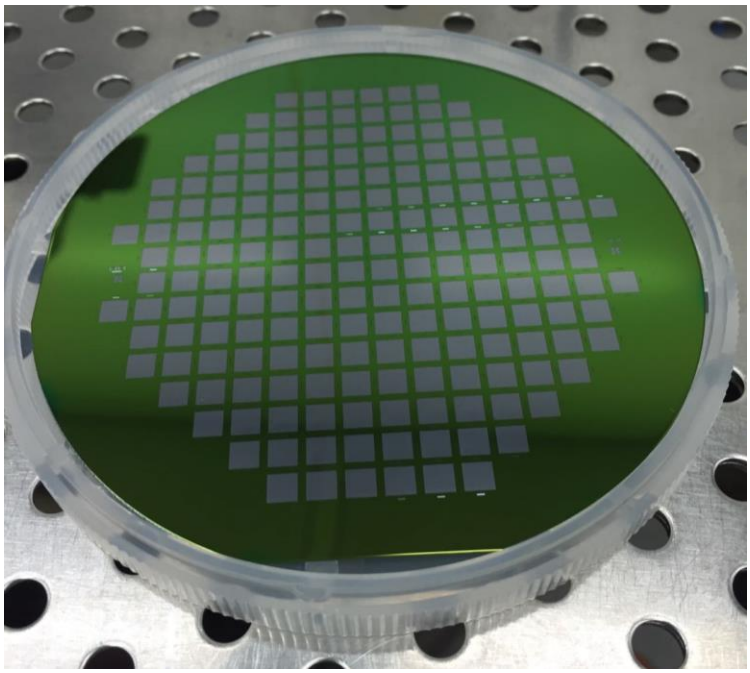

Fig. 9-8. Si wafer with nitride hard mask

9.2.2 Etch wells in the silicon wafer

Using a KOH bath, the silicon gets anisotropically (preferentially in the down direction) etched to create wells in the silicon layer as shown in Fig. 9-9. While it is also possible to etch Si using dry plasma methods, those tend to roughen the surface and make it unsuitable for metallization.

The KOH will etch along crystal planes as illustrated in Figure 9-10, this is the reason that we chose a <100> wafer. The angle between the bottom of the well and the side wall is 125.26°. Essentially, KOH preferentially attacks the <100> crystal plane, and etches the slowly exposed <111> plane at a much slower rate. Of course, if a wafer were to be left in the solution long enough, eventually all of it would be etched away. There is a slight amount of undercutting (etching underneath the mask) that happens with this process, so the final structure is slightly larger than the pattern (but negligibly so in our case). The deepest a silicon wafer could be etched is dependent on the width of the cavity due to the crystalline structure. The etching follows the crystal structure,

causing it to go at an angle of 30°, instead of straight down. Therefore, the smaller the width, the shallower the etching can be (Efremov and Svettsov 2002).

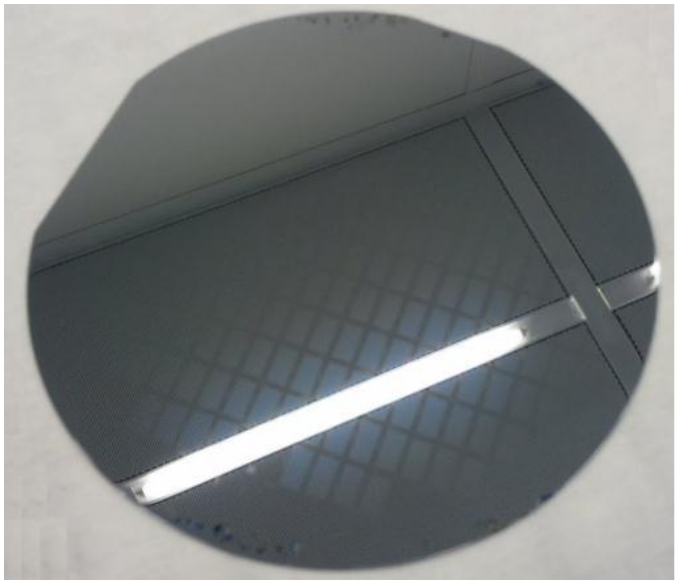

Fig. 9-9. Si wafer with wells, reflecting ceiling

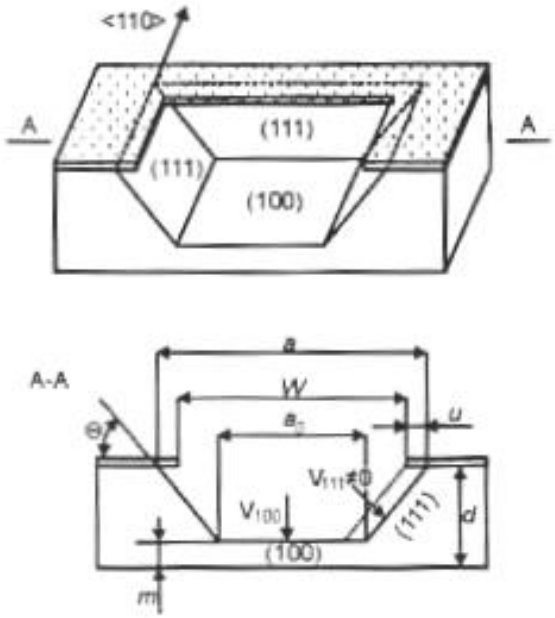

Fig. 9-10. Geometric properties of a KOH Si etch

9.2.3 Insulation layer on silicon well

As discussed in chapter 6, adding an insulator layer between the copper and silicon can improve the sensor performance. A thin insulation layer is deposited on etched silicon wells using the

TYSTAR Oxidation Furnace machine. The result of this step is shown in Fig. 9-11(a). Subsequently a dip of HF bench, filtered 6:1 Buffered oxide etch (BOE) solution is used to remove the SiO_2 on Nitride part. Then the whole wafer with Si_3N_4 and SiO_2 is put in the Nitride wet bench, a phosphoric acid process tank at 170 °C for stripping Si_3N_4. The result of this step is shown in Fig. 9-11(b). The hard mask is removed as it is no longer necessary for further steps (with this fabrication plan). Also, we need a pure silicon surface to realize anodic bonding later. Even though there is also a dry etching method to remove nitride, we use a wet etch method in phosphoric acid. This is to ensure that no nitride remains anywhere on the wafer – in this case on the wafer edges, back side or between the wells. In addition, using dry plasma methods to remove Si_3N_4, may tend to roughen the surface and make it unsuitable for future bonding.

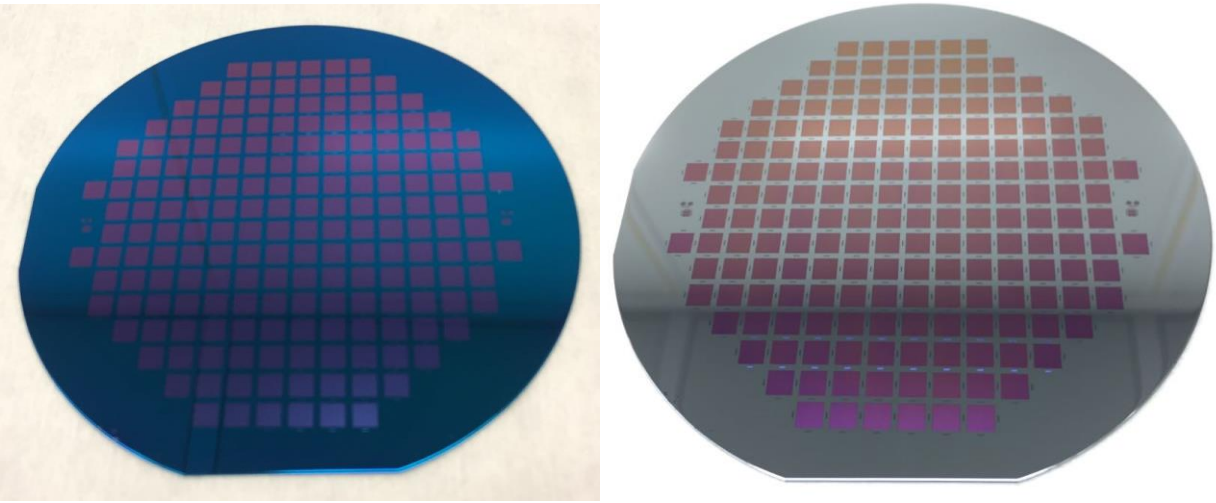

Fig. 9-11. (a) Si wafer with SiO_2 layer **(b)** SiO_2 layer on silicon wells

9.2.4 Create 300 nm seed metal tracks in silicon and glass wafers

Again, photoresist is used to create a pattern, this time covering all the areas that we do not want covered with metal. During the metal evaporation step that follows, the spaces between photoresist tracks get covered with metal, as well as the tops of the photoresist as shown in Fig. 9-12. This

photoresist can be removed later in the liftoff procedure as the photoresist is removed with acetone, taking the metal resting on top of it with it and leaving a pattern in the metal.

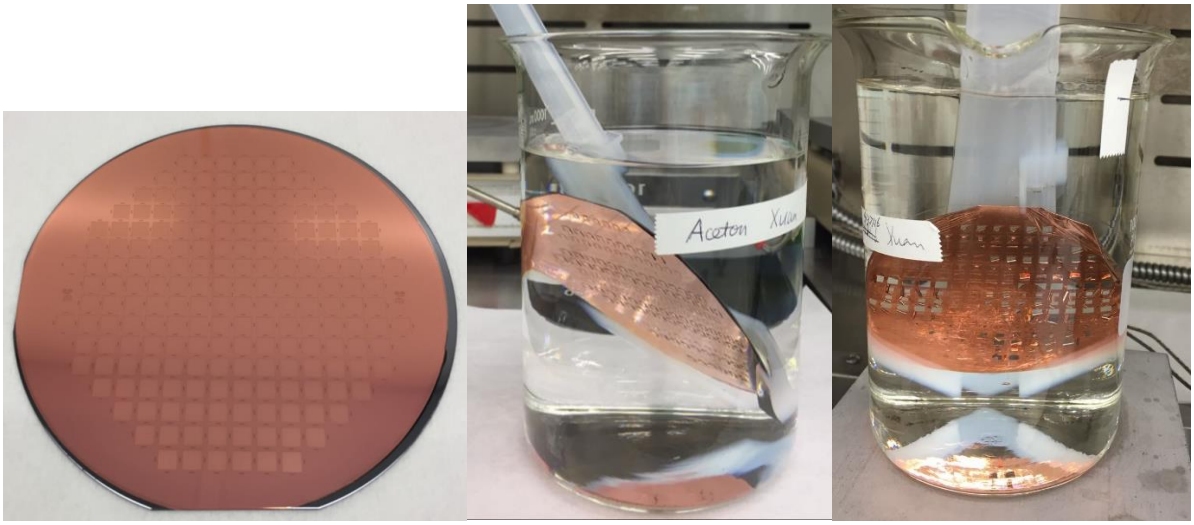

(a) **(b)** **(c)**

Fig. 9-12(a). Metal evaporation covers the spaces between photoresist tracks **(b)** wafer liftoff process **(c)** wafer undergoing liftoff process with 75 °C acetone

9.2.5 Realized final metal thickness

9.2.5.1 Electroplating silicon and glass wafers to final metal thickness

To increase metal trace thickness to the final 20 μm, Cu electroplating equipment outside the cleanroom is tried first using a power supply, and the wafer cathode plus copper sheet anode are immersed in the plating solution for previous electroplating equipment as shown in Fig. 9-13(a). A holder is used in current electroplating equipment as shown in Fig. 9-13(b). This is performed outside of the clean room, as the materials used are not allowed inside due to contamination concerns, so care must be taken to not introduce extra particles onto the wafers during transport and plating. The quality of electroplating is affected by many factors, such as stress of materials, uniformity of plating layer, temperature, current control and timing, which need to be carefully adjusted.

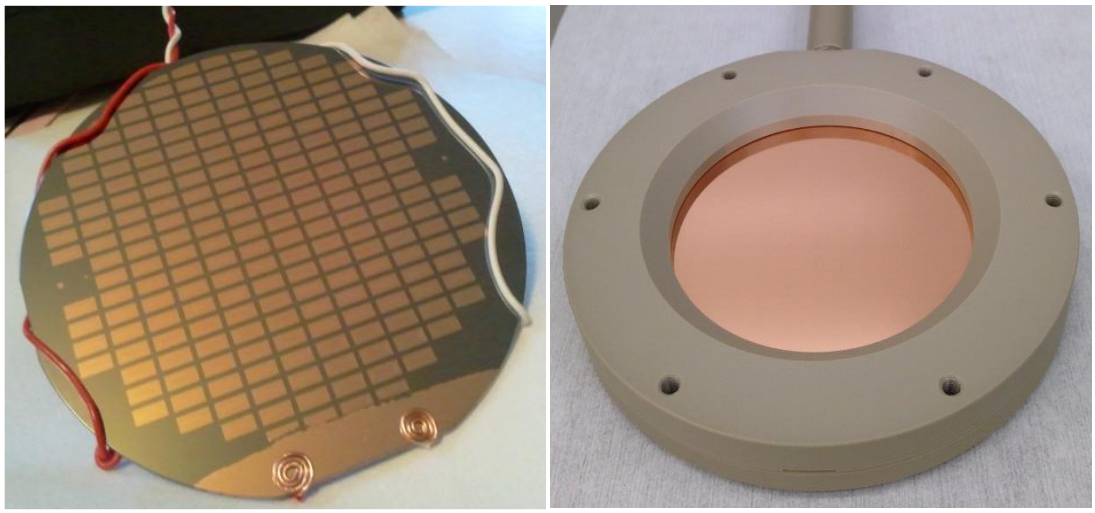

Fig. 9-13 (a) Si wafer set up for Cu electroplating of previous equipment **(b)** Si wafer set up for Cu electroplating with holder for current equipment

9.2.5.2 CVC sputtering silicon and glass wafers to final metal thickness

Subsequently, CVC-sputtering deposition inside the cleanroom is used to increase Cu trace thickness up to 20 µm, as well as place a thin 100 nm adhesion Cr layer onto both silicon and glass substrates in vacuum to achieve more uniform surface and higher quality of deposited Cu layer as shown in Fig. 9-14.

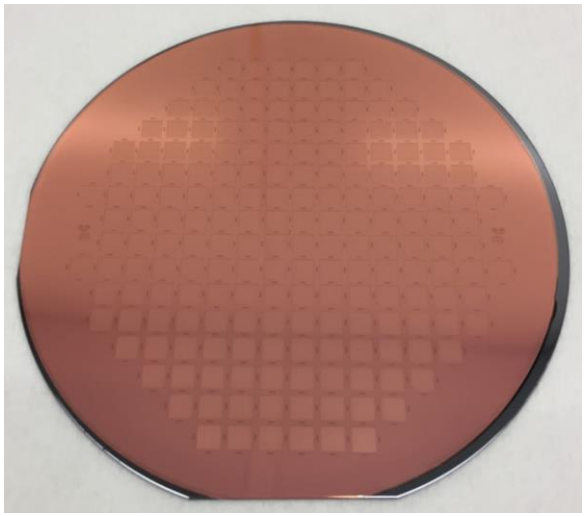

Fig. 9-14 CVC-sputtering high-quality Cu on silicon wafer

9.2.6 Etching metal layer to trim to final shape on both Silicon and glass wafer

A designed photoresist (PR) mask is used to realize the desired metal patterns as shown in Fig. 9-15(a) and Fig. 9-15(b). Copper Etchant APS-100 is used to etch Cu, then form the desired Cu coils structures (patterning). Cr etchant recipe on PlasmaTherm 770 Inductively Coupled Plasma is used to etch Cr with a designed photoresist mask. Because of the undercut effect of wet etch, two etch processes are tried to realize better pattern feature. The first round etch is for the silicon well part and the second round etch is for the metal coils pattern inside the well. In this way, a fine result of Cr and Cu metal coils is shown in Fig. 9-16.

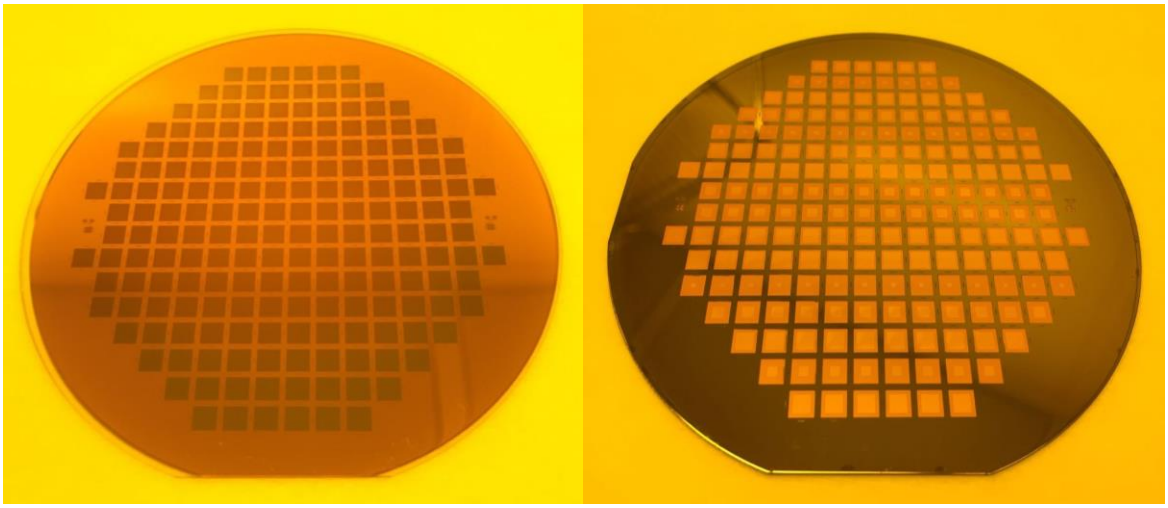

Fig. 9-15. (a) PR on Cu wells on glass wafer **(b)** PR on Cu coils on silicon wafer

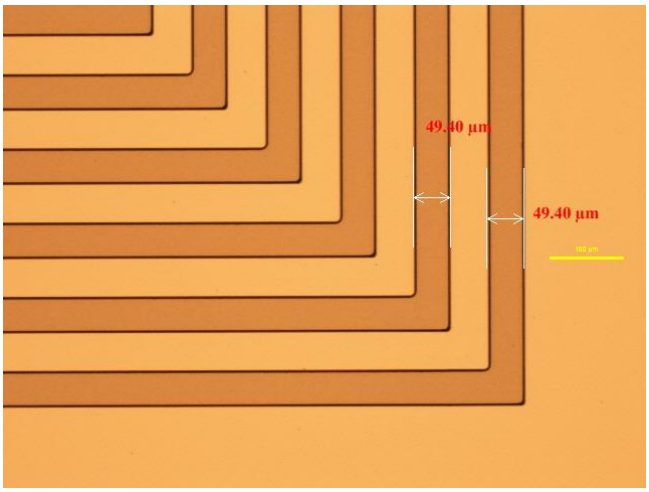

Fig. 9-16. Metal trace result after Cu and Cr etching

9.2.7 Yield calculation on Silicon and glass wafer

Under a microscope, a map of continuous coils without shorts between the tracks must be noted for both the Silicon and glass wafers. This is important to later distinguish sensors that are electrically sound from those that will never yield a functioning sensor due to voids in the tracks or shorts between them. Once the two wafers are bonded there is no way to tell, other than by measuring resonant frequency, at which point an element of uncertainty is added as to why the sensor failed – due to processing before bonding, or processing after bonding, or due to receiver mistakes. Troubleshooting can be more difficult if this step is skipped.

9.2.8 Anodic bonding

Anodic bonding is the suitable and necessary method for the sensor since it has strong bonding quality and the biocompatibility requirement for our project. Table 9-1 shows the comparison result between direct bonding and anodic bonding. Using heat and voltage, the glass and silicon wafers are bonded together under vacuum to create a single piece with sensor cavities.

Usually to avoid undesirable debris on the wafer, a combination of solvent spin cleaning and RCA-1 solution are used to clean the wafer before bonding. RCA-1 is a procedure for removing organic residue, particle and films from silicon wafers. The decontamination works based on sequential oxidative desorption and complexion with H2O2-NH4OH-H2O. However, RCA-1 solution will also attack the Cu layer on both silicon and the glass sample. Acetone, Isopropyl alcohol (IPA) and water are used to clean wafer before bonding instead of RCA-1. The pure cleanness of both bonded surfaces on silicon and glass layer is the key point to realize a fine bonding result. Attention should be paid to every step before bonding to yield a clean surface. Any residues/particles may lead to failure of the whole anodic bonding process though sometimes

interfering particles can just cause voids, but do not prevent the rest of the wafer from bonding, as shown in Figure 9-17. The aligner machine is needed before bonding to guarantee the two layers' coils were aligned well. Figure 9-18(a) shows the anodic bonding machine system overview and Figure 9-18(b) shows the bonding assembly for anodic bonding.

Table 9-1. Comparison between direct bonding and anodic bonding

Method		Process parameters	Remarks
Direct bonding	Plasma-activated	115–400 °C, N_2=O_2 plasma activation of the surface	Weak bonding, the quality of the bonding process can be improved by annealing at 600 °C
	Fusion bonding	650 °C	Strong bonding, special attention must be given to the plastic flow of the glass
Anodic bonding		305–350 °C, 0.05 MPa, 1000 V	Strong bonding with a good yield can be performed over SiO_2 layers (up to 600 nm thick)
		First bonding: 305–350 °C, 0.15 MPa, 1000 V Second bonding: 450 °C, 0.3 MPa, 1500 V	First bonding must be incomplete in order to keep the glass wafer conductive at relatively high temperature

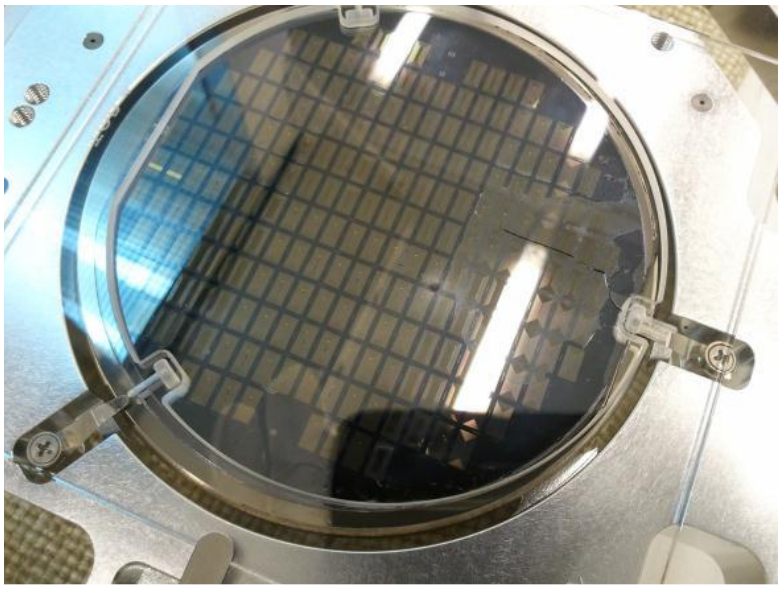

Fig. 9-17. Anodically bonded glass and Silicon wafers on chuck for aligned bonding, with flags retracted. Bottom right flag failed to retract, creating a crack and large void. Wafer could still be diced away from the affected area though

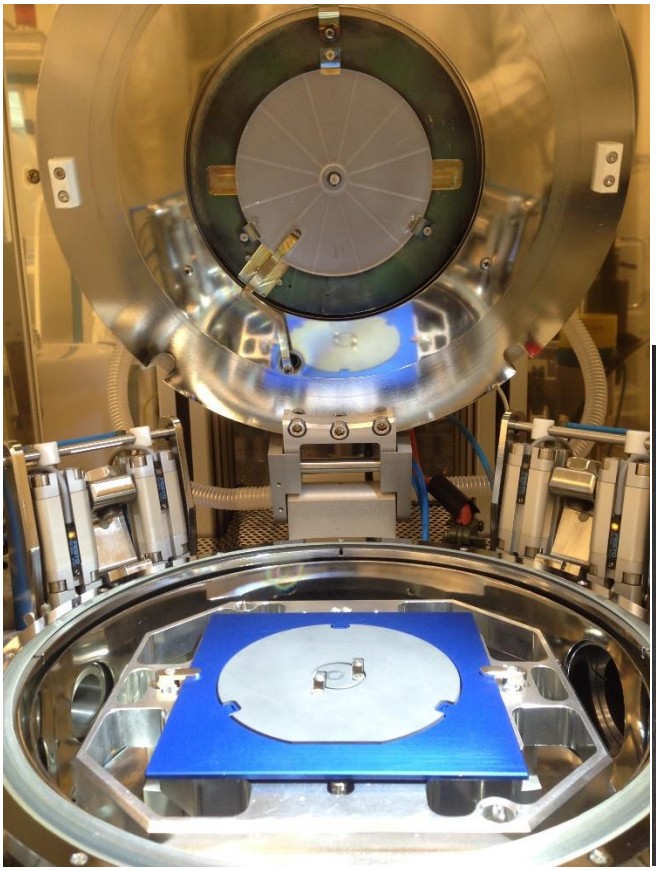

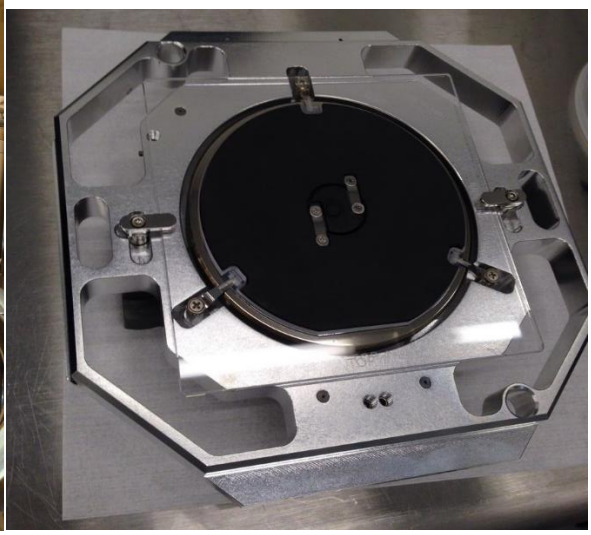

Fig. 9-18(a). Anodic bonding system overview **(b)** Anodic bonding assembly

9.2.9 Dicing

The final sensors are obtained by sawing the wafer stack into corresponding pieces. Currently each sensor is 5 mm × 5 mm in size. The dicing saw inside of the Wisconsin Center for Applied Microelectronics (WCAM) is used to cut the whole 4 inch diameter bonded wafer into multiple small pieces as shown in Fig. 9-19. The wafer is mounted with the Si membrane side facing downwards onto the blue tape. This way the dicing marks can be seen through the glass side. Only saw #1 in the cleanroom can currently cut through such a thick stack, and one that includes glass, but check that the blade type installed is correct, and the spin speed is set to low. It is a good idea to keep the finished diced sensors on the blue tape, so that the sensor type and quality (functionality) of each remains documented.

Outside of the WCAM facilities there are laser cutting instruments that could create any shape sensors, if so desired. However, this takes more time and costs more.

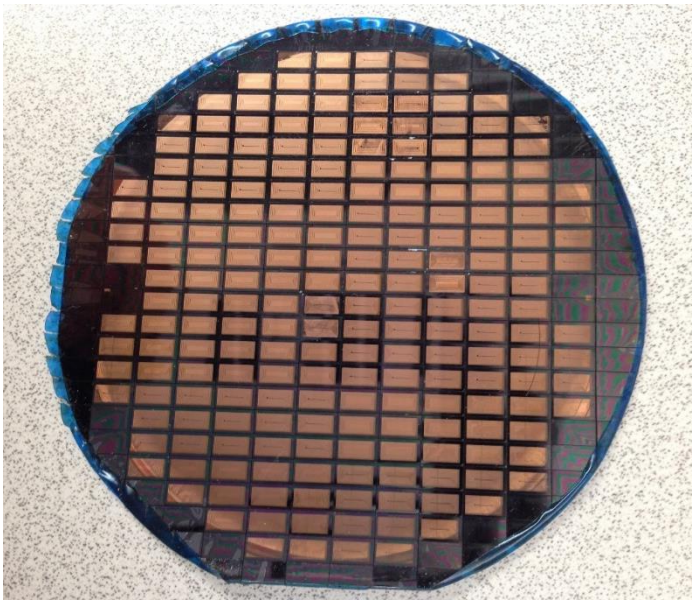

Fig. 9-19 Diced multiple sensors of silicon layer used dicing saw tool

9.2.10 Silicon layer desired membrane thickness realization

The STS Multiplex Deep Silicon (Reactive-Ion Etching) RIE machine is the best option to yield thin silicon membrane. As a reactive ion etcher, plasma is inductively coupled, has low density, and has low pressure. Ion energies are low. The STS Tool can alternate cycles of etching and passivation. The result of STS is good anisotropy in very deep (250 μm or greater) Si etch trenches. However, because metal is not allowed in our university STS machine, an alternative method is the grinding machine shown in Fig. 9-20(a) and Fig. 9-20(b).

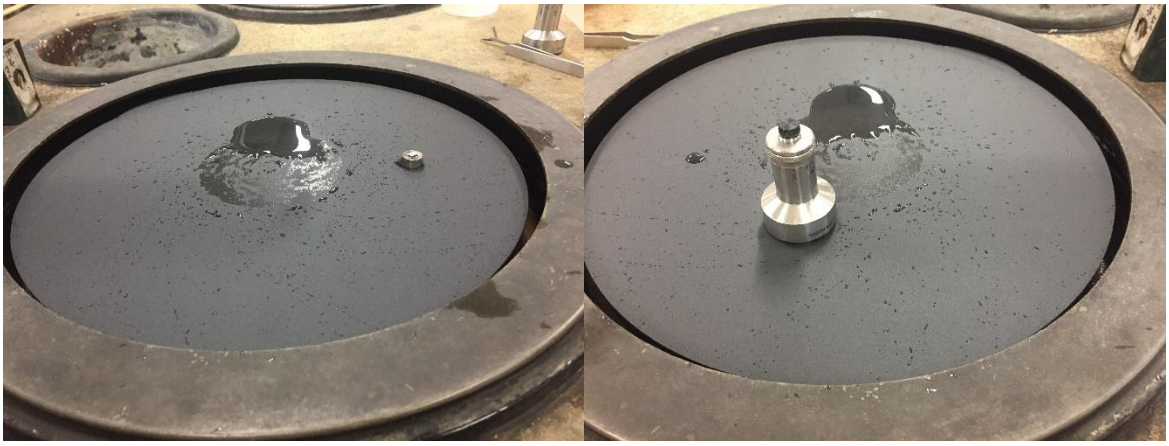

Fig. 9-20 (a) Sensor sample mounted on the tool for grinding **(b)** Grinding tool overview

9.3 Active sensor fabrication procedure – structural sequence summary

The entire fabrication process contains 9 main steps. As for the passive sensor fabrication process, both careful handling and fine-tuning parameters are needed to realize a working sensor prototype.

9.3.1 Deposit nitride layer onto silicon wafer

As for passive sensor fabrication method, the silicon wafer is cleaned in the prefurnace bench before putting in the TYSTAR Nitride Furnace machine. The prefurnace bench is a flow hood and chemical bench for preparing substrates before thermal processing, for example in the low pressure chemical vapor deposition (LPCVD) or oxidation furnaces. The four process tanks are: Piranha

bath; ammonium hydroxide/hydrogen peroxide; hydrochloric acid/hydrogen peroxide; and hydrofluoric acid.

9.3.2 Etch wells in the silicon wafer

The active sensor style does not require as deep KOH wells as the passive sensor (50 μm ~ 70 μm). The passive sensor needs a thick metal trace to decrease the resistance value in order to realize a sensitive resonant tank. The active sensor uses a wire connection method to yield a reliable connection; only two thin metal plates are needed to place in the well to hold electrical charge. Then 5 μm ~ 10 μm thickness wells are etched for the active sensor as shown in Fig. 9-21.

Fig. 9-21. Si wafer with wells

9.3.3 Insulation layer on silicon well

As for the passive sensor, a thin insulation layer is added between silicon and the thin metal plates. The SiO_2 layer has different growth rates on silicon and the Si_3N_4 substrate. Subsequently, the unwanted SiO_2 layer on Si_3N_4 is removed by a quick dip in the HF bench, then the Si_3N_4 mask as well as the backside Si_3N_4 layer is etched in the Nitride wet bench.

9.3.4 Deposit metal plate on silicon and glass wafers

The glass wafer is cleaned in the piranha bench before PR spinning and metal deposition. The Piranha bench is a heated sulfuric acid and hydrogen peroxide solution tank for removing organic material. Then photoresist is used to create the desired pattern on both silicon and glass wafers. PR covers all the areas where we do not want metal deposition. Then a metal evaporation will deposit a Au layer as well as a Cr adhesion layer. Subsequently, a liftoff process is done for both silicon and glass wafers to yield the desired metal plate pattern we want. Fig. 9-22 (a) shows the silicon layer with Au in the well after liftoff and Fig. 9-22 (b) shows the glass layer with Au after the liftoff process. Attention needs paid to make sure no PR/metal remains on the boundary and yields cleanness of both surfaces.

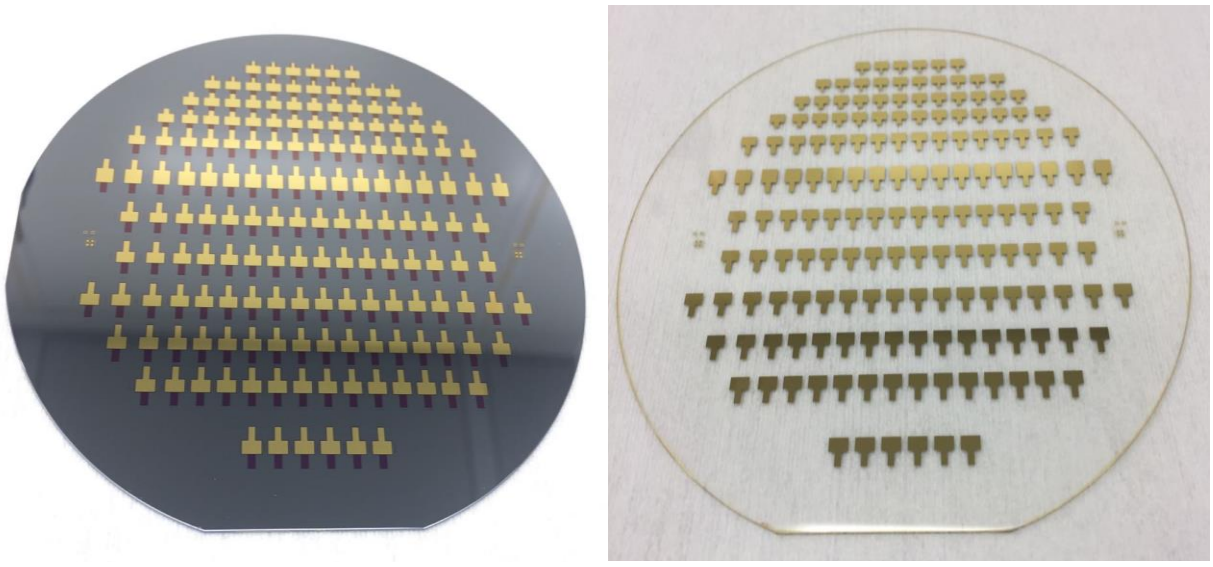

Fig. 9-22. (a) Silicon wafer with Au after liftoff **(b)** Glass wafer with Au after liftoff

9.3.5 Yield calculation on Silicon and glass wafer

As for the passive sensor, under a microscope, both silicon and glass wafer with multiple metal patterns integrity are checked and marked before bonding. It is important to later distinguish sensors functionality after bonding.

9.3.6 Anodic bonding

As for the passive sensor, anodic bonding is used for active sensor bonding because of the strong bonding quality and biocompatibility properties. Fig. 9-23(a) shows the successful bonding sample. Fig. 9-23(b) shows the unsuccessful sample because of the particle/residue left on the boundary. Besides the cleanness of the surfaces, perfect alignment of the two layers is another key point to yield anodic bonding. The alignment markers with the help of the green cross marks under microscope view is shown in Fig. 9-24.

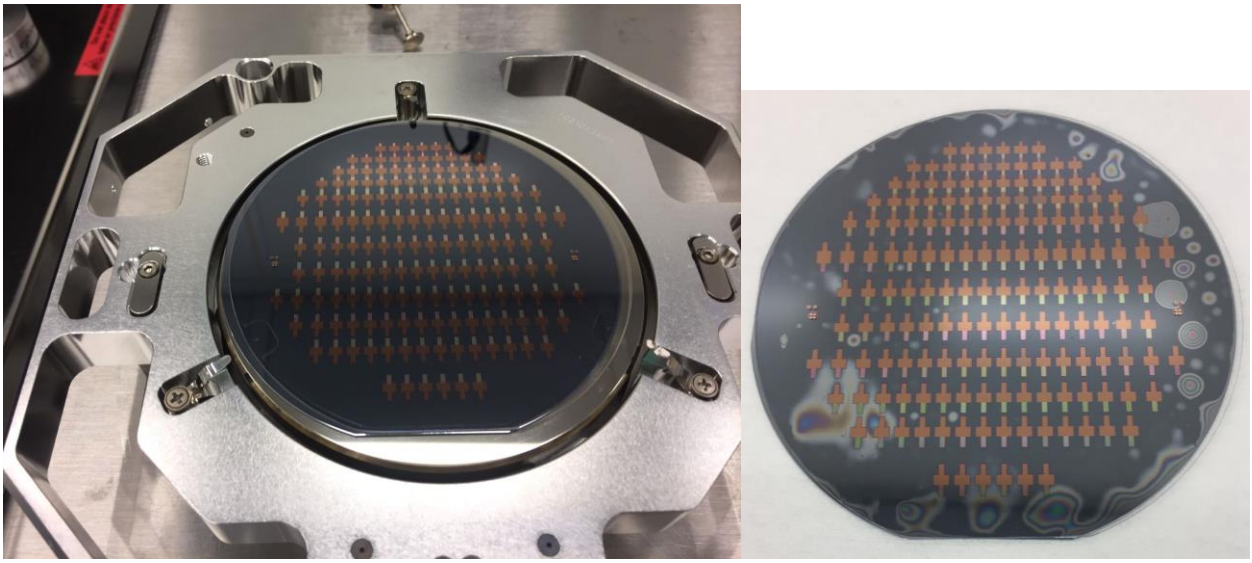

Fig. 9-23 (a) Successful active sensor style sample for silicon and glass wafers **(b)** Unsuccessful sample

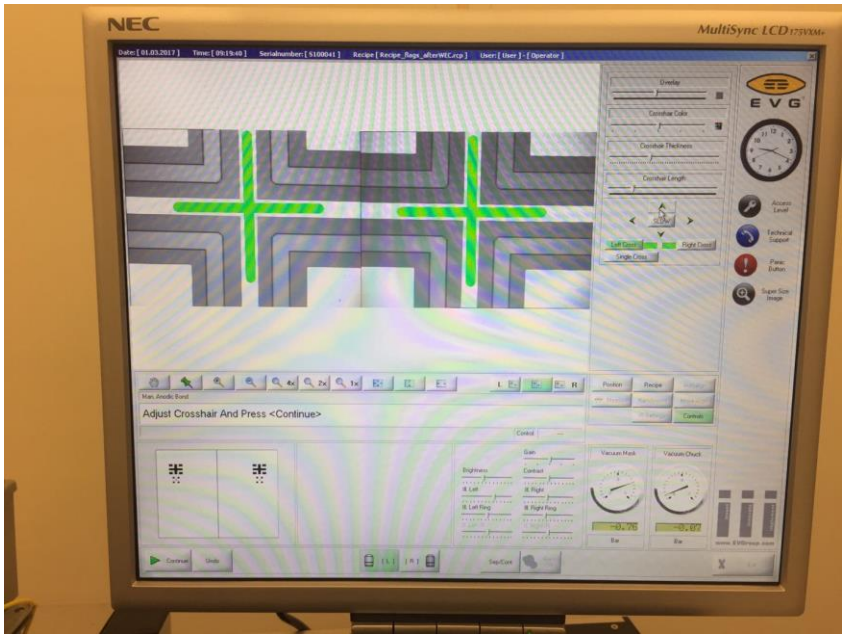

Fig. 9-24 Alignment marks under microscope view of aligner machine before bonding

9.3.7 Dicing

The final sensors are obtained by sawing the wafer stack into corresponding pieces using a programmable high-speed blade. Currently the sensor die is either 4 × 6 × 1.1 mm or 4 × 3 × 1.1 mm. Fig. 9-25 shows a piece of sensor after dicing.

The pieces do not tend to stick very well once the perpendicular cut is made to detach them, probably due to the rather intense water jet that cools the saw. The cover of the saw can be taken off and there is a screen trap that traps escaped sensors, with the caveat that their identity from the original yield calculation may not be re-traceable. The saw blade is much wider than the dicing marks, necessitating a test cut at the edge to fully align the wafer. The dicing marks need to be centered within the saw blade cursors, rather than at the edge. Additionally, when the saw skips to the next index, it is not very reliable and needs adjustments every time, so do not cut wafers in automatic mode. It can also decide to freeze during one of these adjustments, in which case the spindle needs to be stopped before resetting the system.

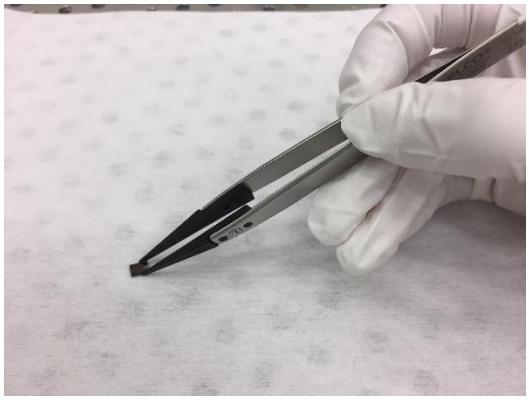

Fig. 9-25 A piece of sensor after dicing

9.3.8 Silicon layer desired membrane thickness yield

Similar to passive sensor, a grinding tool polishes the thick silicon layer of the active sensor to a 50/100 μm thin silicon membrane to decrease the sample thickness from 1.1 mm to 0.55/0.61 mm.

9.3.9 Side connection metal pads deposition

To connect between two metal plates and the external sensor electronics, we have designed extended channels with a separate extended metal layer on the silicon and glass layer. Then a CVC sputter machine with a special holder deposits a Cu layer on the side wall of the active capacitive sensor as shown in Fig. 9-26.

Fig. 9-26 Special holder put in chamber to fix the samples and expose sidewalls of the sensors

9.4 Detailed fabrication information inside the WCAM

9.4.1 Passive sensor: silicon layer fabrication

Table 9-2. Silicon wafer fabrication details for passive sensor

Silicon Layer Process	Bay	Instruments
1. Clean silicon wafer Take an unprocessed wafer only Can leave overnight right before the HF dip Setup time: 15 min for tanks to heat up Process time: approx. 2 h	Furnace	RCA / prefurnace clean
2. Nitride deposition Deposit a hard mask used for the KOH etch because photoresist will not hold up to that process Will need 4 baffle wafers (2 ahead and 2 behind your wafer) Recipe: STDNIT.002 Parameter: Deposition time is 30 min for 2400–2600 Å thick film, deposition rate around 80 Å/min Process time: approx. 2.5–3 h until wafer unload Check film thickness through either approx. deposition time + color or through the filmetrics	Furnace	Nitride furnace Filmetrics
3. Photolithography Photoresist: 1813 (positive) Mask: clean, wells only (dark area around wells) 1) Spin – on using recipe 9 2) Pre-bake at 115 ºC for 1 min 3) Exposure 7.5 s (MA6 centered at 10y 10x) 4) Post-bake at 115 ºC for 1 min 5) Develop for 1–2 mins in MFA 321 developer Clean mask in 1165 at 78 ºC Total process time: approx. 1 h with all steps	Lithography	HMDS, Spinner 1 or 3, hotplate, 1165 remover, MA6 exposure system
4. Creating hard mask – Nitride etch Use recipe CF4_40MT Parameter: etch 3.5 min, turn wafers, etch 3.5 min (7 mins total) Total process time: approx. 30 min total for pump down/up + process time	Plasma Etch	Unaxis 790

(It is recommended to preclean the chamber with recipe Cleaner 15 min)		
5. Strip PR 1165 at 75 ºC for around 15 min, spin dry If stubborn try Piranha wet etch, can be up to 1 h Warm-up period 10–15 min	Lithography	1165 Remover
6. Clean wafer Recipe: 250W_O2 for 1 min Total process time: approx. 20 min total for pump down/up + process time (It is recommended to preclean the chamber with recipe Cleaner 15 min)	Plasma Etch	Unaxis 790
7. KOH Etch of the wells Etch rate needs to be tested, depends heavily on when tank has been changed last For 62 µm, etch for around 150 min at 70 ºC Warm-up period around 20 min Check well depth through profilometer and KLA-Tencor P7 Profiler	Packaging	KOH Wet bench, profilometer KLA-Tencor P7 Profiler
8. Clean silicon wafer Can leave overnight right before the HF dip Setup time: 15 min for tanks to heat up Process time: approx. 2 h (Make sure fully rinse wafer after KOH bench to avoid potassium ion contamination in the prefurnace bench, wafers with metal history are definitely not allowed in prefurnace bench)	Furnace	RCA / prefurnace clean
9. SiO2 deposition Deposit a insolation layers on KOH etched wells Recipe: 1050 wet Parameter: Deposition time is 25 min Process time: approx. 4.5–5 h until wafer unload	Furnace	Oxidation furnace Filmetrics

Check film thickness through either approx. deposition time + color or through the filmetrics		
10. Nitride removal Parameter: 70 s CF4_40MT plus 3~5 s dip in BOE bench and 120 min in Nitride bench 70 s CF4_40MT plus 5 s dip into 6:1 NH_4F: HF (~1.6 nm/s etch rate) to remove ~35 nm SiO_2 on Si_3N_4 120 min in Nitride bench to remove front and back side Si_3N_4 Nitride bench warm-up period 1.5–2 h	Plasma Etch Wet Chemistry	Unaxis 790 BOE Etch Bench Phosphoric acid/nitride etch
11. Prepare coil pattern for liftoff – photolithography Photoresist SPR 220-7 1) Spin – on using recipe 3, let sit for at least 10 min (4 h rehydrating period works well, or overnight) 2) Pre-bake at 90 ºC for 100 s 3) Exposure 18 s (MA6 centered at 10y 10x) – may go up to 30 s for glass wafers 4) NO Post-bake, but wait for 1–2 min 5) Develop for ~4 min in MF 24A developer Clean mask in 1165 at 78 ºC Total process time: approx. 5 h (including the 4 h rehydrating step) (Photoresist 1813 works as well)	Lithography	HMDS, Spinner 1 or 3, hotplate, 1165 remover, MA6 exposure system
12. Descum of photoresist (making sure absolutely no photoresist remains in areas of where we want metal) Recipe: 250 W_O_2 for 2 min (100 W_O_2 for 1 min for PR1813) Total process time: approx. 20 min total for pump down/up + process time (It is better to preclean the chamber with recipe Cleaner 15 min)	Plasma Etch	Unaxis 790
13. Metal deposition / seed layer deposition in Evaporator Need: adhesion layer crucible (Either Cr or Ti, Cr works better as diffusion barrier), metal crucible (Cur or Au for track deposition, Au incurs extra charge that is HUGE for thick layers ~$600 for 2 µm, or Pt for seed layer)	Deposition	CHA-600 E-beam Evaporator

Thickness control through the monitor, it tends to be off by 10–30%, more error on thicker films Adhesion layer thickness for plating: 200 nm Cr layer, 30 nm Pd layer for catalyst (literature suggests use at least 30 nm) Use test wafer for film stress and thickness measurements (at the shadows left behind by wafer holder)		
14. Measure film stress using test wafer At room temperature, right after deposition and 24 h later The adhesion improves significantly if the wafers can rest for 24 h	Furnace	Tencor FLX-2320
15. Electroplating (20 µm thickness Cu) Recipe: Stir rate 260, temperature 80–85 ºC, voltage 2.3 V, effective current 0.820 A, total charge transfer 100 min·A (Minutes × Amperes = Charge) Total process time: approx. 30 min for setup + around 2 h process time	Prof. McDermott's lab	Electroplating equipment
16. CVC sputtering (20 µm thickness Cu) (Step: 11~15 could be ignored for CVC sputtering Cu instead of electroplating Cu) Recipe 1: 0.2 kW 10 mins ramp and 5 min continuous deposition for Cr adhesion 0.5 kW 20 min ramp and 60 min continuous deposition for Cu thickness Recipe 2: 0.2 kW 10 min ramp and 15 min continuous deposition for Cr adhesion 0.2 kW 10 min ramp, 10 min continuous and 20 min fixed position deposition for Cu thickness 0.5 kW 20 min ramp, 10 min continuous and 30 min fixed position deposition for Cu thickness (Lower power leads to better adhesion between metal and silicon) Bake 5 min at 5 ºC after CVC sputtering to realize better adhesion (Always use test wafer first to measure the Cu thickness if machine situation and recipe changed)	Deposition	CVC 601 DC Sputterer

17. Photolithography Photoresist: 5214 Mask: clean, wells only (dark area around wells) 300MIF rinse 30 s Prebake 100 ºC for 1 min before spinning PR 1) Spin – on using recipe 9 2) Pre-bake at 95 ºC for 3 min 3) Exposure soft 6 s (ch2) (MA6 centered at 10y 10x) 4) Post-bake at 115 ºC for 90 s 5) Exposure flood 60 s (ch2) (gap 40) 6) Develop for 30 s in AZ 917 developer Clean mask in 1165 at 78 ºC Total process time: approx. 1 h with all steps	Lithography	Spinner 1 or 3, hotplate, 1165 remover, MA6 exposure system
18. Cu etch (Multiple Cu wells left after etching) APS-100 (ammonium persulfate) heat up to 60~65 ºC. Etch 10~20 min. Rinse ~15 min depends on the Cu thickness	Teaching	Corrosives Bench
19. Photolithography Photoresist: 12XT Mask: clean, coils only Prebake 100 ºC for 1 min before spinning PR 1) Spin – on using recipe 8 on spinner 1 2) Pre-bake at 115 ºC for 3 min 3) Exposure soft 45 s (MA6 centered at 10y 10x) 4) Post-bake at 90 ºC for 1 min 5) Develop for 1min in 300MIF developer Clean mask in 1165 at 78 ºC Total process time: approx. 1 h with all steps	Lithography	Spinner 1, hotplate, 1165 remover, MA6 exposure system
20. Cu etch (Multiple Cu coils left after etching) APS-100 (ammonium persulfate) heat up to 60~65 ºC. Etch 10~20 min. Rinse ~15 min depends on the Cu thickness	Teaching	Corrosives Bench

Pay attention to the sample close to the ending etching time, the color will change obviously when Cu is gone		
21. Strip PR Either 1165 at 75 ºC for around 15 min then DI water rinse, spin dry Or acetone at 75 ºC for around 15 min then IPA then DI water rinse (It is better to use own baker for heated 1165 at wet chemistry bay solvent benches since it is much cleaner than the 1165 remover in lithography bay)	Wet chemistry/ Lithography	Solvent Benches, 1165 remover
22. Photolithography Photoresist: 12XT Mask: clean, coils only Prebake 100 ºC for 1 min before spinning PR 1) Spin – on using recipe 8 on spinner 1 2) Pre-bake at 115 ºC for 3 min 3) Exposure soft 45 s (MA6 centered at 10y 10x) 4) Post-bake at 90 ºC for 1 min 5) Develop for 1 min in 300MIF developer Clean mask in 1165 at 78 ºC Total process time: approx. 1 h with all steps	Lithography	Spinner 1, hotplate, 1165 remover, MA6 exposure system
23. Cr etch Mount samples in the middle of the 6" carrier wafer using Santovac Recipe CrEtch Parameter: Etch for 2.5~3 min (1 min + 1 min + 0.5~1 min separate running recipe way is better considering the cooling effect of 770 Inductively Coupled Plasma, onetime 2.5~3 min may lead to residue or scorched/burned PR, which hard to be removed later) Run plasma recipe on sample mounted to the carrier wafer Remove santovac easily using IPA	Plasma Etch	PlasmaTherm 770 Inductively Coupled Plasma

24. Strip PR Either 1165 at 75 ºC for around 15 min then DI water rinse, spin dry Or acetone at 75 ºC for around 15 min then IPA then DI water rinse (It is better to use own baker for heated 1165 at wet chemistry bay solvent benches since it is much cleaner than the 1165 remover in lithography bay)	Wet chemistry/ Lithography	Solvent Benches, 1165 remover

9.4.2 Passive sensor: glass layer fabrication

Table 9-3. Glass wafer fabrication details for passive sensor

Glass Layer Process	Bay	Instruments
1. Clean glass wafer 100 ºC Sulfuric acid and hydrogen peroxide solution 15 min Setup time: 30 min for tanks to heat up Process time: approx. 1 h	Wet chemistry	Piranha bench
2. CVC sputtering (20 µm thickness Cu) (Step: 11~15 could be ignored for CVC sputtering Cu instead of electroplating Cu) Recipe 1: 0.2 kW 10 min ramp and 5 min continuous deposition for Cr adhesion 0.5 kW 20 min ramp and 60 min continuous deposition for Cu thickness Recipe 2: 0.2 kW 10 min ramp and 15 min continuous deposition for Cr adhesion 0.2 kW 10 min ramp, 10 min continuous and 20 min fixed position deposition for Cu thickness 0.5 kW 20 mins ramp, 10 min continuous and 30 min fixed position deposition for Cu thickness (Lower power leads to better adhesion between metal and silicon) Bake 5 min at 5 ºC after CVC sputtering to realize better adhesion (Always use test wafer firstly to measure the Cu thickness if machine situation and recipe changed)	Deposition	CVC 601 DC Sputterer

3. Photolithography Photoresist: 5214 Mask: clean, wells only (dark area around wells) 300MIF rinse 30 s Prebake 100 ºC for 1 min before spinning PR 1) Spin – on using recipe 9 2) Pre-bake at 95 ºC for 3 min 3) Exposure soft 6 s (ch2) (MA6 centered at 10y 10x) 4) Post-bake at 115 ºC for 90 s 5) Exposure flood 60 s (ch2) (gap 40) 6) Develop for 30 s in AZ 917 developer Clean mask in 1165 at 78 ºC Total process time: approx. 1 h with all steps	Lithography	Spinner 1 or 3, hotplate, 1165 remover, MA6 exposure system
4. Cu etch (Multiple Cu wells left after etching) APS-100 (ammonium persulfate) heat up to 60~65 ºC. Etch 10~20 min. Rinse ~15 min depends on the Cu thickness	Teaching	Corrosives Bench
5. Photolithography Photoresist: 12XT Mask: clean, coils only Prebake 100 ºC for 1 min before spinning PR 1) Spin – on using recipe 8 on spinner 1 2) Pre-bake at 115 ºC for 3 min 3) Exposure soft 45 s (MA6 centered at 10y 10x) 4) Post-bake at 90 ºC for 1 min 5) Develop for 1min in 300MIF developer Clean mask in 1165 at 78 ºC Total process time: approx. 1 h with all steps	Lithography	Spinner 1, hotplate, 1165 remover, MA6 exposure system
6. Cu etch (Multiple Cu coils left after etching) APS-100 (ammonium persulfate) heat up to 60~65 ºC. Etch 10~20 min. Rinse ~15 min depends on the Cu thickness	Teaching	Corrosives Bench

Pay attention to the sample close to the ending etching time, the color will change obviously when Cu is gone		
7. Strip PR Either 1165 at 75 ºC for around 15 min then DI water rinse, spin dry Or acetone at 75 ºC for around 15 min then IPA then DI water rinse (It is better to use own baker for heated 1165 at wet chemistry bay solvent benches since it is much cleaner than the 1165 remover in lithography bay)	Wet chemistry/ Lithography	Solvent Benches, 1165 remover
8. Photolithography Photoresist: 12XT Mask: clean, coils only Prebake 100 ºC for 1 min before spinning PR 1) Spin – on using recipe 8 on spinner 1 2) Pre-bake at 115 ºC for 3 min 3) Exposure soft 45 s (MA6 centered at 10y 10x) 4) Post-bake at 90 ºC for 1 min 5) Develop for 1min in 300MIF developer Clean mask in 1165 at 78 ºC Total process time: approx. 1 h with all steps	Lithography	Spinner 1, hotplate, 1165 remover, MA6 exposure system
9. Cr etch Mount samples in the middle of the 6-inch carrier wafer using Santovac Recipe CrEtch Parameter: Etch for 2.5~3 min (1 min + 1 min + 0.5~1 min separate running recipe way is better considering the cooling effect of 770 Inductively Coupled Plasma, onetime 2.5~3 min may lead to residue or scorched/burned PR, which hard to be be removed later) Run plasma recipe on sample mounted to the carrier wafer Remove santovac easily using IPA	Plasma Etch	PlasmaTherm 770 Inductively Coupled Plasma

10. Strip PR Either 1165 at 75 ºC for around 15 min then DI water rinse, spin dry Or acetone at 75 ºC for around 15 min then IPA then DI water rinse (It is better to use own baker for heated 1165 at wet chemistry bay solvent benches since it is much cleaner than the 1165 remover in lithography bay)	Wet chemistry/ Lithography	Solvent Benches, 1165 remover

9.4.3 Bonding and dicing process for passive sensor

Table 9-4. Bonding and dicing process

1. Observation Make a map of which pieces turned out and which did not on the glass and silicon wafer, check metal thickness at the DIR mark to not damage any of the metal tracks (the profilometer needle cannot fit between the tracks anyway, so it would not be an accurate measurement) It is a good idea to record image using the Nikon	Analysis and metrology	Microscope in any room Nikon LV100
2. Anodic bonding process 1) Pre-clean with the attached cleaner, uses Acetone, IPA and DI water 2) Align: put the glass wafer on first so you can see through it to the alignment marks, then the Si wafer. This means the glass wafer will be sitting on top for the bonding process. There are several recipe options, you WILL need to use flags (see manual for the machine that is constantly rewritten) 3) Bond wafers Recipe is recorded on the machine, the approx. steps are: - vacuum - purge - wait for good vacuum (around 8.5×10^{-5} torr) - flags out - heat to 300 ºC (double check) - Voltage on (300 V) for 5 min (double check) - voltage off, cool down time approx. 3 h	Furnace	EV620 and EV801

3. Dicing Follow the instructions in book, 5 mm and 5 mm spacings between the wells. I align so that the dicing mark is right between the two alignment marks. Do a test cut off to the side to verify alignment etc.	Packaging	Saw #1 only (check for correct blade)
4. Grinding Use the Nikon LV100 to measure the side thickness of bonded samples. Put PR (1813 or PMMA) on the glass side to protect glass layer during grinding. Use crystal bond to mount the sample to the special holder on 175 ºC hotplate. (PMMA is better than 1813 because of the high temperature affordability) Use 600 fine grit silicon carbide paper to grind the silicon membrane from 500 µm to 100 µm /50 µm. Photoresist PMMA recipe 1: Prebake 100 ºC for 1 min before spinning PR 1) Spin – using recipe 7 on spinner 3 2) Bake at 100 ºC for 3 min Photoresist PMMA 950 recipe 2: Prebake 100 ºC for 1 min before spinning PR 1) Spin – using recipe 2 on spinner 3 2) Bake at 165 ºC for 3 min (Steel tweezer is needed for high temperature)	Lithography MSE student lab	Spinner 3, hotplate, 120 grit grinding

9.4.4 Active sensor: silicon layer fabrication

Table 9-5. Silicon wafer fabrication details for active sensor

Silicon Layer Process	Bay	Instruments
1. Clean silicon wafer Take an unprocessed wafer only Can leave overnight right before the HF dip Setup time: 15 min for tanks to heat up Process time: approx. 2 h	Furnace	RCA / prefurnace clean

2. Nitride deposition Deposit a hard mask used for the KOH etch because photoresist will not hold up to that process Will need 4 baffle wafers (2 ahead and 2 behind your wafer) Recipe: STDNIT.002 Parameter: Deposition time is 30 min for 2400-2600 Å thick film, deposition rate around 80 Å/min Process time: approx. 2.5–3 h until wafer unload Check film thickness through either approx. deposition time + color or through the filmetrics	Furnace	Nitride furnace Filmetrics
3. Photolithography Photoresist: 1813 (positive) Mask: clean, wells only (dark area around wells) 1) Spin – on using recipe 9 2) Pre-bake at 115 ºC for 1 min 3) Exposure 7.5 s (MA6 centered at 10y 10x) 4) Post-bake at 115 ºC for 1 min 5) Develop for 1–2 min in MFA 321 developer Clean mask in 1165 at 78 ºC Total process time: approx. 1 h with all steps	Lithography	HMDS, Spinner 1 or 3, hotplate, 1165 remover, MA6 exposure system
4. Creating hard mask – Nitride etch Use recipe CF4_40MT Parameter: etch 3.5 min, turn wafers, etch 3.5 min (7 min totally) Total process time: approx. 30 min total for pump down/up + process time (It is better to preclean the chamber with recipe Cleaner 15 min)	Plasma Etch	Unaxis 790
5. Strip PR 1165 at 75 ºC for around 15 min, spin dry If stubborn try Piranha wet etch, can be up to 1 h Warm-up period 10–15 min	Lithography	1165 Remover
6. Clean wafer	Plasma Etch	Unaxis 790

Recipe: 250 W_O_2 for 1 min Total process time: approx. 20 min total for pump down/up + process time (It is better to preclean the chamber with recipe Cleaner 15 min)		
7. KOH Etch of the wells Etch rate needs to be tested, depends heavily on when tank has been changed last For 62 µm, etch for around 150 min at 70 ºC Warm-up period around 20 min Check well depth through profilometer and KLA-Tencor P7 Profiler	Packaging	KOH Wet bench, profilometer KLA-Tencor P7 Profiler
8. Clean silicon wafer Can leave overnight right before the HF dip Setup time: 15 min for tanks to heat up Process time: approx. 2 h (Make sure fully rinse wafer after KOH bench to avoid potassium ion contamination in the prefurnace bench, wafers with metal history are definitely not allowed in prefurnace bench)	Furnace	RCA / prefurnace clean
9. SiO2 deposition This deposits an insolation layers on KOH etched wells Recipe: 1050 wet Parameter: Deposition time is 25 min Process time: approx. 4.5–5 h until wafer unload Check film thickness through either approx. deposition time + color or through the filmetrics	Furnace	Oxidation furnace Filmetrics
10. Nitride removal Parameter: 70 s CF4_40MT plus 3~5 s dip in BOE bench and 120 min in Nitride bench 70s CF4_40MT plus 5 s dip into 6:1 NH_4F: HF (~1.6 nm/s etch rate) to remove ~35 nm SiO_2 on Si_3N_4 120 min in Nitride bench to remove front and back side Si_3N_4 Nitride bench warm-up period 1.5–2 h	Plasma Etch Wet Chemistry	Unaxis 790 BOE Etch Bench Phosphoric acid/ nitride etch

11. Prepare coil pattern for liftoff – photolithography Photoresist KL 1604 Mask: clean Prebake 100 ºC for 1 min before spinning PR 1) Spin – using recipe 2 on spinner 3 2) Pre-bake at 110 ºC for 1 min 3) Exposure 11.5 s (MA6 centered at 10y 10x) 4) Post-bake at 110 ºC for 1 min 5) Develop for 20 s in MF-CD 26 developer 6) Hard-bake at 100 ºC for 1 min Clean mask in 1165 at 78 ºC Total process time: approx. 1 h with all steps	Lithography	HMDS, Spinner 3, hotplate, 1165 remover, MA6 exposure system
12. Descum of photoresist (making sure absolutely no photoresist remains in areas of where we want metal) Recipe: 50_10_10 for 20 s Total process time: approx. 8 min total for pump down/up + process time (It is better to preclean the chamber with recipe Cleaner 15 min)	Plasma Etch	Unaxis 790
13. Metal deposition / seed layer deposition in Evaporator Need: adhesion layer crucible (Either Cr or Ti for 20 nm, Cr works better as diffusion barrier), metal crucible (Cu or Au for 480 nm metal plate deposition, Au incurs extra charge that is HUGE for thick layers ~$150 for 500 nm) Thickness control through the monitor, it tends to be off by 10–30%, more error on thicker films Adhesion layer thickness for plating: 20 nm Cr layer (Use Cr 20 nm Cu 450 nm Cu 10 nm Au 20 nm combination for the test to save money)	Deposition	CHA-600 E-beam Evaporator
14. Liftoff of excess metal Use either heated 75 ºC acetone or 1165 remover. Can use sonication at 1, consider increasing the number especially if the metal film has had time to rest between deposition and liftoff.	Wet Chemistry	Solvent Bench

This can work against you if it is stubborn to remove, but for you if it tends to peel off, so it depends on the film. For the electroplating process I did liftoff immediately. Adhesion problems usually happen with thicker films or if the film thickness is on the order of photoresist thickness. I like to stick to a PR thickness at least 3x the deposition thickness. Total process time: can be left in a covered beaker overnight.		
15. Descum of photoresist (making sure absolutely no photoresist remains in areas of where we want metal) Recipe: 50_10_10 for 20 s Total process time: approx. 20 min total for pump down/up + process time (It is better to preclean the chamber with recipe Cleaner 15 min)	Plasma Etch	Unaxis 790

9.4.5 Active sensor: glass layer fabrication

Table 9-6. Glass wafer fabrication details for active sensor

Glass Layer Process	**Bay**	**Instruments**
1. Clean glass wafer 100 ºC Sulfuric acid and hydrogen peroxide solution 15 min Setup time: 30 min for tanks to heat up Process time: approx. 1 h	Wet chemistry	Piranha bench
2. Prepare coil pattern for liftoff – photolithography Photoresist KL 1604 Mask: clean Prebake 100 ºC for 1 min before spinning PR 1) Spin – using recipe 2 on spinner 3 2) Pre-bake at 110 ºC for 1 min 3) Exposure 10.5 s (MA6 centered at 10y 10x) 4) Post-bake at 110 ºC for 1 min 5) Develop for 25 s in MF-CD 26 developer 6) Hard-bake at 100 ºC for 1 min Clean mask in 1165 at 78 ºC	Lithography	HMDS, Spinner 3, hotplate, 1165 remover, MA6 exposure system

Total process time: approx. 1 h with all steps		
3. Descum of photoresist (making sure absolutely no photoresist remains in areas of where we want metal) Recipe: 50_10_10 for 20 s Total process time: approx. 8 min total for pump down/up + process time (It is better to preclean the chamber with recipe Cleaner 15 min)	Plasma Etch	Unaxis 790
4. Metal deposition in Evaporator Need: adhesion layer crucible (Either Cr or Ti for 20 nm, Cr works better as diffusion barrier), metal crucible (Cu or Au for 480 nm metal plate deposition, Au incurs extra charge that is HUGE for thick layers ~$150 for 500 nm) Thickness control through the monitor, it tends to be off by 10–30%, more error on thicker films Adhesion layer thickness for plating: 20 nm Cr layer (Use Cr 20 nm Cu 450 nm Cu 10nm Au 20 nm combination for the test to save money)	Deposition	CHA-600 E-beam Evaporator
5. Liftoff of excess metal Use either heated 75 ºC acetone or 1165 remover. Can use sonication at 1, consider increasing the number especially if the metal film has had time to rest between deposition and liftoff. This can work against you if it is stubborn to remove, but for you if it tends to peel off, so it depends on the film. For the electroplating process I did liftoff immediately. Adhesion problems usually happen with thicker films or if the film thickness is on the order of photoresist thickness. I like to stick to a PR thickness at least 3x the deposition thickness. Total process time: can be left in a covered beaker overnight.	Wet Chemistry	Solvent Bench
6. Descum of photoresist (making sure absolutely no photoresist remains in areas of where we want metal) Recipe: 50_10_10 for 20 s Total process time: approx. 20 min total for pump down/up + process time (It is better to preclean the chamber with recipe Cleaner 15 min)	Plasma Etch	Unaxis 790

7. Prepare for back side marker – photolithography Photoresist KL 1604 Mask: clean Prebake 100 ºC for 1 min before spinning PR 1) Spin – using recipe 2 on spinner 3 2) Pre-bake at 110 ºC for 1 min 3) Exposure 10.5 s (**MA6 Back Side Alignment (BSA)** centered at 10y 10x) 4) Post-bake at 110 ºC for 1 min 5) Develop for 25 s in MF-CD 26 developer 6) Hard-bake at 100 ºC for 1 min Clean mask in 1165 at 78 ºC Total process time: approx. 1 h with all steps	Lithography	Spinner 3, hotplate, 1165 remover, MA6 exposure system
8. Metal deposition in Evaporator Need: adhesion layer crucible (Either Cr or Ti for 20 nm, Cr works better as diffusion barrier), metal crucible (Cu for 80 nm or 130 nm) (Since we just need two areas of the alignment marks, using a tin foil as a mask to expose our needed area will save a lot of liftoff time next step.)	Deposition	CHA-600 E-beam Evaporator
9. Liftoff of excess metal Use either heated 75 ºC acetone then IPA then water or 1165 remover then water to rinse) Total process time: 2~3 h	Wet Chemistry	Solvent Bench

9.4.5 Bonding, dicing and grinding process for active sensor

Table 9-7. Bonding and dicing process

1. Observation Make a map of which pieces turned out and which did not on the glass and silicon wafer, check metal thickness at the DIR mark to not damage any of the metal tracks (the profilometer needle cannot fit between the tracks anyway, so it would not be an accurate measurement)	Analysis and metrology	Microscope in any room Nikon LV100

It is a good idea to record image using the Nikon		
2. Anodic bonding process 1) Pre-clean with the attached cleaner, uses Acetone, IPA and DI water 2) Align: put the glass wafer on first so you can see through it to the alignment marks, then the Si wafer. This means the glass wafer will be sitting on top for the bonding process. There are several recipe options, you WILL need to use flags (see manual for the machine that is constantly rewritten) (Backside alignment mark will help a lot during alignment) 3) Bond wafers Recipe is recorded on the machine, the approx. steps are: - vacuum - purge - wait for good vacuum (around 8.5×10^{-5} torr) - flags out - heat to 300 ºC (double check) - Voltage on (300 V) for 5 min (double check) - voltage off, cool down time approx. 3 h	Furnace	EV620 and EV801
3. Dicing Follow the instructions in book, 3 mm and 6 mm spacings between the wells or 3 mm and 4 mm spacings between the wells. I align so that the dicing mark is right between the two alignment marks. Do a test cut off to the side to verify alignment etc.	Packaging	Saw #1 only (check for correct blade)
4. Grinding Use the Nikon LV100 to measure the side thickness of bonded samples. Put PR (1813 or PMMA) on the glass side to protect glass layer during grinding. Use crystal bond to mount the sample to the special holder on 175 ºC hotplate. (PMMA is better than 1813 because of the high temperature affordability) Use 600 fine grit silicon carbide paper to grind the silicon membrane from 500 µm to 100 µm /50 µm.	Lithography MSE student lab	Spinner 3, hotplate, 120 grit grinding

Photoresist PMMA recipe 1: Prebake 100 ºC for 1 min before spinning PR 1) Spin – using recipe 7 on spinner 3 2) Bake at 100 ºC for 3 min Photoresist PMMA 950 recipe 2: Prebake 100 ºC for 1 min before spinning PR 1) Spin – using recipe 2 on spinner 3 2) Bake at 165 ºC for 3 min (Steel tweezer is needed for high temperature)		
5. Deposition Cu on sidewalls for connection Use Polyimide Film Tape 5413 (3M) to cover the protected area and only expose the sidewalls to CVC source target with the help a special holder. The holder could fit 4~5 samples each time. Recipe: 0.1 kW 10 min ramp and 40 min continuous deposition for Cr adhesion 0.1 kW 10 min ramp and 99 min continuous deposition for Cu thickness Check whether short connection happens by the multimeter after deposition Cu on both sidewalls of the bonded sample	Deposition	CVC 601 DC Sputterer

CONCLUSION

This dissertation describes the hydrocephalus disease and emphasizes the importance of monitoring ICP to mitigate hydrocephalus symptoms during the entire life of the patient. It introduces the various methods of measuring ICP. Then it describes comparisons and limitations of methods of ICP measurements.

This dissertation briefly reviews the current existing implantable microsensor devices. Then it presents my own active capacitance pressure sensor and also a passive resonance pressure sensor for wireless continuous ICP monitoring, including the principle, design, challenge, simulation, fabrication and measurement results analysis in detail. The 4 × 6 × 0.61 mm MEMS active capacitive sensor could fit vertically through a skull hole less than 5 mm diameter. The active sensor has good performance. The full scale is 0 mmHg to 1000 mmHg and accuracy is 0.033%. It has high resolution of 0.022 mmHg (0.001 pF) and the drift value of our 10 capacitive pressure sensors are from ±0.136 mmHg to ±0.5 mmHg for 2 months. Here 0.5 mmHg corresponds to 0.05% FSO with a full range of 0 to 1000 mmHg. Though the current 5 × 5 × 0.61 mm MEMS passive sensor signal is weak and it is hard to detect, it still might be a possible solution to wirelessly measure the ICP if the physician could increase the surgery hole limit. Two commercial piezo-resistive pressure sensors are also introduced for comparison of results.

Future work for ICP sensor is the redesign and fabrication of a biosafe & biocompatible container and the auto sensor test platform set up. A biosafety & biocompatible container will make sure the sensor as well as the electronics could work functionally and be implanted in the human brain for a long duration. The auto sensor test platform will save much time as well as avoid important fluctuations from manual control and environment during measurement.

The ICP value from the ICP sensor will control the open/close of the active piezo-valve to realize a smart shunt. The open/close threshold parameters are fully customizable and scalable to the patient's individual physiologic needs. A RFID based sensor tag permits valve programming and ICP waveform transmission between caretakers, provider, and patients. It also provides wireless power to charge the shunt system, eliminating the need for battery replacement. Currently this system was tested to be functional ex-vivo. The next steps involve lengthening the distance from the antenna to the patient.

REFERENCES

Akar O, Akin T and Najafi K 2001 A wireless batch sealed absolute capacitive pressure sensor *Sensors and Actuators A: Physical* **95**(1) 29-38

Akbar M and Shanblatt M A 1992 Temperature compensation of piezoresistive pressure sensors. *Sensors and Actuators A: Physical* **33**(3) pp.155-62

Allocca J A 1980 *Method and apparatus for noninvasive monitoring of intracranial pressure* U.S. Patent 4,204,547

Alperin N J, Lee S H, Loth F, Raksin P B and Lichtor T 2000 MR-Intracranial Pressure (ICP): A method to measure intracranial elastance and pressure noninvasively by means of MR Imaging: baboon and human study 1 *Radiology* **217** 877–85

Alperin N, Hushek S G, Lee S H, Sivaramakrishnan A and Lichtor T 2005 MRI study of cerebral blood flow and CSF flow dynamics in an upright posture: the effect of posture on the intracranial compliance and pressure In Kirkness C J et al. (eds) *Intracranial Pressure and Brain Monitoring* XII (Springer; Vienna) pp. 177–81

Anderson R C, Kan P, Klimo P, Brockmeyer D L, Walker M L and Kestle J R 2004 Complications of intracranial pressure monitoring in children with head trauma *J. Neurosurg.: Pediatrics* **101** 53–8

Aquilina K, Thoresen M, Chakkarapani E, Pople I K, Coakham H B, and Edwards R J 2011 Preliminary evaluation of a novel intraparenchymal capacitive intracranial pressure monitor *J. Neurosurg*. **115** pp. 561-9

Asiedu D P, Lee K J, Mills G and Kaufmann E E 2014 A Review review of non-invasive methods of monitoring intracranial pressure *J. Neurolog. Res.* **4** 1–6

Avan P, Büki B, Lemaire J J, Dordain M and Chazal J 1996 Otoacoustic emissions: a new tool for monitoring intracranial pressure *In Intracranial and intralabyrinthine fluids* (Springer; Berlin Heidelberg) 165–73

Baldi A, Choi W and Ziaie B 2003 A self-resonant frequency-modulated micromachined passive pressure transensor *IEEE Sensors J*. 3(6) pp. 728–33

Baurmann M 1925 Über die entstehung und klinische bedeutung des netzhautvenenpulses *Dtsch. Ophthalmol. Ges.* **45** 53–9

Bekar A, Doğan Ş, Abaş F, Caner B, Korfalı G, Kocaeli H, Yılmazlar S and Korfalı E 2009 Risk factors and complications of intracranial pressure monitoring with a fiberoptic device *J. Clin. Neurosci.* **16** 236–40

Bellner J, Romner B, Reinstrup P, Kristiansson K A, Ryding E and Brandt L 2004 Transcranial Doppler sonography pulsatility index (PI) reflects intracranial pressure (ICP) *Surg. Neurol.* **62** 45–51

Berlin T, Murray-Krezan C and Yonas H 2015 Comparison of parenchymal and ventricular intracranial pressure readings utilizing a novel multi-parameter intracranial access system. *SpringerPlus* **4** 10

Bershad E M, Urfy M Z, Pechacek A, McGrath M, Calvillo E, Horton N J and Voss S E 2014 Intracranial pressure modulates distortion product otoacoustic emissions: A proof-of-principle study *Neurosurgery* **75** 445–55

Bhatia A and Gupta A K 2007 Neuromonitoring in the intensive care unit. I. Intracranial pressure and cerebral blood flow monitoring *Intens. Care Med.* **33** 1263–71

Binz D D, Toussaint III L G, and Friedman J A 2009 Hemorrhagic complications of ventriculostomy placement: a meta-analysis *Neurocrit. Care* **10** 253–6

Borchert M S and Lambert J L 1998 Non-invasive measurement of intracranial pressure WO Patent 98034536

Borchert M S and Lambert J L 2000 *Non-invasive method of measuring cerebral spinal fluid pressure* U.S. Patent 6,129,682

Bratton S L, Chestnut, R M, Ghajar J, McConnell H F, Harris O A, Hartl R, Manley GT, Nemecek A, Newell DW, Rosenthal G and Schouten J 2006 Guidelines for the management of severe traumatic brain injury. VII. Intracranial pressure monitoring technology *J. Neurotraum.* **24** S45–54

Bruce B B 2014 Noninvasive assessment of cerebrospinal fluid pressure *J. Neuro-Ophthalmol.* **34** 288–94

Bruder N, N'Zoghe P, Graziani N, Pelissier D, Grisoli F and François G 1995 A comparison of extradural and intraparenchymatous intracranial pressures in head injured patients *Intens. Care Med.* **21** 850–2

Butler J C, Vigliotti A J, Verdi F W and Walsh S M 2002). Wireless, passive, resonant-circuit, inductively coupled, inductive strain sensor *Sensors and Actuators A: Physical.* **102**(1) 61-6

Chen G, Ghaed H, Haque R U, Wieckowski M, Kim Y, Kim G, Fick D, Kim, D, Seok M, Wise K and Blaauw D 2011 February A cubic-millimeter energy-autonomous wireless intraocular pressure monitor In *2011 IEEE Int. Solid-State Circuits Conf.* (pp. 310–2) IEEE

Chen L Y, Tee B C K, Chortos A L, Schwartz G, Tse V, Lipomi D J, Wong H S P, McConnell M V and Bao Z 2014 Continuous wireless pressure monitoring and mapping with ultra-small passive sensors for health monitoring and critical care *Nature communications* 5

Chen L Y, Tee B C K, Chortos A L, Schwartz G, Tse V, Lipomi D J, Wong H S P, McConnell M V and Bao Z 2014 Continuous wireless pressure monitoring and mapping with ultra-small passive sensors for health monitoring and critical care. Nat. *Commun.* **5** 5028

Baxter L K, 1997 Capacitive Sensors: Design and Applications *New York, NY, USA: IEEE Press*

Chen P J, Saati S, Varma R, Humayun M S and Tai Y C 2010 Wireless intraocular pressure sensing using microfabricated minimally invasive flexible-coiled *LC* sensor implant. *Journal of Microelectromechanical Systems* **19**(4) 72-34

Cheong J H, Ng S S Y, Liu X, Xue R F, Lim H J, Khannur P B, Chan K L, Lee A A, Kang K, Lim L S and He C 2012 An inductively powered implantable blood flow sensor microsystem for vascular grafts. *IEEE Trans. Biomed. Eng*. 59(9) pp. 2466–75

Chitnis G, Maleki T, Samuels B, Cantor L B and Ziaie B 2013 A minimally invasive implantable wireless pressure sensor for continuous IOP monitoring. *IEEE Trans. Biomed. Eng*. 60(1) pp. 250–6

Citerio G, Piper I, Chambers I R, Galli D, Enblad P, Kiening K, Ragauskas A, Sahuquillo J and Gregson B 2008 Multicenter clinical assessment of the raumedic neurovent–P intracranial pressure sensor: a report by the Brainit group *Neurosurgery* **63** 1152–8

Collins C C 1967 Miniature passive pressure transensor for implanting in the eye. *IEEE Trans. Biomed. Eng*. (2) pp.74–83

Cong P, Chaimanonart N, Ko W H and Young D J 2009 February A wireless and batteryless 130 mg 300 μW 10b implantable blood-pressure-sensing microsystem for real-time genetically engineered mice monitoring. In 2009 IEEE Int. *Solid-State Circuits Conf.-Digest of Technical Papers* (pp. 428–9) IEEE

Cong P, Ko W H and Young D J 2008 June Wireless less-invasive blood pressure sensing microsystem for small laboratory animal in vivo real-time monitoring. In *5th Int. Conf. Networked Sensing Syst*. 2008 INSS 2008 (pp. 80–6) IEEE

Coosemans J, Catrysse M and Puers R 2004 A readout circuit for an intra-ocular pressure sensor. *Sensors and Actuators A: Physical* **110**(1-3) pp. 432-8

Czosnyka M and Pickard J D 2004 Monitoring and interpretation of intracranial pressure *J. Neurol. Neurosur. Ps.* **75** 813–21

Czosnyka M, Czosnyka Z and Pickard J D 1996 Laboratory testing of three intracranial pressure microtransducers: technical report *Neurosurgery* **38** 219–24

Di Ieva A Schmitz E M and Cusimano M D 2013 Analysis of intracranial pressure past, present, and future *Neuroscientist* 1073858412474845

Du R, Meeker M, Bacchetti P, Larson M D, Holland M C and Manley G T 2005 Evaluation of the portable infrared pupillometer *Neurosurgery* **57** 198–203

Dunn L T 2002 Raised intracranial pressure *J. Neurol. Neurosur. Ps.* **73** i23–7

Duschek S and Schandry R 2007 Reduced brain perfusion and cognitive performance due to constitutional hypotension *Clin. Auton. Res.* **17** 69–76

Efremov A M and Svettsov V I 2002 Dry etching of copper using chlorine: a review *Russian Microelectronics* **31**(3), pp.179-92

Eide P K 2008 Comparison of simultaneous continuous intracranial pressure (ICP) signals from ICP sensors placed within the brain parenchyma and the epidural space *Med. Eng. Phys.* **30** 34–40

Eide P K and Brean A 2006 Lumbar cerebrospinal fluid pressure waves versus intracranial pressure waves in idiopathic normal pressure hydrocephalus *Brit. J. Neurosurg.* **20** 407–14

Eide P K and Sæhle T 2010 Is ventriculomegaly in idiopathic normal pressure hydrocephalus associated with a transmantle gradient in pulsatile intracranial pressure? *Acta Neurochir.* **152** 989–95

El-Dairi M A, Holgado S, O'Donnell T, Buckley E G, Asrani S and Freedman S F 2007 Optical coherence tomography as a tool for monitoring pediatric pseudotumor cerebri *J AAPOS* **11** 564–570

Faller L M, Mitterer T, Leitzke J P, and Zangl H 2017 Design and Evaluation of a Fast, High-Resolution Sensor Evaluation Platform Applied to MEMS Position Sensing *IEEE Trans. Instrum. Meas.* **67** pp. 1014-27

Firsching R, Schütze M, Motschmann M and Behrens-Baumann W 2000 Venous ophthalmodynamometry: a noninvasive method for assessment of intracranial pressure *J. Neurosurg.* **93** 33–6

Fonseca M A, Allen M G, Kroh J and White J 2006 June Flexible wireless passive pressure sensors for biomedical applications. In *Tech. Dig. Solid-State Sensor, Actuator, and Microsystems Workshop (Hilton Head 2006)* (pp. 37–42) (liquid crystal polymers, ceramic-encapsulated)

Fonseca M A, English J M, Von Arx M and Allen M G 2002 Wireless micromachined ceramic pressure sensor for high-temperature applications. *J. Microelectromechanical Syst*. 11(4) pp. 337–43

Fountas K N, Kapsalaki E Z, Machinis T G, Boev A N, Robinson III J S and Troup E C 2006 Clinical implications of quantitative infrared pupillometry in neurosurgical patients *Neurocrit. Care* **5** 55–60

Fountas K N, Sitkauskas A, Feltes CH, Kapsalaki E Z, Dimopoulos V G, Kassam M, Grigorian A A, Robinson J S and Ragauskas A, 2005 Is non-invasive monitoring of intracranial pressure waveform analysis possible? Preliminary results of a comparative study of non-invasive vs. invasive intracranial slow-wave waveform analysis monitoring in patients with traumatic brain injury *Med Sci. Monit.* **11** CR58–63

Freimann F B, Sprung C, Chopra S S, Vajkoczy P and Wolf S 2013 Large-scale referencing of the telemetric Neurovent-P-tel intracranial pressure sensor in a porcine model. *Pediatr. Neurosurg.* **49** 29–32

Fried H I, Nathan B R, Rowe A S, Zabramski J M, Andaluz N, Bhimraj A, Guanci M M, Seder D B and Singh J M 2016 The insertion and management of external ventricular drains: an evidence-based consensus statement *Neurocrit. Care* **24**(1) pp. 61-81

Frischholz M, Sarmento L, Wenzel M, Aquilina K, Edwards R, and Coakham H B 2007 Telemetric implantable pressure sensor for short-and long-term monitoring of intracranial pressure *In Eng.Med. Biol.Soc.* 2007. EMBS 2007. 29th Ann. Int. Conf.IEEE (pp. 514-514). IEEE Aug. 2007.

Gaihede M, Felding J U and Elbrônd O 1995 Biomechanical characteristics of the middle ear system measured by a new method: III: Comparisons with tympanometric measurements *Acta oto-laryngol.* **115** 522–7

Gardner P A, Engh J, Atteberry D and Moossy J J 2009 Hemorrhage rates after external ventricular drain placement: clinical article *J. Neurosurg.* **110** 1021–5

Gelabert-Gonzalez M, Ginesta-Galan V, Sernamito-Garcia R, Allut A G, Bandin-Dieguez J and Rumbo R M 2006 The Camino intracranial pressure device in clinical practice. Assessment in a 1000 cases *Acta Neurochir. (Wien)* **148** 435–41

Gevorgian S, Berg H, Jacobsson H and Lewin T 2003 Application notes-basic parameters of coplanar-strip waveguides on multilayer dielectric/semiconductor substrates, Part 1: high permittivity superstrates *IEEE microwave magazine* **4**(2) pp. 60-70

Glick R P, Niebruegge J, Lee S H, Egibor O, Lichtor T and Alperin N 2006 Early experience from the application of a noninvasive magnetic resonance imaging-based measurement of intracranial pressure in hydrocephalus *Neurosurgery* **59** 1052–61

Graham D I, Gennarelli T A, Cooper P R, and Golfinos J G 2000 Pathology of brain damage after head injury. In P R Cooper and J Golfinos (eds) *Head injury* 4th edn (New York: McGraw-Hill) 133–54

Guild S J, McBryde F D and Malpas S C 2015 Recording of intracranial pressure in conscious rats via telemetry *J. Appl. Physiol.* **119** 576–81

Hanlo P W, Peters R J A, Gooskens R H J M, Heethaar R M, Keunen R W M, van Huffelen A C, Tulleken A F, and Willemse J 1995 Monitoring intracranial dynamics by transcranial Doppler—A new Doppler index: Trans systolic time *Ultrasound Med. Biol.* **21** 613–21

Hawthorne C and Piper I 2014 Monitoring of intracranial pressure in patients with traumatic brain injury *Front. Neurol.* **5** 121

Hee M R, Izatt J A, Swanson E A, Huang D, Schuman J S, Lin C P, Puliafito C A and Fujimoto J G 1995 Optical coherence tomography of the human retina *Arch. Ophthalmol-chic.* **113** 325–32

Hicks T R and Atherton P D 1997 The NanoPositioning Book. Queensgate Instruments Limited, Torquay, Torbay, UK

Hong W C, Tu Y K, Chen Y S, Lien L M and Huang S J 2006 Subdural intracranial pressure monitoring in severe head injury: clinical experience with the Codman MicroSensor *Surg. Neurol.* **66** S8–13

Hori H, Moretti G, Rebora A and Crovato F 1972 The thickness of human scalp: normal and bald *Journal of Investigative Dermatology* **58**(6) pp.396-9

Hydrocephalus Association 2016 http://www.hydroassoc.org/

Jacks A S and Miller N R 2003 Spontaneous retinal venous pulsation: aetiology and significance *J. Neurol. Neurosur.* Ps. 74 7–9

Jonas J B, Pfeil K, Chatzikonstantinou A and Rensch F 2008 Ophthalmodynamometric measurement of central retinal vein pressure as surrogate of intracranial pressure in idiopathic intracranial hypertension *Graef. Arch. Clin. Exp.* **246** 1059–60

Jonas J B, Wang N and Yang D 2012 Retinal vein pulsation is in phase with intracranial pressure and not intraocular pressure *Invest. Ophth. Vis. Sci.* **53** 6045

Jow U M and Ghovanloo M 2007 Design and optimization of printed spiral coils for efficient transcutaneous inductive power transmission. *IEEE Transactions on biomedical circuits and systems 1*(3) pp. 193-202

Kaiser S T J 2006 Passive telemetric readout system *IEEE Sensors Journal* 6.5: 1340-5

Kang S K, Murphy R K, Hwang S W, Lee S M, Harburg D V, Krueger N A, Shin J, Gamble P, Cheng H, Yu S and Liu Z 2016 Bioresorbable silicon electronic sensors for the brain *Nature* **530** 71–9

Kapadia F N and Jha A N 1996 Simultaneous lumbar and intraventricular manometry to evaluate the role and safety of lumbar puncture in raised intracranial pressure following subarachnoid haemorrhage *Brit. J. Neurosurg.* **10** 585–8

Kashif F M, Verghese G C, Novak V, Czosnyka M, and Heldt T 2012 Model-based noninvasive estimation of intracranial pressure from cerebral blood flow velocity and arterial pressure *Sci. Transl. Med.* **4** 129ra44

Kawoos U, Mugalodi G K, Tofighi M R, Neff S and Rosen A 2005 April A permanently implantable intracranial pressure monitor Proc. IEEE *31st Annu. Northeast Bioeng. Conf.* 2005. 17–9

Kemp D T 1978 Stimulated acoustic emissions from within the human auditory system *J. Acoust. Sci. Am.* **64** 1386–91

Kiefer M, Antes S, Leonhardt S, Schmitt M, Orakcioglu B, Sakowitz O W and Eymann R 2012 Telemetric ICP measurement with the first CE-approved device: data from animal experiments and initial clinical experiences. *In Intracranial Pressure and Brain Monitoring XIV* (pp. 111–6) Springer Vienna

Kiefer M, Antes S, Leonhardt S, Schmitt M, Orakcioglu B, Sakowitz O W and Eymann R 2012 Telemetric ICP measurement with the first CE-approved device: data from animal experiments and initial clinical experiences *Acta Neurochir. Suppl*. **114** 111–6

Kiening K L, Schoening W N, Stover J F and Unterberg A W 2003 Continuous monitoring of intracranial compliance after severe head injury: relation to data quality, intracranial pressure and brain tissue PO2 Brit. *J. Neurosurg.* **17** 311–8

Kiening K L, Schoening W, Unterberg A W, Stover J F, Citerio G, Enblad P and Nilsson P 2005 Assessment of the relationship between age and continuous intracranial compliance *In Intracranial Pressure and Brain Monitoring XII* pp. (Springer; Vienna) 293–7

Koskinen L O D and Olivecrona M 2005 Clinical experience with the intraparenchymal intracranial pressure monitoring Codman MicroSensor system *Neurosurgery* **56** 693–8

Kowalski G 1987 Miniature pressure sensors and their temperature compensation *Sensors and Actuators* **11**(4) pp.367-76

Kristiansson H, Nissborg E, Bartek Jr J, Andresen M, Reinstrup P and Romner B 2013 Measuring elevated intracranial pressure through noninvasive methods: a review of the literature *J. Neurosurg. Anesth.* **25** 372–85

Lang J M, Beck J, Zimmermann M, Seifert V and Raabe A 2003 Clinical evaluation of intraparenchymal Spiegelberg pressure sensor *Neurosurgery* **52** 1455–9

Langfitt T W, Weinstein J D, Kassell N F and Simeone F A 1964 Transmission of increased intracranial pressure. I. Within the craniospinal axis *J. Neurosurg.* **21** 989–97

Larson M D and Muhiudeen I 1995 Pupillometric analysis of the 'absent light reflex' *Arch. Neurol-Chicago* **52** 369–72

Law S K 1993 Thickness and resistivity variations over the upper surface of the human skull *Brain topography* **6**(2) pp.99-109

Lee J I, Huang X, and Chu P B 2009 Nanoprecision MEMS capacitive sensor for linear and rotational positioning *J. Microelectromech. Syst.* **18** pp. 660–70

Lee Y S 1981 A silicon capacitive pressure transducer: performance characteristics and limitations *University of MICHIGAN*

Lemkin M and Boser B E 1999 A three-axis micromachined accelerometer with a CMOS position-sense interface and digital offset-trim electronics *IEEE J. Solid-State Circuits* **34**(4) pp. 456–68

Lenfeldt N, Koskinen L O, Bergenheim A T, Malm J and Eklund A 2007 CSF pressure assessed by lumbar puncture agrees with intracranial pressure *Neurology* **68** 155–8

Lescot T, Reina V, Le Manach Y, Boroli F, Chauvet D, Boch A L and Puybasset L 2012 In vivo accuracy of two intraparenchymal intracranial pressure monitors *Applied Physiology in Intensive Care Medicine* **37** (Springer; Berlin Heidelberg) pp. 249–53

Levin B E 1978 The clinical significance of spontaneous pulsations of the retinal vein *Arch. Neurol-Chicago* **35** 37–40

Levinsky A, Papyan S, Weinberg G, Stadheim T and Eide P K 2016. Non-invasive estimation of static and pulsatile intracranial pressure from transcranial acoustic signals. *Med. Eng. Phys.* **38** 47784

Li Z and Luo Y 2010 Finite element study of correlation between intracranial pressure and external vibration responses of human head. *Adv. Theor. Appl. Mech*.**3** 139–49

Liebeskind D S, Marcinkevicius E, Pranevicius M, Pranevicius O, Ragauskas A, Matijosaitis V, Zakelis R, Petrikonis K, Rastenyte D, Piper I and Daubaris G 2013 Clinical assessment of noninvasive intracranial pressure absolute value measurement method *Neurology* **80** 507–8

Lilja A, Andresen M, Hadi A, Christoffersen D and Juhler M 2014 Clinical experience with telemetric intracranial pressure monitoring in a Danish neurosurgical center *Clin. Neurol. Neurosur.* **120** 36–40

Liu H, Wang W, Cheng F, Yuan Q, Yang J, Hu J and Ren G 2015 External ventricular drains versus intraparenchymal intracranial pressure monitors in traumatic brain injury: a prospective observational study World *Neurosurg.* **83** 794–800

Lozier A P, Sciacca R R, Romagnoli M F and Connolly Jr E S 2002 Ventriculostomy-related infections: a critical review of the literature *Neurosurgery* **51** 170–82

Luerssen T G 1997 Intracranial pressure: Current status in monitoring and management *Semin. Pediatr. Neurol.* **4** 146–55

Mack W J, King R G, Ducruet A F, Kreiter K, Mocco J, Maghoub A, Mayer S and Connolly Jr E S 2003 Intracranial pressure following aneurysmal subarachnoid hemorrhage: monitoring practices and outcome data *Neurosurg. Focus* **14** 1–5

Maloney-Wilensky E, Gracias V, Itkin A, Hoffman K, Bloom S, Yang W, Christian S and LeRoux PD 2009 Brain tissue oxygen and outcome after severe traumatic brain injury: A systematic review* *Crit. Care Med.* **37** 2057–63

Marchbanks R J 1989 *Method and apparatus for measuring intracranial fluid pressure* U.S. Patent 4,841,986

Marioli D, Sardini, E, Serpelloni M and Taroni A 2005 A new measurement method for capacitance transducers in a distance compensated telemetric sensor system. *Measurement Science and Technology* **16**(8) p.1593

Medow. J Doctor's 2011 October 25 Madison doctor creates possible life-saving device for children with hydrocephalus *Wisconsin State Journal*

http://host.madison.com/wsj/news/local/health_med_fit/madison-doctor-creates-possible-life-saving-device-for-children-with/article_ba627bc2-fe9b-11e0-802d-001cc4c03286.html

Meeker M, Du R, Bacchetti P, Privitera C M, Larson M D, Holland M C and Manley G 2005 Pupil examination: validity and clinical utility of an automated pupillometer *J. Neurosci. Nurs.* **37** 34–40

Mertz K. Bencsik B, Büki B and Avan P 2004 Noninvasive testing of intracranial pressure changes due to body position in infants *Orv Hetil.* **145** 1427–30

Michaeli D and Rappaport Z H 2002 Tissue resonance analysis: a novel method for noninvasive monitoring of intracranial pressure: Technical note *J. Neurosurg.* **96** 1132–7

Mick E C 1991 *Method and apparatus for the measurement of intracranial pressure* U.S. Patent 5,074,310

Mick E C 1992 *Method and apparatus for the measurement of intracranial pressure* U.S. Patent 5,117,835

Miesel K A and Stylos L 2001 *Intracranial monitoring and therapy delivery control device, system and method* U.S. Patent 6,248,080

Miyake H, Ohta T, Kajimoto Y and Matsukawa M 1997 A new ventriculoperitoneal shunt with a telemetric intracranial pressure sensor: clinical experience in 94 patients with hydrocephalus *Neurosurgery* **40** 931–5

Mohan S S, del Mar Hershenson M, Boyd S P and Lee T H 1999 Simple accurate expressions for planar spiral inductances *IEEE Journal of solid-state circuits* **34**(10) pp. 1419-24

Mokri B 2001 The Monro–Kellie hypothesis applications in CSF volume depletion *Neurology* **56** 1746-8

Moreno J A, Mesalles E, Gener J, Tomasa A, Ley A, Roca J and Fernández-Llamazares J 2000 Evaluating the outcome of severe head injury with transcranial Doppler ultrasonography *Neurosurg. Focus* **8** 1–7

Morgalla M H, Cuno M, Mettenleiter H, Will BE, Krasznai L, Skalej M, Bitzer M and Grote E H 1997 ICP monitoring with a re-usable transducer: Experimental and clinical evaluation of the Gaeltec ICT/b pressure probe *Acta Neurochir.* **139** 569–73

Muehlmann M, Koerte I K, Laubender R P, Steffinger D, Lehner M, Peraud A, Heinen F, Kiefer M, Reiser M and Ertl-Wagner B 2013 Magnetic resonance–based estimation of intracranial pressure correlates with ventriculoperitoneal shunt valve opening pressure setting in children with hydrocephalus *Invest. Radiol.* **48** 543–7

Mukherjee B, George B and Sivaprakasam M 2014 An ophthalmic anesthesia training system using integrated capacitive and hall effect sensors *IEEE Trans. Instrum. Meas.*, **63**(5) pp.1153-62

Münch E C, Bauhuf C, Horn P, Roth H R, Schmiedek P and Vajkoczy P 2001 Therapy of malignant intracranial hypertension by controlled lumbar cerebrospinal fluid drainage *Crit. Care Med.* **29** 976–81

Neagu, C R, Jansen HV, Smith A, Gardeniers J G E and Elwenspoek M C 1997 Characterization of a planar microcoil for implantable microsystems *Sensors and Actuators A: Physical* **62**(1-3) pp. 599-611

Nopper R, Niekrawietz R and Reindl L 2010 Wireless readout of passive LC sensors *IEEE Transactions on Instrumentation and Measurement* **59**.9: 2450-7

North B 1997 Chapter 10 Intracranial pressure monitoring In Reilly P and Bullock R (eds) *Head Injury* London: Chapman & Hall

North B 1997 Chapter 10 Intracranial pressure monitoring In Reilly P and Bullock R (eds) *Head Injury*. London: Chapman & Hall

Olson W H 2010 Basic concepts of medical instrumentation. In J. G. Webster ed *Medical Instrumentation Application and Design* 4th ed, Hoboken NJ: John Wiley & Sons, pp.1–43

Olzowy B, von Gleichenstein G, Canis M and Mees K 2008 Distortion product otoacoustic emissions for assessment of intracranial hypertension at extreme altitude? *Eur. J. Appl. Physiol.* **103** 19–23

Piper I 1997 Chapter 6 Intracranial pressure and elastance In Reilly P and Bullock R (eds) *Head Injury*. London: Chapman & Hall.

Piper I, Barnes A, Smith D and Dunn L 2001 The Camino intracranial pressure sensor: is it optimal technology? An internal audit with a review of current intracranial pressure monitoring technologies *Neurosurgery* **49** 1158–65

Pople I K, Muhlbauer M S, Sanford R A and Kirk E 1995 Results and complications of intracranial pressure monitoring in 303 children *Pediatr. Neurosurg.* **23** 64–7

Popovic D, Khoo M, and Lee S 2009 Noninvasive monitoring of intracranial pressure *Recent Patents on Biomedical Engineering* **2** 165–79

Pranevicius O, Pranevicius M, Pranevicius H, Marcinkevicius E and Liebeskind D S 2012 *Noninvasive method to measure intracranial and effective cerebral outflow pressure* U.S. Patent 8,109,880

Quincke H 1891 Lumbalpunktion des hydrocephalus *Berl. Klin. Wochenschr.* 929–33

Raboel P H, Bartek J, Andresen M, Bellander B M, and Romner B 2012 Intracranial pressure monitoring: invasive versus non-invasive methods—a review *Crit. Care Res. Pract.* **2012** ID 950393

Ragauskas A, Daubaris G, Dziugys A, Azelis V and Gedrimas V 2005 Innovative non-invasive method for absolute intracranial pressure measurement without calibration *In Intracranial Pressure and Brain Monitoring XII* (Springer; Vienna) pp. 357–61

Ragauskas A, Daubaris G, Ragaisis V and Petkus V 2003 Implementation of non-invasive brain physiological monitoring concepts *Med. Eng. Phys.* **25** 667–78

Ragauskas A.and Daubaris G 1995 *Method and apparatus for non-invasively deriving and indicating of dynamic characteristics of the human and animal intracranial media* U.S. Patent 5,388,583

Rai P and Varadan V K 2010 March Organic electronics based pressure sensor towards intracranial pressure monitoring *SPIE Smart Structures and Materials Nondestructive Evaluation and Health Monitoring* 764617

Rajajee V, Vanaman M, Fletcher J J and Jacobs T L 2011 Optic nerve ultrasound for the detection of raised intracranial pressure *Neurocrit. Care* **15** 506–15

Raju S, Wu R, Chan M and Yue C P 2014 Modeling of mutual coupling between planar inductors in wireless power applications *IEEE Transactions on Power Electronics* **29** 481-90

Rangel-Castillo L, Gopinath S, and Robertson C S 2008 Management of intracranial hypertension *Neurol. Clin.* **26** 521–41

Rebolleda G and Munoz-Negrete F J 2009 Follow-up of mild papilledema in idiopathic intracranial hypertension with optical coherence tomography *Invest. Ophth. Vis. Sci.* **50** 5197–200

Reid A, Marchbanks R J, Bateman D E, Martin A M, Brightwell A P and Pickard J D 1989 Mean intracranial pressure monitoring by a non-invasive audiological technique: a pilot *study J. Neurol. Neurosur. Ps.* **52** 610–2

Reina M A, Lopez-Garcia A and Dittmann M 1996 Structural analysis of the thickness of human dura mater with scanning electron microscopy *Revista espanola de anestesiologia y reanimacion*, **43**(4) pp.135-7

Rosenberg J B, Shiloh A L, Savel R H and Eisen L A 2011 Non-invasive methods of estimating intracranial pressure *Neurocrit. Care* **15** 599–608

Rosenfeld J G Watts C and York D H 1986 *Method and apparatus for intracranial pressure estimation* U.S. Patent 4,564,022

Ross N and Eynon C A 2005 Intracranial pressure monitoring *Trends in Anaesthesia & Critical Care* **16** 255–61

Rossi S, Buzzi F, Paparella A, Mainini P and Stocchetti N 1998 Complications and safety associated with ICP monitoring: a study of 542 patients *Acta Neurochir Suppl.* **71** 91–3

Saladino A, White J B, Wijdicks E F and Lanzino, G 2009 Malplacement of ventricular catheters by neurosurgeons: a single institution experience *Neurocrit. Care* **10** 248–52

Savini G, Bellusci C, Carbonelli M, Zanini M, Carelli V, Sadun A A and Barboni P 2006 Detection and quantification of retinal nerve fiber layer thickness in optic disc edema using stratus OCT *Arch. Ophthalmol.* **124** 1111–7

Schade R P, Schinkel J, Visser L G, Van Dijk J M C, Voormolen J H and Kuijper E J 2005 Bacterial meningitis caused by the use of ventricular or lumbar cerebrospinal fluid catheters *J. Neurosurg.* **102** 229–34

Schmidt B, Czosnyka M, Raabe A, Yahya H, Schwarze J J, Sackerer D, Sander D and Klingelhöfer J 2003 Adaptive noninvasive assessment of intracranial pressure and cerebral autoregulation *Stroke* **34** 84–9

Schmutzhard J, Aregger FC, Otieno A, Bunk S, Zorowka P and Schmutzhard E 2013 Release of intracranial pressure leads to improvement of otoacoustic emissions–a case report of a Kenyan child with complicated tuberculous meningitis. *J. Trop. Pediatr.* **59**: 326–9

Shen Q, Stuart J, Venkatesh B, Wallace J and Lipman J 1999 Inter observer variability of the transcranial Doppler ultrasound technique: impact of lack of practice on the accuracy of measurement *J. Clin. Monitor. Comp.* **15** 179–84

Shimbles S, Dodd C, Banister K, Mendelow A D and Chambers I R 2005 Clinical comparison of tympanic membrane displacement with invasive ICP measurements *In Intracranial Pressure and Brain Monitoring XII* (Springer; Vienna) pp. 197–9

Sinha D N 2000 *Method for noninvasive intracranial pressure measurement* U.S. Patent 6,117,089

Skau M, Yri H, Sander B, Gerds T A, Milea D and Jensen R 2013 Diagnostic value of optical coherence tomography for intracranial pressure in idiopathic intracranial hypertension *Graefe Arch. Clin. Exp.* **251** 567–74

Smith M 2008 Monitoring intracranial pressure in traumatic brain injury *Anesth. Analg.* **106** 240–8

Soldatos T, Karakitsos D, Chatzimichail K, Papathanasiou M, Gouliamos A and Karabinis A 2008 Optic nerve sonography in the diagnostic evaluation of adult brain injury *Crit. Care* **12** R67

Speck V, Staykov D, Huttner H B, Sauer R, Schwab S and Bardutzky J 2011 Lumbar catheter for monitoring of intracranial pressure in patients with post-hemorrhagic communicating hydrocephalus *Neurocrit. Care* **14** 208–15

Stehlin E F, McCormick D, Malpas S C, Pontré B P, Heppner P A and Budgett D M 2015 MRI interactions of a fully implantable pressure monitoring device *J. Magn. Reson. Imaging* **42** 1441–9

Steiner L A and Andrews P J D 2006 Monitoring the injured brain: ICP and CBF *Brit. J. Anaesth.* **97** 26–38

Stendel R, Heidenreich J, Schilling A, Akhavan-Sigari R, Kurth R, Picht, T, Pietilä T, Suess O, Kern C, Meisel J and Brock M 2003 Clinical evaluation of a new intracranial pressure monitoring device *Acta Neurochir.* **145** 185–93

Stettin E, Paulat K, Schulz C, Kunz U and Mauer U M 2011 Noninvasive intracranial pressure measurement using infrasonic emissions from the tympanic membrane *J. Clin. Monitor. Comp.* **25** 203–10

Stojanović G, Živanov L and Damnjanović M 2005 Optimal design of circular inductors *Facta universitatis-series: Electronics and Energetics* vol. **18** pp. 57-70

Tan Q, Kang H, Xiong J, Qin L, Zhang W, Li C, Ding L, Zhang X and Yang M 2013 A wireless passive pressure microsensor fabricated in HTCC MEMS technology for harsh environments *Sensors* **13**(8) pp. 9896–908

Taylor G A and Madsen J R 1996 Neonatal hydrocephalus: hemodynamic response to fontanelle compression--correlation with intracranial pressure and need for shunt placement *Radiology* **201** 685–9

Timoshenko S P and Woinowsky-Krieger S 1959 Theory of plates and shells: McGraw-hill)Troedsson N, Sjöland H 2004 A distributed capacitance analysis of co-planar inductors for a CMOS QVCO with varactor tuned buffer stage. Analog Integrated Circuits and Signal Processing **42**.1: 7-19

Tranquart F, Bergès O, Koskas P, Arsene S, Rossazza C, Pisella P J and Pourcelot L 2003 Color Doppler imaging of orbital vessels: personal experience and literature review *J. Clin. Ultrasound* **31** 258–73

Tsivgoulis G, Alexandrov A V and Sloan M A 2009 Advances in transcranial Doppler ultrasonography *Curr. Neurol. Neurosci.* **9** 46–54

Tsung J W, Blaivas M, Cooper A and Levick N R 2005 A rapid noninvasive method of detecting elevated intracranial pressure using bedside ocular ultrasound: application to 3 cases of head trauma in the pediatric emergency department *Pediatr. Emerg. Care* **21** 94–8

Tuettenberg J, Czabanka M, Horn P, Woitzik J, Barth M, Thomé C, Vajkoczy P, Schmiedek P and Muench E 2009 Clinical evaluation of the safety and efficacy of lumbar cerebrospinal fluid drainage for the treatment of refractory increased intracranial pressure: Clinical article *J. Neurosurg.* **110** 1200–8

Verweij B H, Muizelaar J P and Vias F C 2001 Hyperacute measurement of intracranial pressure, cerebral perfusion pressure, jugular venous oxygen saturation, and laser Doppler flowmetry, before and during removal of traumatic acute subdural hematoma *J. Neurosurg.* **95** 569–72

Voss S E, Horton N J, Tabucchi T H, Folowosele F O and Shera C A 2006 Posture-induced changes in distortion-product otoacoustic emissions and the potential for noninvasive monitoring of changes in intracranial pressure *Neurocrit. Care* **4** 251–7

Voulgaris S G, Partheni M, Kaliora H, Haftouras N, Pessach I S and Polyzoidis K S 2005 Early cerebral monitoring using the transcranial Doppler pulsatility index in patients with severe brain trauma *Ann. Transpl.* **11** CR49–52

Wang F, Zhang X, Shokoueinejad M, Iskandar B J, Medow J E, Webster J G 2017 A Novel Intracranial Pressure Readout Circuit for Passive Wireless LC Sensor *IEEE Trans Biomed Circuits Syst.* 11(5):1123-32

Weerakkody R A, Czosnyka M, Zweifel C, Castellani G, Smielewski P, Keong N, Haubrich C, Pickard J and Czosnyka Z 2010 Slow vasogenic fluctuations of intracranial pressure and cerebral near infrared spectroscopy—an observational study *Acta Neurochir.* **152** 1763–9

Weerakkody R A, Czosnyka M, Zweifel C, Castellani G, Smielewski P, Brady K, Pickard J D and Czosnyka Z, 2012 Near infrared spectroscopy as possible non-invasive monitor of slow vasogenic ICP waves *Acta Neurochir Suppl.*: **114** 181–5

Welschehold S, Schmalhausen E, Dodier P, Vulcu S, Oertel J, Wagner W and Tschan C A 2012 First clinical results with a new telemetric intracranial pressure-monitoring system *Neurosurgery* **70** Suppl 44–9

Wiegand C and Richards P 2007 Measurement of intracranial pressure in children: a critical review of current methods *Dev. Med. Child Neurol.* **49** 935–41

Wong S H and White R P 2013 The clinical validity of the spontaneous retinal venous pulsation *J. Neuro-Ophthalmol.* **33** 17–20

Wu X and Ji Z 2007 Non-invasive detection for intracranial high pressure with FVEP picked-up by independent component analysis *Sheng Wu Yi Xue Gong Cheng Xue Xa Zhi* **24** 1015–8

Xu P, Kasprowicz M, Bergsneider M and Hu X 2010 Improved noninvasive intracranial pressure assessment with nonlinear kernel regression *IEEE Trans. Inf. Technol.* 14 971–8

Xue N, Chang S P and Lee J B 2012 A SU-8-based microfabricated implantable inductively coupled passive RF wireless intraocular pressure sensor. *J. Microelectromechanical Syst.* **21**(6) pp. 1338–46

Yang J, Charif A C, Puskas J E, Phillips H, Shanahan K J, Garsed J, Fleischman A, Goldman K, Luebbers M T, Dombrowski S M and Luciano M G 2015 Biocompatibility evaluation of a thermoplastic rubber for wireless telemetric intracranial pressure sensor coating *J. Mech. Behav. Biomed.* **45** 83–9

Yoon H J, Jung J M, Jeong J S and Yang S S 2004 Micro devices for a cerebrospinal fluid (CSF) shunt system Sensors Actuat. A-Phys. **110** 68–76

York D H, Pulliam M W, Rosenfeld J G and Watts C 1981 Relationship between visual evoked potentials and intracranial pressure *J. Neurosurg.* **55** 909–16

York D, Legan M, Benner S and Watts C 1984 Further studies with a noninvasive method of intracranial pressure estimation *Neurosurgery* **14** 456–61

Yost W T and Cantrell J H 2004 *Method and apparatus for non-invasive measurement of changes in intracranial pressure* U.S. Patent 6,761,695

Yue X and Wang L 2009 Deformation of skull bone as intracranial pressure changing *Afr. J. Biotechnol.* **8** 745–50

Zhang et al 2017 Invasive and noninvasive means of measuring intracranial pressure: a review *Physiological measurement* **38**(8) R143

Zhang X 2014 Intracranial Pressure Sensor *Master of Science in Electrical and Computer Engineering, University of Wisconsin-Madison*

Zhao Y L, Zhou J Y and Zhu G H 2005 Clinical experience with the noninvasive ICP monitoring system *Intracranial Pressure and Brain Monitoring XII* (Springer; Vienna) pp. 351–5

Zhong J I, Li Y, Minhui X, Yihua Z 2012 Realization of a comprehensive non-nvasive detection of intracranial pressure analyzer based upon FVEP and TCD *Acta Neurochir. Suppl.* **114** 127–9

Zhong J, Dujovny M, Park H K, Perez E, Perlin A R and Diaz F G 2003 Advances in ICP monitoring techniques *Neurol. Res.* **25** 339–50

Zweifel C, Castellani G, Czosnyka M, Helmy A, Manktelow A, Carrera E, Brady K M, Hutchinson P J, Menon D K, Pickard J D and Smielewski P 2010 Noninvasive monitoring of cerebrovascular reactivity with near infrared spectroscopy in head-injured patients *J. Neurotraum.* **27** 1951-8.